Durham E-Theses

Micro-fabricated devices for manipulating terahertz radiation

MARYAM HAJJI

How to cite:

HAJJI, MARYAM (2018) Micro-fabricated devices for manipulating terahertz radiation. Doctoral thesis, Durham University.

Use policy

Micro-fabricated devices for manipulating terahertz radiation

Maryam Hajji

A Thesis presented for the degree of

Doctor of Philosophy

Department of Engineering

University of Durham

England

July 2018

Dedicated to

To my darling husband, Amir, and my parents

Micro-fabricated devices for manipulating terahertz radiation

Abstract

This thesis reports on the design, fabrication and testing of microstructured devices for the manipulation of terahertz radiation. In particular, there is an emphasis on the fabrication and test of diffractive optics type components; including a surface micromachined, multilevel SU-8 based Fresnel lens and a micromilled aluminium Fresnel Zone Plate Reflector (FZPR). For both of these devices, the focal spot is characterized by measuring the electric field intensity and phase as a function of distance along the optical axis. This is carried out using a THz Vector Network Analyzer with associated free space optics. The results are compared directly with Finite Difference Time Domain simulations. A commercial FDTD solver, Lumerical, is used throughout the thesis. FDTD is first introduced for the design of antireflective subwavelength surfaces. These surface structures are bulk micromachined in silicon and their performance experimentally validated using THz Time Domain Spectroscopy and Durham's THz VNA.

A compact THz VNA based S11 measurement configuration is presented which uses the FZPR and a single parabolic mirror. This reflection configuration is used for the characterization of liquid samples (e.g. water and Isopropyl Alcohol mixtures) in microfluidic channels. Two types of channels are presented; one is formed using bulk micromachined silicon whereas the other type uses acetate films to create low cost, disposable devices. The results from the compact measurement configuration

are compared with those obtained using a more conventional four parabolic mirror transmission arrangement (as found in THz Time Domain Spectroscopy systems). Even in the compact configuration, the alignment of the components is found to be a significant factor in determining the measurement performance. Consequently, a six-axis micropositioner (Hexapod), is used to automatically sweep the reflector with the aim of producing a self-aligning system.

Declaration

The work in this thesis is based on research carried out at the Department of Engineering, Durham University, England. No part of this thesis has been submitted elsewhere for any other degree or qualification and it is all my own work unless referenced to the contrary in the text.

Acknowledgements

Firstly, I would like to express my sincere gratitude to my supervisors Dr Andrew Gallant, Dr Claudio Balocco and Professor Dagou Zeze for the continuous support of my PhD study and related research in THz technology, for their patience, motivation, and immense knowledge. In particular, I would like to thank Andrew for his guidance which helped me in all the time of research and writing of this thesis. I could not have imagined having a better supervisor and mentor for my PhD study. I would like to thank Dr Michael Cooke for his help, ideas and advice in the clean-room.

I wish to thank all my colleagues I have worked with during my PhD work and for all the fun we have had in the last four years. In particular, I am grateful to Iman for his help in Solidworks and sketching some of my thesis images. Also I thank my friends in Durham University.

I would like to thank my family, primary my parents who have believed in me and surrounded me with their love and blessing. Thanks to my sister, Leila who inspired me to step forward for a new challenging life and I am very grateful for all her support and effort to cheer me up.

Finally, my special thanks to my husband Amir for his encouragement

throughout my time at Durham and who has endured the inevitable long-distance life. I am very thankful for his patience on all my stresses during difficult times and I am genuinely grateful for his constant support and love.

Contents

List of Figures

xix

List of Tables

List of publications

Journal Paper

- M. Hajji, J. Hammler, D. Zeze, C. Balocco, and A.J. Gallant, "Field imaging near to the surface of terahertz reflective optics using a vector network analyzer", Applied Optics, 56(31), 8746-8750(2017).

Conference Papers

- M. Hajji, D. Zeze, C. Balocco, and A.J.Gallant, "Microfabrication of SU-8 Fresnel lenses for THz imaging", IMMEA Conference, Marrakech-Morocco, 2015.

- M. Hajji, Y. Pan, J. Hammler, D. Zeze, C. Balocco, and A.J.Gallant, "Microfabrication of SU-8 Fresnel lenses for THz imaging", In Terahertz, RF, Millimeter, and Submillimeter-Wave Technology and Applications IX (Vol. 9747, p. 97470N), International Society for Optics and Photonics, 2016.

- M. Hajji, D. Zeze, C. Balocco, and A.J. Gallant, "Artificial microstructured dielectric layers for terahertz applications" In Infrared,

Millimeter, and Terahertz waves (IRMMW-THz), 41st International Conference on (pp. 1-2)IEEE, 2016.

- X. Raimundo, M. Hajji, A. Klein, C. Balocco, A.J. Gallant, and S. Salous, "Channel characterisation at THz Frequencies for high data rate indoor communications ", 12th European Conference on Antenna and Propagation (pp. 1-2)IEEE, 2018.

List of Abbreviation

ADL	Artificial Dielectric Layer
CW	Continuous Wave
DMSO	Dimethylsulfoxide
EBG	Electromagnetic Band Gap
EO	Electro-Optic
FDTD	Finite Difference Time Domain
FEM	Finite Element Method
FFT	Fast Fourier Transform
FIR	Far Infrared
FZPR	Fresnel Zone Plate Reflector
FMM	Fourier Model Method
FSS	Frequency Selective Surfaces
GaAs	Gallium Arsenide
HDPE	High-Density Polyethylene
HDMS	Hexamethyldisilazane
HF	Hydrofluoric acid

IF	Intermediate Frequency
IMPATT	IMPact Avalanche and Transit Time
InSb	Indium Antimonide
LO	Local Oscillator
LT-GaAs	Low Temperature-GaAs
MW	Microwave
n	refractive index
NIR	Near Infrared
PCA	Photoconductive Antenna
PEC	Perfect Electric Conductors
PML	Perfectly Matched Layer
QCL	Quantum-Cascade lasers
RF	Radio Frequency
RMS	Root Mean Square
Rx	Receiver
SEM	Scanning Electron Microscopy
Si	Silicon
SI-GaAs	Semi-Insulating GaAs
SNR	Signal-to-Noise Ratio
Ti	Titanium
THz	Terahertz

THz-TDS	THz Time Domain Spectroscopy
TMM	Transfer Matrix Method
Tx	Transmitter
SEM	Scanning Electron Microscopy
VNA	Vector Network Analyzer
ZnTe	Zinc Telluride

Chapter 1

Introduction

The terahertz region of the electromagnetic spectrum is typically defined as frequencies between 100 GHz and 10 THz. Due to the lack of coherent sources, this region has remained unexplored for many years compared to its nearest neighbours, the microwave and infrared regions.

One hundred years after first quantitative measurement of the heating power of the sun in both the visible and the near-infra-red regions by Sir William Herschel, Heinrich Rubens and his group in Berlin carried out the first experiments in the far infrared (FIR) region for so-called 'longer wavelength radiation 'in 1893 [1]. In 1911, the mercury arc lamp was demonstrated to be an excellent long-wavelength infrared source which, to this day, is still a preferred source for the grating interferometer and has the equivalent black-body temperature of over 4000K in the THz region [2]. Between 1920 to 1940, many FIR research papers were published which had a particular emphasis on the absorption bands of gases. In 1935, Benedict et al published a complete spectrum of water vapour absorption up to 170 μm [3, 4].

By 1947, Marcel Golay had invented the pneumatic infrared detector [5].

Twelve years later, the first cooled detector, a carbon bolometer, and the first photoconductive detector for long wavelengths were invented [6, 7]. Progress in detector development continued in the 1960s with the invention of the n-InSb electron bolometer [8]; and the germanium bolometer [9].

An important development in this period was the high powered far-infrared laser (the water vapour laser) [10]. From this followed the optically pumped far-infrared laser [11] to produce output at many wavelengths throughout the THz region. Since then, THz laser facilities have been installed globally. A major breakthrough in compact THz laser sources was the development of the quantum cascade laser with the first reported example producing radiation up 4.4 THz with a pulsed power of 2 mW [12].

In the last 30 years of development in terahertz technology, the need for the generation and detection of terahertz radiation gave rise to a technique, which is known as terahertz time-domain spectroscopy (THz-TDS). The emergence of THz-TDS systems enabled the generation and detection of picosecond pulses in the time domain. Frequency components are obtained using Fast Fourier Transforms. More recently, a conventional microwave measurement technique, using Vector Network Analyzers (VNA) has been developed to operate at THz frequencies. Schottky diode based multiplier heads can be coupled with microwave (GHz) VNAs to enable S parameter measurements above 1 THz.

Research in the terahertz region has led to novel applications in terahertz technology such as spectroscopy, imaging [13] and communication. Another interesting application of terahertz radiation is in biochemical science for the

2

analysis of DNA and protein structure [14]. Since the terahertz band is sandwiched between the infrared and microwave regions there have been many attempts to utilize the attributes of the terahertz band which are common in both neighbouring bands. Some of the properties of the terahertz region can be described as follows: the wavelength of THz radiation is longer than infrared wavelengths, the wavelength of THz radiation is longer than infrared wavelengths and therefore THz radiation is less sensitive to surface roughness based scattering effects which, in turn, can lead to a greater penetration depth ($\sim cm$) versus infrared ($\sim \mu m$). The penetrability of the THz wave makes it a promising alternative to X-ray and ultrasound imaging for the quality control of material [15]. On the other hand, the wavelength of THz radiation is shorter than in the microwave region and this enables smaller features to be distinguished and can probe a wide number of spectral features. It can also probe a wide number of spectral features which has an application in security control. Terahertz imaging technology has a large potential in the field of non-destructive evaluation [16], biology and medical science. Since the terahertz wave can penetrate to a few hundredths of a micrometres in human tissues, it is a good method for surface diagnosis in skin, cancer detection and dental imaging [17–19]. Terahertz imaging is also a very powerful imaging method for studying art work, for example, to show the reflection images of hidden paint layers in a painting on canvas. Although different optical techniques have been used to study paintings and their structures, as well as as X-ray radiography, they cannot easily penetrate layers of high density pigments such as lead paint and therefore the layer underneath will be remain unknown. Thus, a terahertz

time-resolved reflectography technique is used which monitors the time delay between reflections of different layers, and the optical thickness of hidden layers can be measured [20]. THz imaging also has potential application in personal screening and security [15, 21]. This thesis focuses on the design, fabrication and testing of microscale structures that can be used to manipulate THz radiation. These structures can be utilized in many of the aforementioned THz applications.

1.1   Structure of Thesis

This thesis is organized as follows: Chapter 2 introduces THz generation and detection methods. Specifically, the THz-Time Domain Spectroscopy (TDS) method is introduced in detail and the Durham configuration, including methods for the reduction of internal reflections, is outlined. This is contrasted with the THz-Vector Network Analyzer (Agilent Technologies N5224A PNA with Virginia Diodes WR1.0-VNAX frequency extension modules) approach. The THz-VNA provides continuous wave (CW) THz radiation and operates directly in the frequency domain with a high spectral resolution.

Chapter 3 presents the finite-difference time-domain (FDTD) simulation techniques which are used in chapters 5 to 7 to evaluate the experimental results. A brief introduction of the Yee algorithm and important simulation parameters such as boundary conditions, geometry, periodic structure have been explained. An artificial dielectric layer is used as an exemplar structure.

Chapter 4 explores the simulated artificial dielectric layer of chapter 3 experimentally. The experimental results for micromachined silicon artificial

dielectrics operating as an antireflection coating with a trapezoidal structure at terahertz frequencies are presented. A double-sided artificial dielectric layer(ADL) is introduced as an antireflection layer at THz frequencies.

Chapter 5 presents the design and fabrication of two examples of diffractive microstructures: i) a multilevel SU-8 micro Fresnel lens and ii) an aluminium the Fresnel Zone Plate reflector. The FDTD solver has been used as a method for designing both structures. First, the electric-field intensity and phase of a transmitted signal through the micro Fresnel lens is measured using the VNA. In the second part, the VNA is used for electric field intensity and phase mapping as a function of distance from the surface of a Fresnel reflector. Measurements obtained by the VNA technique are validated by comparing to the simulation data.

Chapter 6 proposes a new simple integrated configuration for material characterisation measurement. The setup consists of the Fresnel Zone Plate reflector from chapter 5 combined with microfluidic devices based on both acetate films and silicon; measurements are carried out using the THz VNA. A range of samples are analysed, including IPA/water mixtures and coffee/water.

Systematic alignment of the terahertz optical system forms the basis of chapter 7. A novel alignment method using a Hexapod micropositioner with 6 degrees of freedom enabled sweeping of the optical component positions to maximize the signal intensity and maintain the alignment of the THz beam.

Chapter 8 provides the conclusions obtained from this work. The achievements are highlighted. Furthermore, a variety of suggestions for future research topics are proposed.

Chapter 2

Measurement Techniques

The now traditional THz time domain spectroscopy (TDS) arrangement which typically relies on femtosecond laser excitation of a photoconductive source to generate a broadband pulse of terahertz radiation has become the mainstay system for measurements in this region. TDS systems have the ability to resolve a pulsed signal, and associated reflections, in the time domain and where the pulses have a broad spectral bandwidth as well as higher power density. Coherent detection, used in the TDS configuration, leads to an excellent signal to noise but the combination of both laser and THz beam alignment can make it difficult to extract reliable, reproducible electric field and phase information over long measurement runs. Laser beam drift affects both the emitter and receiver performance, introducing a time-varying systematic error that is difficult to remove and leads to unwanted peak signal and bandwidth variation [22].

A THz Vector Network Analyzer (VNA), which relies on a microwave (GHz) source that is frequency multiplied into the THz region, eliminates the need for laser alignment and removes concerns about beam drift. The THz radiation emerges from

and is received by horn antennas which are mechanically coupled to waveguides.

The frequency upmixing process is described in detail in [23], where measurements of the achievable dynamic range are reported as approximately 90 dB, within a rectangular waveguide. The systematic errors introduced by the inclusion of antennas, beam steering mirrors and propagation through the ambient environment have been shown to be negligible by the sensitivity analysis performed in [24]. Following an appropriate calibration procedure, the typical precision of measured scattering-(S-) parameters (complex transmission and reflection) is ± 1 %. Work is ongoing in comparing the system performance of THz-TDS and VNA systems in order to establish full interoperability [25].

The stable nature of the network analyzer's oscillators is well suited for the measurement and characterization of narrowband devices. Measuring directly in the frequency domain provides the ability to rapidly acquire many single-frequency measurements to increase SNR, or to investigate time-variant effects with a continuous wave (CW) source.

There is a need for light, compact and rugged optics to be incorporated into portable THz systems with field applications that include the space sector [26]. These optical components are required to focus, beam shape and to realize devices such as reflectarrays. It is essential that reliable characterization techniques are developed to validate the performance. Ideally, these techniques need to fully reveal the phase and amplitude of the electromagnetic field in the proximity to the components. Direct analysis in the frequency domain is desirable for diffractive components such as zone plates. Source technologies such as Quantum Cascade

Lasers offer excellent power [27] but suffer from limited frequency sweep range compared to a THz-VNA and have yet to be implemented for use in the sub-THz region.

The transmission properties of terahertz (THz) radiation allow for the characterization of many optical components such as microstructures in this regime. The fabrication and characterization of such components in the terahertz region are the main goals of this thesis. This chapter will explain two different experimental techniques for carrying out THz measurements, the use of a vector network analyzer and time domain spectroscopy.

The vector network analyzer, which was developed for lower frequency devices (MHz and GHz frequencies) and recently extended to the higher frequencies (millimetre-wave and THz frequencies), is the main platform for electronics-based THz measurements and operates directly in the frequency domain, and is able to measure the amplitude and phase of a signal interacting with a sample. The calibration procedure necessary for the VNA measurement is also mentioned in this chapter. A typical dynamic range of around 70 dB is achieved by applying narrowband detection of IF (intermediate frequency) measurement signals. The IF signal is produced when the RF (radio frequency) is down-converted through a down-converter by subtracting it from the Local oscillator (LO) frequency.

In THz-TDS, one of the most established techniques in optical THz measurements, the frequency spectrum of the radiated field is obtained by applying a Fast Fourier Transform to the electric field in the time domain. TDS is based on the coherent detection that measures the field amplitude and phase of the

electromagnetic wave.

2.1 The terahertz spectrum

Terahertz radiation is typically described as existing in the region of the electromagnetic spectrum between 100 GHz (3 mm) to 10 THz (30 μm) and, hence, placed between microwave and infrared frequencies [28, 29]. The radiation has a wavelength of 300 μm at 1 THz and photon energy of around 4.14 meV. The electromagnetic spectrum including the terahertz band is shown in fig. 2.1.
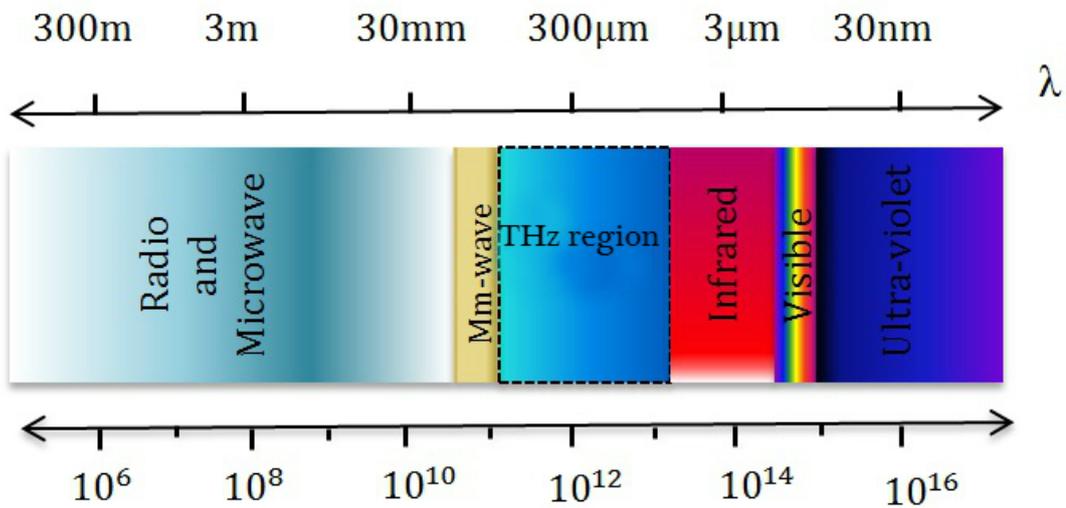
Figure 2.1: The electromagnetic spectrum showing the terahertz region.

2.2 Terahertz Generation and detection

In this section, the generation of THz radiation based on photoconductive antenna sources is explained. In many established terahertz systems, femtosecond laser sources are used to excite optoelectronic sources. Common devices [30] for the generation and detection of THz waves are photoconductive antennas [31] and

electro-optic crystals [32]. Photoconductive antennas consist of two metal antenna electrodes, which are patterned on low-temperature-grown GaAs (LT-GaAs) or semi-insulating GaAs (SI-GaAs). The antenna shape is typically a strip line or bow-tie geometry. A typical photo-conductive antenna is used in Durham's THz-TDS is a bow-tie antenna as shown fig. 2.2. The bow-tie design, which includes sharp electrode ends and a narrow gap, leads to high electric fields and more efficient generation of terahertz (THz) radiation [33]. The sharp edges in bow-tie antenna accumulate more charge which causes the surface charge density to be increased and enhances the electric field such that morecurrent can be generated. The pulse width from a bow-tie antenna is much broader and stronger signal amplitude than the other antenna such as coplanar strip line. The gap size of photo-conductive antenna is an important parameter which can affect the output power from a photoconductive antenna. The geometry of the photoconductive antenna is in the few micrometres (for the small gap) to a few millimetre length scales which is necessary to obtain proper coupling between the free-space electromagnetic field at THz frequencies and the photocurrent. Smaller gap antennas with the gap size of 5-50 μm perform better than the large gap with the gap size of 0.1-5 mm antenna even if more optical power can be applied to the larger gap antenna [34]. With small gap antennas, broader spectral ranges can be achieved compared to the larger gap antennas and the spectral characteristics are dependent on the electrodes' geometry(large electrodes dissipate the heat generated by photo-current). The main advantage of the large gap antenna is ease of fabrication, better dissipation of heat due to the larger deposited electrode area

and the possibility of higher THz power compared to the small gap antenna (but with a larger bias voltage) before saturation and break down of the device.
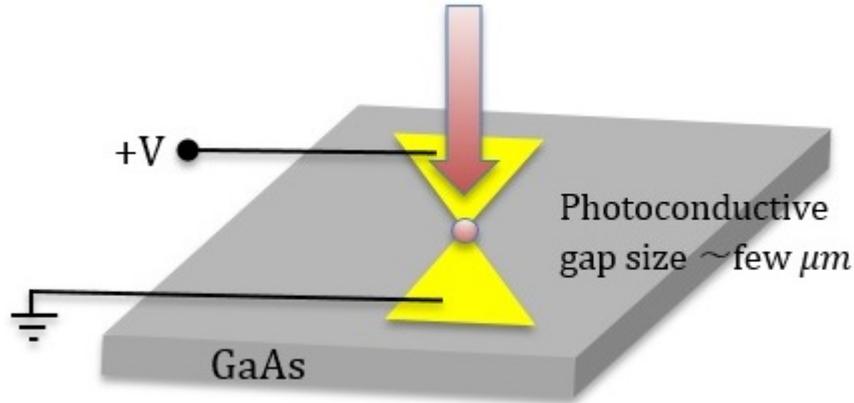
Figure 2.2: Sketch of a bowtie photoconductive antenna.

LT-GaAs is more suitable for THz antenna materials compared with SI-GaAs due to its shorter carrier lifetime (three orders of magnitude smaller); the carrier lifetimes of LT-GaAs and SI-GaAs are sub picosecond and sub-nanosecond, respectively [35].

LT-GaAs substrates have a very high breakdown field, sub-picosecond carrier lifetime and a good mobility; hence, it is one of the best materials for the fabrication of photoconductive devices [36]. For generating THz pulses, an external electric field is applied across the electrode's gap to accelerate the photocarriers. When the photoconductive gap is illuminated by femtosecond laser pulses with energy greater than the band gap energy of the semiconductor, electrons and holes are generated [37]. When the PC antenna's gap is illuminated by a laser pulse, the resistance drops by several orders of magnitude. The photocarrier generation varies with time and can yield electromagnetic pulses, in the far field, produced by a Hertzian dipole; the radiated electric field is proportional to the time derivative of

the current, $dI_{pc}(t)$:

$$E_{THz}(t) \propto \frac{dI_{pc(t)}}{dt}, \tag{2.1}$$

where E_{THz} is the THz electric field and I_{pc} is the photocurrent generated in the gap which can also be proportional to the current density, J_{pc} as

$$E_{THz}(t) \propto \frac{\partial I_{pc}(t)}{\partial t} \propto \frac{\partial J_{pc}(t)}{\partial t} \tag{2.2}$$

In order to detect the low power (pulse order of) μW [38] produced by the photoconductive antenna, a very efficient detector is needed [39]. When an electro-optic crystal [40] is used as a detector, the electric field induced by the incident terahertz radiation changes the birefringence in the EO crystal. Birefringence occurs in anisotropic crystalline materials and the refractive index of optical medium changes for polarisations along the different axes of crystal. Figure 2.3 shows a photograph of a mounted ZnTe crystal with a thickness of $200~\mu m$. A near infrared (NIR) femtosecond laser beam illuminates the crystal, along with the incident THz radiation.
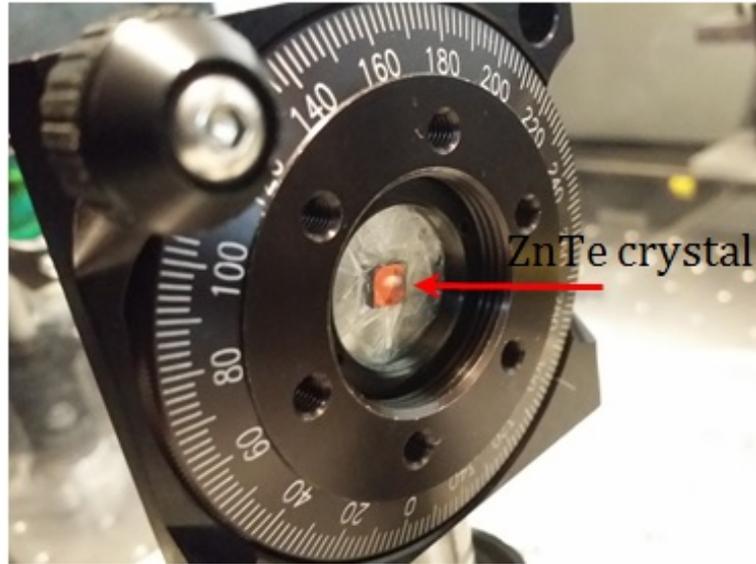
Figure 2.3: Photo of a mounted ZnTe crystal with a thickness of 200 μm.

When there is no external incident THz field, the polarisation of the NIR pulse remains unchanged (it is linearly polarised). If this linearly polarised pulse is then passed through a quarter wave plate, it will be circularly polarized. In fact, the linearly polarised beam co-propagates inside the crystal with the terahertz beam. In the presence of an external electric THz field, the femtosecond pulse is polarized elliptically after the quarter wave plate. After that, passing through a Wollaston prism, the elliptically polarized beam is split into two unequal components which can be detected and their intensity measured by a pair of balanced photodiodes. Commonly used EO crystals for nonlinear optical detection are ZnTe [29].

Figure 2.4 shows a diagram of the terahertz detection based on the EO crystal where the I_0 shows the optical pulse intensity and the $\Delta\varphi$ represents the phase difference caused by the Pockel's effect. The sensitivity of the detector to incoming THz detection depends on the thickness of the crystal. The bandwidth of the detector also relies on the crystal thickness where the thinner crystal displays the larger bandwidth. The sensitivity of THz detection decreases similarly for all frequencies

13

within the bandwidth with reducing crystal thickness [41].
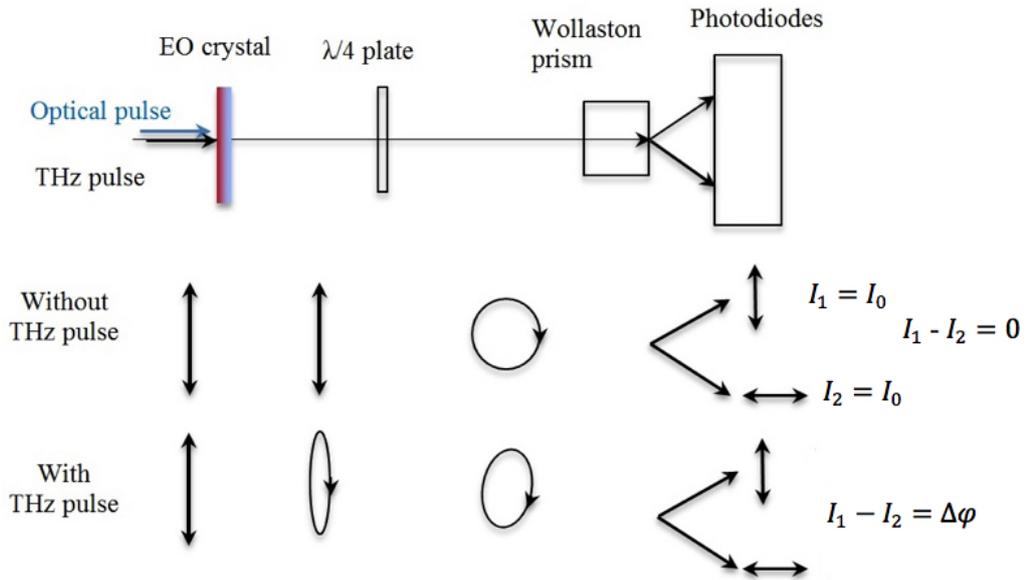
Figure 2.4: Diagram of THz detection where the wave propagates through an EO crystal. I_0 is the optical pulse intensity and $\Delta\varphi$ is the phase delay due to the Pockels effect [42].

2.3   Terahertz sources

Terahertz radiation was first observed about hundred years [43] ago but this region has been limited by the availability of powerful, coherent radiation sources. This, however, has been changed in recent years due to the rapid development of terahertz sources such as solid-state oscillators [43], quantum cascade sources [41] and optically pumped solid state lasers [44]. For a better understanding of the historical developments that have led to new THz sources, we need to appreciate the research that has been carried out, which has moved both RF/microwave and optical technologies towards the THz frequency region [45].

Terahertz sources can be categorised in three different groups: (1) RF/microwave sources (2) optical sources and (3) a combination of the RF/Microwave and optical

technologies.

In the RF/microwave sources category, diodes and THz vacuum tubes can be considered. There are several type of diodes such as high frequency Gunn [46], IMPATT [47] and resonant tunnelling diodes. These types of devices are compact and can operate at room temperature. However, by increasing the frequency of these types of sources, the power will also be decreased. Figure 2.5 shows the RF power performance of microwave solid-state devices versus frequency. The RF performance of the solid-state devices is lower than electronic vacuum devices due to the low applied bias, decreased electron velocity in semiconductors and thermal limitations [48].
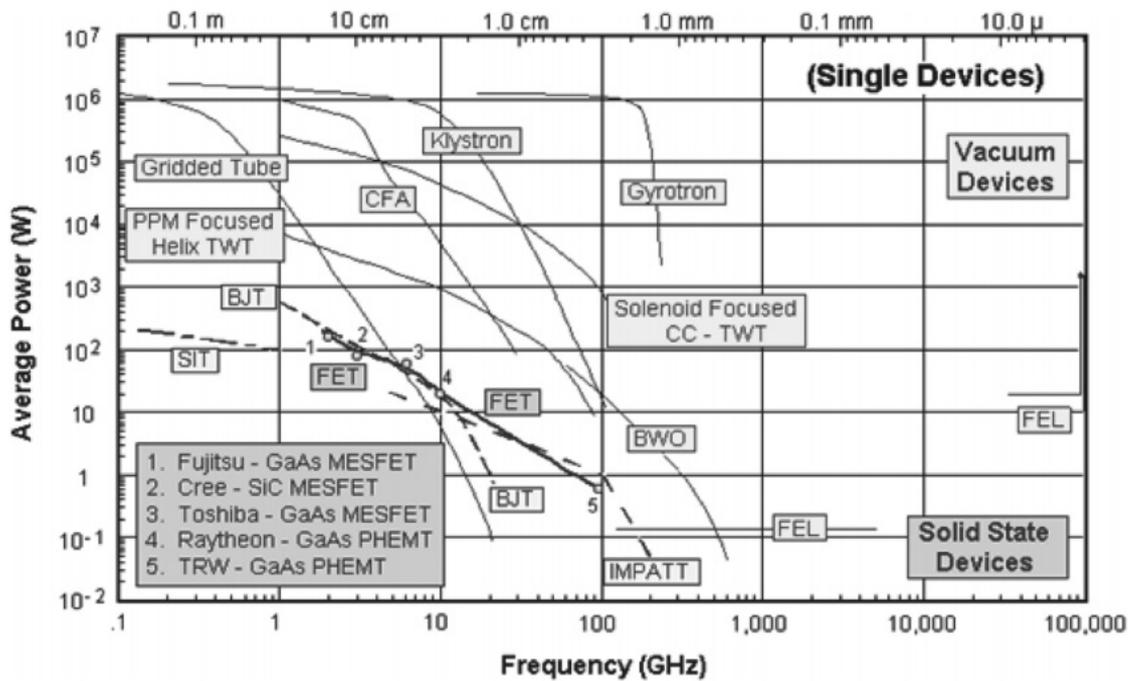
Figure 2.5: Average RF output power versus frequency for electronic devices [48]

Free electron sources such as Klystrons and Backwards Wave Oscillators (BWO) have been developed in order to operate at the high frequency end of the microwave spectrum but these kinds of sources have problems with scaling, lossy metallic walls and the need for high magnetic fields [47, 49].

Terahertz sources from the optical side can be categorised into two groups: laser sources such as molecular lasers and, recently, THz quantum-cascade lasers (QCL) and nonlinear crystals. Although the semiconductor diode lasers have been developed in the near-infrared and visible regions, to operate in the terahertz band, materials needed to be artificially engineered via bandgap engineering. Because of the lack of suitable semiconductors, the light generated by radiative recombination of carriers across the bandgap of the active material cannot be extended into the mid infrared [50]. Therefore, quantum cascade lasers have been introduced, with several layers of semiconductor heterostructures, using the concept of inter-sub-band or inter-mini-band transition, to generate light in the mid-infrared and then into the far infrared, now known as the THz region [45]. Their operating frequency can be controlled by engineering the band gap which has ranged from 0.84 THz to 5 THz at different cryogenic temperatures [51,52] with a peak optical power about 200mW at 4.5 THz [53]. Another method for THz generation involves nonlinear crystals with a high second order susceptibility for down conversion. One of the optical down-conversion methods is optical rectification where a visible/near infrared pulse illuminates a semiconductor crystal and induces a second-order susceptibility of the crystal, producing spectrally broad optical pulses up to THz frequencies. As a combination of RF/microwave and optical techniques, a photoconductive antenna

as an optoelectronic device can be used as a THz source. These kinds of sources
which are micro-fabricated on a photoconductive substrate (normally LT-GaAs) rely
on voltage-biased antennas. Ti:Sapphire femtosecond NIR laser pulses are normally
used for the excitation of THz antenna gap to produce THz waves. Depending on
the excitation source, these photoconductive antennae can be used in both pulsed
systems and continuous wave (CW) systems [54].

The CW system, as with the pulsed system, is a coherent method but for
spectroscopy applications that need a very narrow linewidth, this technique can
offer a better frequency resolution than a pulsed system [55].

2.4   Terahertz time domain spectroscopy (THz-TDS)

Terahertz time-domain spectroscopy (THz-TDS) is recognised as a key
spectroscopic technique to provide properties of materials using short pulses of
terahertz radiation. In time domain spectroscopy, the measurement is performed
directly in the time domain by varying the time-delay between the THz and optical
pulse using a delay stage, and this allows terahertz frequency interactions to be
explored on picosecond timescales. The delay stage is moving in discrete spatial
steps Δx, which corresponds to the time steps of

$$\Delta t = \frac{2\Delta x}{c}, \tag{2.3}$$

where c is the speed of light, for each data point on the delay stage the signal can be
defined as $E(t) = n\Delta t$ and $n = 1, 2, ..., N$. By Fast Fourier transforming (FFT) the

electric field signal, the frequency spectrum of the radiated field is obtained which consist of discrete values, where the frequency resolution is given by

$$\Delta\nu = \frac{\Delta t}{N}. \tag{2.4}$$

The data measurement can be post-processed with the proper signal processing techniques in order to obtain optical frequency-dependent properties e.g refractive index. When undertaking THz-TDS measurements, the waveform of the THz pulse is compared with the free space reference. A sample waveform is different to the reference waveform due to the refractive index of sample. There are other parameters which affect the magnitude of the sample waveform such as the reflection at each interface and absorption inside the sample.

2.4.1 Durham TDS system

The schematic diagram and experimental setup of a typical pulsed THz wave generation and detection setup is shown in fig. 2.6. In this setup, the THz photoconductive antenna is used as the emitter and a ZnTe crystal with a thickness of 200 μm (EO crystal) is employed as the detector. The emitter is an antenna with a 50 μm gap between the two electrodes on a SI-GaAs substrate of 350 μm thickness. A mechanical (optical) chopper is used to modulate the laser pump beam at a rate of 2.6 kHz which is used as a reference for lock-in amplifier. The antenna is a small gap design [56], and a larger bandwidth can be achieved compared to large gap emitters [34]. The excitation source is a Femtolasers Ti:Sapphire laser with an average power of 500 mW, pulse repetition rate of 75 MHz, and a pulse

width of < 20 fs. A beam splitter is used to split the laser pulses into the emitter (pump pulse) line and the detector line (probe pulse). The pump beam is used to generate the THz pulse and the probe beam is used to receive the pulse. The photoconductive antenna is illuminated by the laser pulses and the generated THz waves are coupled out of the antenna from the substrate side.

The radiation is then collected and focused using 90° off-axis parabolic mirrors in the set up to a ZnTe crystal for detection. In the detector line, a time delay line which consists of a pair of corner reflector mirrors and a linear displacement stage is used and permits variation of the optical path length and, as a result, introduces a phase shift between the probe pulse and the pump pulse. The THz pulse passes through the EO crystal, which affects the polarisation of the probe pulse, as described earlier, with an output from a balanced photodetector measured by a lock-in amplifier. The pulse information is obtained in the time domain, which can be transferred to the frequency domain using a Fast Fourier Transform (FFT). Since THz signals are sensitive to water vapours, a terahertz measurement is typically enclosed and purged with nitrogen gas.
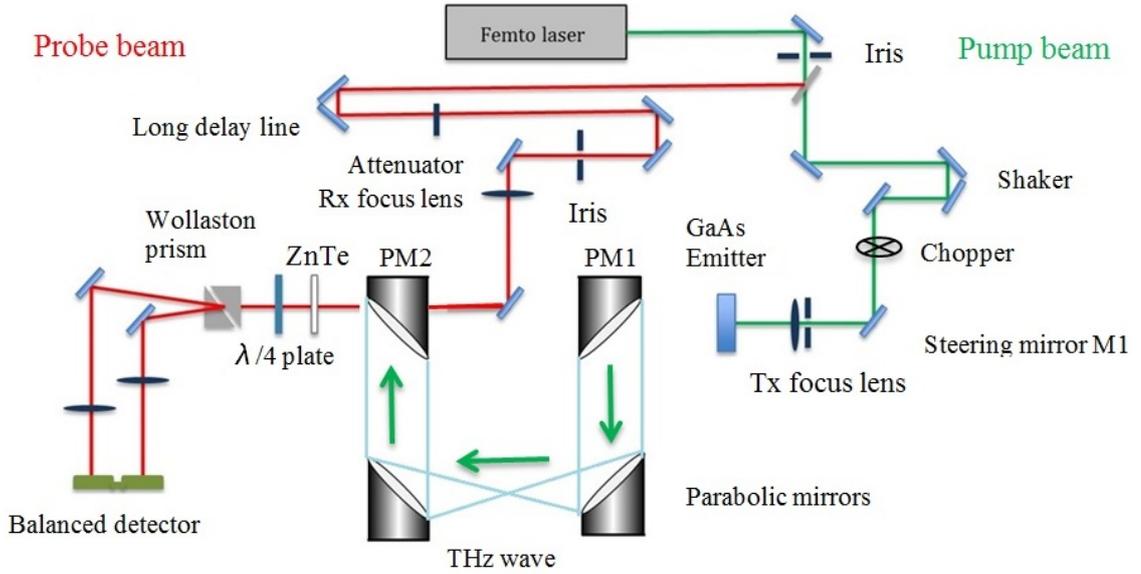
Figure 2.6: Schematic diagram of the THz pulsed set-up including optical components with a photoconductive antenna as an emitter and an EO crystal as detector.

2.4.2   THz-TDS Reference Pulse

A terahertz TDS measurement typically starts with a reference scan for which there is no sample mounted in the system i.e. free space. For a transmission measurement, the sample is placed in the collimated beam. When no sample is present, an iris can be placed at the focal point of the parabolic mirrors to find out the THz beam size and suppress the lower frequencies in the measurements Figure 2.7 shows a THz-TDS reference pulse with three reflections at times of 8, 15 and 23 ps at A, B and C respectively. The first oscillation could be from internal reflections of the emitter substrate; the source of the third oscillation could be the ZnTe crystal (detector). The reflections can be removed or minimized in various ways. One way is to use a hemispherical silicon lens placed on the back of the emitter. The silicon lenses used for this application have a high resistivity which

gives low absorption and low dispersion over the terahertz frequency range [57].
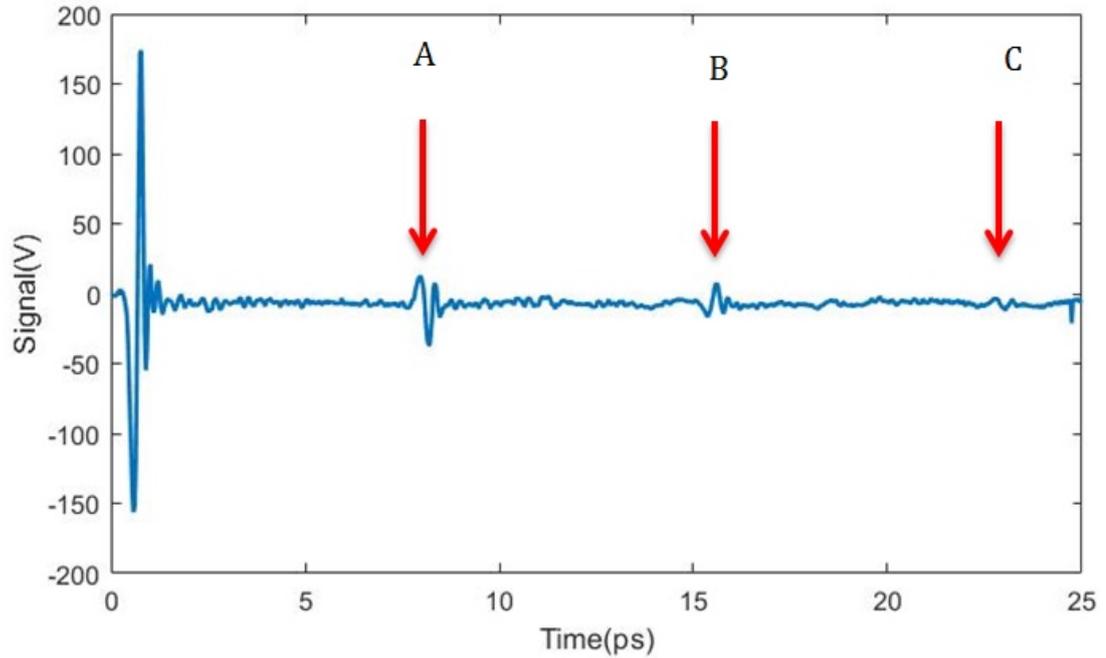
Figure 2.7: THz references pulse in THZ-TDS system.

The LT-GaAs emitter and high resistivity silicon lens have almost identical refractive indices (3.42 at terahertz frequencies) which minimizes the internal reflection losses. The emitted THz field is collected by a hemispherical silicon lens to obtain a divergent beam which is then collimated and focused by a couple of off-axis parabolic mirrors (PMs). Figure 2.8 shows the effect of a 4 *mm* hemispherical silicon lens place on the emitter, a delay of almost 2 *ps* in the main pulse can be seen and a 14% improvement in the peak voltage when the voltage of 50 V has been applied. The lens with 4 *mm* diameter is mounted on the back side of a 300 *μm* LT-GaAs substrate using S1813 photoresist. Using the silicon lens has removed the additional internal reflections inside the emitter and no secondary pulses have been observed. The lenses in the system introduce a delay which shifts the secondary pulse.
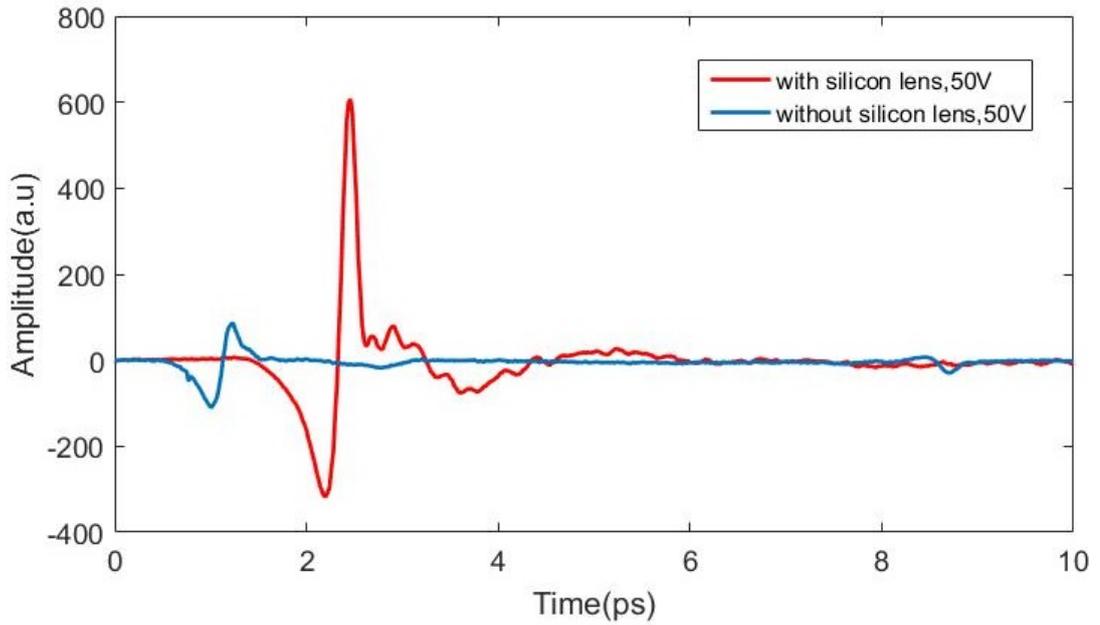
Figure 2.8: Effect of a 4mm hemispherical silicon lens in THz beam without a sample.

In the time domain, the change in the pulse shape is an important factor for analyzing a sample's interaction with the THz pulse which also affects the frequency domain characterization of the samples. As we already mentioned the FFT is utilized to convert between the time domain and frequency domain. The sample interval, T, and the truncation length are an important factor for introducing the second modification of FFT.

If the waveform is sampled at the frequency of at least twice the maximum frequency component, no information will be lost due to sampling.

The modified transform differs from the original(continuous)transform because of sampling. The truncation function of the continuous data set introduces ripples into the frequency domain. If the truncation (rectangular) function is increased in length, then the function approaches an impulse, the less ripple or error is introduced from truncation.

22

To reduce the ripple effect, it is desirable to choose the length of the truncation function, or sample length, as long as possible. There are various functions to reduce the ripple effect or error caused by a finite length such as rectangular, triangular, Hann and Hamming windowing. For instance, applying the windowing functions changes the results of the frequency domain by multiplying each data point by a value between zero and one and reducing the amplitude of each data point, results in reducing the amplitude of the discontinuities in the FFT in the time domain [58].

2.5 Vector network analyzer

Vector network analyzers are commonly used for measuring scattering (S-) parameters and are important measurement instruments at microwave and millimetre wave frequencies. The accuracy of vector network analyzers depends on the source, receivers and the calibration methods that can be used. Durham University has a THz frequency Vector Network Analyzer (Agilent Technologies N5224A PNA with Virginia Diodes WR1.0-VNAX frequency extension modules). The WR1.0-VNAX extension modules are the current state-of-the-art in mm-wave metrology systems and have an operating range from 0.75 to 1.1 THz. A WR1.0H diagonal horn antenna with an 11° divergence and horizontal polarization is coupled to each extension module waveguide [24]. A sketch of the vector network analyzer is shown in fig. 2.9.
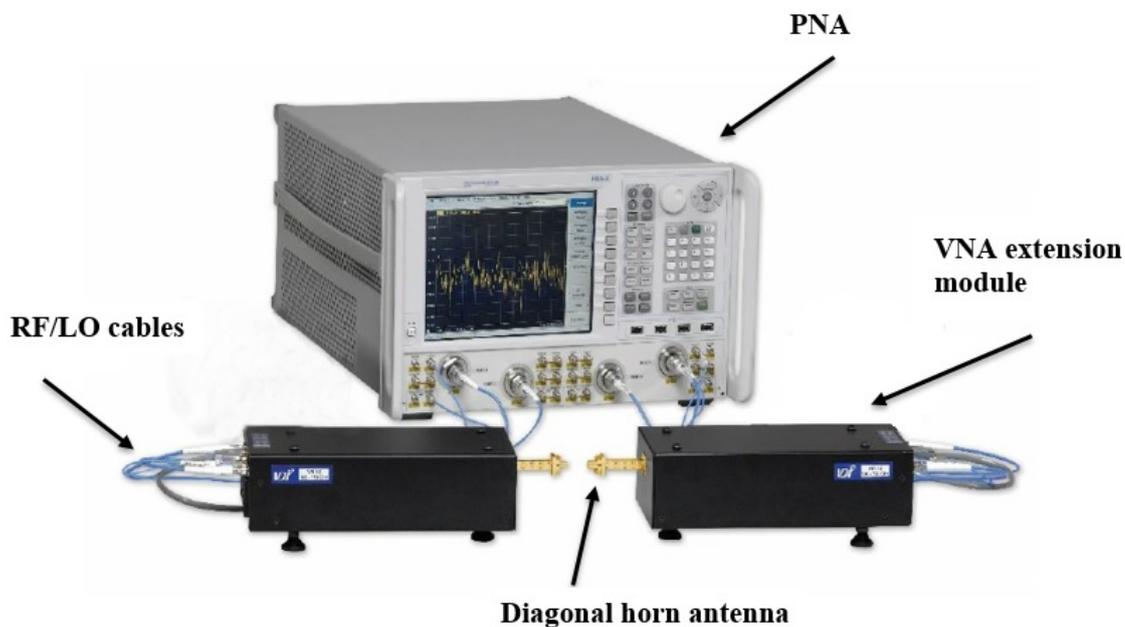
Figure 2.9: Schematic diagram of the THz VNA used at Durham.

Figure 2.10 shows a WM-250(WR-1.0) waveguide with the (a) diagonal horn antenna (b) aperture diameter of 1.6 mm and (c) length of 16 mm.
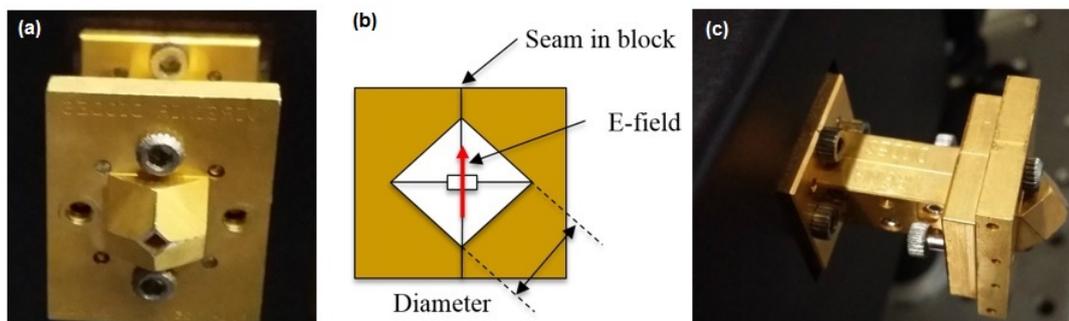
Figure 2.10: WM-250(WR-1.0) waveguide (a) diagonal horn antenna (b) aperture diameter (c) 16 mm waveguide length.

The extender consists of a transmitter and receiver. The transmitter consists of an amplifier followed by a series of multipliers. The couplers at the transmitter output are used to sample the input and output signals' power that is received from the test port. The input power could be a signal transmitted and reflected

off the device under test (e.g. S11) or a signal transmitted through the DUT (e.g. S21). The receiver part also consists of an amplifier and multipliers that generate the Local Oscillator (LO) signal power and a subharmonic mixer for decreasing LO noise. The mixer converts signal power from one frequency band to another preserving the signal phase and amplitude information through an intermodulation process with the LO signal.

Figure 2.11 shows a schematic of the VDI extender head which consists of Schottky diode based, frequency doublers and triplers. The frequency doublers are passive microwave (MW) components that create an output signal with a frequency which is larger than that of the input signal. The output is a harmonic signal which is driven through a bandpass filter to select the desired harmonic (multiplied) signal. Subharmonic mixers are composed of a passive mixer with a subharmonically pumped ($\times 2$) local oscillator. These mixers permit the use of a low LO frequency, which eases the need to generate a high-frequency LO signal. For high-frequency application design, Analog Devices subharmonic mixers offer a simpler alternative to traditional mixers but with no LO multiplier to suppress conversion loss of the local oscillator and increase output power yielding to the output frequency generated by the VNA [23, 24]. For calibration of the VNA short, open, load, and through (SOLT) WR1.0 waveguide standards were used with a calibration kit.
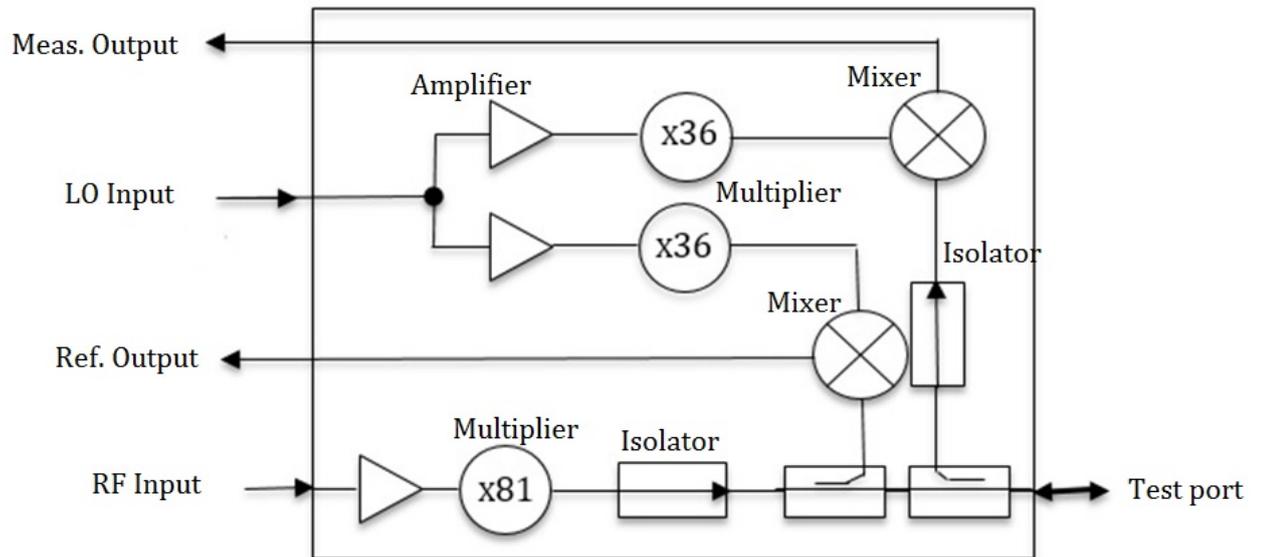
Figure 2.11: VDI TxRx frequency extender configuration [23].

2.5.1   Dynamic range

One important factor to establish the measurement performance of many types of microwave devices such as network analyzers consists of knowing its highest possible dynamic range. However, to obtain the highest dynamic range from the measurement system, it is essential to understand what is meant by the dynamic range in this context and the methods that can improve it.

Dependent on measurement application, there are two different dynamic ranges: system dynamic range and receiver dynamic range. The difference between the highest input power level P_{max}, with no error and the minimum input power level P_{min}, that the system can measure, which is set by receiver's noise floor, is known as the receiver's dynamic range. The receiver's dynamic range is considered as the system's real dynamic range if an external amplifier added to the system or a device under test is considered in the measurement system. The difference between the

available nominal power at the test port of the VNA, P_{ref} , and the minimum input

power P_{min} , is shown as the system dynamic range.

The system dynamic range can occur when there is no amplification such as

when measuring passive components: in this case, the power difference between

the nominal power available at the test port from source and minimum input power

shows the system dynamic range. Figure 2.12 shows the system dynamic range based

on the measurement application [59]. The noise floor is an important parameter

which can help to determine the dynamic range; there are different ways to define the

noise floor of the system. One way is to calculate the RMS power of a signal during

the measurement. Figure 2.13 depicts the noise floor and transmission between four

parabolic mirrors without any sample in the system. By calculating the RMS power

of a signal, the dynamic range of system can be calculated. The dashed line shows

the RMS value of the noise which is equal to the noise floor of -70 dB.
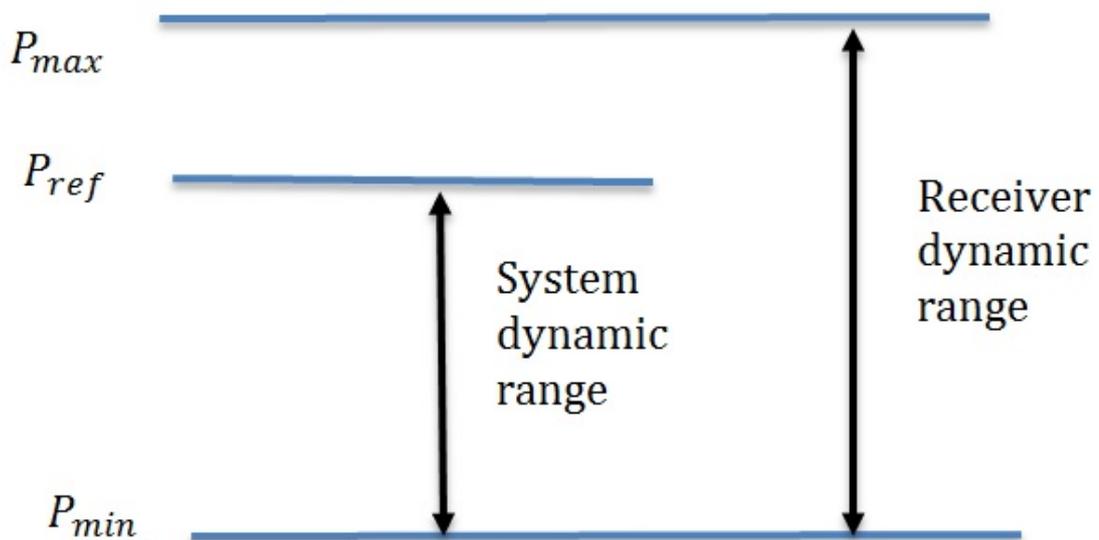
Figure 2.12: The system and receiver dynamic range, Receiver dynamic range = $P_{max} - P_{min}$, System dynamic range = $P_{ref} - P_{min}$ [59].
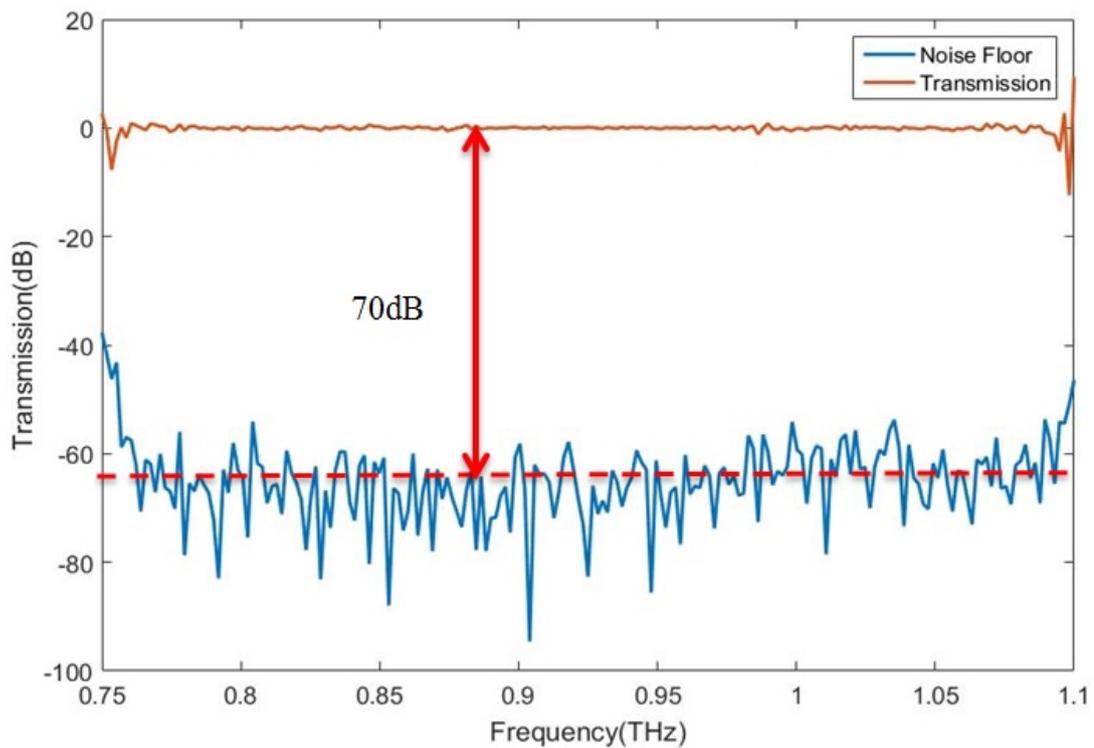
Figure 2.13: Dynamic range for the VNA frequency of 0.75-1.1 THz at 100 Hz IF bandwidth.

The receiver's noise floor is one of the important parameters that helps to determine the dynamic range. The noise floor can be obtained by taking a measurement over the range of 750 GHz to 1.1 THz at different RF bandwidths. By making a setup containing four parabolic mirrors that can both collimate and focus the THz beam between two horn antennas, the transmission losses of the system can be measured. The diagram of the THz system has been shown in fig. 2.14.
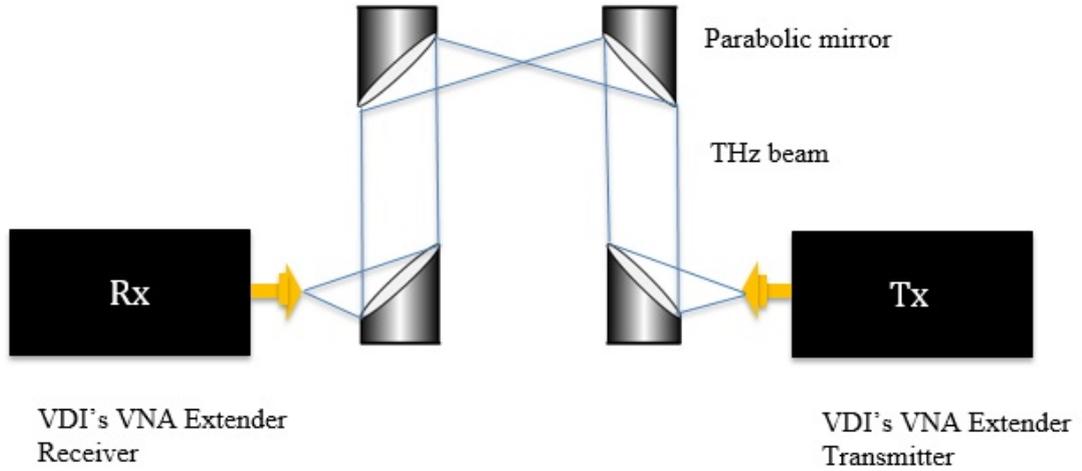
Figure 2.14: Diagram of the THz VNA system with parabolic mirror of 10 *cm* focal point.

It is possible to improve the dynamic range of a VNA, and decrease the noise floor in this setup, by decreasing the intermediate frequency (IF) bandwidth by filtering out noise outside the bandwidth. Reducing the IF bandwidth results in high IF gain. The root of the noise floor in the VNA receiver is the thermal noise which is directly proportional to IF bandwidth. The noise power is given by:

$$P_n = k_B T B \tag{2.5}$$

where P_n is the noise power, k_B is Boltzmann's constant, and T is the absolute temperature in K, and B is the receiver bandwidth in Hz.

Figure 2.15 shows the relation between RMS noise and the IF bandwidth, in which by varying the IF bandwidth, the RMS noise will be changed. The effect of decreasing the IF bandwidth of the normalised signal is shown in fig. 2.15 with offsets of 2 dB and 4 dB, respectively. Another way of improving the noise floor is to carry out multiple averaging of the VNA signal which results in a significant

improvement in the noise floor.
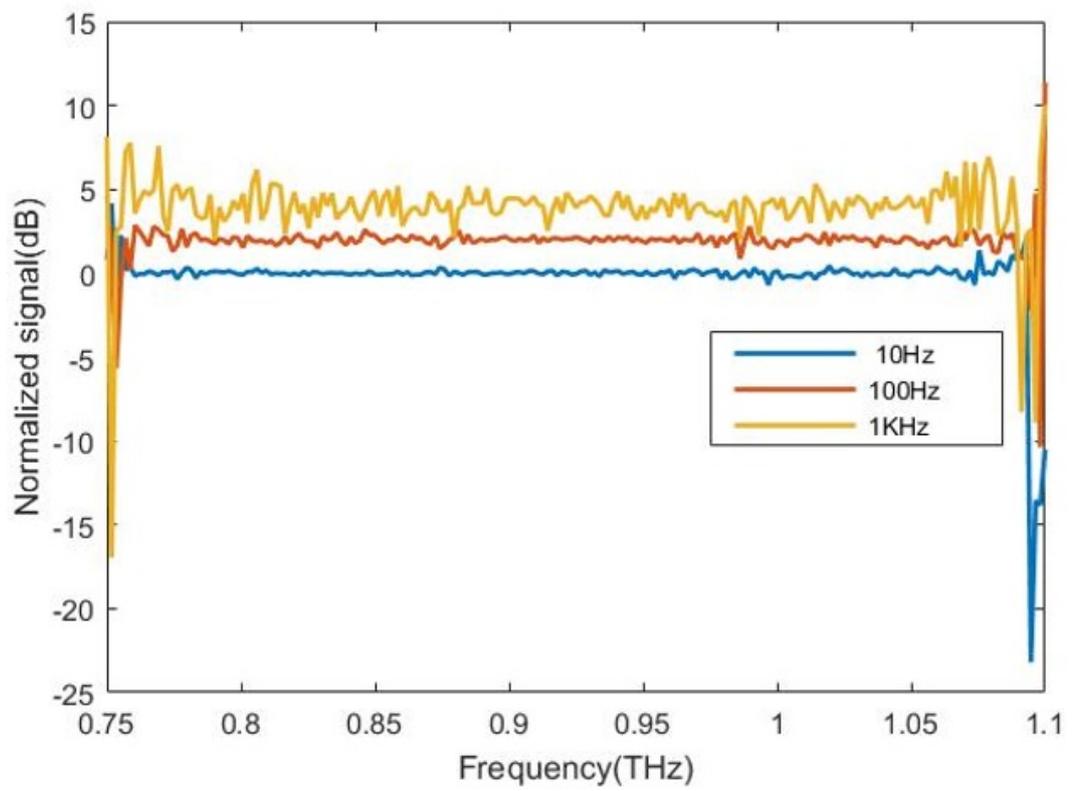
Figure 2.15: The normalized transmission signal at IF bandwidth 10 Hz, 100 Hz and 1 kHz.

2.6 Conclusion

Two different THz measurement techniques TDS-THz and VNA-THz have been presented. The operation area for each system is growing very fast, and even THz technology is transitioning from academic to industrial applications. Powerful measurement methods are needed to support both scientific and industrial applications. There are always some problems with these techniques which need to be pointed out in particular. The principles of operation for each system are largely different. For time domain spectroscopy(TDS), the system calibration, standard measurement set-up and data analysis can be an issue. In VNA, engineering high-precision waveguides is challenging.

The Durham TDS-THz system has been explored, in this system, the generation and detection of THz pulse is based on photoconductive antenna (emitter) and EO crystal(detector). Various source categories based on RF/microwave, optical source and their combination for terahertz generation have been described. A Ti:Sapphire femtosecond NIR laser source is used for producing THz radiation in the TDS-THz system. The THz-TDS measurements are undertaken directly in free space for a reference measurement and by Fast Fourier transforming of data from the time domain into the frequency domain, the amplitude and phase information are obtained. In the TDS-THz measurements, the multiple internal reflections acquired from the emitter substrate or detector are suppressed using a hemispherical silicon lens.

The operation of THz-Vector Network Analyzer (Agilent Technologies N5224A PNA with Virginia Diodes WR1.0-VNAX frequency extension modules)

are also detailed, demonstrating the s-parameters dynamic range and the information extracted directly in frequency domain. In addition to these, although THz-TDS is operating with a larger bandwidth, the information provided by measurement technique should be comparable with the VNA's results for material characterization. Utilizing these two techniques for material characterization and imaging applications is a goal of this thesis.

Chapter 3

Finite-Difference THz Simulations

Over the last few decades, there has been significant progress in computational hardware through both improved processing speed and increased storage. This has opened up new possibilities for the numerical simulation of systems. In electromagnetic simulations, numerical methods play a key role in device and system design. Typical numerical methods include the Transfer Matrix Method (TMM) [60], the Fourier Model Method (FMM) [61], the Finite Element Method(FEM) [62] and the Finite-Difference Time Domain (FDTD) method. Furthermore, the application of Effective Medium Theory(EMT) [63, 64] plays an important role in simulation.

In particular, the FDTD method has been popular for microwave and terahertz applications [65] because of its flexibility in dealing with inhomogeneous, anisotropic materials.

This chapter provides an overview of the FDTD method using the commercial package, Lumerical. The Yee algorithm is briefly introduced, followed by technical aspects of the simulation such as boundary conditions, geometry, handling

periodicity and monitoring the output.   This gives guidelines for the practical implementation of the FDTD method. An artificial dielectric layer(ADL) based on a sub-wavelength structure (rectangular, trapezoidal, triangular) which works as an anti reflection coating is used as an exemplar structure for the technique to show the calculated frequency dependence of its reflection and transmission properties.

3.1   Introduction to FDTD method

The FDTD method is based on solving Maxwell's curl equations.   It is a time domain method and broadband pulse propagation can be simulated without frequency sweeping as is carried out with other techniques. The FDTD algorithm was first introduced by Yee in 1966 and later refined by Taflove [66, 67].

The computational domain, i.e. the physical volume space in which we want to solve for the electromagnetic wave propagation, is discretized both in space and time into a Yee lattice. The 3D Yee lattice is a cube which has staggered electric field and magnetic field components. A standard Cartesian Yee cell in FDTD method is shown in fig. 3.1. The configuration defines the electric and magnetic field components at the cell edges and cell-face centres, respectively [68].

The problem is to solve for the electric field and magnetic field values throughout the computational domain's lattice.   Maxwell's curl equations are replaced by difference equations which can be solved to give updated equations which need to be evaluated for electric field and magnetic field to obtain known values.   By repeating these steps the field will be calculated over the desired simulated time. To gain a better understanding of the theory of the method and the use of finite
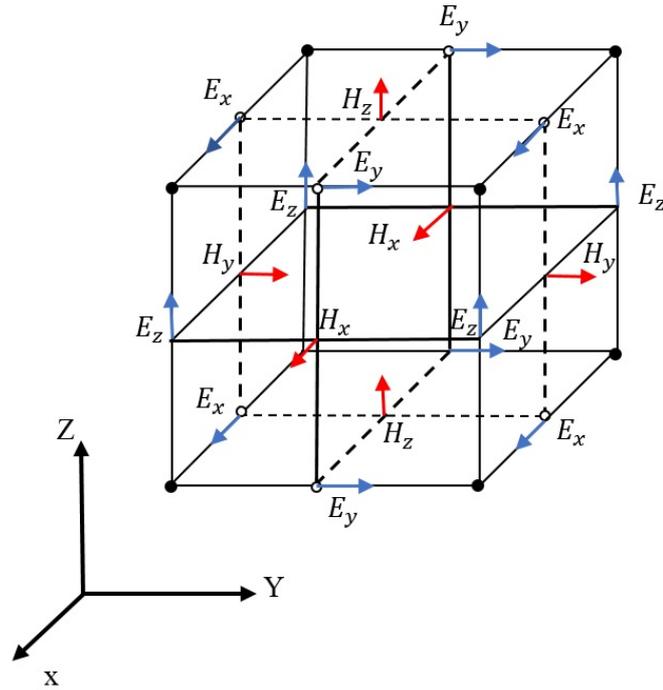
Figure 3.1: The Yee-cube with various grid positions. Arrows show the directions of E and H fields [66].

difference equations, consider a one-dimensional sample and assume that the propagation occurs in free space and the Maxwell's equations are written as :

$$\frac{\partial E}{\partial t} = \frac{1}{\varepsilon_0} \nabla \times H \tag{3.1}$$

$$\frac{\partial H}{\partial t} = -\frac{1}{\mu_0} \nabla \times E \tag{3.2}$$

In the one-dimensional case, we assume that the electric field is E_x and magnetic field H_y. Therefore, Ampere's Law and Faraday's Law can be written as

$$\frac{\partial E_x}{\partial t} = -\frac{1}{\varepsilon_0} \frac{\partial H_y}{\partial Z} \tag{3.3}$$

$$\frac{\partial H_y}{\partial t} = -\frac{1}{\mu_0} \frac{\partial E_x}{\partial Z} \tag{3.4}$$

35

Eq.(3.3) gives the temporal derivative of the electric field in terms of the spatial derivative of the magnetic field and eq.(3.4) shows the temporal derivative of the magnetic field with respect to the spatial derivative of the electric field.

In this process, eq.(3.3) is utilized to advance the electric field and eq.(3.4) is used to advance the magnetic field in time. The next step is to replace the eq.(3.3) and eq.(3.4) with the finite difference equations. To do this, space and time need to be discretized as mentioned earlier. Figure 3.2 shows the arrangement of electric and magnetic field nodes in space and time, where the electric field nodes are shown as black circles and the magnetic field nodes as triangles.

This is known as a leap-frog algorithm which approximates Maxwell's equations in space and time. In this scheme, all the H and E field values will be calculated and shifted in space by half of the discretization Δx.

In fig. 3.2 it is assumed that all the field values below the dashed-line are known and belong to the past and above the dashed-line are unknown and considered to be the future. The FDTD algorithm provides a way to obtain the future fields from the past fields.

In the Yee lattice E_x and H_y are shifted in space by half a cell and in time by half a time step. In such a case, eq.(3.3) and eq.(3.4) can be written as

$$\frac{E_x^{n+\frac{1}{2}}(k) - E_x^{n-\frac{1}{2}}(k)}{\Delta t} = -\frac{1}{\varepsilon_0}\frac{H_y^n(k+\frac{1}{2}) - H_y^n(k-\frac{1}{2})}{\Delta Z} \tag{3.5}$$

$$\frac{H_y^n(k+\frac{1}{2}) - H_y^n(k+\frac{1}{2})}{\Delta t} = -\frac{1}{\mu_0}\frac{E_x^{n+\frac{1}{2}}(k+1) - E_x^{n+\frac{1}{2}}(k)}{\Delta Z} \tag{3.6}$$

Eqs.(3.5) and (3.6) show the Yee lattice to have a central difference approximation

for both temporal and spatial derivatives. In these two equations, "n"is the time

index and "k"is the space index. H uses the arguments $k + 1/2$ and $k - 1/2$ which

show that the H values are located between the E field values. The updated equation

can be derived from eqs.(3.5) and (3.6) obtaining

$$E_x^{n+\frac{1}{2}}(k) = E_x^{n-\frac{1}{2}}(k) + \frac{\Delta t}{\varepsilon_0 \Delta Z}(H_y{}^n(k - 1/2) - H_y{}^n(k + 1/2)) \qquad (3.7)$$

$$H_y^{n+1}(k + 1/2) = H_y^n(k + 1/2) + \frac{\Delta t}{\mu_0 \Delta Z}(E_x{}^{n+1/2}(k) - E_x{}^{n+1/2}(k + 1)). \qquad (3.8)$$

In eq.(3.7) and eq.(3.8)the new value of E_x and H_y are calculated from the recent

values of E_x and H_y.
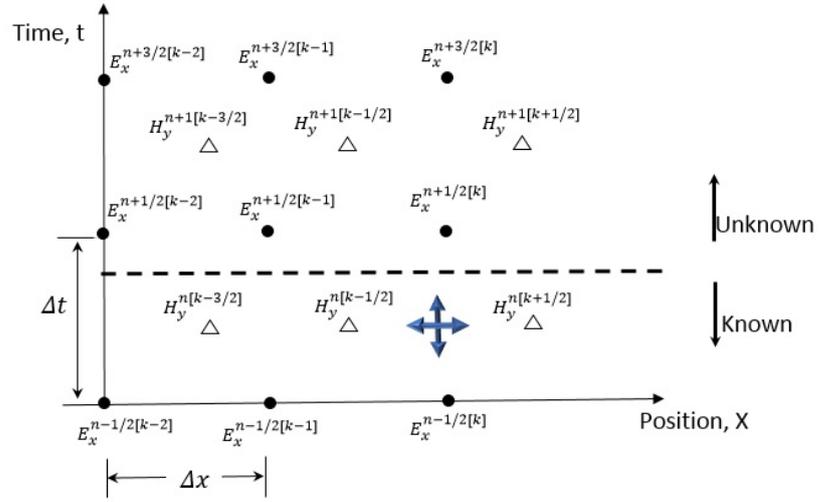
(a) Space-time before updating Electric-field
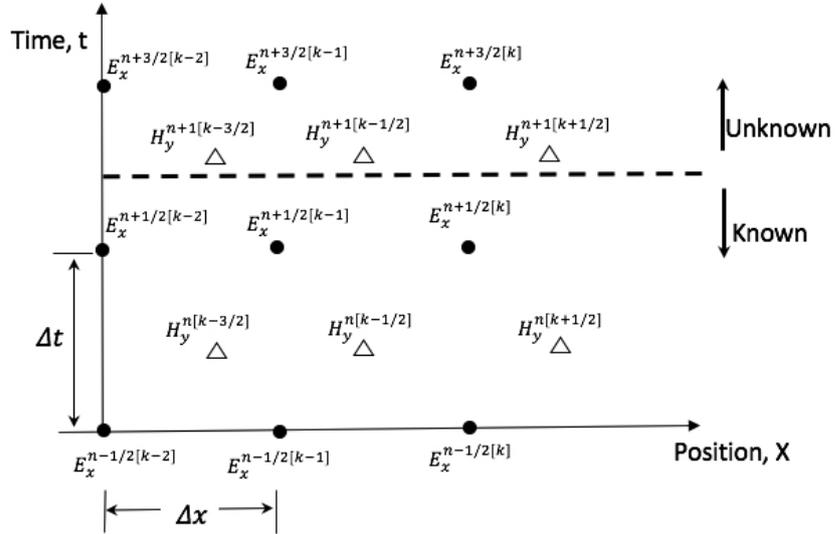
(b) Space-time after updating Electric-field

Figure 3.2: The arrangement of electric-and magnetic field nodes in space and time.The electric field nodes are circle form and the magnetic-field nodes are triangles and the indicated point is the place where the difference equation is to be updated.

There is a trade off between an acceptable accuracy and the grid (mesh size) which will be discussed in the next section. The FDTD algorithm requires that the entire simulation region is meshed and therefore the mesh size is an important factor which affects the computation time.

In this thesis, a commercial FDTD solver (Lumerical) has been used. The benefits of using FDTD in the design of anti-reflective sub-wavelength structures has

been described by [69] for solar applications and to improve the solar cell efficiency. In this work, the cost of installing solar panels has reduced using an anti-reflective sub-wavelength structure and minimising the light reflection losses at interfaces.

As another example, for optical antireflective coatings based on periodic structures, Lumerical has been used to simulate a bio-inspired moth-eye periodic structure which acts as a broadband anti-reflection layer in the region from 50 to 400 nm [70]. The simulation results show that the layer is anti-reflective over the 50 to 350 nm range of wavelengths at 0° angle of incidence. Ellipsometer reflection measurements which match the results of the FDTD solver and measurements of the samples at multiple angles of light incidence show a 10 to 15% decrease in reflection for 240 to 400 nm wavelengths. The simulation of such periodic structures provides a good starting point in the development of antireflective surfaces for use in the THz region.

In the THz region, a broadband antireflection coating based on dimethylsulfoxide (DMSO)-doped poly (3, 4-ethylenedioxythiophene)/poly (4-styrenesulfonate) (PEDOT/PSS) for quartz and silicon substrates has been simulated using Lumerical [71]. The FDTD simulation shows that the internal reflection of the THz waves can be suppressed by using 6% DMSO-doped PEDOT/PSS films on quartz and ∼101-nm-thick 6% DMSO-doped PEDOT/PSS films on silicon. 6% DMSO-doped PEDOT/PSS thin films are a good option for low-cost and broadband THz and far-infrared anti-reflection coatings.

3.2 Numerical Limitations

As with many other numerical methods, in FDTD there is a trade-off between the speed of computation and accuracy, with finer meshes requiring more storage and calculations to reach a solution. Resulting solutions will contain numerical artefacts arising from the level of discretization chosen for the simulation because an accuracy of a computer based simulation is limited. A computer is always willing to solve the problem but debugging a process is not always easy. When a program runs, it is assumed that all bugs have been fixed which is not always true. There is a huge difference between running a program and achieving a correct result or even a precise result. The numerical solution may be correct for specific implementation, but its implementation may not be able to produce sufficiently accurate results. For example, a solution may be obtained at one level of discretization and then another solution using a finer discretization. If the two solutions are not close enough, one has not yet coincide to the "true"solution and a finer discretization must be used or there is some systemic error in the implementation. Therefore, both solution and implementation needed to be tested multiple times to suppress a systematic error.

Although FDTD provides accurate predictions for many different electromagnetic interaction problems [68], it is both memory and computationally intensive and, therefore, may not be suitable for huge scale problems. The need for memory comes from the spatial increment Δx and time-steps Δt. The time step must be small enough to satisfy the stability condition which is defined by the numerical stability factor, or Courant number. Numerical instability can lead to systematic errors, thus producing invalid results.

The Courant number can be defined as below

$$S_c = \frac{c\Delta t}{\Delta x} \tag{3.9}$$

where c is the speed of light in free space, Δt is a single spatial step and the maximum distance energy can travel in one time step is $c\Delta t$ and for the one-dimensional simulation will be used. Since, in the FDTD algorithm, each node is influenced by its nearest neighbour, the energy propagation cannot be any further than a single spatial grid step for each temporal step [72].

$$c\Delta t \leq \Delta x \tag{3.10}$$

Hence, for the one-dimensional simulations the eq.(3.9) can be shown

$$S_c = \frac{c\Delta t}{\Delta x} \leq 1. \tag{3.11}$$

For a 2D geometry, the solution consists of both X,Y spatial stepsize of Δx and distance of $\sqrt{2}\Delta x$ between these points. The eqs.(3.9) and 3.10 can be updated and gives

$$S_c = \frac{c\Delta t}{\Delta x} \leq \frac{1}{\sqrt{2}}. \tag{3.12}$$

A three-dimensional uniform grid includes X,Y and Z spatial steps of size Δx. It takes 3 time-steps to transfer the information across the diagonal of a cubic grid. The distance travelled across the diagonal is $\sqrt{3}\Delta x$. To have a certain stability, the distance travelled over three time-steps, should be less than the distance over which

the grid can transfer the information. Thus, we must have $c3\Delta t \leq \sqrt{3}\Delta x$ which combines with eq.(3.9) gives

$$S_c = \frac{c\Delta t}{\Delta x} \leq \frac{1}{\sqrt{3}}. \tag{3.13}$$

3.3 Perfect electric conductors and conductivity

Charge carriers in conductive materials can be affected by an electric field which leads to current flow. In the case of materials with non-zero conductivity σ, the current density is given by

$$J = \sigma E. \tag{3.14}$$

Perfect Electric Conductors (PEC) are materials with zero resistivity, which means that both the tangential and normal component of the electric field at the surface of the PEC are equal to zero. The normal component of the electric flux density is continuous across the interface of the conductor and is equal to the charge density at the conductor's surface. The zero field values inside a PEC cause all points of the material to be at the same potential [73, 74].

3.4 Boundary conditions

Since computational domains are finite, boundary conditions are necessary to calculate the wave propagation and to minimize the computing time and memory, hence truncating the computational domain used in the simulation [75]. Although the original FDTD algorithm was introduced in 1966, its applicability to solving practical problems was improved in the 1980s by Mur's introduction of

an absorbing boundary condition [76]. Other absorbing boundary conditions were proposed afterwards, but they mostly suffered instability problems and/or led to inaccurate solutions. The perfectly matched layer (PML) condition was proposed by Berenger [77]. Compared to the previously proposed boundary conditions, the PML condition is able to absorb the incoming wave at all frequencies and all incident angles. Without any boundary conditions, it is assumed that the lattice is surrounded by a PEC. This leads to significant scattering in the solution. The PML acts to overcome this problem as it provides a boundary condition where there is no reflection, i.e. with the layer that surrounds the lattice absorbing all incident waves [77, 78].

In Lumerical, various types of boundary conditions can be introduced including PMLs but also periodic boundary conditions and symmetric/anti-symmetric conditions. The benefit of applying periodic boundary conditions is that an infinite regular system can be simulated with a single cell [79–81].

In symmetric/anti-symmetric conditions, simulation involves one or more planes of symmetry through the middle of simulation region. The source and boundary condition should have the similar symmetry. When electric and magnetic field components have a plane of symmetry, some field components must be zero at the plane of symmetry such as normal E-field and tangential magnetic field for symmetric boundary and tangential E-field and normal magnetic field for anti-symmetric boundary. The boundaries are same for the electric field component while they are different for the magnetic field. The symmetrical boundary condition reduces the simulation time and volume by factor of 2, 4 or 8, for 1D, 2D and 3D

respectively [70, 82].

3.5   Simulation time and Geometry

As mentioned earlier, FDTD solvers use a rectangular Cartesian style mesh which includes fundamental material properties such as geometrical information as well as the permittivity and permeability at each mesh point. During simulation, the electric field and magnetic fields are calculated throughout the mesh structure. Using a smaller mesh size can lead to a more accurate simulation but increases the required time and memory for simulation [83].

The mesh size and mesh form dominates the accuracy of the simulation. However, there is a balance between simulation accuracy, simulation time, computational resources and mesh size. The mesh size should not be larger than one-tenth of the wavelength. A smaller mesh size, allows finer features to be simulated but increases the simulation time but with the risk of running out of memory resources [84, 85].

The Cartesian 3D FDTD mesh grid is shown in fig. 3.3 which occupies a volume of $\triangle L_x \times \triangle L_y \times \triangle L_z$, where $\triangle L_x$, $\triangle L_y$, $\triangle L_z$ denotes the cell size in $x-$, $y-$, and $z-$ directions and N_x, N_y, N_z are the number of cells. If the time for one cell is $\triangle t$ the total simulation time T is proportional to the $N_x N_y N_z$ $/\triangle t$.
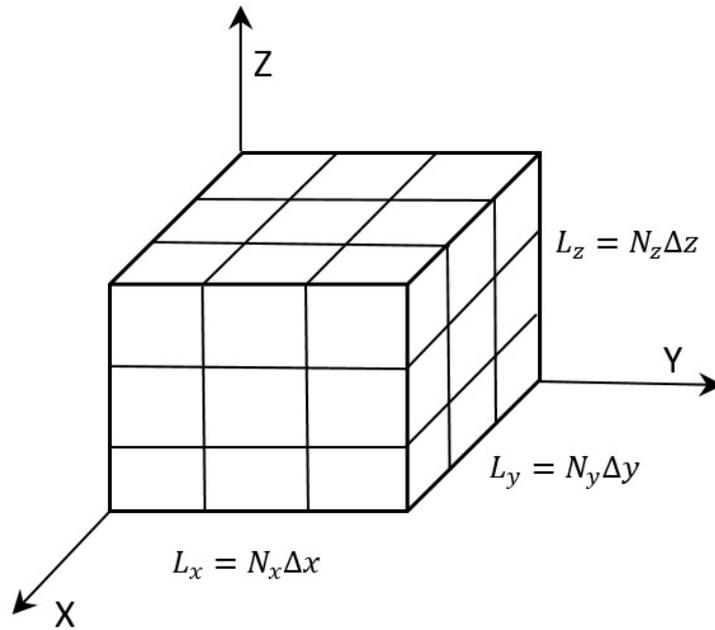
Figure 3.3: FDTD three dimensional mesh grid.

3.6   Electromagnetic sources

As FDTD solves Maxwell's equations in the time domain, it can solve electromagnetic scattering problems for a broad range of frequencies in a single simulation run using a broadband pulse source. For example, a Gaussian pulse could be used as a source for the simulations but for such pulses the most energetic frequency is dc. A dc component can lead to errors in the simulation. Instead, a second order derivative of a Gaussian pulse, known as a Ricker wavelet is used which has no dc component. Its most energetic frequency can be set to whatever frequency is desired. The corresponding spectral form of a pulse source with a centre frequency at 4 THz and the bandwidth of 7 THz is shown in fig. 3.4.
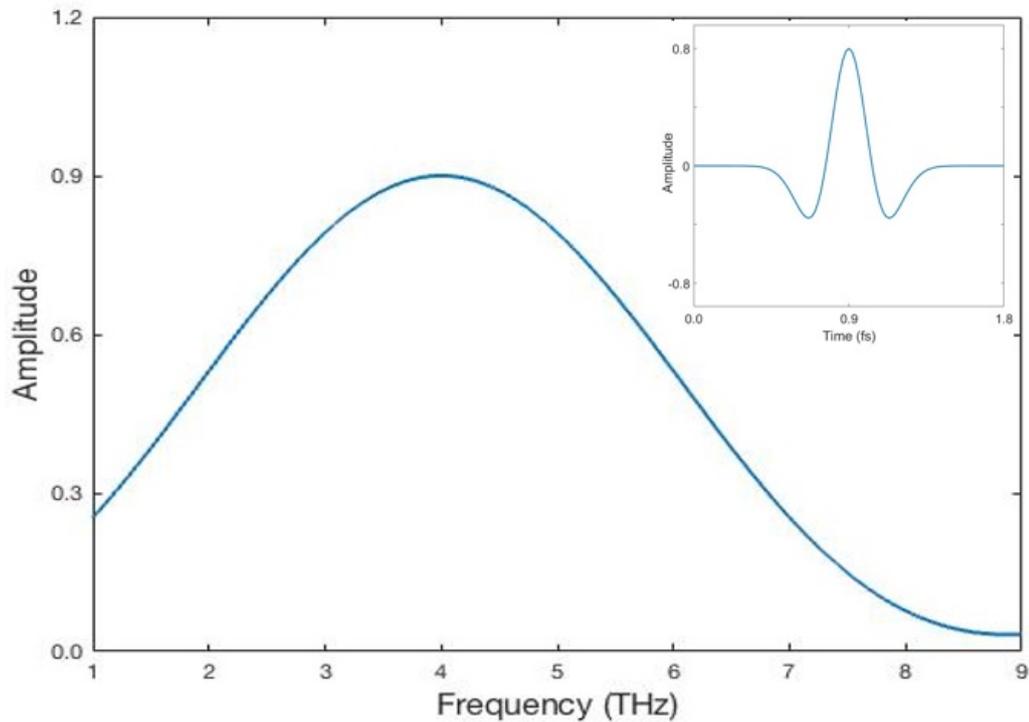
Figure 3.4: Spectrum of Ricker wavelet with a centre frequency at 4 THz. The temporal spectrum is shown in inset box.

3.7   Transmission and reflection in simulation

Electromagnetic plane waves are affected by objects present in their path of propagation. Depending on the size of the object this can result in diffraction and scattering effects. If a plane wave is incident on a planar boundary between two media, the scattered waves remain as plane waves. Depending on the properties of the medium at the boundary, these waves can be either reflected and/or transmitted from/into the material.

Figure 3.5 shows two lossless dielectric media which are separated by a planar interface. The electric field E_i propagates in medium 1 towards the interface and parallel to the X-axis. A part of the electromagnetic wave will be reflected from medium 1, and a part will be transmitted to medium 2.
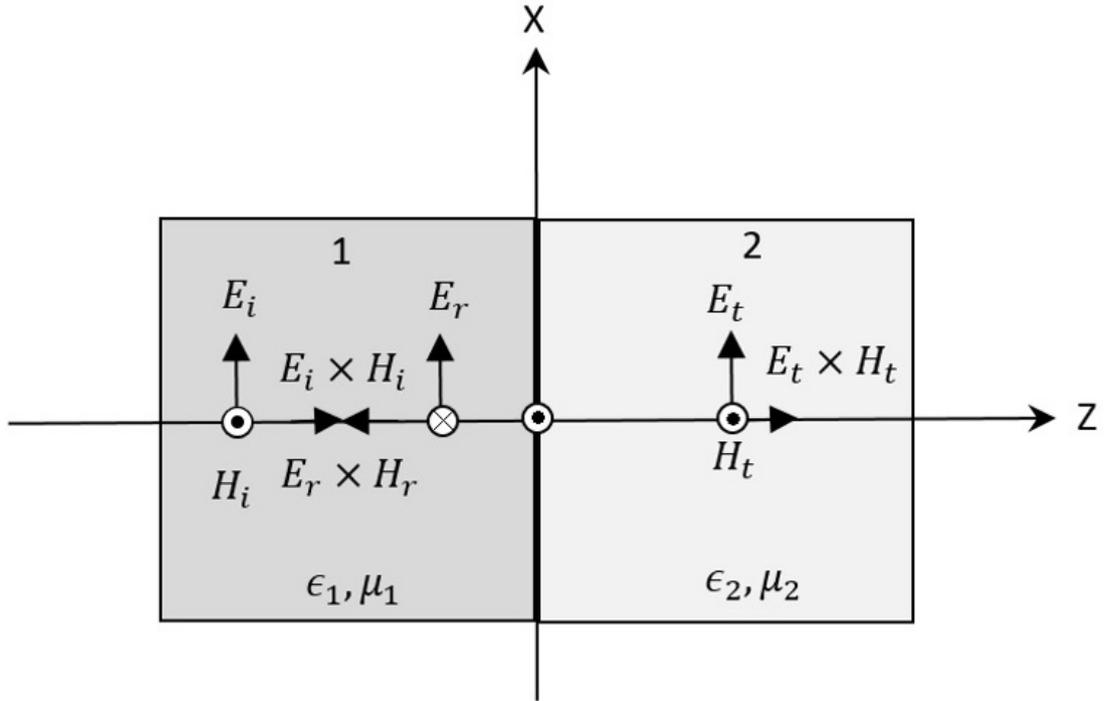
Figure 3.5: Two lossless dielectric media. A part of incident wave reflected from medium 1 and transmitted to medium 2 [86].

The relative intensities E_{1r} and E_2 of the electric field of the interface for both transmission and reflection can be determined. The reference direction of the H field for three waves are shown

$$E_i(z) = E_{1i}e^{-ikz}e^{iwt}, H_i(z) = \frac{E_{1i}}{\eta_1}e^{-ikz}e^{iwt}, \tag{3.15}$$

$$E_r(z) = E_{1r}e^{+ikz}e^{iwt}, H_r(z) = \frac{E_{1r}}{\eta_1}e^{+ikz}e^{iwt}, \tag{3.16}$$

$$E_t(z) = E_2e^{-ik_2z}e^{iwt}, H_t(z) = \frac{E_2}{\eta_2}e^{-ik_2z}e^{iwt}, \tag{3.17}$$

The boundary condition of the interface can be written when the tangential

components of E and H on both sides of the interface are the same [86]:

$$E_{1i} + E_{1r} = E_2, \frac{E_{1i}}{\eta_1} - \frac{E_{1r}}{\eta_1} = \frac{E_2}{\eta_2} \tag{3.18}$$

and by solving eq.(3.18) for E_{1r} and E_2, we achieve

$$E_{1r} = \frac{\eta_2 - \eta_1}{\eta_1 + \eta_2} E_{1i}, E_2 = \frac{2\eta_2}{\eta_1 + \eta_2} E_{1i}. \tag{3.19}$$

The amplitudes of electric field of the reflected and transmitted waves are related to the incident wave through the reflection and transmission coefficients:

$$r = \frac{\eta_2 - \eta_1}{\eta_1 + \eta_2}, t = \frac{2\eta_2}{\eta_1 + \eta_2}. \tag{3.20}$$

Section 3.9 will discuss the way in which FDTD simulation could be used to measure the transmission and reflection associated with eq.(3.20) at THz frequencies for three different periodic grating profiles such as a rectangle, triangle and trapezoidal sub-wavelength structures.

3.8   Periodic structure

Periodic structures are widely found in electromagnetic applications in the form of frequency selective surfaces (FSS), electromagnetic band gap (EBG) and metamaterials [87, 88].

When the FDTD method is used to analyse periodic structures, as mentioned previously, periodic boundary conditions are used to simplify the computation by

permitting the simulation of a single repeating cell in place of the entire structure. In the direction of the periodicity, the simulation period must correspond to exactly one unit cell of the device. A plane wave source is used for all PBC problems involving normal incidence illumination.

If, however, the plane wave source is incident at an angle other than 90 degrees in the direction of the periodicity then a Bloch boundary condition is used. Based on a Bloch theorem, the field inside the periodic structure takes on the same symmetry and periodicity of the structure but when the propagation is at an angle, the fields from one period to another period will be out of phase. The Bloch boundary condition compensates for this.

As an example of a periodic structure, consider a two-dimensional, sub-wavelength structure which is bounded by a periodic boundary condition, PBC on the left and right sides and a PML on the top and bottom. This is shown in fig. 3.6 with two frequency-domain field and power monitors at the top and the bottom of the periodic structure to measure the transmission and reflection (parallel to the X-Y plane) respectively.
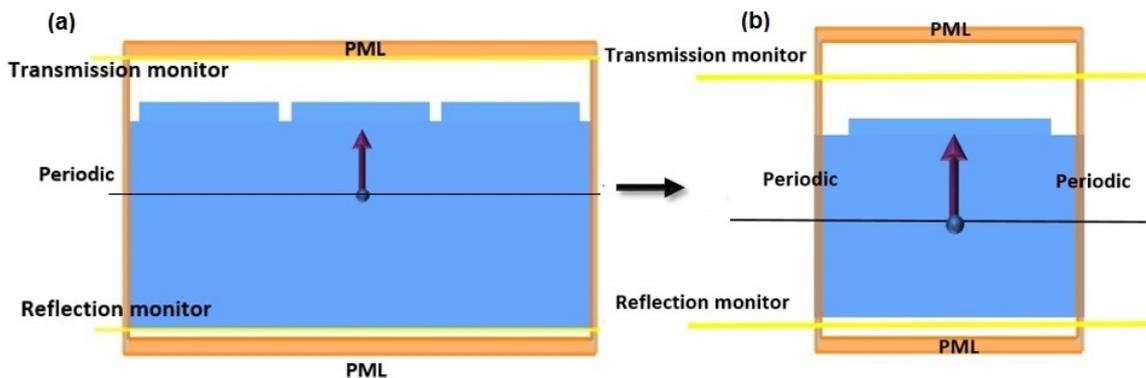
Figure 3.6: Periodic structure with transmission and reflection monitor with (a) large and (b) smaller simulation time.

There are different types of monitors available in the Lumerical including time-domain, frequency-domain field only and combined frequency domain field and power. Each of these monitors records data at a particular point, line or area depending on the specific purpose. The frequency-domain field and power monitors are mostly used for capturing steady state electric and magnetic field data in the frequency-domain. For capturing over a particular period of time within the FDTD simulation region a time-domain monitor is used.

In this case, a frequency-domain field and power monitor is used to collect the electric and magnetic field information in X-Y plane in the frequency-domain. Owing to the inherent geometrical periodicity, only the fields within the unit cell need to be determined. The orange box in fig. 3.6(a) denotes the edge of the unit cell which acts to reduce the computational requirements. Therefore, the structure simulated is shown in fig. 3.6(b).

3.9   Three-Dimensional FDTD example

In THz measurement systems, which are reliant on low power sources, it is important to ensure that unwanted signal losses are minimized. Reflections at material-air interfaces, e.g. in sample holders and the sources themselves introduce losses. For THz-TDS systems, where long time scans are required to achieve a high spectral resolution, the presence of unwanted étalon reflections also complicates signal processing into the frequency domain [89]. Using an anti-reflection layer provides a solution to eliminate reflections at the material-air interface.

In the simplest case, an anti-reflection coating designed for normal incidence

consists of a single quarter-wave layer with a refractive index of $n = \sqrt{n_{air}.n_{substrate}}$ and thickness of $\lambda/4$. In this situation, two reflections of equal magnitude arise at the two interfaces and cancel each other out by destructive interference. These anti-reflection coatings are applicable in narrowbands.

The use of dielectric coatings for minimizing reflections at a material-air interface is commonplace in the optical region. However, this approach does not transfer well to the terahertz region where many dielectric materials exhibit high absorption losses; a problem which is further exacerbated by the need for thick dielectric coatings (e.g. tens to hundreds of microns) to meet $\lambda/4$ thickness requirements [90]. These issues can be overcome by using an artificial dielectric layer. Such layers are produced from patterns of subwavelength features at the material-air interface.

A sub-wavelength periodic structure based on the effective medium theory (EMT) was reported for an inhomogeneous medium in 1998 [91]. In this method, the effective refractive index of the sub-wavelength structure is obtained from the geometry, based on the fill factor of the multiple materials. The EMT only works in the case where the period of the structure is less than one-tenth of the free space wavelength [69].

For sub-wavelength structures, gratings can be used which work as an effective medium for a certain spectral range. They are defined by their period of Λ, width of w, and height of h [92]. Several grating cross-sections are possible, for example, rectangular, triangular and trapezoidal and have been shown in fig. 3.7.

The polarization of the incoming wave is an important consideration, i.e. whether the E-field is parallel or perpendicular to the subwavelength grating structure. This

leads to polarization dependent wave vectors and, hence, an effective refractive index [93]. Figure 3.7 shows a schematic of 1D sub-wavelength grating for rectangular, triangular and trapezoidal profiles where the incident beam is polarized in either the X or Y direction and propagates in the Z direction.

A rectangular grating has a fixed effective refractive index in the Z direction, whereas for the trapezoidal and triangular gratings it varies in Z (e.g. from the bulk substrate value to air for the triangular case). The effective refractive index of a 1D sub-wavelength structure depends on the normalized grating period Λ/λ [94] and normalized grating thickness h/λ. However, as the normalized grating period Λ/λ ratio increases, the medium is no longer homogeneous and cannot be well described by an effective refractive index.

In the sub-wavelength regime, the diffraction efficiency is dependent on the diffraction orders; the maximum intensity is concentrated in the desired diffraction order(particularly zeroth order) while the residual intensity in the other orders is minimized. The period should be small enough for only the zeroth diffraction order wave (reflected anti-parallel order to the illuminating plane wave) wave to be transmitted [95] as is shown in fig. 3.8 with all higher diffraction orders considered evanescent. Figure 3.8 shows the diffraction orders inside the rectangular sub-wavelength grating structures. For the rectangular structure at normal incidence, if the period is not smaller than the wavelength, there is a possibility of higher diffraction orders starting to occur.

For the triangular sub-wavelength grating, at normal incidence, based on the filling factor of the grating and the period size, the zeroth diffraction order

dominates. The transmission starts decreasing as the wavelength approaches the grating period and the higher diffraction orders are generated. The grating period for first-order diffraction can be given as

$$\Lambda_c = \lambda/n, \tag{3.21}$$

where λ is the wavelength and n is the relative refractive index of the medium [96]. If the grating period is close to the zeroth-order region it is called the cut-off limit period. For the trapezoidal structure, the mesa introduces higher diffraction orders compared to the triangular structure but not as high orders as exist in the rectangular grating.

The effective index is also polarization dependent. The transmission will be slightly different when the direction of polarization is parallel to the grating wave vector($E\|k$) as opposed to having a polarization direction perpendicular ($E\perp k$) to the grating wave vector. The effective refractive index with this theory can be determined by $n_{eff,\perp}^0$ and $n_{eff,\|}^0$. where $n_{eff,\perp}^0$ is the zeroth-order effective index perpendicular to the grating vector and $n_{eff,\|}^0$ is the zeroth-order effective index parallel to the grating vector.

In some grating structures, such as the trapezoidal grating, the effective index and transmission properties are sensitive to the polarization direction of the incident radiation, and in particular, the parallel polarization due to the existence of structural fluctuation on top of each mesa. The trapezoidal grating consists of a periodic grating of trapezoids fig. 3.7(b). In this structure, the aim is to obtain a gradient in the refractive index to increase the fill factor of material in

the direction of propagation Z, leading to a reduction in reflection over a broad range of frequencies. However, the mesa still leads to relatively low transmission compared to the triangular case.

The triangular structure which is illustrated in fig. 3.7(c) has the best transmission, and hence lowest reflection loss. The cross-section of a 1D triangular grating, consists of triangles with widths and periods that are much smaller than the wavelength of the incoming beam in the direction of propagation Z, it acts as a homogeneous medium with an effective refractive index. The effective refractive indices for the triangular grating are expressed as [97]

$$n_{eff}(z) = \sqrt{\frac{q(z)(n^2 - 1)}{1 + (1 - q(z))(n^2 - 1)l} + l}, \qquad (3.22)$$

where $q(z)$, n and l are the fill factor of the substrate, the refractive index of substrate and l is the parameter which depends on the direction of polarization. For polarization direction perpendicular $(E \perp k)$ to the grating vector $l = 0$ and for the polarization parallel to the grating vector$(E \| k)$, $l = 1$ when the grating is 1D structure. The effective refractive index for parallel polarization to the grating vector is given as [98]

$$n_{eff}(z) = \sqrt{l - q(z) + q(z)n^2} = \sqrt{l + \frac{Z}{h}(n^2 - 1)}, \qquad (3.23)$$
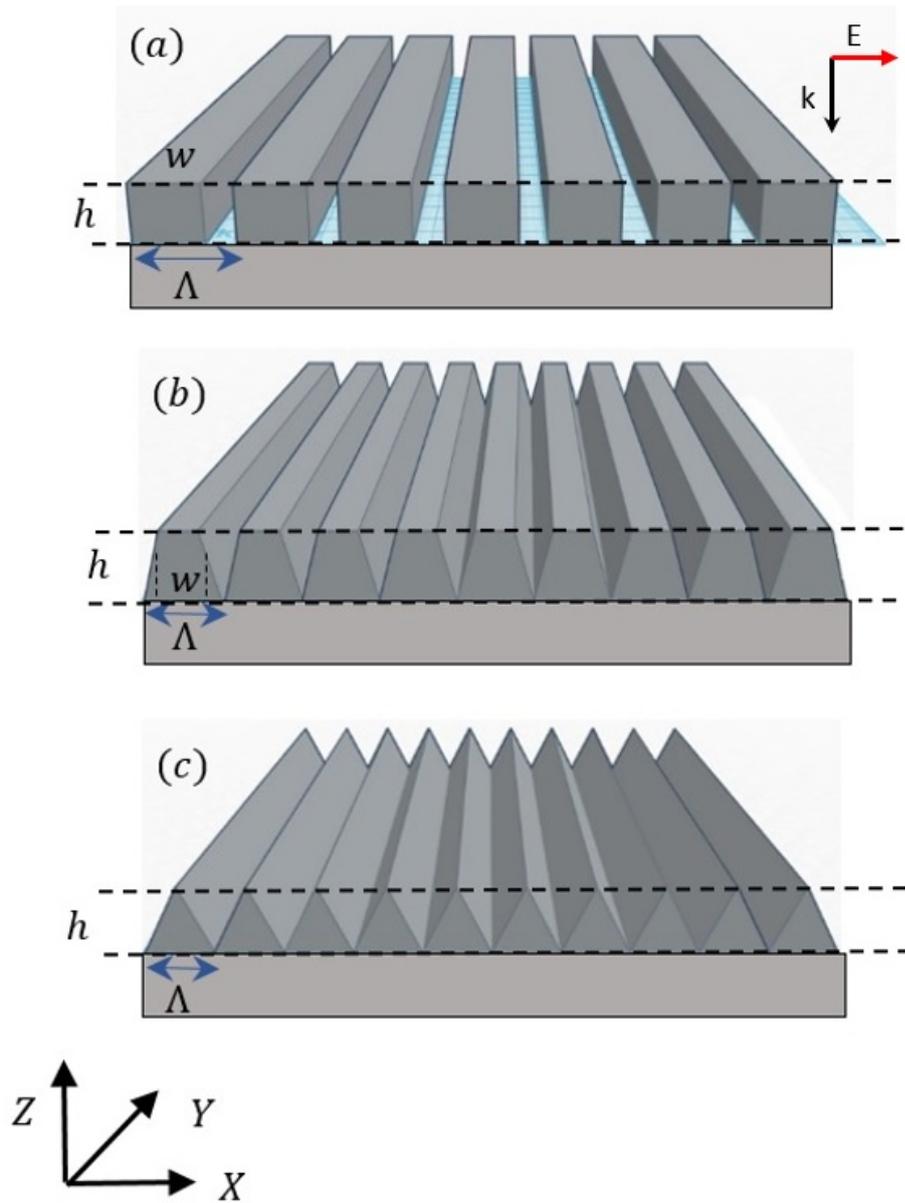
Figure 3.7: The sub-wavelength grating structure design for rectangular, triangular and trapezoidal shaped grooves with pitch Λ. The incident light polarized in the x-direction and propagates in the z-dierection.

Figure 3.8: Sketch of transmitted and reflected diffraction orders by rectangular sub-wavelength grating.

The effective refractive index for different depths has been calculated based on eq.(3.22). Figure 3.9(a-d) shows the calculated effective refractive index as a function of normalized position for triangular and trapezoidal gratings. As it can be seen, the effective refractive index increases by increasing the normalized position Z in the triangular gratings, the refractive index between the air and the surface changes gradually and that suppresses the reflections at the material-air interface fig. 3.9(a-b).

As the normalized position of the grating increases in the trapezoidal grating structure, the effective refractive index reduces due to the existance of the mesa on top of the trapezoidal grating. However, there is a shift between the refractive index of the air and the upper surface compared with triangular grating, fig. 3.9(c-d).

Figure 3.9: The calculated effective refractive index as a function of normalized position for triangular(a) and trapezoidal (c)grating, which increases by increasing the normalized position Z/h in triangular profile(b) and reduces due to the top mesa in the trapezoidal profile(d).

The first simulation to be discussed is based on the rectangular shape sub-wavelength grating. Figure 3.10 shows a 3D model of the rectangular shaped grating and the side view of the grating in fig. 3.10(b).
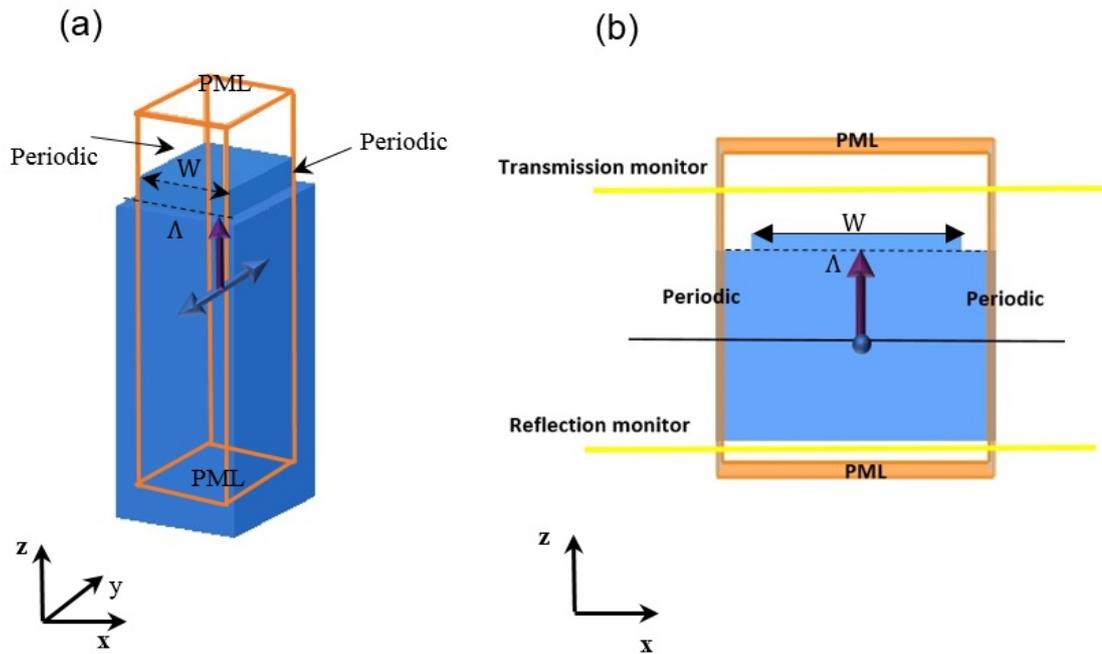
Figure 3.10: Rectangular sub-wavelength structure with period Λ and width W (a) 3D, (b) side-view.
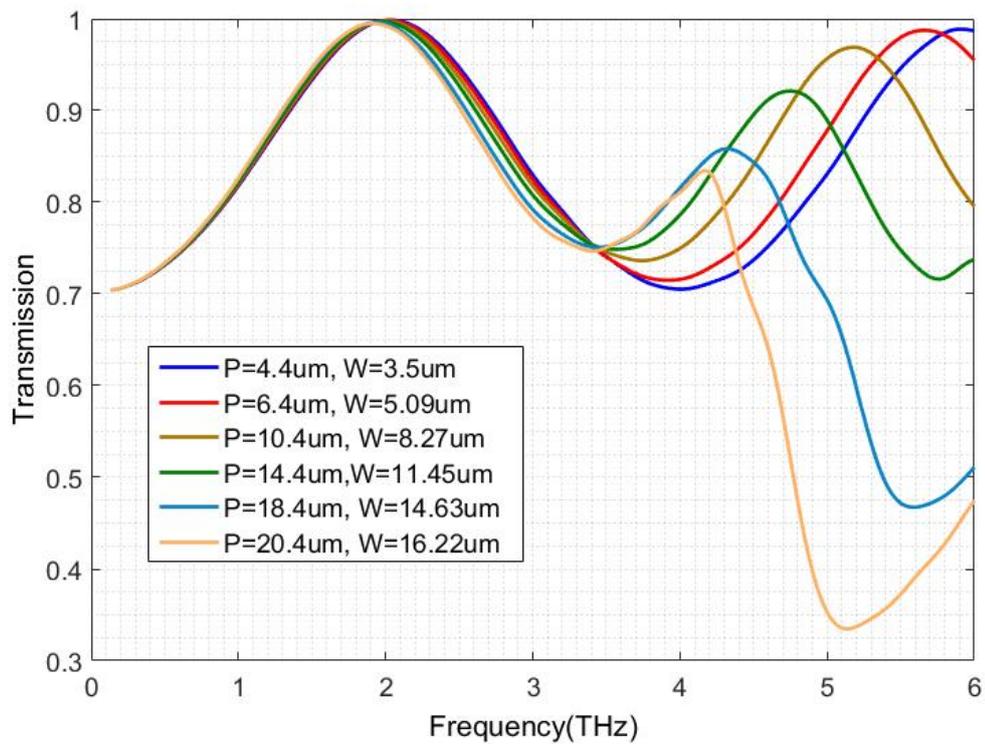
Figure 3.11: Simulated transmission of rectangular shaped grating with a thickness of 20 μm and various pitches(P) and grating widths (W).
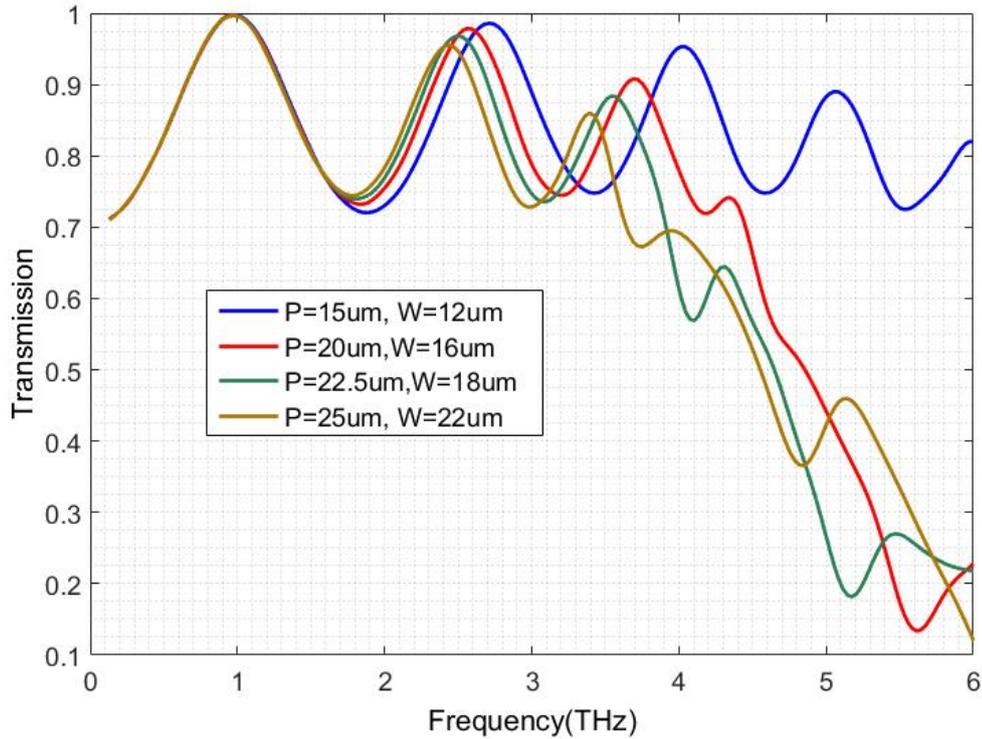
Figure 3.12: Simulated transmission of rectangular shaped grating with a thickness of 40 μm and various pitches(P) and grating widths (W).

Figures 3.11 and 3.12 show the simulated transmission of rectangular shaped gratings with various pitches, widths and etch depths of 20 μm and 40 μm respectively.

The groove pitches and depths have been chosen to be compatible with bulk micromachining techniques whilst maintaining an effective medium approximation in the region of interest but fabrication of groove widths lower than 10 μm for depths greater than 20 μm is not practical using Durham University's clean-room facilities.

As can be seen in fig. 3.11, there is a clear peak transmission at 2 THz for all pitch/width combinations. The observation can be made that with increasing pitch size, the transmission is drastically reduced for frequencies higher than 4 THz. This is due to the generation of higher order diffraction modes that originate from

changing the pitch and width of grating, based on eq.(3.21). It also can be seen that the secondary transmission peak moves towards lower frequencies, and reduced in magnitude with an increase in the pitch and width.

Figure 3.12 shows the transmission spectra of the rectangular grating with various grating periods and a thickness of 40 μm. As can be seen, the first peak in transmission is obtained at 1 THz, with a clear reduction in transmission for frequencies higher than 3 THz. This reduction is due to the generation of higher diffraction orders. We are expecting to have less transmission in a rectangular grating compared to the other structures, but by reducing the pitch and width of the grating, the maximum transmission can be achieved. More peaks and troughs in transmission compared with fig. 3.11 in the range up to 6 THz can be seen in fig. 3.12.

In both figs. 3.11 and 3.12 the effect of normalized depth and period on the performance of transmission have been investigated. As can be seen by increasing the pitch and width the transmission has been reduced. At smaller pitch and width due to exitance of zeroth diffractive order the first and second peak transmission appear entirely but by increasing the pitch and width the second trammission start decreasing, for example at pitch 20.4 μm and width 16.22 μm in fig. 3.11 due to the creation of higher diffraction order in subwavelength structure an absorption appears at 5 THz . The obtained absorption is real which is expected to achieve the same result for the device under test.

Taking into account even more realistic dimensions for bulk micromachined devices, simulations have been carried out with larger pitch and width combinations.

The results are shown in Figure 3.13. Sub-wavelength gratings with pitches of 86 and 76 μm, a width of 60 μm and thickness of 40 μm have been investigated. These pitches have been calculated based on eq.(3.21).

As it can be seen from the fig. 3.13 when radiation with a frequency below the cut-off region [99] is incident on the sub-wavelength grating, it means that its zeroth-order diffraction dominates at normal incidence, and both structures achieve maximum transmission at around 600 GHz.

If the grating period is close to the cut-off limit, some important variations of the effective refractive index occur [99], and the transmission starts decreasing at 1.7 THz. When the ratio Λ/λ is 0.28 for the grating with 86 μm pitch higher transmission will be achieved compared to the other grating with Λ/λ= 0.25. For the sub-wavelength grating with Λ/λ=0.28, the cut-off occurs at 960 GHz and the corresponding cut-off is 1.1 THz for Λ/λ =0.25 [99].
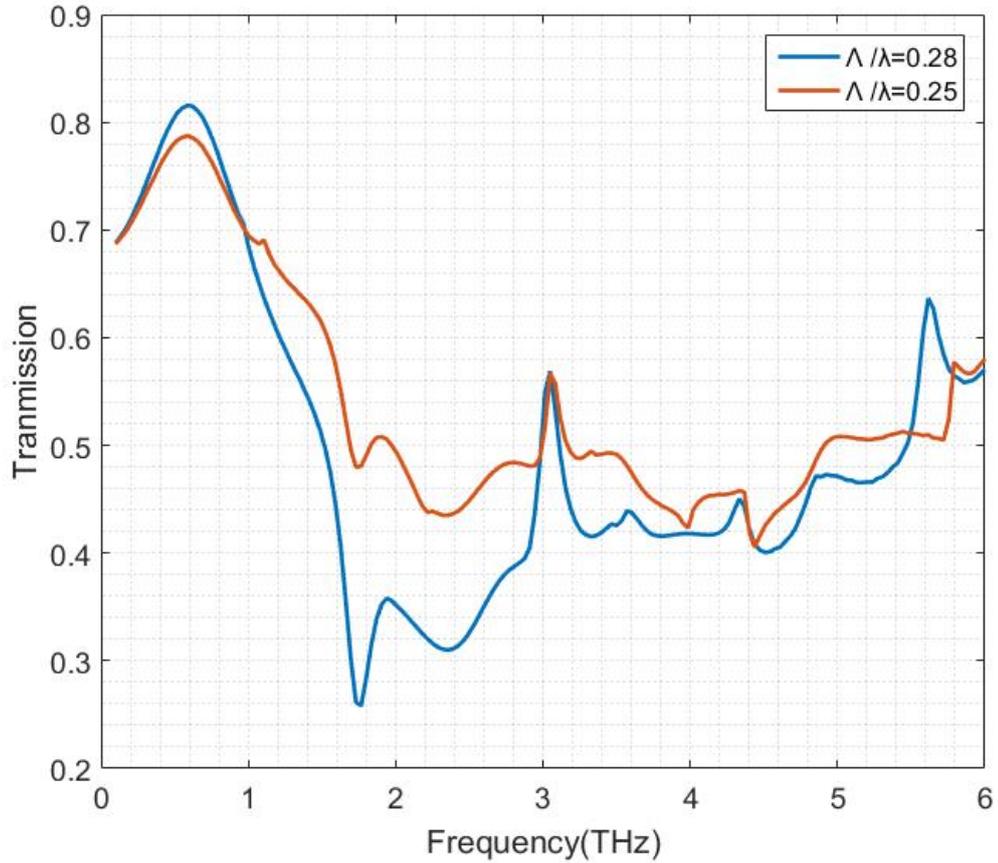
Figure 3.13: Simulated transmission of rectangular shaped grating with a thickness of 40 μm and pitches 86 μm and 76 μm and grating width 60 μm.

In summary, the etched region behaves as a quarter wave plate with the maximum transmission frequency related to the etch depth. Several 'peaks' are evident in figs. 3.11 and 3.12 throughout the frequency range where destructive interference can occur, suppressing reflections. However, at higher frequencies, corresponding to shorter wavelengths - the grating dimensions become comparable to the wavelength of the incident radiation. In this case, the effective medium approximation is no longer valid, and overall transmission is suppressed and, in effect, cut-off beyond a certain frequency.

The next design to be discussed is based on the trapezoidal profile. For a trapezoidal structure with 76 μm pitch, the first order diffraction happens at around

260 μm (1.17 THz). The period of the grating has been calculated at 86 μm based on eq.(3.21). A plane wave at normal incidence will be considered to be coming from the +Z direction. Figure 3.14 shows the 3D trapezoidal grating which is modelled in 3D space on the left side and a side-view to the right side. To study the effective refractive index, it is assumed that E-field polarization is parallel to the grating direction.
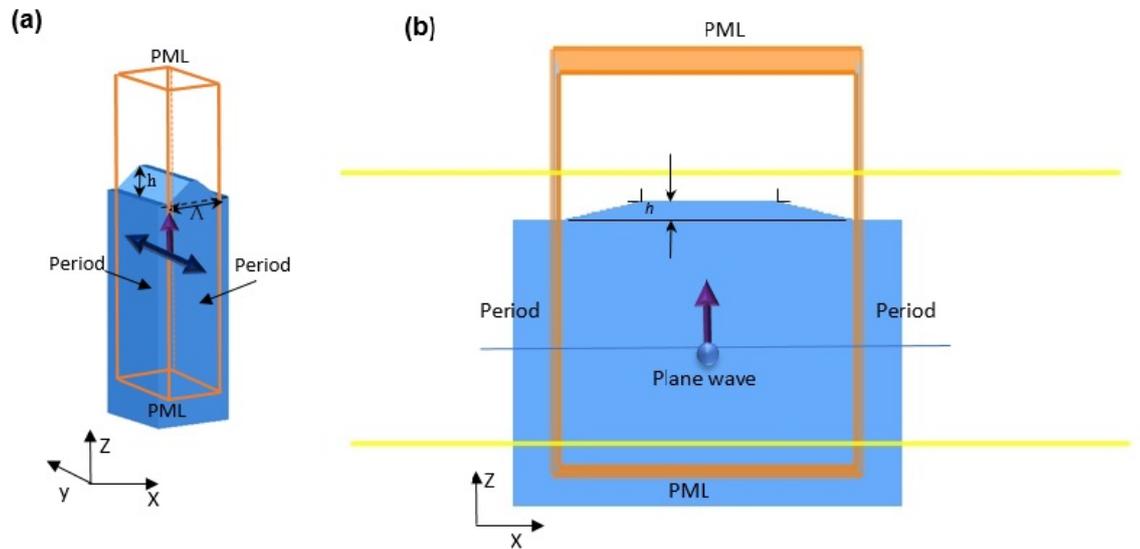
Figure 3.14: Trapezoidal sub-wavelength structure with period Λ and height h (a) 3D, (b) side-view.

As before, different pitches and heights of gratings have been investigated. A comparison of varying pitch is shown in fig. 3.15; the peak transmission is achieved at 1 THz for a pitch of 86 μm and a depth of 30 μm. It can be seen by decreasing the pitch, the peak transmission has slightly shifted to the higher frequencies and exceeded 1.25 THz with 90 % transmission. When the period of the grating decreases, reduced amounts of higher diffraction orders can be generated at lower frequencies and ensures that the reflections are minimized.

In fact, the zeroth order diffraction dominates and effective medium theory will

be valid as long as the period-to wavelength-ratio is much smaller than one.

If, in the subwavelength structure, the period-to-wavelength ratio becomes too small, the incident radiation will be diffracted by more than one diffraction order, and the EMT will not be applicable to this structure. On the other hand, if the grating period is larger than the wavelength, the zeroth order cannot be used, and higher order diffraction must be considered [95].
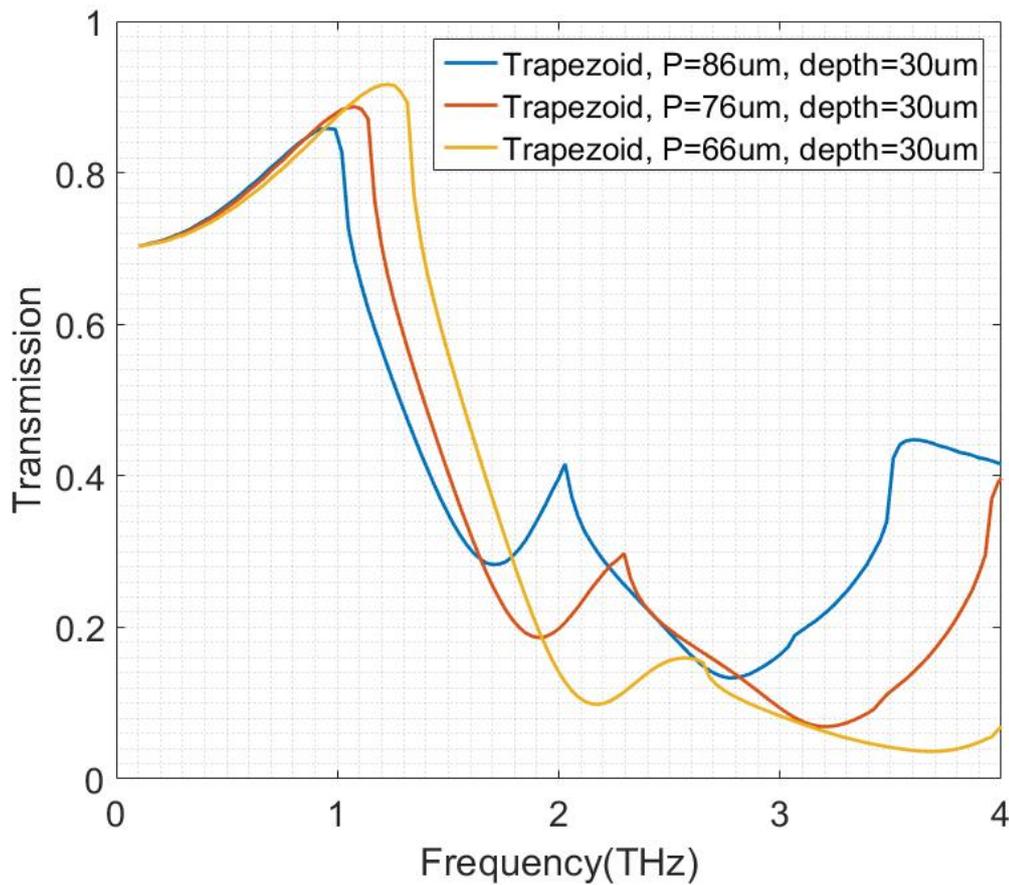
Figure 3.15: Simulated transmission of trapezoidal shaped grating with a thickness of 30 μm and various pitches (P) with the 85% peak transmission at 1 THz for the pitch of 86 μm and 90% transmission at 1.2 THz for the pitch 66 μm.

Figure 3.16 shows the transmittance spectra of the trapezoidal grating with various grating periods and a depth of 40 μm. It can be seen for all pitch sizes, the highest transmission is achieved at around 1 THz, and it is suppressed for frequencies higher than 2 THz. In this simulation, the plane wave source is placed inside the substrate.

As we already mentioned the normalized grating depth h/λ affects the effective refractive index. In fact, when the depth-to-wavelength ratio changes, it also affects the diffraction efficiency [95]. The diffraction efficiency of a grating is a defined as the ratio of intensities of the desired diffracted beam and the illuminated beam. At the higher depth, 40 μm, most of the illuminating beam is transmitted in the zeroth diffraction order and maximizes the diffraction efficiency compared to the 30 μm grating thickness.

The diffraction efficiency has the strong dependence on the diffraction orders for the given range of depths, grating periods and the refractive index of the substrate.
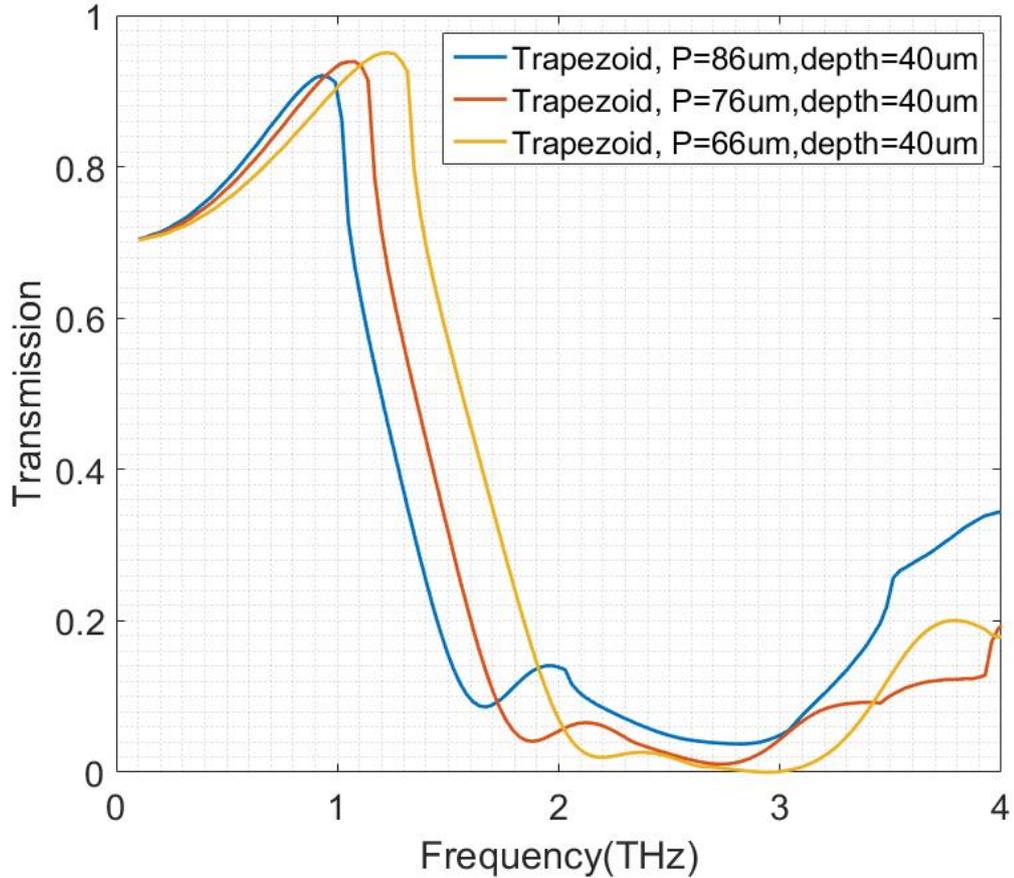
Figure 3.16: Simulated transmission of trapezoidal shaped grating with a thickness of 40 μm and various pitches (P) with the 92% peak transmission at 1 THz for the pitch of 86 μm and 95% transmission at 1.2 THz for the pitch 66 μm.

Figures 3.15 and 3.16 show the effect of changing of normalized depth on the effective refractive index for 30 μm and 40 μm thickness. As can be seen the higher transmission will be achieved at 1THz for depth of 40 μm in Figure 3.16 due to the higher efficiency of the diffraction order for thicker normalized depth compared with thinner normalized depth 30 μm. Increasing the depth to wavelength ratio causes the higher diffraction orders to occur and peak transmission move toward the higher frequencies.

The next design is a double-sided trapezoidal grating, which consists of the same size pitch and depth grating of the front side of grating on the back side of the

substrate. Figure 3.17 shows the double-sided grating profile with period, Λ, and height h. In this simulation, the plane wave source is placed outside the substrate and that enables the the power monitor to measure the transmission and reflection of the beam which passes through both sides of the structure.
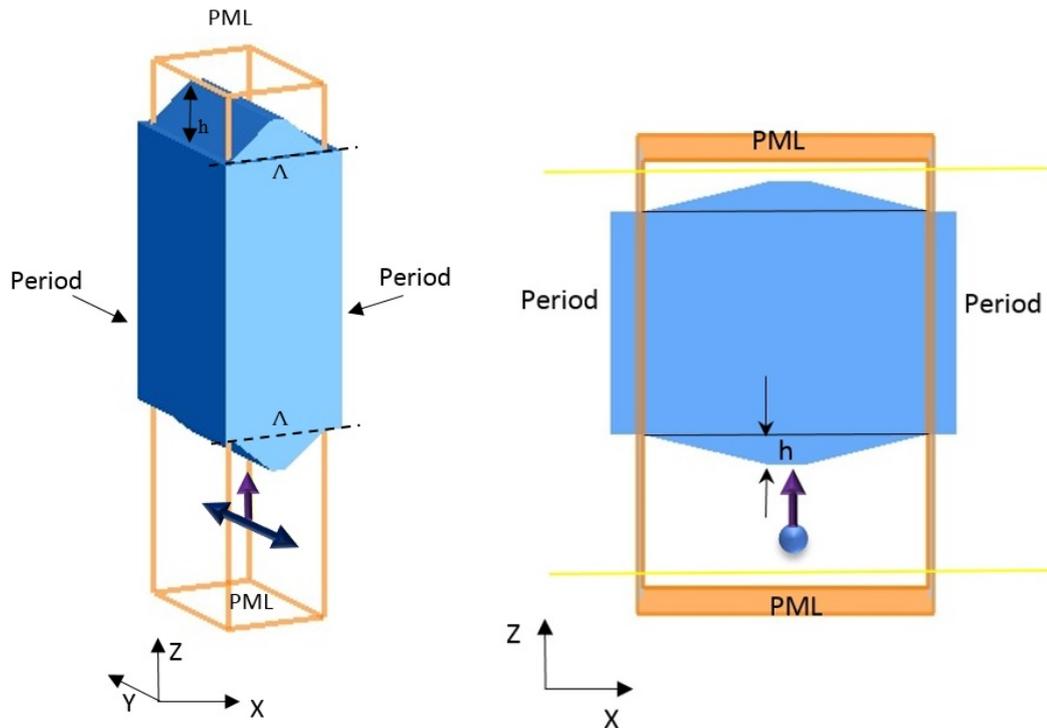
Figure 3.17: Double sided trapezoidal sub-wavelength structure with period Λ and height h (a) 3D,(b) side-view.

Figure 3.18 shows the simulated relative transmission spectra of the double-sided grating profiles optimized between 0.1 THz to 4 THz. The comparison of the pitch size of 76 μm and 87 μm for a thickness 40 μm is shown in fig. 3.18. A comparison of a double-sided trapezoidal grating with the single-sided structure of equivalent dimensions shows an increase in the transmission peak fig. 3.18(a) from 55% to 60% which shows that the pitch is not optimized properly. Decreasing the pitch to 76 μm (based on initial design) in fig. 3.18 (b) leads to even higher transmission from 64% in single-side to 80% in double-sided structures. This can be attributed to the

generation of higher order diffraction in the larger pitch structure which increases

the transmission in double-sided structures.

(a) 86 μm pitch
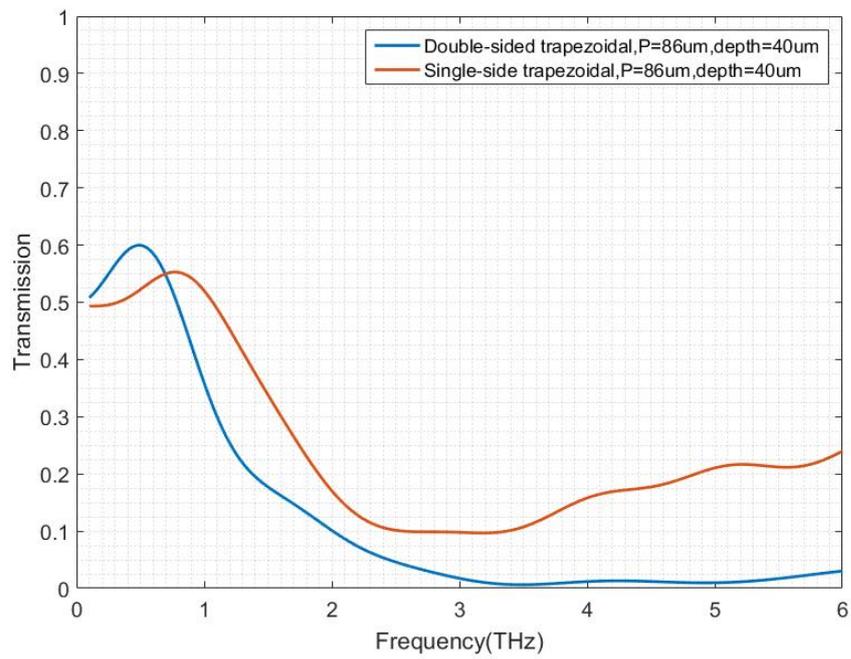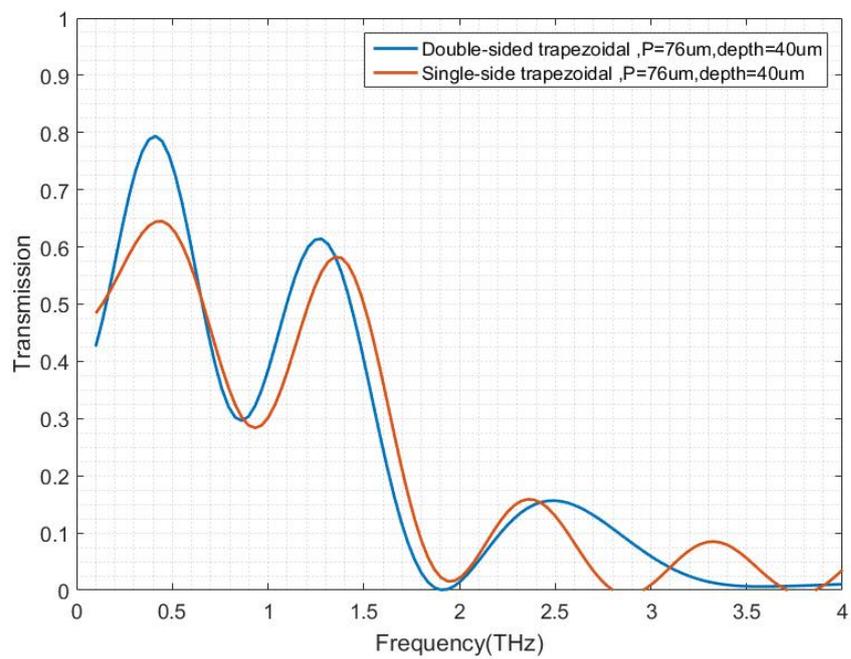
(b) 76 μm pitch

Figure 3.18: Simulated relative transmission of double sided and single side grating for trapezoidal shaped with pitch (a) 86 μm and (b) 76 μm and thickness of 40 μm.

The final sub-wavelength grating that has been investigated has a triangular profile. A 1D sub-wavelength triangular grating is illustrated in fig. 3.19. The side view cross-section of the triangular grating is assumed to be a sequence of triangles with height, h, and period, Λ, where the period is smaller than the wavelength. In this case, the effective refractive index can be calculated by eq.(3.23). Figure 3.19 shows the side view of the triangular grating with a power monitor on top and bottom of the simulation area and a plane wave source inside the substrate.
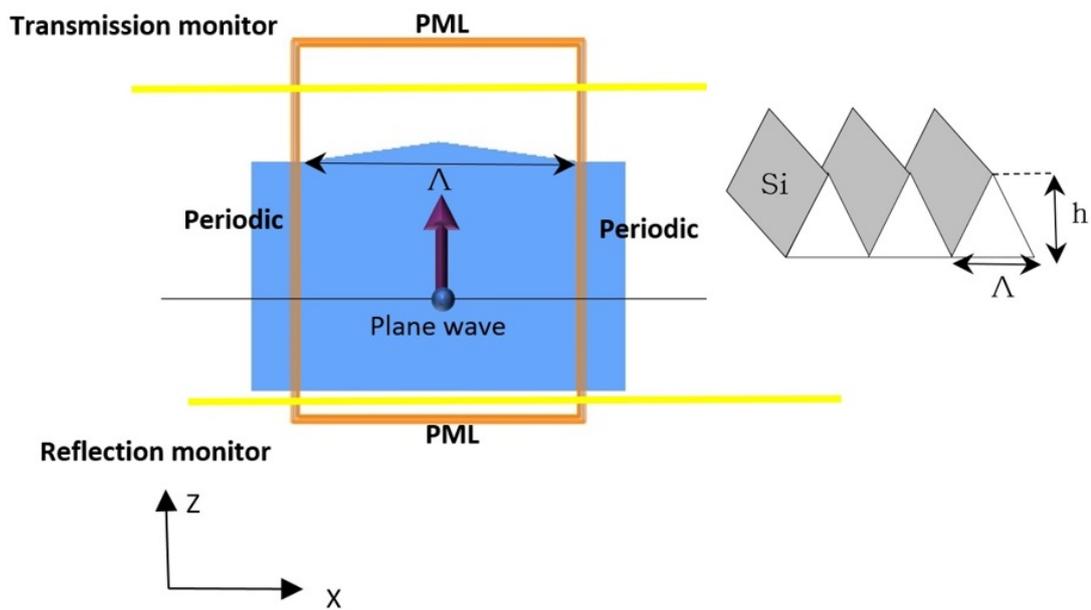
Figure 3.19: Side view of triangular sub-wavelength structure with period Λ and height h.

Periods equal to 66, 76 and 86 μm and heights $h = 30$ and 40 μm were used to investigate the frequency dependence of transmission on the thickness of the silicon structure. The results for a depth of 30 μm are shown in fig. 3.20. As can be seen, by increasing the period, the fill factor of the triangular structure changes.This alters the effective refractive index, which in turn shifts the peak transmission to shift towards lower frequencies. A reduction in transmission is obtained when the pitch is 86 μm and depth 30 μm compared with the 66 μm pitch.

The effect of triangular grating depth on transmission is shown in fig. 3.21. When the triangular structure depth increases to 40 μm, 4% higher transmission can be seen at 1 THz in comparison with a depth of 30 μm. The same variation, as a result of a change in the period is achieved with the higher grating thickness. As mentioned in the previous section, the diffraction efficiency of the zeroth diffraction order depends on the grating depth.

When the depth increases, better index matching close to the substrate at the zeroth diffraction order can be seen. When the grating period is in the cut-off limit the effective refractive index depends on the grating depth and the refractive index of the surrounding media.
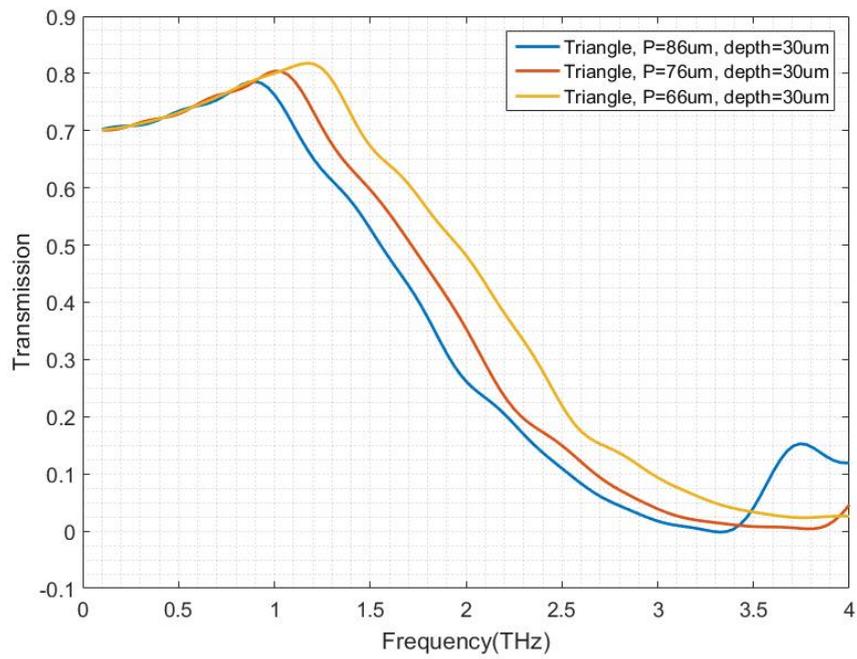
Figure 3.20: Simulated transmission of triangle grating with a various pitch(P) and depth 30 μm.
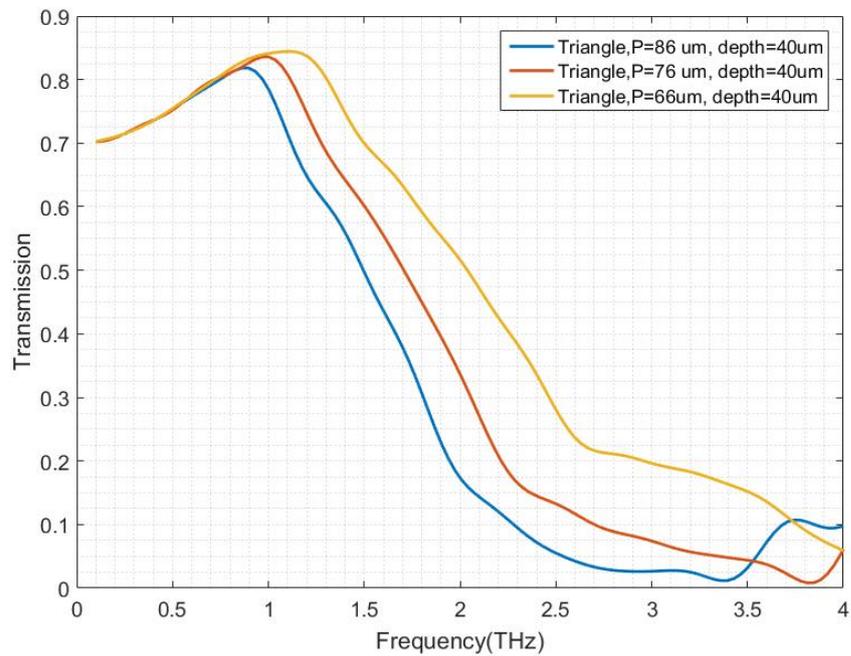
Figure 3.21: Simulated transmission of triangle grating with a various pitch(P) and depth 40 μm.

3.10   Conclusion

In conclusion, the FDTD method has been introduced as a computational method for the design and simulation of sub-wavelength grating structures which can be used to reduce THz reflection losses at air/material boundaries.   The sub-wavelength gratings can be considered as artificial dielectric layers and have been simulated for various structural shapes and pitch/width/depth combinations. When the sub-wavelength grating has a shorter period than the wavelength of the propagated beam, it acts as a homogeneous medium with an effective refractive index based on effective medium theory (EMT).

The results show that the reflection losses are higher for rectangular-shaped sub-wavelength gratings than for trapezoidal and triangular structures. This has been discussed taking into account the change in effective refractive index along the direction of beam propagation which occurs in the latter two configurations. In the simulations, periodic boundary conditions have been applied to reduce the computing time and memory. The simulation results will be compared with VNA experimental measurements of an artificial dielectric layer based on a sub-wavelength grating structure on a silicon wafer in chapter 4.

Chapter 4

Artificial Dielectric layer for Terahertz applications

In recent years, terahertz radiation has been cited as having potential applications in material characterisation and imaging. However, most THz measurement systems are reliant on very low powered, coherent sources. With limited power, it is especially important to minimize unwanted signal losses. These losses can be caused by surface reflections. In this chapter, we explore the use of artificial dielectric layers for refractive index matching at air-material interfaces; leading to a suppression of unwanted reflections. We report on experimental results for low-loss micromachined silicon artificial dielectrics operating as an antireflection coating at terahertz frequencies. The artificial layers consist of sub-wavelength microgrooves with a trapezoidal structure. Finite-difference time-domain (FDTD) simulations have been used in the previous chapter to optimize the grating pitch, and to maximize transmission over the frequency range of interest. The VNA and

74

THz-TDS system are used to characterize the transmission through the artificial dielectric layer.

4.1   Introduction

In THz Time Domain Spectroscopy (TDS) systems where inefficient, low power photoconductive sources are often used, it is important to ensure that unwanted signal losses are minimized. Reflections at material-air interfaces, e.g. in sample holders and the sources themselves introduce losses. For TDS, where long time scans are required to achieve high spectral resolution,the presence of unwanted étalon reflections also complicates signal processing into the frequency domain [89]. For getting higher resolution the sample spacing should be chosen as $T = 1/(2f_c)$. If the component of the signal is above the Nyquist frequency (f_c), twice the highest frequency component in the signal, a sampling error or aliasing occur which affects the resolution. The frequency function is the bandwidth limited at the frequency f_c [58]. For example, using the short step size of 0.02 ps, can cover up to 25 THz frequencies and higher resolution will be achieved.

In fact, the coherent property of the THz radiation produces a critical issue to obtain optical parameters from data because of étalon effect caused by multiple reflections inside the sample. When the THz radiation propagates through a sample, it experiences the internal reflection, multiple reflection inside the sample give rise to the étalon effect [100]. For these reasons, the spectral measurement of these samples contains periodic attenuation due to the étalon effect. Multiple reflections at the interfaces generate oscillation [101–103].

Different computational and experimental methods have been proposed to perform the accurate removal of étalon effects in the sample. The reflection from a flat material can be reduced by a layer of anti-reflection coating [104] but choice of material with appropriate refractive index is difficult [105]. Recently, Bomba et al have proposed the use of a cost-effective 3D printed dielectric anti-reflection coating for the frequency range 0.1-0.3 THz [106].

In most previous work, removal of the étalon effect depends on the material thickness and their refractive indices [104, 107, 108]. The recent approaches mostly focused on both the profile structure and the thickness together. Therefore, the sub-wavelength structures provide changes in refractive index of the material as mentioned in the previous chapter that ensure excellent anti-reflective properties compared to the flat layer profile [109].

A key benefit of this effective medium type approach is that precise control can be gained over the dielectric properties, which have the scope to be varied spatially (e.g. for use in beam shaping, focusing and Fourier optics). One of the problems is to identify an artificial dielectric structure which not only performs appropriately (e.g. as an antireflective coating) for a particular target frequency range but is also practically manufacturable at a commercially viable cost. In our procedure, we can successfully remove the étalon effect using the sub-wavelength structure.

In this work, we explore the use of a bulk micromachined silicon artificial dielectric interface layer. High resistivity silicon ($10\ k\Omega - cm$)is used which has high transparency and low dispersion in THz regime with a refractive index of 3.42 [92].

4.2   Fabrication Process

4.2.1   ADL micro-machining

Potassium Hydroxide (KOH) based anisotropic etching of $< 100 >$ oriented silicon leads to a trapezoidal etch profile.Figure 4.1 shows the fabrication process used to achieve a trapezoidal grating structure. KOH etching requires a hard mask of silicon dioxide or silicon nitride (preferably nitride) for the desire thickness.

A $< 100 >$ Si wafer was cleaned by Piranha etch ($H_2SO_4 : H_2O_2(3 : 1)$) and then oxidized with a thickness of 700 nm as is shown in fig. 4.1 (b). Hexamethyldisilazane (HMDS) was spun onto the silicon oxide wafer as an adhesion promoter, using soft baking, followed by spin-coating of 2 μm of positive photoresist S1813 at 3700 rpm for 60 sec. This is followed by exposure using an EVG 620 mask aligner broadband mercury UV source 436 nm and the power of 75 mJ/cm^2 (fig. 4.1(c),(d)). When resist is exposed to a radiation source of a specific a wavelength, the chemical resistance of the resist to developer solution changes. It is important to expose the resist correctly (right amount of time and energy). If the exposure time is too short the resist will not be acidic enough and the areas of photoresist remaining after development (under-exposed) and if the exposure time is too long the diffraction and focus resolution can make the protected areas exposed (over exposed).

Then, the exposed photoresist was developed in MF319 (Microchem) for 1 min, and was rinsed with deionized (DI) water. The oxide layer was wet etched in buffered hydrofluoric acid (HF) for 20 minutes fig. 4.1 (e);and then removal of photo resist with 1112A remover for 5 minutes, prior to KOH etching for 1 hour at 85°C in a water bath to achieve 40 μm deep V grooves, fig. 4.1 (f).

The oxide layer is fully removed using buffered HF solution before THz testing is carried out. The same process has been repeated for the back side of the silicon wafer. The photoresist is used to protect the front side of the sample from damage.

Table 4.1: The microfabrication process of an artificial dielectric layer.

Process	Condition	Time
Substrate preparation (silicon wafer piranha etch)	$H_2SO_4 : H_2O_2$ (3:1)	20 mins
Oxidized wafer(700 nm)	1050°C	4hr
Spin HDMS	3700 rpm	10
Spin S1813(2 μm)	500 rpm	10 sec
Spin S1813(2 μm)	3700 rpm	60 sec
Soft bake(hot plate)	95°C	5 mins
Expose(EVG 620 mask aligner, UV light 436 nm)	$75\,\text{mJ/cm}^2$	4 sec
Develop(MF-319 developer)	20°C	1min
Remove oxide in buffered hydrofluoric acid (HF)	20°C	20 mins
Removal of photo resist (1112A remover)	20°C	5 mins
KOH etch grooves (1.1 $\mu m/min$)	30%, 85°C	60 min
Repeat whole process for the other side		
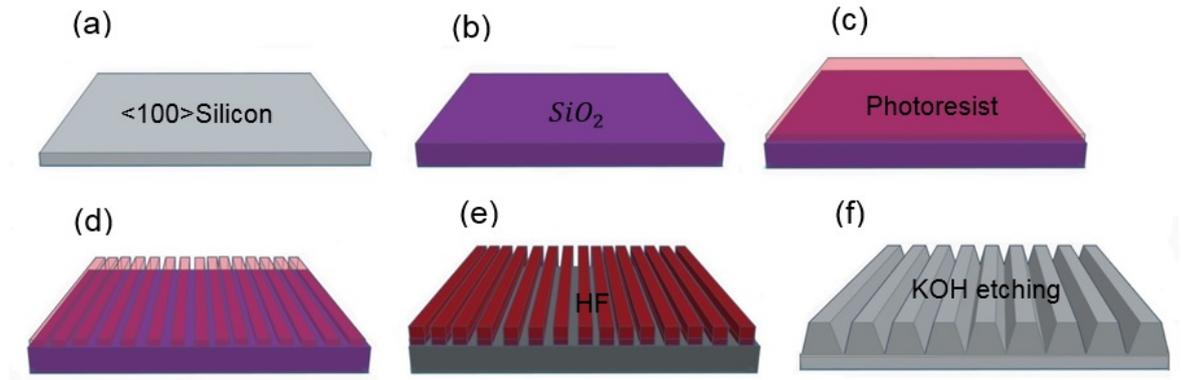
Figure 4.1: Fabrication process of ADL based on a bulk silicon micromachining.

4.2.2   Preparation of KOH

KOH (Potassium hydroxide) is an etchant that is used for producing characteristic anisotropic V-etch on $< 100 >$ oriented silicon wafer with sidewalls that form a 54.74° angle with the surface (35.3° from the normal) [110] as shown in fig. 4.2. The KOH etchant is mixed of 600 ml DI water with 156 g Potassium (granular) for 30% KOH concentration and with the etch rate $1\,\mu\text{m}/\min$. The KOH rate is strongly affected by the crystallographic orientation of the silicon (anisotropic), and it varies for different KOH concentration of 30 to 50% at temperatures from 60 to 85°C [111].The etch rate increases with increasing temperature. The 30% KOH gives the smoother surface than the lower concentration and faster etch rate for plane (110) relative to (100) at 85°C.

The etch depth relies on the size of top width of mask opening and the etch time. For the larger opening, a longer time is needed to reach the (111)plane. Whether the structure formes a sharp tip or a pyramidal shape, depends on the etching time.

The angle with the top surface (54.74°) can be engineered manually by aligning

the flat side of the silicon wafer (the plane of (100)) either parallel or perpendicular to the direction of etching in order to produce trapezoidal (V-groove) etching.

The angles can be measured with the Image J software from SEM images. The etch rate in the (100) direction was determined to be 1.1 $\mu m/mm$ for 30% KOH. Depending on the silicon crystalline plane the straight line etching showed that the etching of the (100) crystal plane dominates the etching along (100) direction until the (100) crystal plane is etched away, leaving the extremely slow etching (111) crystal plane, which forms the trapezoidal structure with (111) crystal plane. Etching other silicon wafer orientations results in changing the trapezoidal (or V groove) shape and changes the angles with respect to the surface and it is expected to have larger reflection loss and lower transmission in these subwavelength structures due to larger top mesa.
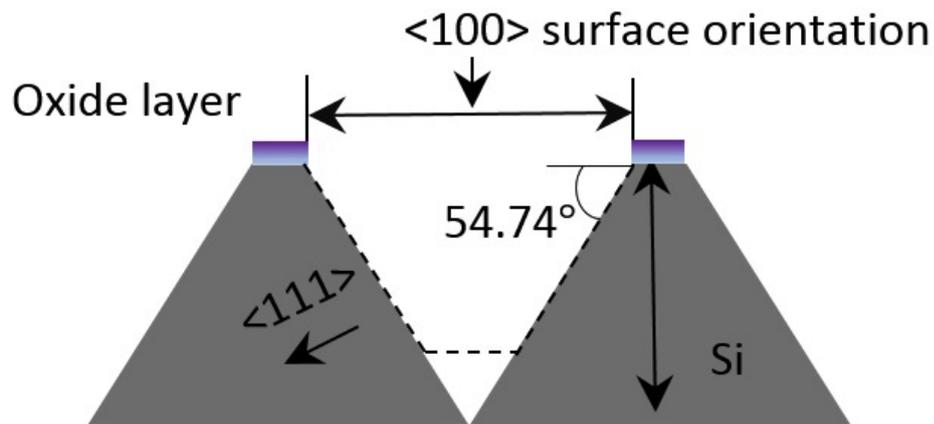
Figure 4.2: Schematic of anisotropic etched features in $< 100 >$ oriented silicon wafer.

Figures 4.3 and 4.4 show an example of an etched silicon surface pattern. The etch depth is self-limited by the formation of V grooves (from the (111) planes);

the depth of which is determined by the top width of the groove. This leads to the possibility of defining a range of groove depths from a single etch/masking step and, hence also the possibility of producing spatially varying dielectric properties. In our case we fabricated structures with pitch 75 μm and top widths 40, 50 and 60 μm.
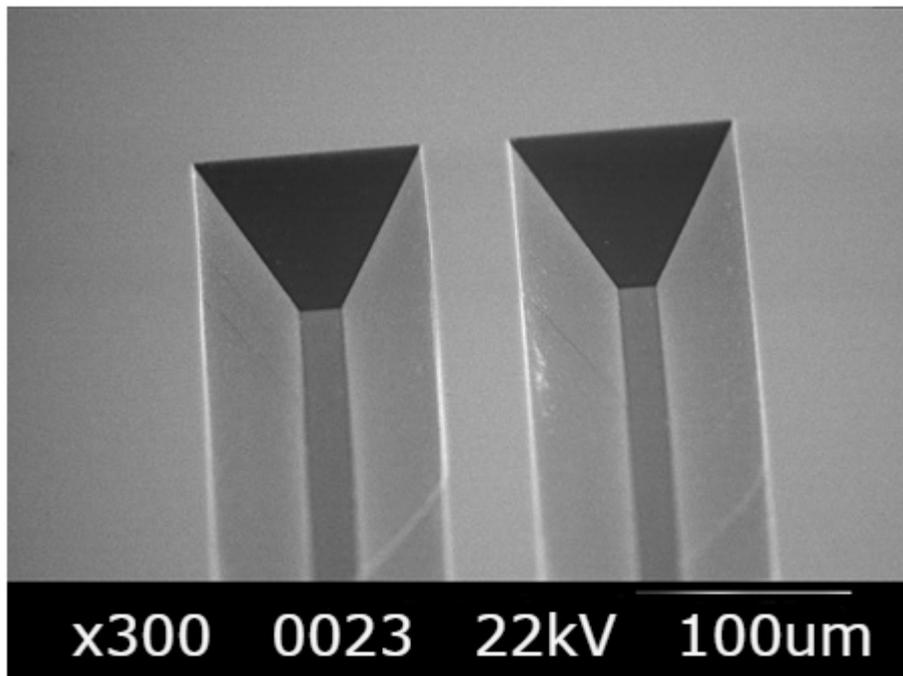
Figure 4.3: The SEM image of a subwavelength grating using KOH etching with depth of 40 μm.
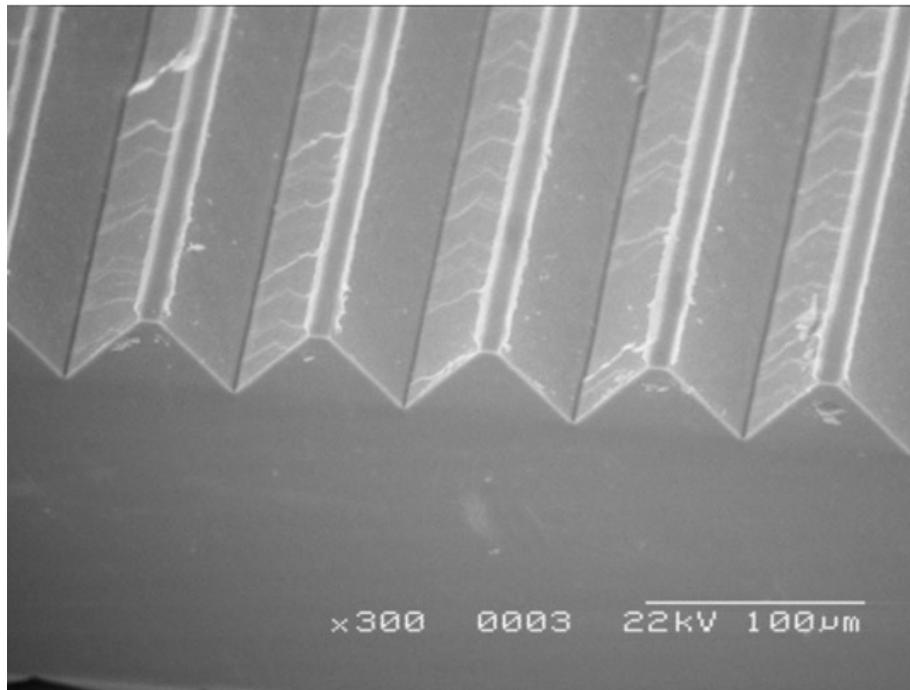
Figure 4.4: The SEM image of a subwavelength grating using KOH etching with depth of 40 μm on double side structured.

4.3   Experiments

4.3.1   VNA measurements

To validate the simulations from previous chapter, the transmission through the sub-wavelength grating was experimentally measured using a THz vector network analyzer (VNA). Figure 4.5 shows the experimental set-up to characterize the spectral transmittance and reflectance of the sub-wavelength structure.   In his configuration, four 90° off-axis parabolics mirrors have been used for collimating the focused THz beam from transmitter VNA extender towards the receiver VNA extender M1 and M4. An artificial dielectric layer (ADL) sample has been placed at the focal point of parabolic mirrors M2 and M3 to measure the transmission through it.
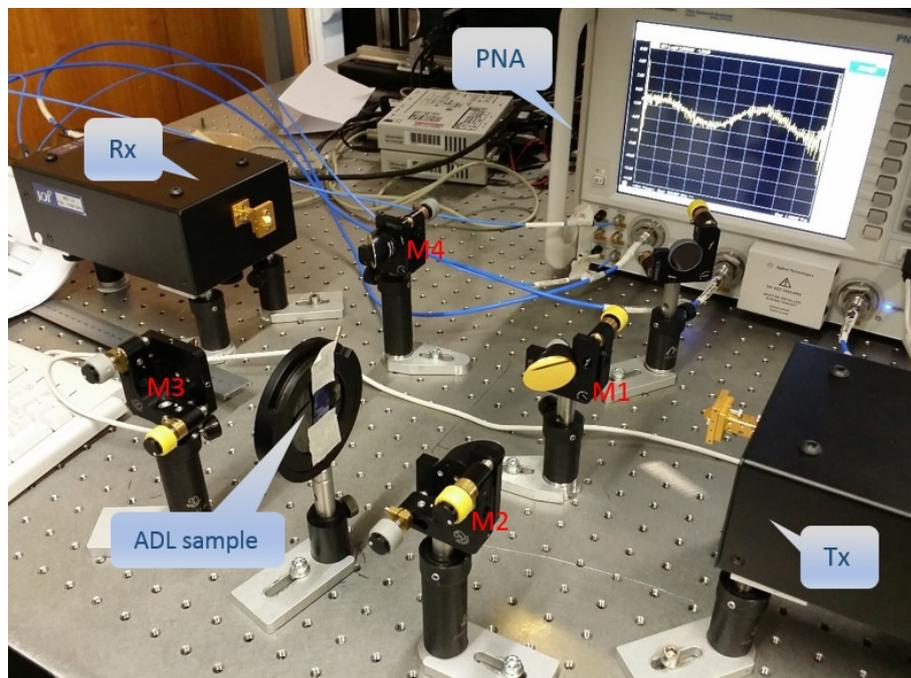
Figure 4.5:   The experimental set-up of transmittance measurement of the trapezoidal sub-wavelength structure using a THz-VNA.

Figure 4.6 shows the transmission for a silicon wafer with the ADL structure compared with a bare silicon wafer with the thickness 600 μm. The measurement was performed with the grooves parallel to the plane of incidence.

The S12 measurement shows that the minimum transmission increased from -5 dB for bare silicon to -2 dB for silicon (with thickness 600 μm) with an ADL. As we mentioned in the previous chapter, for sub-wavelength structures to work as anti-reflection, the period has to be smaller than the wavelength based on EMT.

As the étalon effect at the material-air interface reduces, the transmission will be increased (fig. 4.6). Apart from the overall improvement in transmission, the characteristic étalon effect oscillations are highly reduced for single-side structures.

As it shown in (fig. 4.6) multiple resonances and the standing-waves are created inside the structure, under the normal incidence the resonance frequency is determined by $f = qc/2nl$ and the number of oscillations depends on the thickness of the silicon. There are two regions where the ADL sample has a higher anti-reflective effect:around both the 0.8 and 1 THz the transmittance of the ADL sample is higher compared to the other region.

By using a double sided ADL with thickness 260 μm (after etching)has improved the transmission to -0.5 dB (fig. 4.7). Fewer oscillations can be observed in fig. 4.7 compared with bare silicon in fig. 4.6 due to the reduced thickness of the etched silicon. The use of a double sided ADL allowed the redirection of the THz beam from a reflected one to the transmitted beam, leading to more transmission compared with one-sided ADL.

We have demonstrated that the ADL can be optimized to operate in the terahertz

frequency range and we also have determined these sub-wavelength structures work

effectively as an anti-reflection layer. The spectral features are due to the calibration

artefacts.
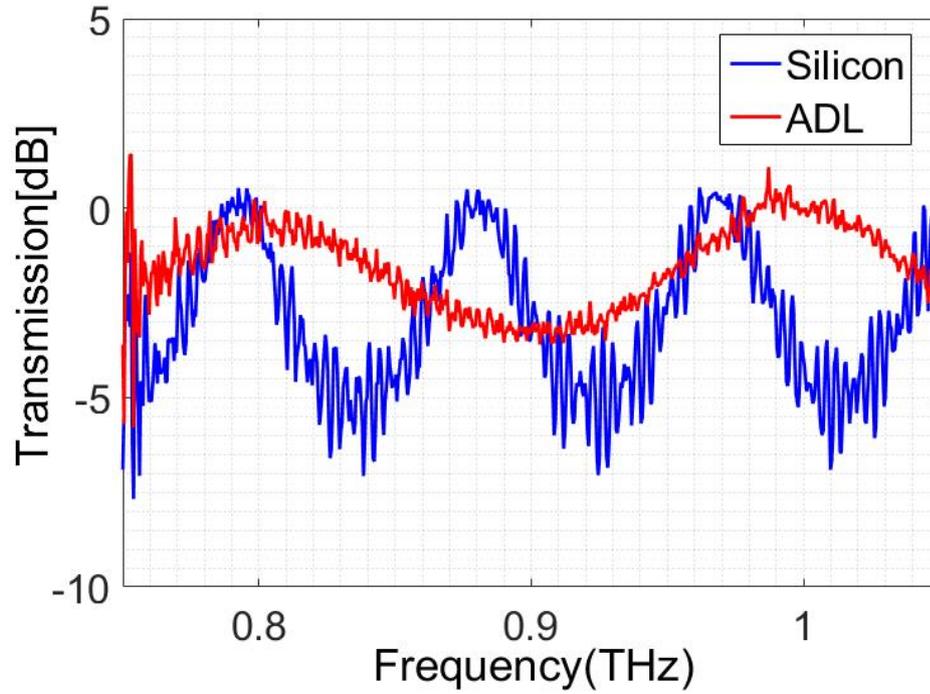
Figure 4.6: The transmission as a function of frequency for ADL and silicon wafer with no grooves with pitch of 75 μm.
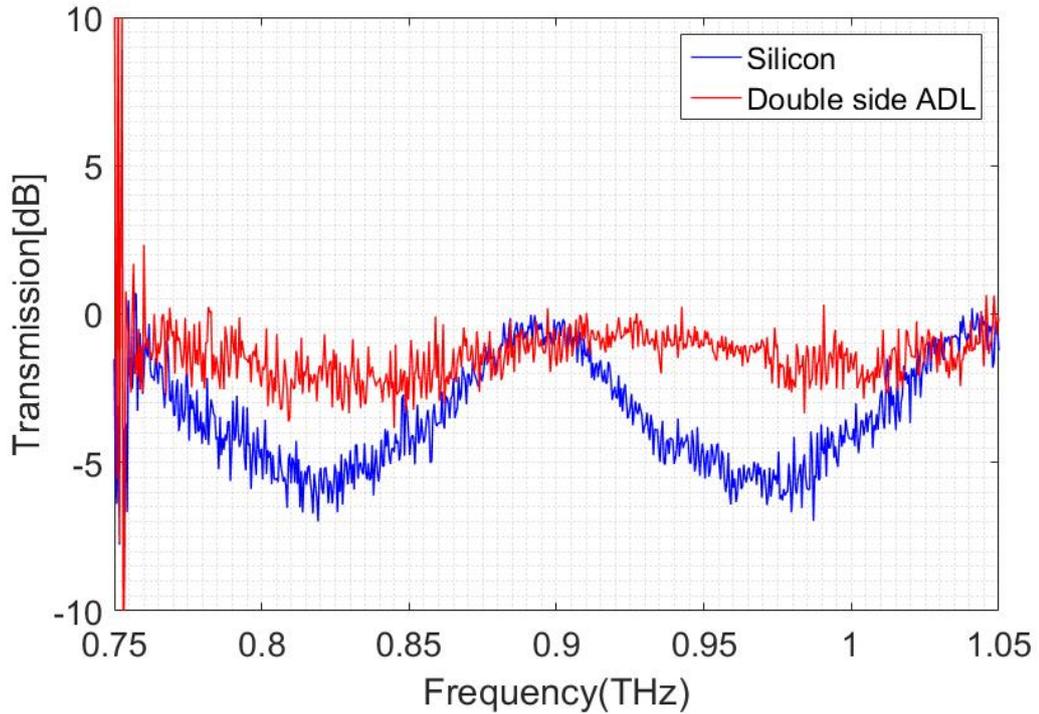
Figure 4.7: The transmission as a function of frequency for double side ADL and silicon wafer with no grooves with pitch of 75 μm.

4.3.2   TDS measurements

The time domain signal of the artificial dielectric layer (ADL) and 2-inch silicon wafer with the thickness of 300 μm has been obtained. The time scan and frequency domain are shown in fig. 4.8 without any smoothing. For an unstructured silicon wafer with 300 μm thickness, the calculated time of 3.42 ps at 1 THz as shown in

$$t = \frac{dn_{si}}{c} = \frac{300 \times 10^{-6} \times 3.4}{3 \times 10^8} = 3.4 \ ps \tag{4.1}$$

where is d is the silicon wafer thickness and n is the refractive index of silicon at THz frequencies; c is the speed of light. The measured THz waveform peak at 1 THz for silicon wafer is 3.4 ps and corresponds to the calculated time for passing through

the sample. For the ADL with the sub-wavelength structure the effective refractive index occurs which is different at each depth of the etched silicon and its thickness is lower than silicon wafer after etch. As shown in fig. 4.8(a) the measured peak time for ADL is 3.24 ps which shows a shift in time due to the higher thickness of the silicon compared to the double sided structured silicon wafer, with an improvement in signal amplitude of artificial dielectric layer (ADL) sample which improves signal to noise ratio(SNR). A lower amplitude of the first reflection is due to the effect of the ADL. The measured time delay between silicon wafer and ADL structures is 0.16 ps. With the etched layer depth of 40 μm the measured effective refractive index of the profile from eq.(4.1) is obtained as 1.2.

Figure 4.8(b) displays frequency domain between 0.1 to 2.5 THz without water absorption lines due to nitrogen purging. This response has been obtained without any smoothing.
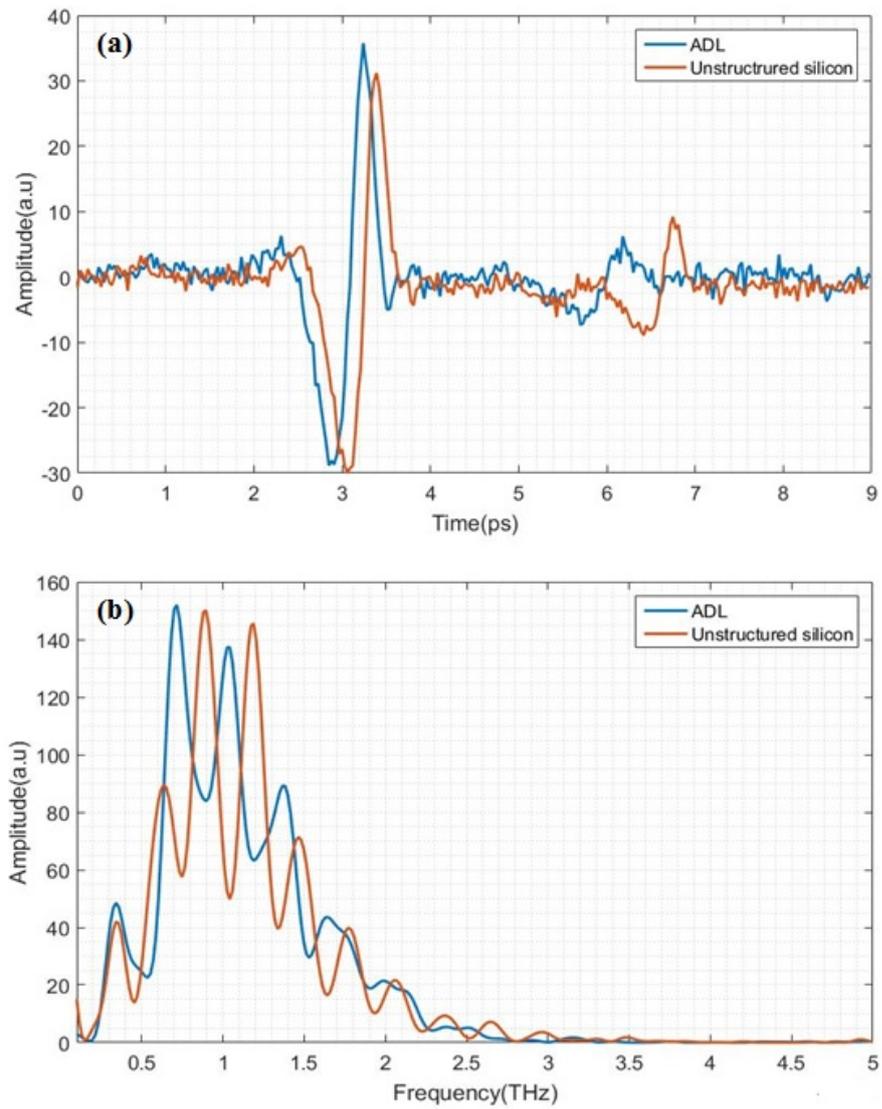
Figure 4.8: (a) THz-TDS of the silicon wafer and artificial dielectric layer at 10 ps(b) FFT resultant.

4.4   Conclusion

The microstructuring of a silicon surface is shown to act as an antireflective layer which offers the possibility of being a spatially tunable dielectric layer. The double-sided ADL can be optimized to operate in the terahertz frequency range and these subwavelength structures were determined to work effectively as an antireflection layer. The improvement in transmission through the ADL has been demonstrated experimentally using a THz-VNA. The fabricated ADLs were tested in THz-TDS set-up and successfully reduced the reflected and suppressed internal reflection leading to reduction of the étalon effect. Moreover, the transmission has been improved.

The performance of the proposed ADL may be improved in the future work by optimising the groove profile to 2D structure. Nevertheless, the most significant problem in THz experiments is the presence of unwanted reflections which can be reduced by the proposed structure.

Chapter 5

Diffractive microstructure

Diffractive optical elements such as lenses and mirrors have been developed for use in many areas of the electromagnetic spectrum ranging from microwave to visible light [112–117]. In particular, the use of a Fresnel zone plate (FZP) as a focusing element, which was first recognized by Soret in the late 19th century [118], has attracted attention in recent years. This is beneficial in the millimeter wave region where conventional dielectric lenses and reflective optics are typically bulky. Although binary FZPs are lossy compared to multilevel zone plates, due to higher diffraction orders, they are much easier to fabricate and are well suited to test the reported measurement system. In the Ka-band (26.5 to 40 GHz), Karimkashi and Kishk reported on the focusing behavior of Soret Fresnel zone plate lenses in the near field region with target applications for remote sensing [119].

In 2016, Pan et al [120] characterized FZPs in the THz region, at 350 GHz, with the aim of improving the focusing properties and directionality. They proposed a square grooved dielectric (PTFE) lens where the conventional concentric circular rings grooves found in a Soret FZP are replaced with square annuli. This was

derived from a diagonal horn antenna and is for use in THz wireless communication systems.

For reconfigurable structures, various groups have explored the use of optically tuned FZPs which rely on the photoexcitation of carriers in silicon to produce a spatially varying electron plasma. This produces the metallic/dielectric variation required for an FZP shape but can be tuned by changing the light pattern which is used to illuminate the semiconductor. Such configurations have been experimentally studied in a transmission configuration. However, the tunability comes at the expense of requiring additional optical components to manipulate the non-THz beam [121–123].

The components used for focusing and beam steering terahertz radiation are mostly based on optical technology such as refractive lenses [124], reflective mirrors [125] and diffractive structures [126–129]. The different types of optical element have various advantages and disadvantages; conventional THz refractive lenses are made mostly from low refractive index materials which normally had a large diameter and thickness(eg.PTFE). Reflective mirrors also can induce aberration, and they are not compact. Diffractive optics could solve these issues by using small compact elements that could work for both narrowband and broadband applications. This chapter provides a detailed background to the fundamental principles of diffractive and reflective optics such as micro Fresnel lenses and reflectors and their application to the terahertz region. This chapter describes the design and fabrication of a multilevel SU8 based, Fresnel type microlens for operation in the terahertz region. The method for designing the lens uses FDTD solvers to simulate the interaction of

91

the THz signal with the micro Fresnel lens.

As described in chapter 2, a vector network analyzer is used as a technique for measuring the field intensity amplitude and phase of a transmitted signal through the micro Fresnel lens. The focal point of Fresnel lens has been confirmed experimentally using four 90° off-axis parabolic mirrors and a VNA at the 3 mm from the Fresnel lens.

In the second section of this chapter, a micromilled aluminum FZP reflector structure, based on a binary Fresnel zone plate, will be explained as a reflective terahertz component. The electric field intensity and phase of reflected signal from Fresnel reflector at the vicinity of the surface of the reflective terahertz component is characterised using a VNA. The amplitude and phase are measured simultaneously by scanning in 3D space and are compared with the FDTD simulation data.

5.1   Micro Fresnel lens

Micro-lenses are well-known as an optical components that have applications in laser printers, facsimile machines and optical communications [130, 131]. A Fresnel structure is an optical component which can be used as a low-cost, alternative to conventional continuous surface optics. Micro-Fresnel lenses which are fabricated with series of annular gratings are particularly attractive due to their small size, viability for mass production; diffraction limited focusing characteristics and applications in imaging systems [132].

In THz spectroscopy and imaging applications, free space focusing of terahertz light is normally achievable through the use of parabolic mirrors or, for 'local' focusing on to a substrate or sample, polished high resistivity silicon lenses are commonly used. One of the optical components that can be fabricated by using microfabrication technology, which gives a large numerical aperture with a short focal length, is the Fresnel lens. These kinds of lenses are attractive for use in THz imaging applications due to their compact design and aspect ratio, and the lens design presented here provides a low-cost alternative to silicon lenses [133, 134].

In 2012, Maciej et al. proposed a new type of double-sided Fresnel lens which is made of HDPE and works over broad bandwidth with an optimized thickness to focus terahertz radiation above 0.5 THz [135].

The design of the Fresnel lens presented in this chapter is based on a simple hemispherical lens in the paraxial approximation [136] (where incoming rays arrive at shallow angles with respect to optical axis), as shown in fig. 5.1. Assuming that

the hemispherical lens has a radius R, and a refractive index, n, then [136]

$$\frac{1}{S_0} + \frac{n}{S_i} = \frac{n-1}{R} \tag{5.1}$$
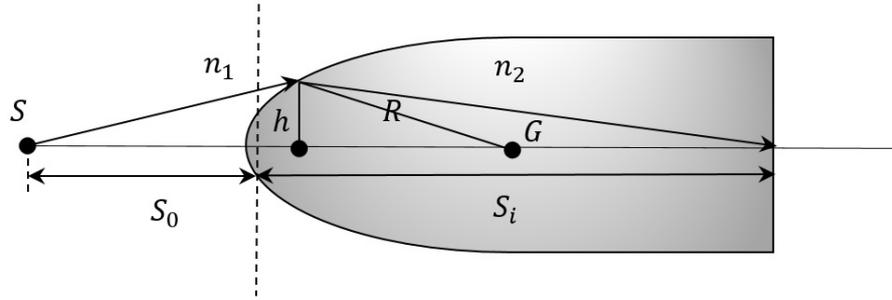
Figure 5.1: Diagram of a hemispherical lens with radius R, with the light emerging from the source S, at a distance S_0, is focused at S_i.

The development of a Fresnel microlens can be seen in fig. 5.2, starting from a prototype conventional hemispherical lens. The traditional shape of a Fresnel lens with sharp edges can be produced by slicing the original lens, separating the continuous lens surface into discrete sections, as shown in fig. 5.2(b). These curved surfaces resulting from the Fresnel structure are very challenging to be manufactured with conventional microfabrication facilities.

A possible alternative consists of approximating these surfaces with steps, resulting in a lens composed of a series of overlapping concentric ring structures, as shown in fig. 5.2(c)
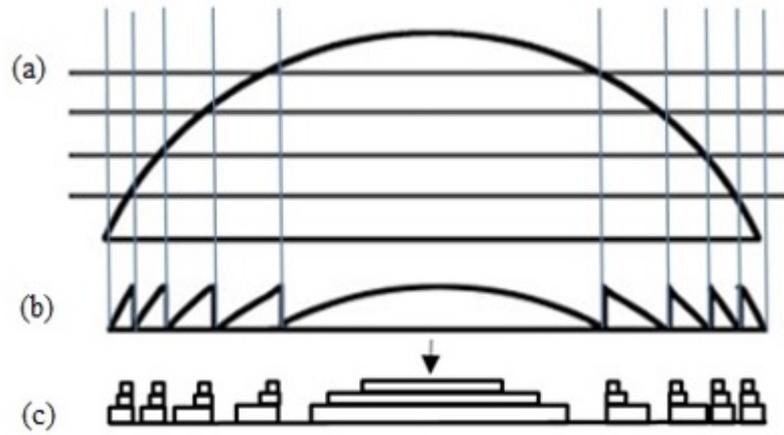
Figure 5.2: Fresnel lens design from spherical lens.

5.1.1   Methodology

The microlenses were fabricated on a silicon (THz transparent) wafer with resistivity of 25-50 Ω cm which had initially been cleaned in Piranha etch, $H_2SO_4 : H_2O_2$ (3:1), followed by a deionized water rinse.

A layer of negative photoresist MicroChem SU-8 2025, which is commonly used for surface micromachining and can be patterned with near vertical sidewalls and high aspect ratio features [137], was spun at 3000 rpm (1 min) to obtain a thickness of about 30 μm after baking.

To avoid bubble formation (which can reduce the yield of multilayer SU-8 structures), the substrate was rested for 120 mins in the spinner after coating. This was followed by soft baking at 65°C/95°C for 3 min/6 min respectively. The concentric ring pattern was exposed by an EVG 620 mask aligner broadband mercury UV source 436 nm with an exposure dose of $250 - mJ/cm^2$. The thickness of SU8- 2025 for each layer was 30 μm which is thicker than the S1813 photoresist described in the previous chapter, hence it needs a higher UV dose in order to

completely expose, and initiate crosslinking in, the layer.

In order to obtain vertical sidewalls in the SU-8, a filter was used during the exposure. A post exposure bake was then performed at 65°C/95°C for 1 min/6 min respectively. The baked pattern was developed with EC solvent for 4 minutes and rinsed with IPA for 10 seconds.

Finally, the sample was hard baked at 150°C for 15 minutes. This process was repeated for a further two layers of SU-8 resist in order to achieve an overall thickness of around 100 μm with a stepped ring pattern which provides an approximation of the 'ideal' Fresnel lens shape, as shown in fig. 5.2. The size of the steps, both in terms of height and width, is limited by the SU-8 fabrication process (equipment tolerance).

Figure 5.3 shows the fabrication process used to produce the Fresnel microlenses and fig. 5.4 shows an SEM image of the sidewall profile after the deposition of two SU-8 layers. A summary of the fabrication process can be seen in table.(5.1) as noted earlier.

Table 5.1: The microfabrication process for SU-8 Fresnel lens.

Process	Condition	Time
Substrate preparation(silicon wafer piranha etch)	$H_2SO_4 : H_2O_2$ (3:1)	20 mins
Spin SU-8 2025(30 μm)	500 rpm	10 sec
Spin SU-8 2025(30 μm)	3000 rpm	1 min
Soft bake(hot plate)	65°C/ 95°C	3 mins/6 mins
Expose(EVG 620 mask aligner, UV light 436 nm)	$250\,\text{mJ/cm}^2$	4 sec
Post exposure bake (hot plate)	65°C/ 95°C	1 mins/6 mins
Develop(EC developer)	20°C	4min
Rinse and dry(IPA)	20°C	10 sec
Hard bake	150°C	15 mins
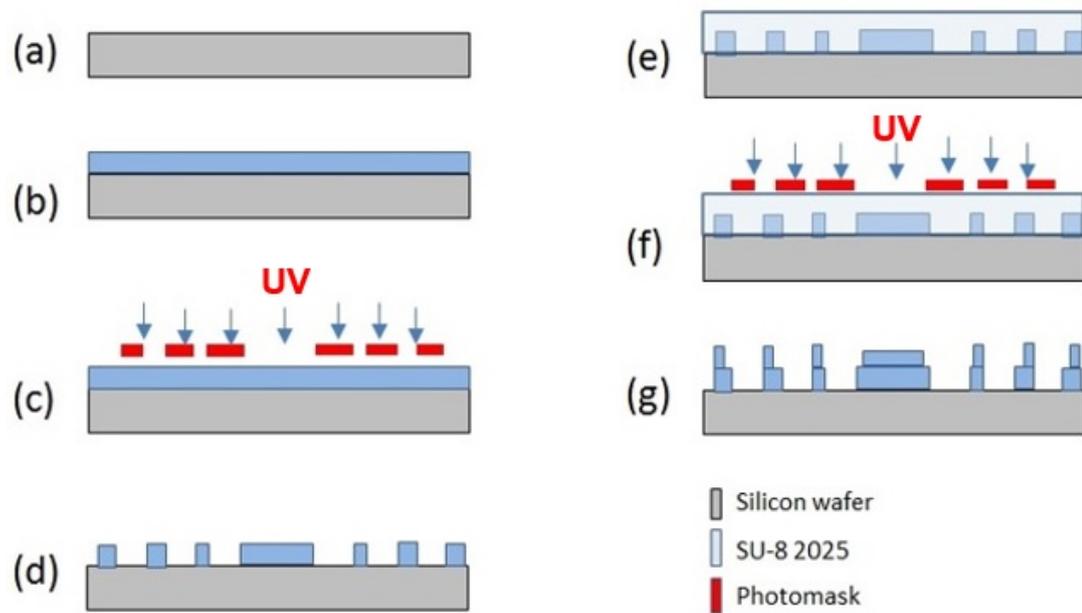
Figure 5.3: Fabrication steps of the SU-8 Fresnel lens. (a)Substrate cleaning. (b)Spin coating 3000 rpm (1min).(c) Soft baking $65°C/95°C$ and expose at $250-mJ/cm^2$. (d) Post baking, development of the resist and hard baking at $150°C$.(e) Spin coating second layer. (f) Soft baking $65°C/95°C$ and exposure at $250-mJ/cm^2$. (g) Post baking, developing the resist and hard baking at $150°C$.
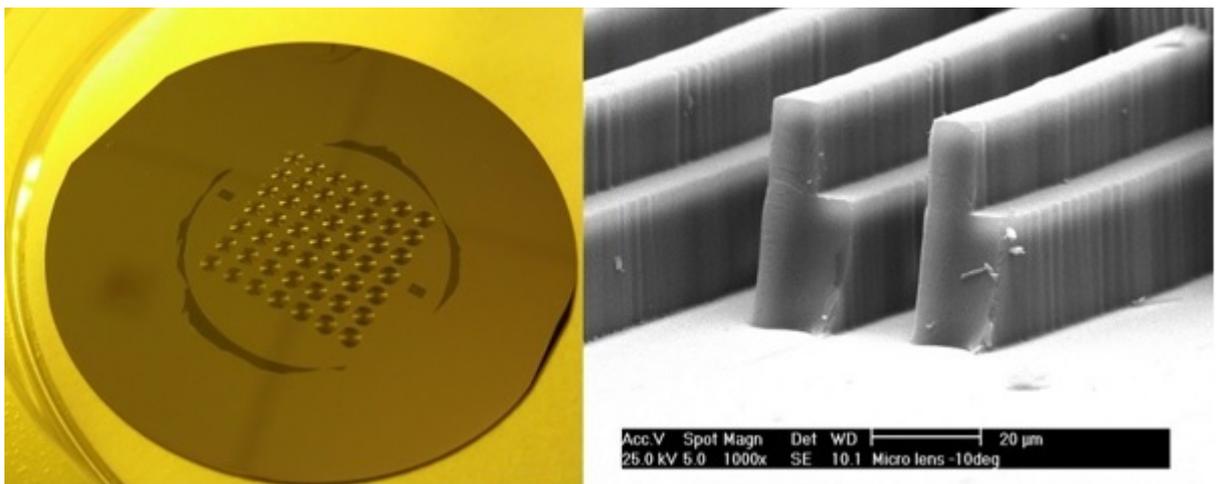
Figure 5.4: Fabricated Fresnel lens(left) and SEM image with showing two layers(right).

5.1.2   Experiment

The microlenses were tested in free space using a THz frequency vector network analyzer. Figure 5.5 shows a schematic drawing of the experimental set up with a Fresnel lens mounted on an X-Y stage. An off-axis parabolic mirror M1 is used to form a collimated beam from the horn antenna of the THz extender towards the Fresnel lens under test.
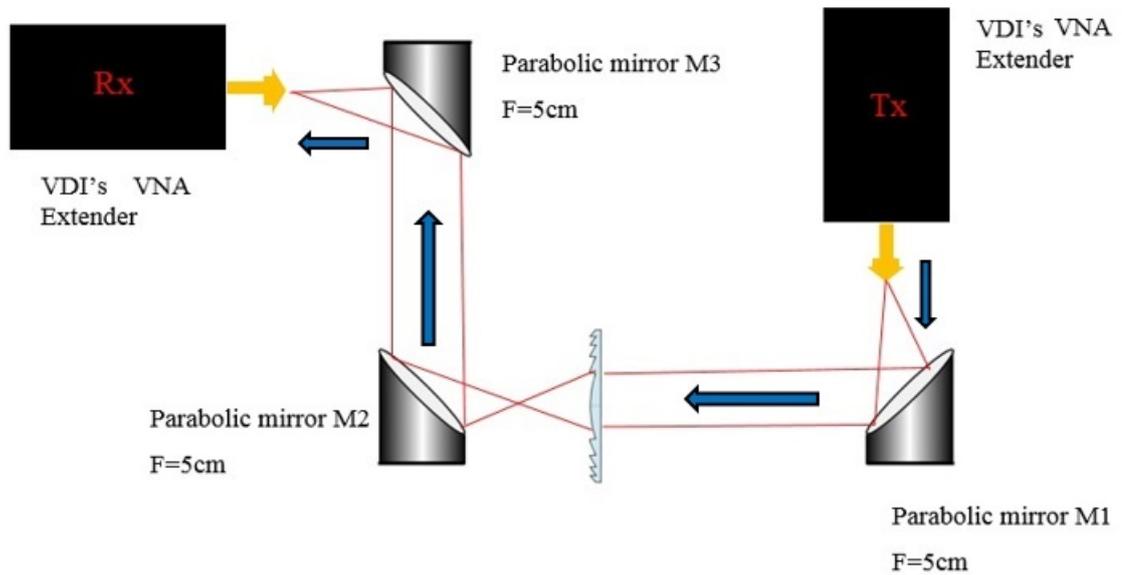
Figure 5.5: A schematic drawing of VNA setup for lens imaging

The Fresnel lens is placed into this collimated beam at a distance, from M2, of 50 mm (i.e. the focal length of mirror M2) plus the expected focal length, f, of the Fresnel microlens. A collimated beam is formed between M2 and M3, which is then focused onto the VNA extender head's receiver antenna, leading to a high measured signal power.

In contrast, if the actual focal length of the microlens does not correspond to the expected focal length, due to misalignment in the system, the beam after M3 will broaden and the receiver will not receive the focused beam which is expected,

leading to a lower measured field amplitude incident on the receiver antenna.

The microlens substrate was raster scanned in the beam to form an image where the brighter spots represent regions of higher signal power and darker regions represent lower signal power. Figure 5.6 shows an image of a microlens array, taken at 1 THz, and positioned for an expected focal length of 3 mm (as calculated using eq.(5.1) in the introduction).

However, in this figure, the microlenses show as dark regions which suggest, not unreasonably, that the focal length differs from that predicted by the simple paraxial approximation for a hemispherical lens.
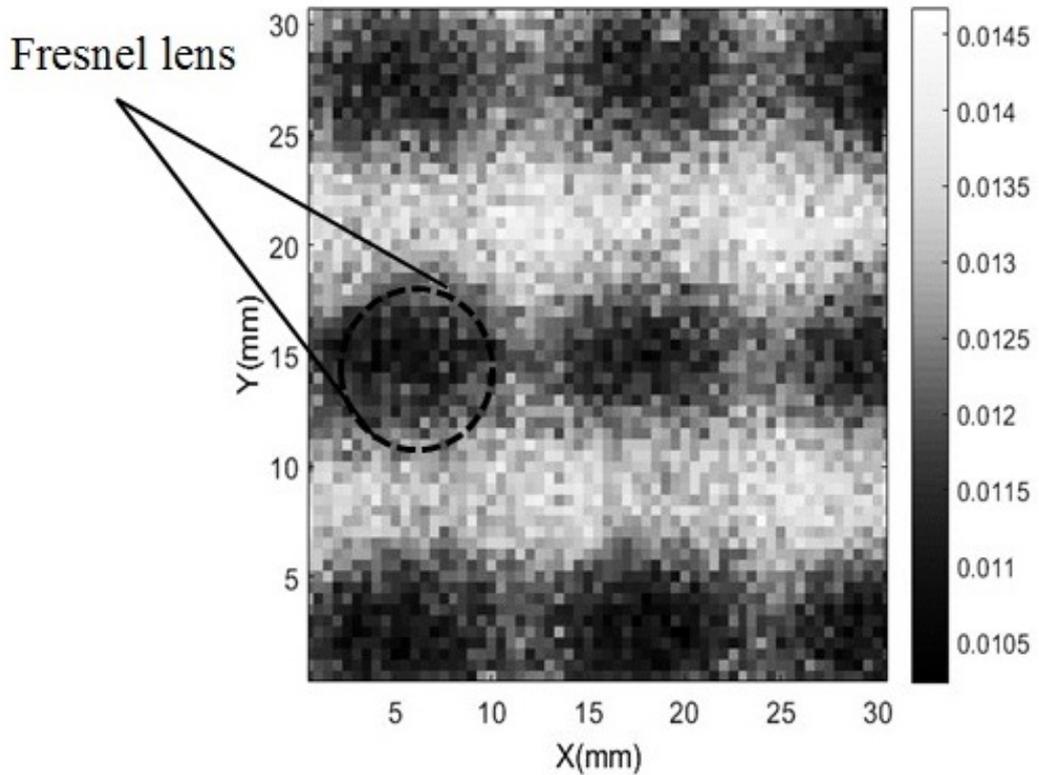
Figure 5.6: Image of the E-field intensity at the expected focal plane of the Fresnel lens array at 1 THz. Dark spots are observed where increased brightness is instead expected.

5.1.3   Simulation and Results

Lumerical 2016a (V8.15.736), a commercial FDTD solver, has been used to simulate the interaction of the THz radiation with the microlenses. The experimental microlens characterization measurements presented in the previous section indicated that the microlens focal point differed from the expected value that had been obtained via a paraxial approximation. An FDTD model has been developed to match the thickness and shape of the fabricated structure and the slightly negative side-wall slope of the SU-8 is approximated as being vertical; with a refractive index of 3.42 for the silicon substrate and 1.5 for the SU-8.

A full 3D FDTD simulation was carried out with a plane wave with a centre frequency of 1 THz, going through the Fresnel lens of diameter of 2 mm fabricated on a silicon wafer with thickness 300 μm. Figure 5.7 shows the electric field intensity (E^2) along the $x - z$ axis at 1 THz and 0.8 THz. Figure 5.8(a) shows a line profile through the $x - z$ axis, and the dark region observed in the experiments at z = 2 mm is also present in the FDTD results, where a low intensity region can be observed at around x = 0 mm, i.e. the center of the microlens, and with Z approximately between 2.5 and 3 mm from the expected focal point. Although the precise focal point of the structure is not well defined, peak intensity can be observed at 5 mm from the substrate. To verify this result experimentally, the microlens substrate was moved to this position in the VNA setup described in the previous section. Figure 5.9 shows the received signal intensity with the microlens array placed at distance z = 5 mm. The lenses are now represented by the bright regions and are, therefore, acting to focus the collimated beam.

This shows that there is good agreement between the simulation and experimental results.   Figures 5.7 and 5.8 (b) shows the E-field intensity at, 0.8 THz. There is a dark region at around 2 mm and a lower intensity after 2 mm, which means that, at this frequency, the lens did not focus properly: this could be due to the frequency dependence of the Fresnel lens which makes it focus different terahertz frequencies at differing positions. In figs. 5.7 to 5.9 for small z distances, the apparent noise in simulation results is actually due to the effect of the substrate but note that it is not resolved well for the presented image scales.
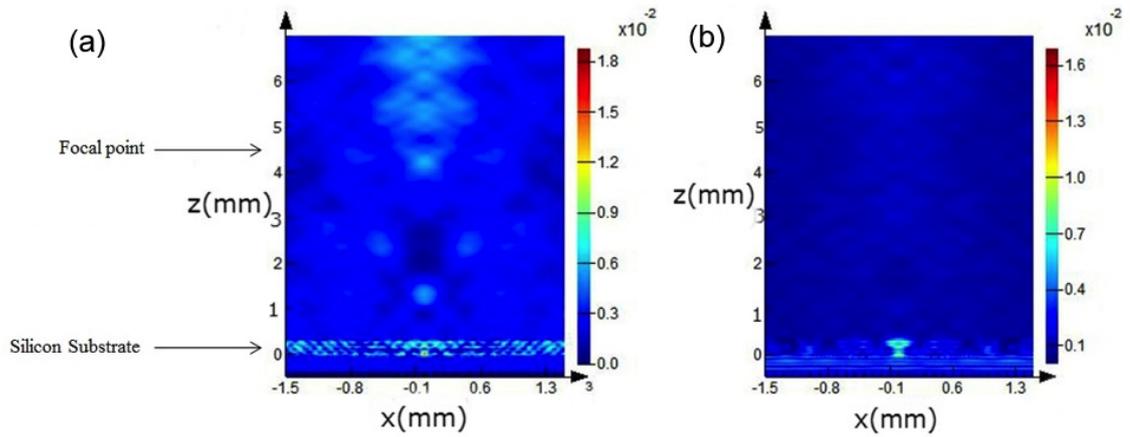
Figure 5.7: The FDTD simulation of the Fresnel microlens design along the x-z axis at 1 THz (a) and 0.8 THz (b). The high E-field intensity is observed at z=5 mm(focal point) and low E-field intensity at z=0 (substrate) at 1 THz, and low E-field intensity along the x-z at 0.8 THz.
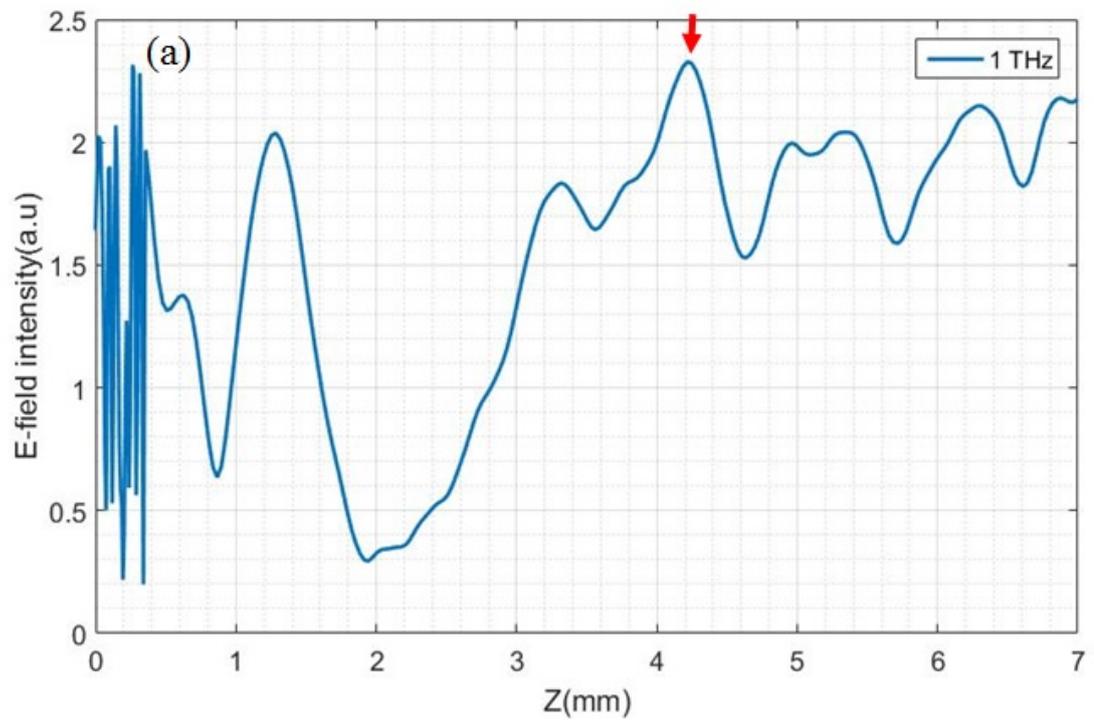
(a) 1 THz
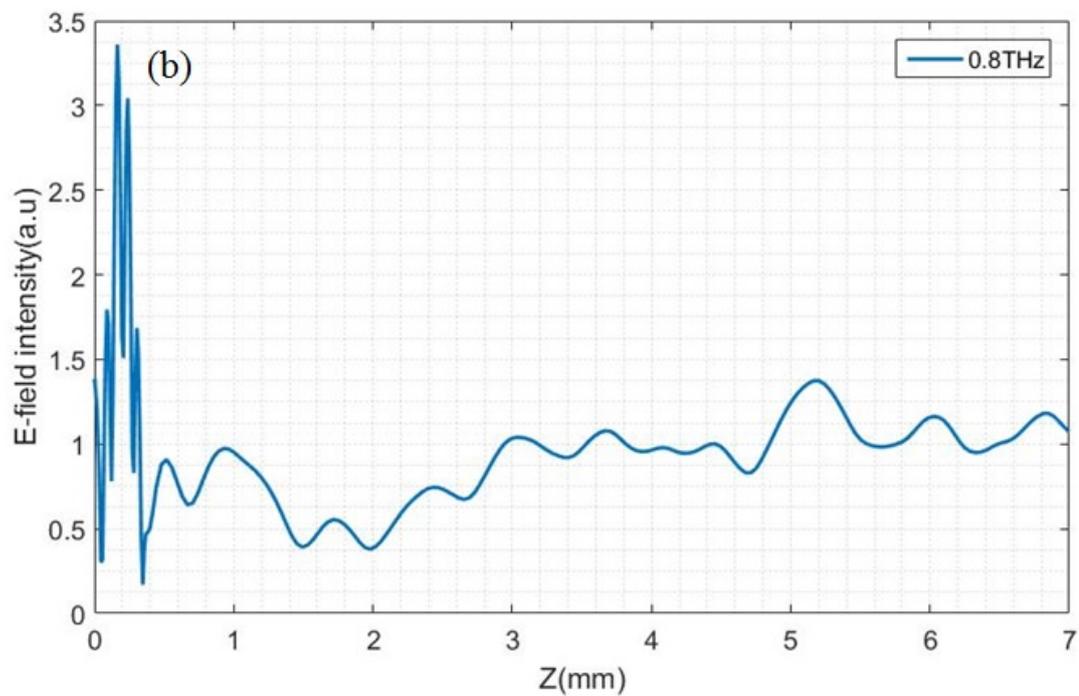
(b) 0.8 THz

Figure 5.8: E-field intensity as function of distance from the focal point at 1 THz (a) and 0.8 THz (b). The red arrow at 1 THz (a) shows the highest electric field intensity which represents of focal point and the low E-field intensity at 0.8 THz (b).

103
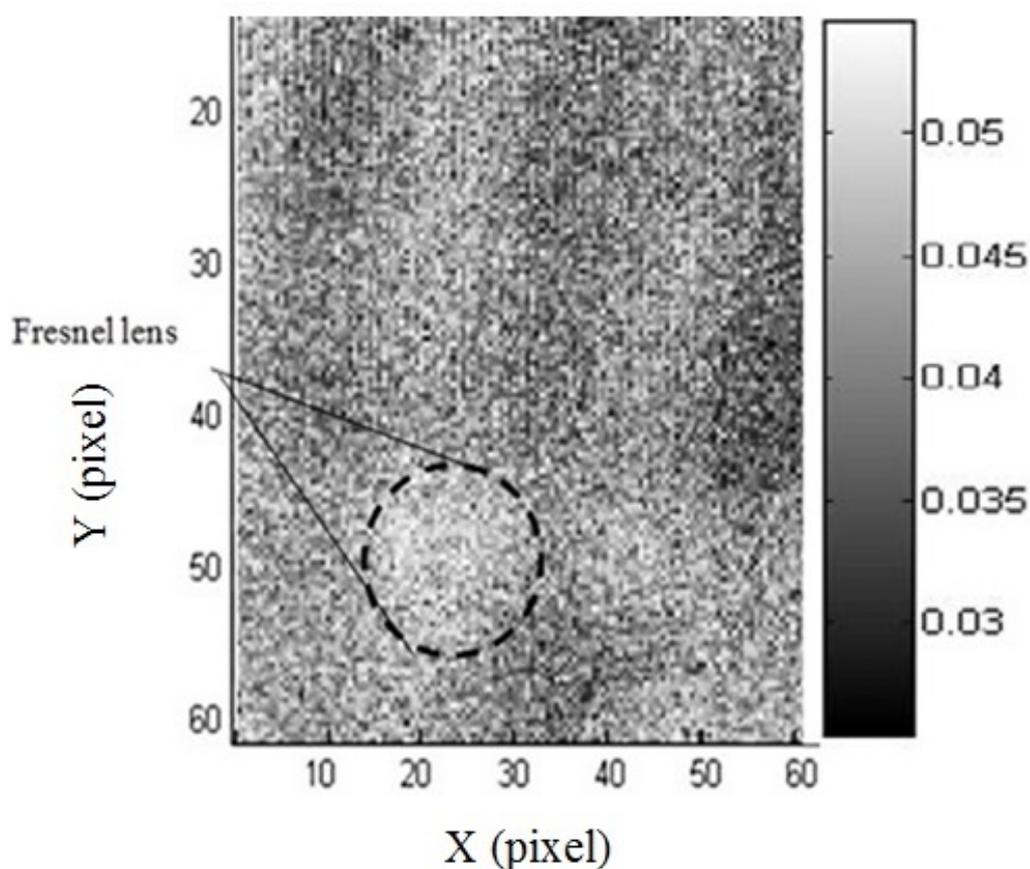
Figure 5.9: Image of microlens array placed at the focal plane (5 mm) which is obtained by raster scan all over the sample along the x-y plane. Bright regions represent the Fresnel lens focal points.

Making different stacks of SU-8 resist with 10s of micron size spatial dimensions led to some issues such as finding the pattern's alignment keys during mask aligning due to transparency of the SU-8 alignment marks. The lens was originally designed to have 4 layers of SU-8 (of 25 μm thickness each) with each layer half the feature size of the previous one, but since the narrowest layer was less than 5 μm size the mask aligner could not reliably expose the pattern for last layer. For this reason, the final implementation uses just 3 layers, but with thicker layers in order to produce almost 100 μm thickness in total.

Using SU-8 2025 resist during the spinning of the second layer of resist on silicon

substrate introduced many bubbles into the layer due to the topography of the first patterned layer of SU-8. The bubbles can introduce non-uniformity to the surface structure which, in turn, affects the focusing property of micro lenses resulting in degraded optical performance.

In order to remove the bubbles, various techniques were trialled including the use of edge bead remover but this also changes the thickness of the resist and the resist needed to be spread uniformly. Leaving the spun sample before soft baking was another way of removing bubbles but it should not be left for a long time (24 hours) to avoid any cross-linking occurring prior to exposure and development. This work leads on to the fabrication and characterization of other diffractive optics components in terahertz region such as a Fresnel reflector which will be explained in the next section.

5.2   Fresnel Reflector

5.2.1   Introduction

When used as reflective components, FZPs can be fabricated from metals. Headland et al [138] recently reported the development of a 3D printed metal zone plate. They characterized the focal spot and beam shape using a THz-TDS system; with the highest reflective efficiency recorded at 530 GHz limited by the surface roughness and surface oxide due to the 3D printing process and the use of a titanium alloy respectively.

Here we report on the use of a THz-VNA for the measurement and mapping of electric field intensity and phase near to the surface of reflective THz components. A fixed five parabolic mirror and transmitter/receiver head arrangement is presented which has the advantage of requiring only the sample to be swept during measurement. A micromilled aluminium FZP reflector structure has been fabricated as an exemplar structure. It uses a binary design which, although lossy compared to multilevel zone operating at 1 THz plates (due to higher diffraction orders), is easier to fabricate and is well suited to test the measurement system. Finite difference time domain (FDTD) simulations are used to support the experimental results presented in this work.

5.2.2   Design and Simulations

As a model component, we have fabricated a zone plate reflector based on the traditional Fresnel design (see fig. 5.10(a)). Manufacturing has been carried out

using a bespoke micromilling system on an aluminium substrate (fig. 5.10(b)) leading to a cost-effective, compact and light design. Figure 5.11 shows the SEM image of micromilled aluminium substrate based on Fresnel zone structure.
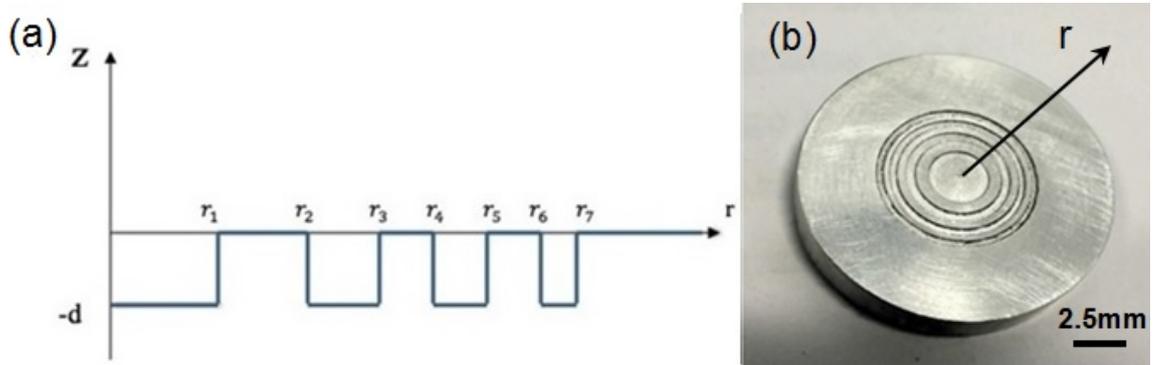
Figure 5.10: (a) Schematic profile of FZPR with 4 zones (b) photograph of aluminium FZPR. The radial dimensions have been obtained from equation (1) given in the main text.
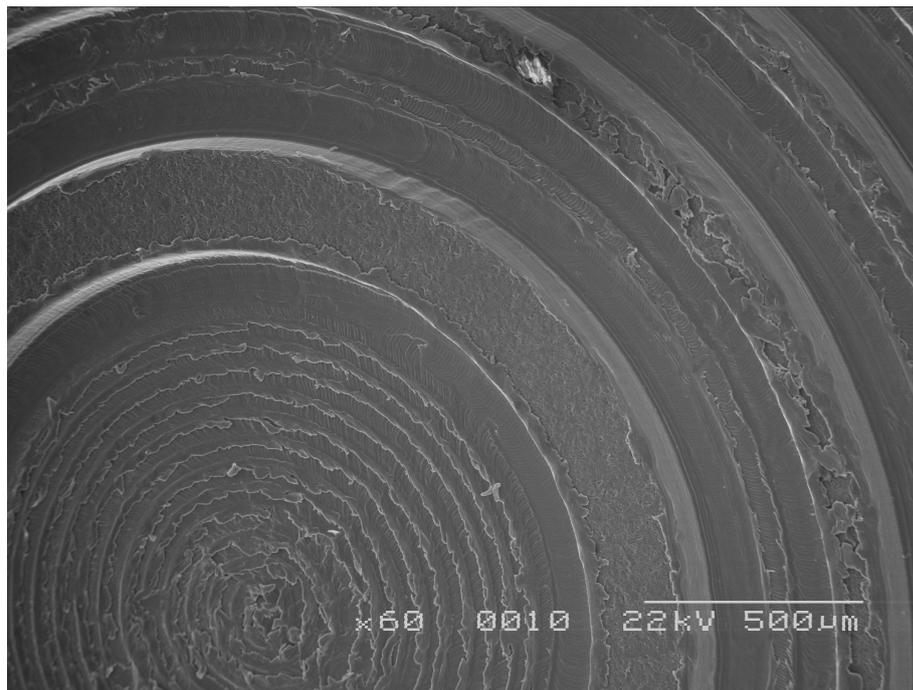
Figure 5.11: The SEM image of Fresnel reflector.

Figure 5.10(a) shows the configuration of the Fresnel zone plate reflector (FZPR) which consists of a set of concentric milled grooved zones. The Fresnel zone radii are periodic in r^2 with a period in r_p^2. The mth zone radius, r_m is determined by

$$r_m^2 = m r_p^2 \qquad\qquad (5.2)$$

The incoming beam is diffracted by the Fresnel zones interfering constructively at multiple focal points on the main optical axis with the first focal point located at [139]

$$F = \frac{r_p^2}{\lambda} \qquad\qquad (5.3)$$

where F is the distance from the reflector and λ is the wavelength of interest. The reflector contains of four zones with a 13 mm overall diameter, r_p= 2.5 mm. This corresponds to a first focal point centered at 20 mm (for 1 THz). The numerical aperture (NA) for this configuration is 0.357. This structure offers the potential to choose a trade-off between resolution and depth of field and, with a low NA, the bias here is towards a longer depth of field. A nominal zone depth of 75 μm has been micromilled to produce the necessary π phase shift. The final fabricated structures had a measured zone depth of 62 μm with a 2.3 μm rms surface roughness at the bottom of each milled zone (compared to 0.32 μm in the unmilled area). It should be noted that this surface roughness is two orders of magnitude smaller than the free space wavelength at 1 THz. Therefore, it is reasonable to neglect its effect on the optical performance of the reflector.

A commercial 3D FDTD solver (Lumerical) has been used to simulate the effect of the zone plate reflector on an incident 1 THz frequency plane wave. The reflectors have been simulated using the same dimensions as the micromilled devices and within the same frequency range as the THz VNA operates. In the simulations, aluminium is assumed to be a perfect electrical conductor. Reflections are minimized

through the use of a perfectly matched layer (PML) [140] located along the two boundaries perpendicular to the reflector axis. Periodic boundary conditions have been imposed on the sides of the reflector (i.e. equivalent to simulating a reflector array). This permits the simulation of plane wave.

Figure 5.12(a) shows the electric field intensity on a plane perpendicular to the reflector at 1 THz and the electric field intensity along the main optical axis. As is also evident in the optical axis profile (fig. 5.12(b)), the simulated electric field intensity FWHM in the region of the first focal point is spread between 15 and 25 mm with a plateau at 20 mm. At Z = 6 mm, there is evidence of a higher order focal point. This is to be expected with the FZPR configuration which leads to higher order (closer to the reflector, but lower intensity) focal points. The simulated field intensity, plotted in the XY plane, for various Z distances from the reflector is shown in fig. 5.13. It can be seen that by moving towards the focal point of the reflector, the spot size becomes smaller and the electric field intensity has increased.
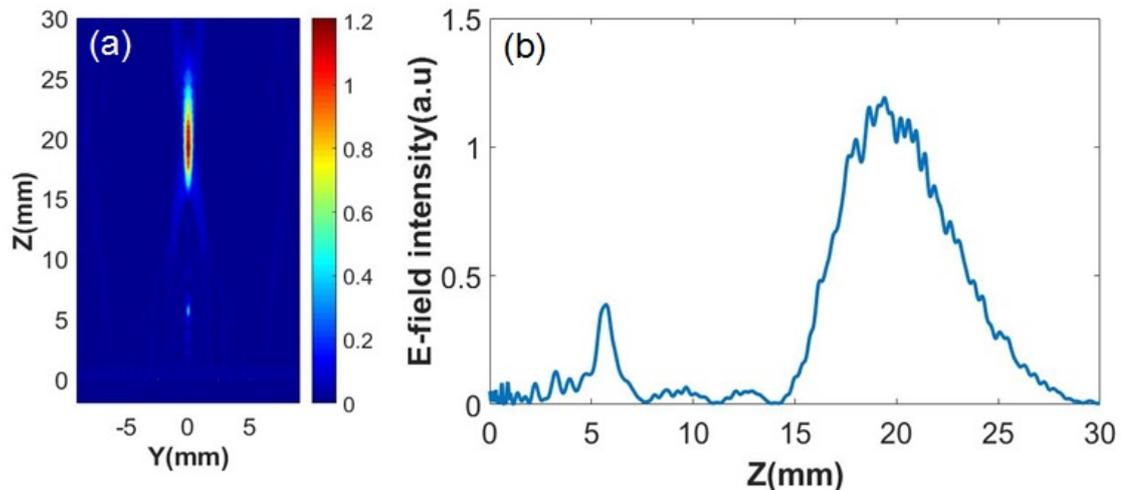
Figure 5.12: FDTD simulated field intensity distribution in the (a) YZ plane (with X= 0 mm) and (b) along the optical, Z axis (with both X and Y= 0 mm).
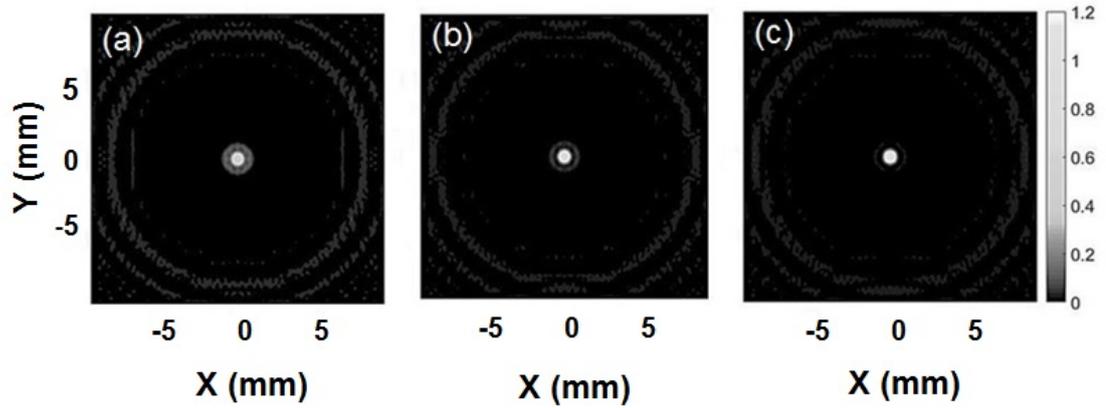
Figure 5.13: FDTD simulated field intensity distribution in the XY plane at a distance, Z, along the optical axis, of (a) 19, (b) 20, (c) Z=21 mm from the reflector.

The simulated phase image at the focal point, $Z = 20$ mm, is shown in fig. 5.14. The focal spot can be seen as a bright circular region of constructive interference $(+\pi)$, flanked by an area of destructive interference $(-\pi)$. A speckle pattern is superimposed on the simulation image; its shape arises from the use of periodic boundary conditions leading to interference from the adjacent reflectors. The effect of this interference can be minimized by using a larger simulation domain but at the expense of a much longer simulation time.
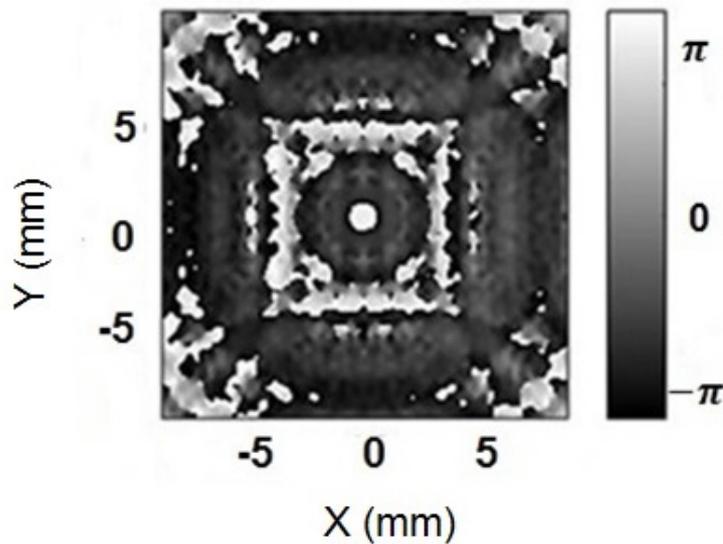
Figure 5.14: Simulated phase image at 20 mm, showing the focal spot as a bright region of constructive interference $(+\pi)$.

5.2.3   Experiment

The micro-milled aluminium reflector was tested with the THz-VNA. Figure 5.15 shows a schematic drawing of the experimental setup with the reflector mounted on a motorized XYZ optical stages. All components are rigidly mounted on an optical bench. This permits the measurement of XY scans with respect to the distance from the reflector, Z. The receiver detects the part of the reflected beam that is focused by the ZPR. Such scans allow a direct measurement comparison with the simulations presented previously. The alignment is carried out by using a white LED and diffuser screen at the receiver side and replacing a camera with extender head in the set up. The beam will be illuminated from the white LED light (in the receiver side) to an object through the mirror M5 and (silicon wafer) beam splitter. The collimated beam between M1- M2 will be focused on the iris position. The transmission is maximized by fine alignment of the mirrors and beam splitter, while reducing the iris size. The focused beam will be collimated between M3 and M4. Then the collimated beam from M4 will be focused and detected by camera at the receiver position. By optimizing the parabolics and iris we could improve the resolution of the image. Tracing the beam using white LED light instead of THz beam can help to improve the alignment setup.

The VNA measurement simultaneously provides information on both the amplitude and phase of the horizontally polarized electric field. The polarized radiation emerging from the horn antenna is collimated by an off-axis parabolic mirror M5. This collimated beam is used to illuminate the Fresnel reflector through a silicon beam splitter which is set at a 45° angle with respect to the

reflector's optical axis. The collimated beam illuminates all of the reflector and its surrounding region such that at maximum scan displacement the reflector is still fully illuminated. The electric field is imaged through an objective system, M1-3 and then focused by M4 to the receiver antenna. An iris is placed between M2 and M3 to minimize the effect of the scattered field and can influence the SNR.

The distance from the origin on the Z axis is determined between the reflector and the focal point of M1 (as shown in fig. 5.15). The uniformity of excitation is maintained because a fixed beam has been used and the sample moved. A key benefit of this configuration is that, by using fixed optics, the effect of parabolic mirrors and the beam splitter on the phase information during measurement is negligible.
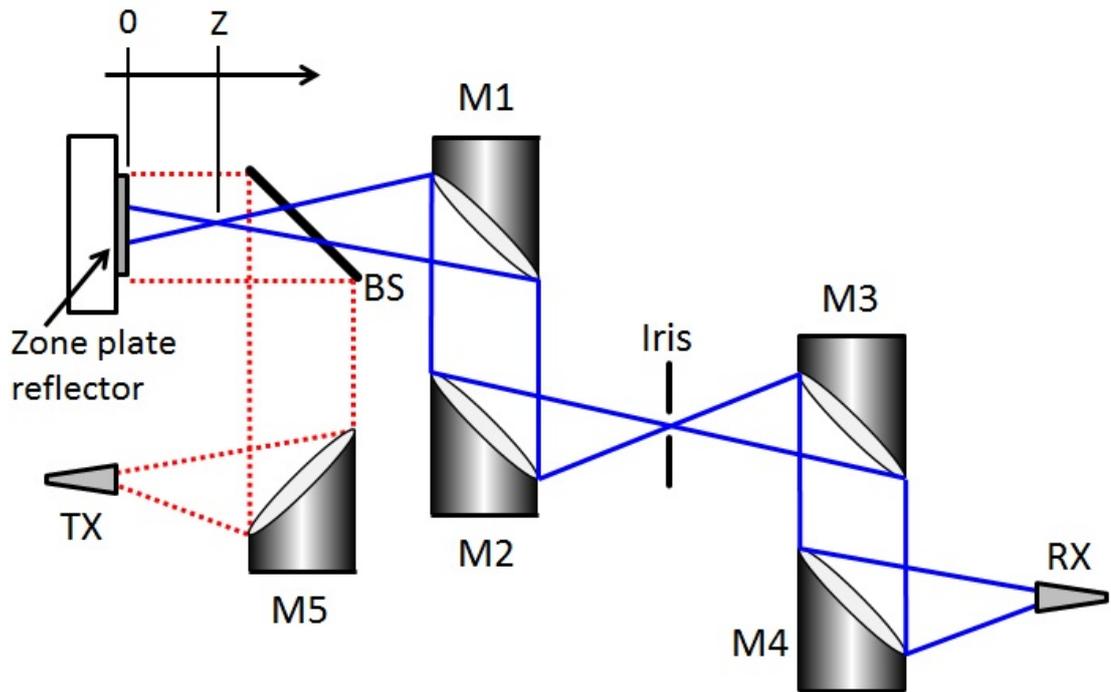
Figure 5.15: Schematic diagram of the experimental setup with the reflector mounted as shown. All of the parabolic mirrors have a focal length of 10 cm.

The measured field intensity distributions, at 1 THz, in the XY plane are shown in fig. 5.16 where the focal point is flanked by a dark ring structure resulting from

destructive interference of the reflected beam. The round focal spots indicate low astigmatic aberrations. No smoothing or other post-processing has been applied to the images. There is good agreement between the simulated and measured results; although the measured central spot at the 20 mm focal point is slightly larger. The low numerical aperture of M1 limits the minimum resolvable feature size to 1.2 mm. However, there is a faint ring around the spot in the simulated image. This cannot be resolved by the measurement setup but will act to enlarge the measured spot. The outer bright ring in fig. 5.16 relates to a reflection from the unpatterned aluminium area and also acts to confirm that illumination uniformity from M5 and the beam splitter is good.
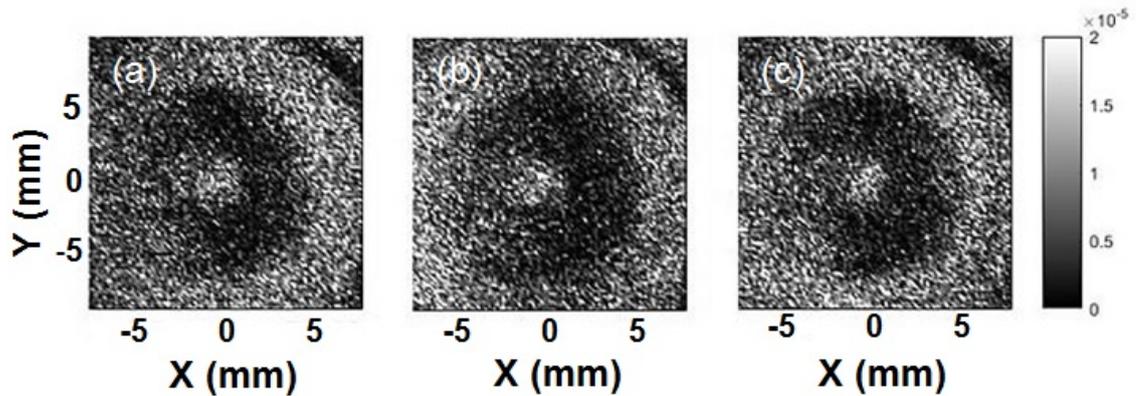
Figure 5.16: The measured field intensity images, at 1 THz, for planes at (a) Z = 19 mm, (b) Z = 20 mm, (c) Z = 21 mm. All of the captured images are 100 × 100 pixels, corresponding to an area of 20 × 20 mm.

The spot size at the focal point has been obtained from the FWHM of a Gaussian fit to the intensity profile. The fitting has been carried out using the least squares method. Figure 5.17 shows the FWHM plot as a function of distance with respect to the reflector. As it can be seen, the smallest FWHM is observed at Z = 20 mm which corresponds to both the designed and simulated focal point. Here we report in the

FWHM either side of the focal point which is also seen in field intensity distribution (fig. 5.12). However, direct comparison between the simulated and measured FWHM away from focal point is not possible since the simulation displays very well-defined side lobes which prevent fitting with a Gaussian shape. Away from the focal point, the experimentally obtained FWHM plotted in fig. 5.17 also factors in the effect of these side lobes. Figure 5.18 shows the simulated Gaussian fit of the E-field intensity distribution as a function of distance, Z with respect to the reflector. As can be seen at distances Z=16 mm to 25 mm the field intensity and the Gaussian fit are completely overlapped in simulation and it is difficult to compare with measured FWHM.
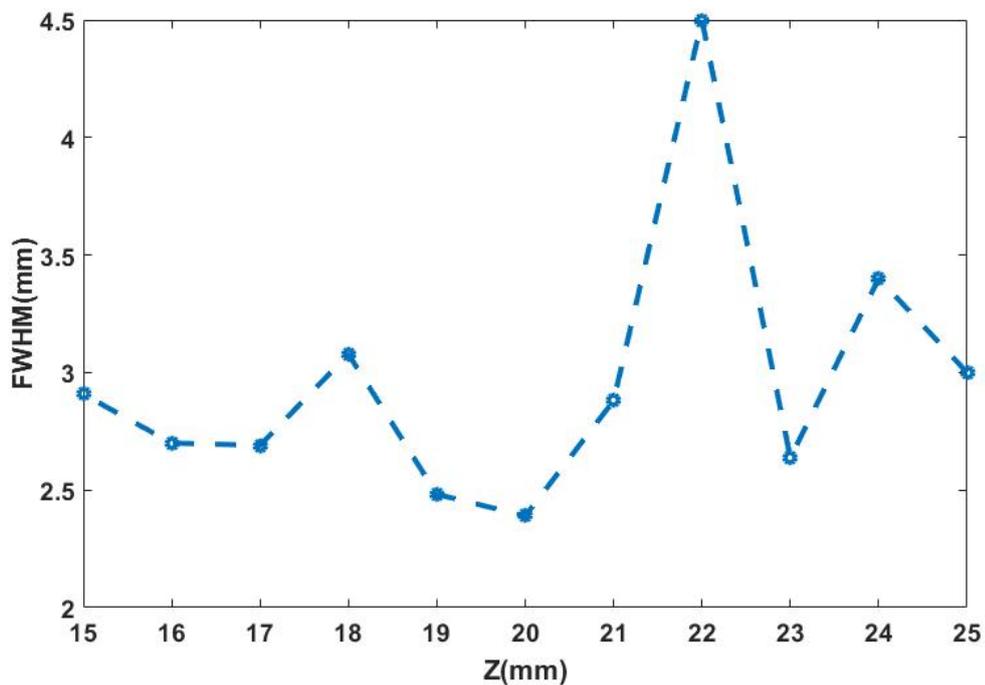
Figure 5.17: FWHM of the measured focal point at distance, Z, from the reflector surface.
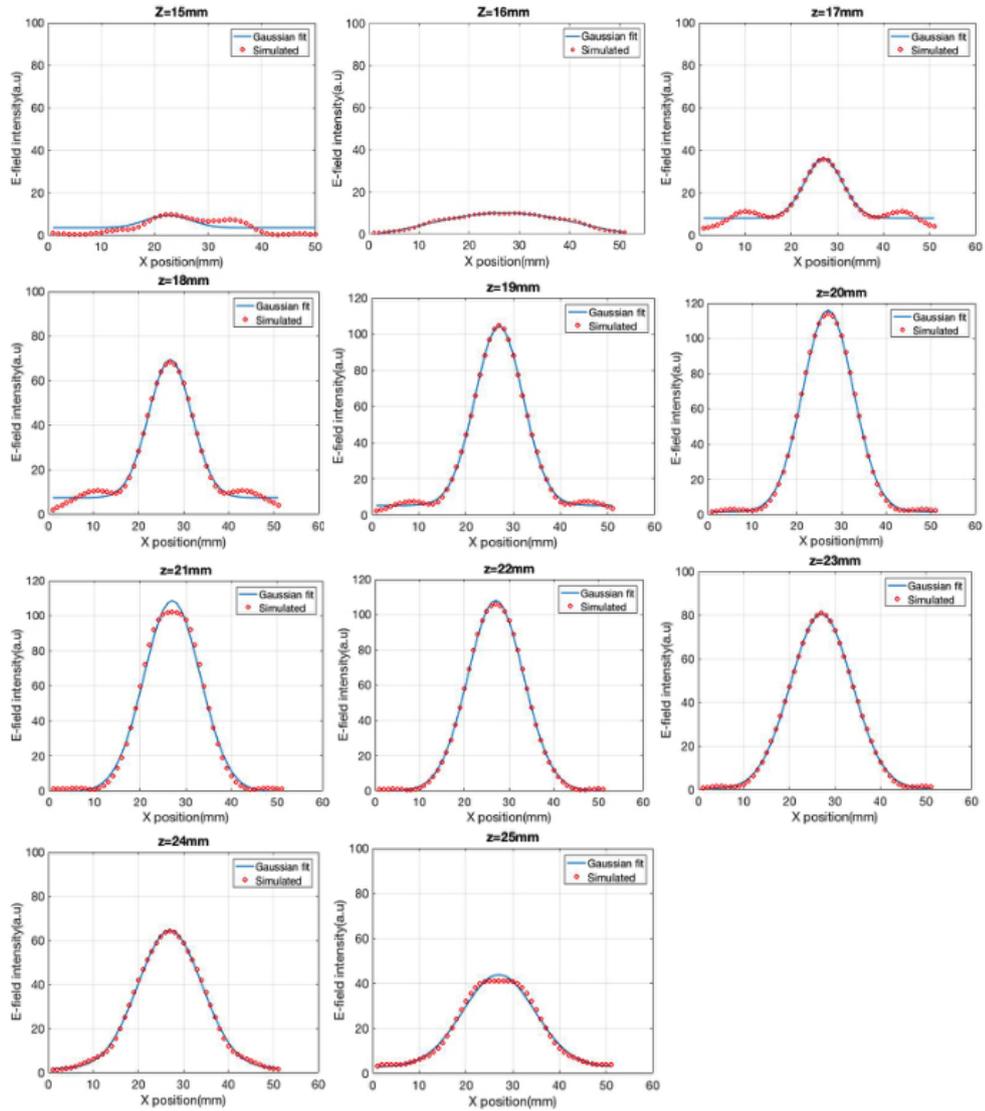
Figure 5.18: The simulated Gaussian fit of the E-field intensity at distance Z from the reflector.

The experimental data is further supported by comparing the measured and simulated phase images, shown in fig. 5.14 and fig. 5.19 respectively. As explained earlier, the phase data is obtained simultaneously with the amplitude and also therefore, intensity data during the XY scanning. The phase data is very sensitive to surface tilt which is readily observable as linear banding on the images. Surface tilt effects on the phase are minimized during the system alignment procedures. However, any remaining tilt is corrected via a software levelling approach. To
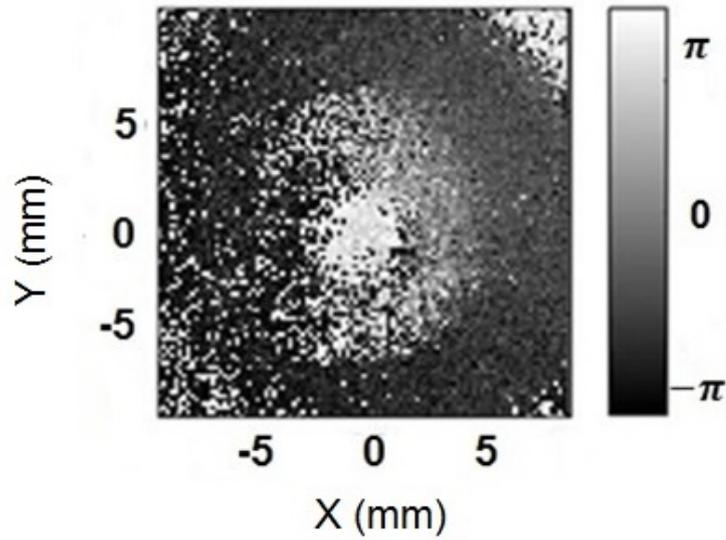
Figure 5.19: FWHM of the measured focal point at distance, Z, from the reflector surface.

do this, a linearly variable phase offset $\Delta\theta(x, y)$ is calculated using the following equation

$$\Delta\theta(x, y) = \frac{2\pi}{\lambda}x\tan\alpha + \frac{2\pi}{\lambda}y\tan\beta, \tag{5.4}$$

where α and β are the tilt angles of the reflector along the x and y direction, respectively. The value of phase is then wrapped between $(-\pi)$ and $(+\pi)$ radians. The levelled phase image shown in fig. 5.19 clearly shows the transition from the focal spot, a region of constructive interference, to the surrounding circular region, with a lower field intensity formed by destructive interference.

The area of destructive interference in the measured phase image is smaller than in the simulation for two main reasons. First, as seen in the intensity images, the focal spot is larger than in the simulations which, in turn, enlarges the area of constructive interference in the phase images. Second, in the simulation, the area surrounding the focal spot includes an area of high contrast light and dark regions. However, as discussed earlier, the measurement system is resolution limited by the

NA of mirror M1 (fig. 5.15) and is unable to resolve such regions of high contrast in the phase images and instead is evident as a gradual grayscale transition from white to black. The bright area in the top right corner of the experimental phase image is a region of background reflection from the metallic substrate. To the left of the focal spot is a darker region, which is also evident in the intensity images (fig. 5.16) as an area of higher intensity. This could be attributed to slight imperfection in the reflector manufacture (e.g. the surface is not completely flat).

The ability to image the phase of the reflected beam in the region of the reflector surface could aid the design and characterization of next generation THz beam shaping devices, e.g. passive and active phased arrays. To open up techniques which are commonly used in the microwave field to the THz region, such as near field to far field transformation (or vice versa), details of both phase and amplitude are required.

5.2.4 Conclusion

We have demonstrated a micromachined, multilevel SU-8 based Fresnel type microlens for operation in the terahertz region. The design, which was derived by a simple hemispherical lens, has been simulated using FDTD. The simulation results support the experimental results, which indicated that the focal point of the microlens differed from that which would be predicted by a paraxial approximation. The actual focal point has subsequently been verified experimentally using a THz-VNA with free space optics. However, there is scope to improve the design of the lens to provide low-cost lenses with a large numerical aperture and short focal

length which can be used in terahertz systems.

A THz-VNA based quasi-optical configuration which can be used for electric field intensity and phase mapping as a function of distance from the surface of reflective optics has been presented. As an exemplar optical component, a zone plate reflector has been designed for operation at 1 THz and micromilled into aluminium. To obtain intensity and phase maps, the reflector was scanned in 3D space whilst the VNA extender heads and all other optical components were spatially fixed. The intensity and phase data has been compared with FDTD simulations and, in general, they showed good correspondence with the focal spot clearly visible and located at 20 mm away from the reflector surface. The reported setup permits the characterization of a wide range of beam shaping devices likely to provide light, compact and rugged optics necessary for incorporation into next generation THz systems.

Chapter 6

Liquid characterization using a THz FZPR

This chapter describes a platform that integrates a THz-VNA and microfluidic devices based on both acetate films (i.e. extremely low cost) and silicon for material characterisation. Firstly, the conventional setup with a VNA and four parabolic mirrors has been used for measuring the transmission of terahertz radiation through the microfluidic channels. Secondly, a very simple terahertz setup which combines the Fresnel Zone Plate reflector (FZPR) from the previous chapter and with just one parabolic mirror for measuring the reflected beam from FZPR through the microfluidic devices is presented.

The idea of the simple setup is to exploit diffractive optics (FZPR) to reduce losses and increase the transmission. A range of samples, including IPA-water mixtures with different concentrations and coffee-water mixture are analysed with these two microfluidic devices and also using the two terahertz set-ups.

Figure 6.1 shows the simple setup integrated, with a parabolic mirror, microfluidic channel and Fresnel reflector.

The microfluidic devices presented in this chapter are different in structure but not in operation in a terahertz system. This compact setup has been designed to minimize the optical path length by using a low number of optical components and short distance of FZPR relative to the microfluidic channel. Reducing the wave travelling path in liquid samples provides better sample interaction with the transmitted signal and minimizes water absorption effects in the THz system.

Since silicon and acetate film are transparent to the THz radiation; they are good options for producing a microfluidic channel. But the strong Fresnel reflections at material-air layers in the microfluidic devices structure reduce the transmission through the channel.
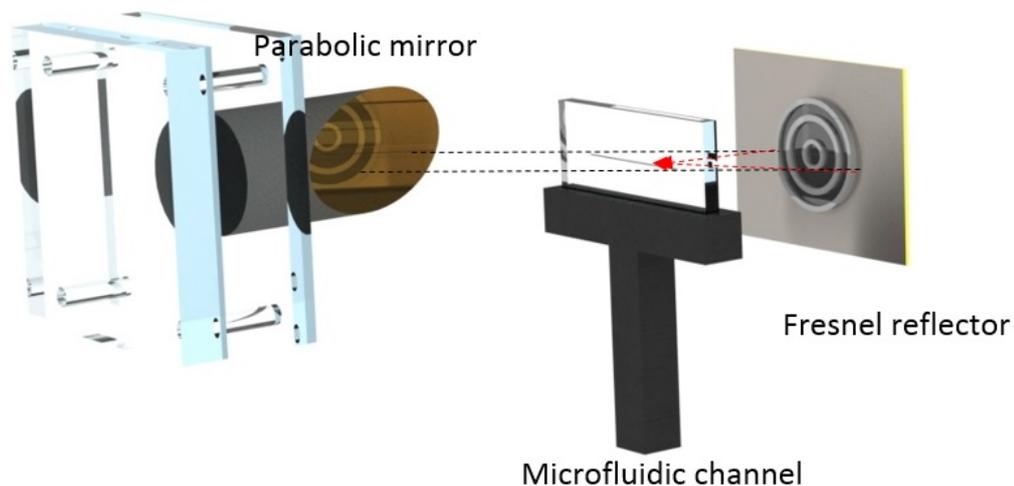
Figure 6.1: The integrated setup, with a parabolic mirror, microfluidic channel and Fresnel reflector.

6.1   Introduction

In recent years, terahertz spectroscopy has developed rapidly for studying the structure and behaviour of many biological systems [141]. Microfluidic channels have several attractive features in line with lab-on-chip applications such as their flexibility in design, the capability of integration, and freedom in the choice of material such as glass, silicon or a polymer (e.g PDMS). However, the terahertz characterization of liquid samples is challenging due to water absorption [142, 143]. Using a microfluidic channel in combination with terahertz technology could be a possible solution to solve this problem by minimizing the optical path length [144]. Reducing the wave travelling path in liquid samples reduces losses and improves the detection of the terahertz signal. Although, terahertz time-domain spectroscopy (THz-TDS) systems based on femtosecond lasers, have been widely used for this purpose [145, 146]; having a combined and integrated setup with a terahertz component operating directly in the frequency domain using a vector network analyzer would open up alternative THz techniques for monitoring the material present in the channel.

Conventional microfluidic channel forming materials such as polydimethylsiloxane (PDMS) [147] and Zeonor 1020R [147], are not well suited for use in the terahertz region due to their high intrinsic water content. In contrast, there were attempts to utilize silicon [148] due to its natural transparency in THz region and the ease of micromachining in order fabricate a microfluidic device.

6.2   Design and Fabrication

6.2.1   Silicon based microfluidic channel

The initial design was based on a silicon wafer (refractive index 3.42 at THz) with a simple design which includes two inputs and output capillaries connected to the main chamber (with a depth of 40 μm). The fluidic access ports are placed on the top layer of the silicon wafer to allow liquid to pump through the device. The width of capillaries was kept to 200 μm to reduce pumping pressures. The chamber dimension was big enough for straightforward alignment of the terahertz beam.

Standard lithography techniques have been used for the fabrication of the silicon microfluidic channel; with KOH bulk etching defining the channel. First, a layer of 2 μm thick positive photoresist (S1813) was spun on the silicon wafer, followed by soft baking at 95° C for 5 minutes. This is followed by exposure using an EVG 620 mask aligner, UV light 436 nm and then wet etching of the oxide in buffered hydrofluoric acid (HF) for 20 minutes; and the removal of the photoresist, before KOH etching for 1 hour at 85° C in a water bath to achieve 40 μm depth. KOH etching is also used to define the input and output ports on the separate silicon wafer and seal the channel using photoresist. The device has been placed between two polymer-clamping structures and sealed with a PDMS coupling. A pipe is also used on the input port to pump liquid samples through the device. Figure 6.2 shows the diagram of capillaries, chamber and the ports into the silicon wafer. A summary of the fabrication process can be seen in table 6.1.
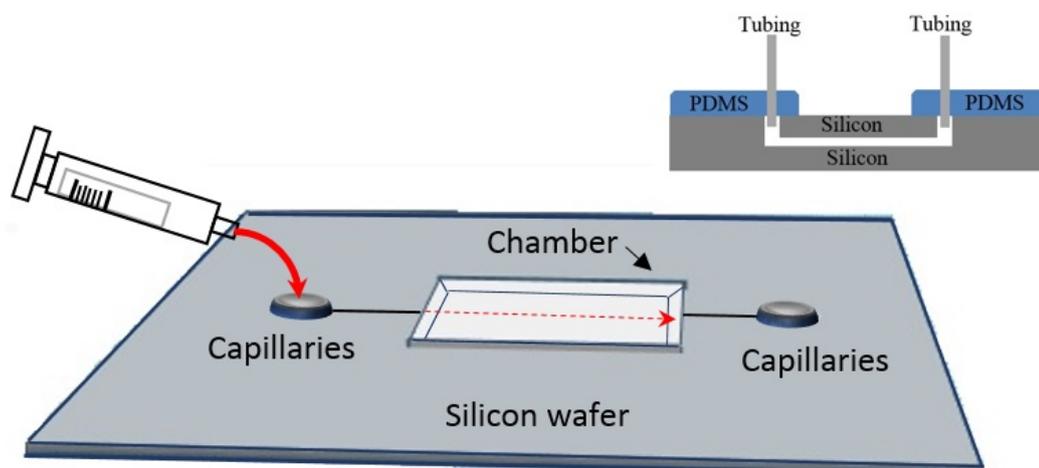
Figure 6.2: Side view of ports, chamber and capillaries etched into the silicon wafer.

Table 6.1:   The microfabrication process parameters used for creating a silicon microfluidic chamber.

Process	Condition	Time
Substrate preparation (silicon wafer piranha etch)	$H_2SO_4 : H_2O_2$ (3:1)	20 mins
Oxidized wafer(700 nm)	1050°C	4hr
Spin HDMS	3700 rpm	10
Spin S1813(2 μm)	500 rpm	10 sec
Spin S1813(2 μm)	3700 rpm	60 sec
Soft bake(hot plate)	95°C	5 mins
Expose(EVG 620 mask aligner, UV light 436 nm)	$75\,\mathrm{mJ/cm^2}$	4 sec
Develop(MF-319 developer)	20°C	1min
Remove oxide in buffered hydrofluoric acid (HF)	20°C	20 mins
KOH etch grooves (1.1 $\mu m/min$)	30%, 85°C	60 min

6.2.2 Acetate film based microfluidic channel

The second design is based on an acetate film defined channel with a thickness of 150 μm and refractive index of 1.87 at terahertz frequencies [149, 150]. The alternative microfluidic device is fabricated using Scotch tape spacer. This technique is an easy and much lower cost alternative to using lithography techniques in the cleanroom. The fabrication of this microfluidic device consists of three simple steps. The first step is using an acetate film composed of features with millimetre dimensions and sub-mm thickness. In the second step, two strips of Scotch tape (3M Scotch Transparent Tape 600) are attached on the left and right side of acetate film with the desired width. The tape thickness defines the depth of the channel. Depending on the target depth of the channel, more layers of Scotch tape can be used. After positioning of strip tapes, another acetate film with the same dimension as the base film will cover the tapes. The inlet and outlet ports of the microfluidic device were opened using a syringe to pump a liquid through the channel. Figure 6.3 shows the sketch of acetate microfluidic channel.
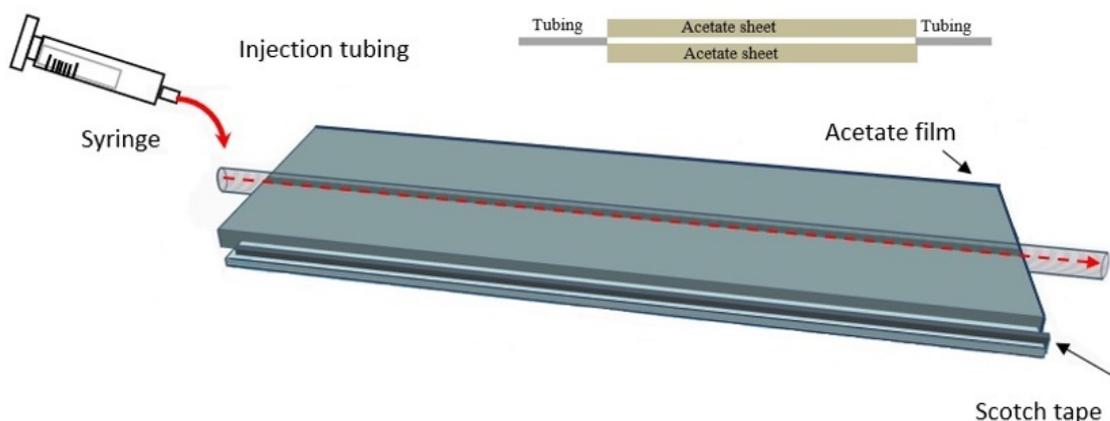
Figure 6.3: Diagram of an acetate microfluidic channel.

6.3   Simulation

For the simulation of the device, we consider a THz Fresnel Zone Plate reflector (the same design as presented earlier) integrated with a microfluidic channel placed between two metallic layers (a Fresnel Reflector and a back reflector). Lumerical FDTD has been used for the simulation of the device. Figure 6.4 shows the sketch of microfluidic channel integrated with the Fresnel reflector. A microfluidic device with total thickness of 260 μm, refractive index of 1.87 (acetate film) and channel depth of 80 μm is placed at a distance of 15 mm from the reflector (focal point).

Since the microfluidic device consists of different layers with different dielectric constants, when the plane wave travels through the channel, multiple reflections occur at each interface. The transmitted waves from different layers differ from each other in both magnitude and phase, which depend on the thickness of each layer and dielectric constant. The transmitted wave has sufficient strength to pass through the microfluidic channel and illuminate the Fresnel reflector. The reflected wave from the Fresnel reflector is focused at the focal point of Fresnel reflector where the microfluidic device placed. At the focal point of Fresnel reflector, the wave will reach its maximum field intensity. Also, multiple reflections will occur inside the channel. The transmittance, reflections inside the channel and the field intensity along the optical axis can be simulated for various materials inside the channel.

A back reflector (perfect metal) with a width of 2 mm is also placed as shown in fig. 6.4. This structure has been designed to confine the THz beam at the focal point of the reflector on the microfluidic channel. The expectation is for most of the pulse to be trapped in the channel, then reflected to the FZPR and then collimated

back from the FZPR and finally received by a monitor (to be explained in the next section) which is placed behind the source.
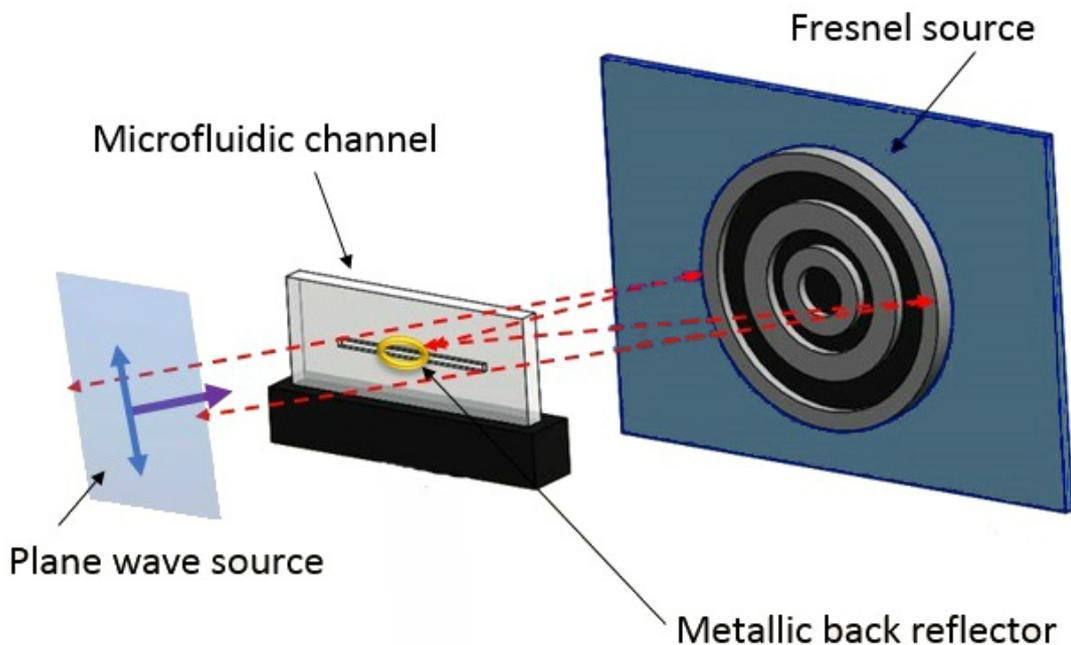
Figure 6.4: Sketch of simulated microfluidic channel integrated with the Fresnel reflector and metallic back reflector place at the back of channel.

In principle, when we have a multilayer structure, étalon oscillations appear due to the reflecting property of surfaces in this structure. However, the channel can be designed such that constructive interference will occur for a specific wavelength and other wavelengths will act destructively with other reflections and so only the required wavelength is transmitted.

In the microfluidic device produced by the microfabrication techniques detailed in section 6.2, it is straightforward to engineer the depth of channel and minimize the path length to maximize the THz transmission. Figure 6.5 shows a schematic of the reflection and transmission at each interface through the empty microfluidic channel. The incident THz pulse is propagating through to the microfluidic channel

from air. At the air-material interface a part of beam will be transmitted T_0 and the rest will be reflected $R_0(1)$. To reduce the reflection of the beam in (2), better refractive index matching is required at the interface between (2) and (3) which depends on the material of media (2) and (3). More transmission than reflection occurs between (3) to (4) but it is still affected by the loss in the medium (3) and finally more transmission occurs from (3) to (4).
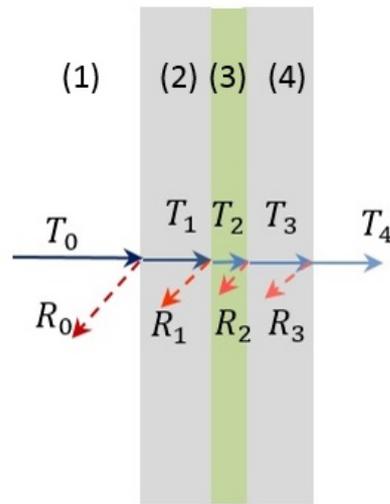
Figure 6.5: Transmission and reflection of the beam through the microfluidic channel for each interface(1-2) less T_1 and more R_1, (2-3) more T_2 and less R_2,(3-4) more T_3 and less R_3.

6.3.1 Simulation with various back reflectors

Various back reflectors with different shapes such as rectangular and toroidal as shown in fig. 6.6(a-b) have been used to simulate electric field intensity as a function of distance from the FZPR. In fig. 6.7, a rectangular shape back reflector has been placed at the back of the microfluidic channel. At a distance between 10 to 15 mm, a spread of high E-field intensity along the X-Z axis can be observed which corresponds to the focal point of the FZPR (fig. 6.7(a)). The variation of signal

between the 10 to 15 mm is due to a Fabry Perot resonance in which a standing wave is formed between the FZPR and the microfluidic channel.

The simulated field intensity, in the XY plane, for different Z distances from the FZPR is shown in fig. 6.7 (b). Using the back reflector and the microfluidic channel at the focal point of FZPR is the main reason for not having the same focal length obtained in the chapter 5. As can be seen, maximum E-field enhancement is obtained at 15 mm whereas a weaker enhancement is observed at 10 mm.
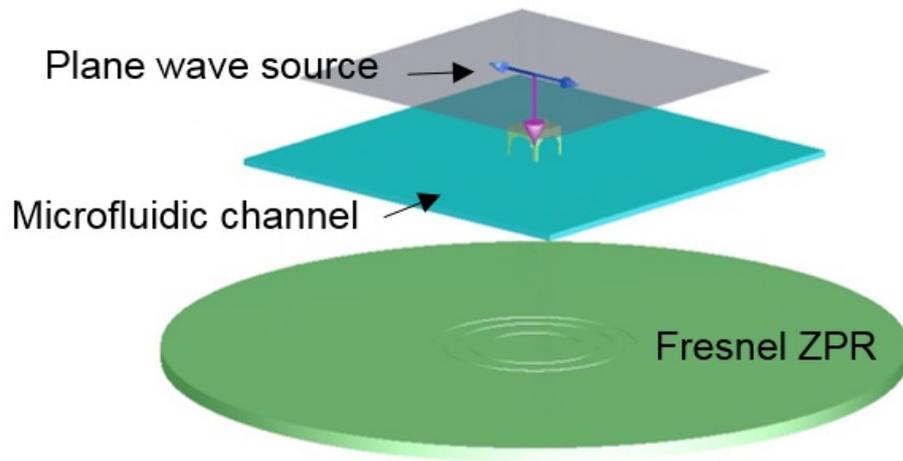
(a) Rectangular
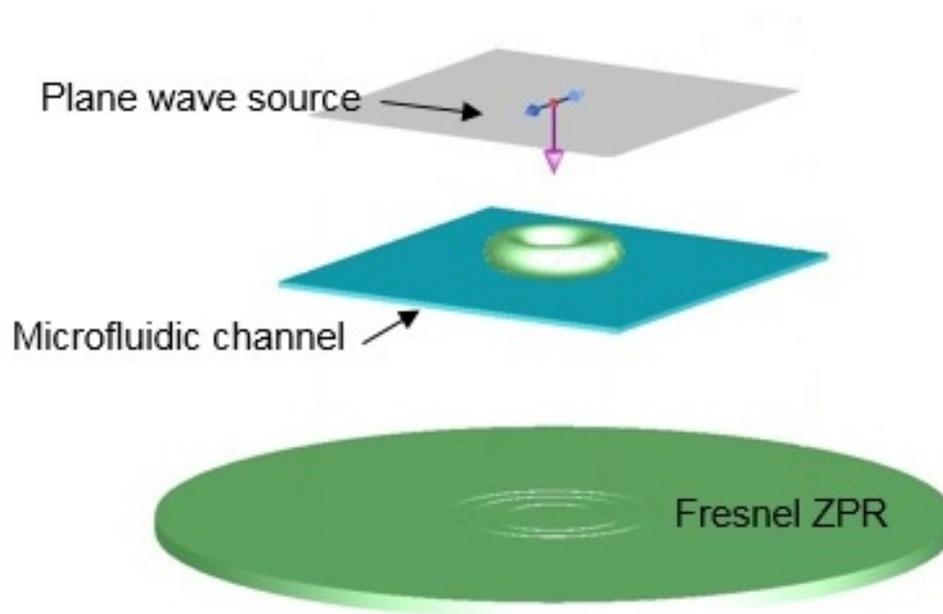
(b) Toroidal

Figure 6.6: Back reflector structure(a) Rectangular, (b) Toroidal.
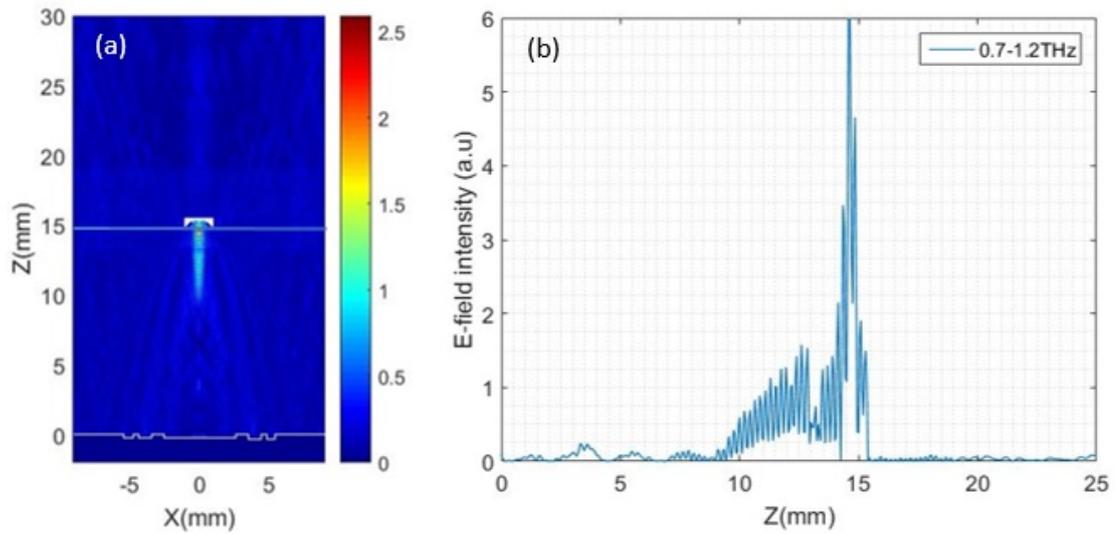
Figure 6.7: FDTD simulated E-field intensity in the (a) X-Z plane(b) along the optical Z axis at X=0 for the rectangular back reflector.

As is seen in fig. 6.8 in this simulation, a part of the incoming wave is reflected from the surface of the rectangular back reflector and the rest passes through the microfluidic channel fig. 6.8(a-b). When the wave has reflected back from the FZPR, it is focused at the focal point of FZPR with high E-field intensity as shown in fig. 6.8(c) and multiple reflections occur between the FZPR and rectangular back reflector fig. 6.8(d).
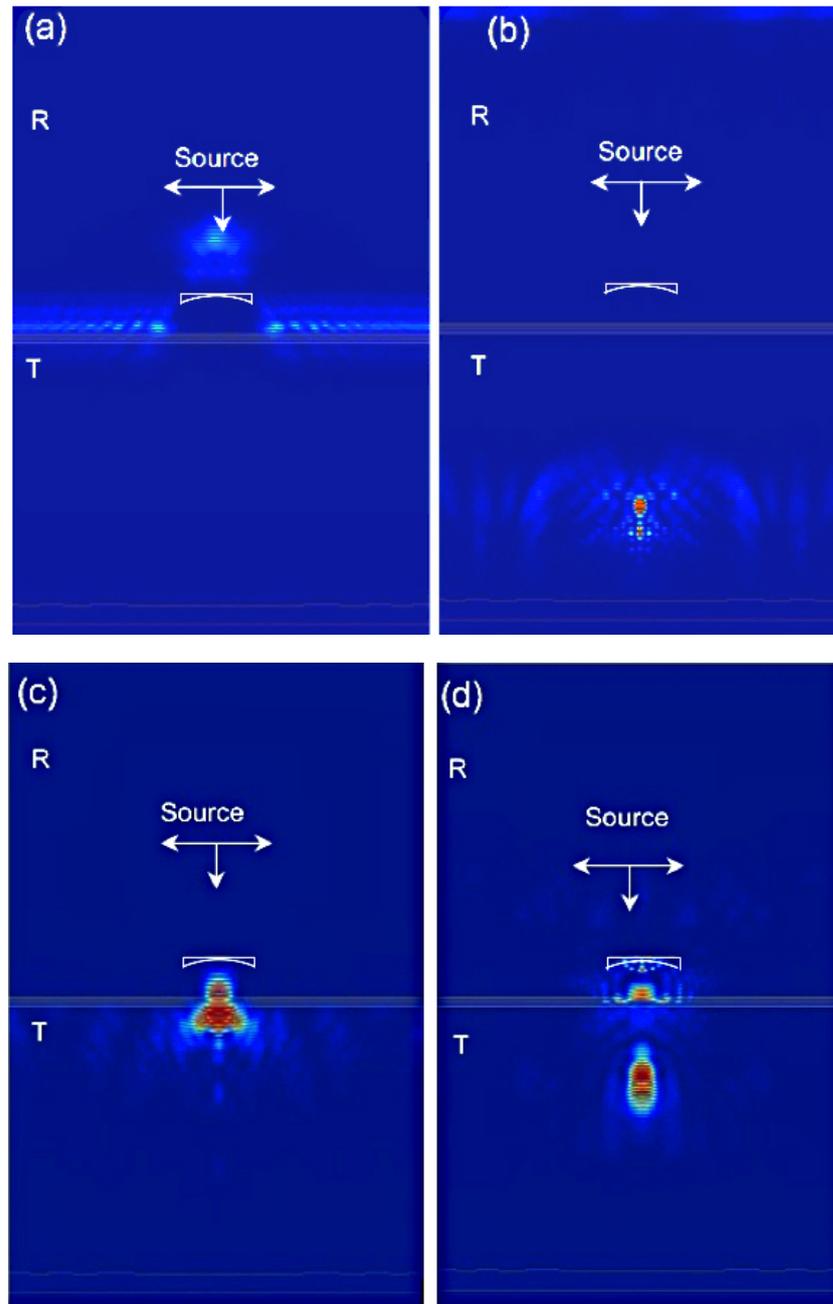
Figure 6.8: The simulated transmission of a beam through the microfluidic channel(a-b) and the reflection from the FZPR(c-d).

The next back reflector to be discussed is based on the toroidal shape. This type of back reflector allows more of the beam to pass through the reflector and reach the FZPR with many more reflections occurring from the back reflector compared with the rectangular shape. The electric field intensity along the optical axis with a

toroidal back reflector is shown in fig. 6.9(a). As it can be seen, in fig. 6.9(b) there

is a spread of high E-field intensity along the X-Z axis at distance of 10 to 20 mm

with the peak intensity at 15 mm (the place of the focal point of the FZPR).
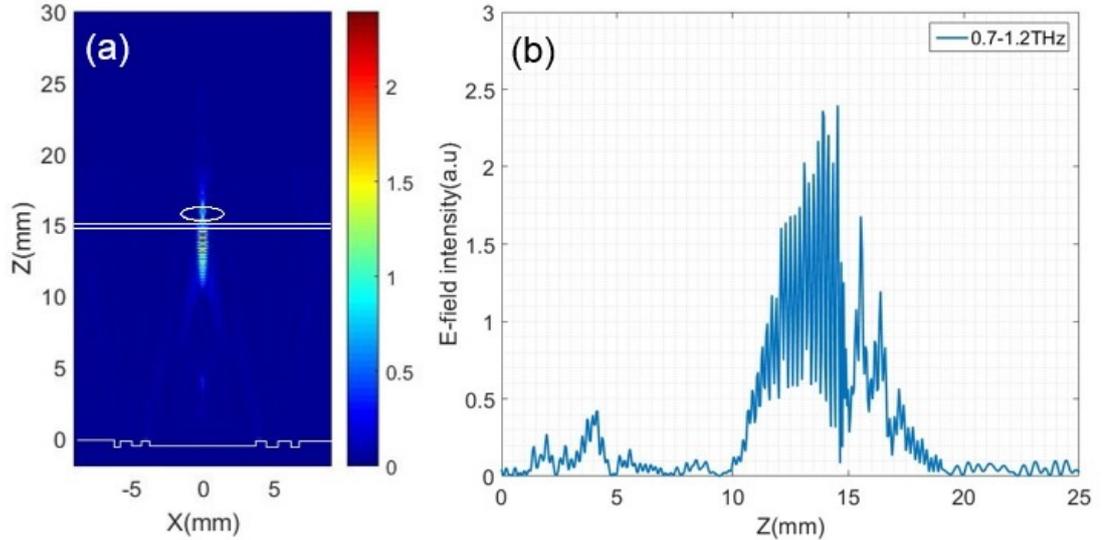
Figure 6.9: FDTD simulated E-field intensity in the (a) X-Z plane(b) along the optical Z axis for the toroid back reflector.

When a plane wave source illuminates the back reflector, most of the incoming

beam is passing through the microfluidic channel (through the centre of the toroidal

back reflector). As it can be seen in fig. 6.10(a-c) just a part of the beam has

reflected back from the channel, fig. 6.10(c). After passing through the channel, a

slight reduction in intensity can be observed fig. 6.10(d-f) and reflected from the

FZPR and focused at the focal point of FZPR. Due to the toroidal shape of the

back reflector, much more of the reflected beam could pass through the microfluidic

channel with less reflection loss compared with the rectangular back reflector used

in the previous section. However, the back reflector profile is an essential factor to

capture the highest E-field intensity from the FZPR. Based on the comparison of two

types of back reflector; the toroidal shape back reflector provided better performance

which will be utilized in experimental measurements.
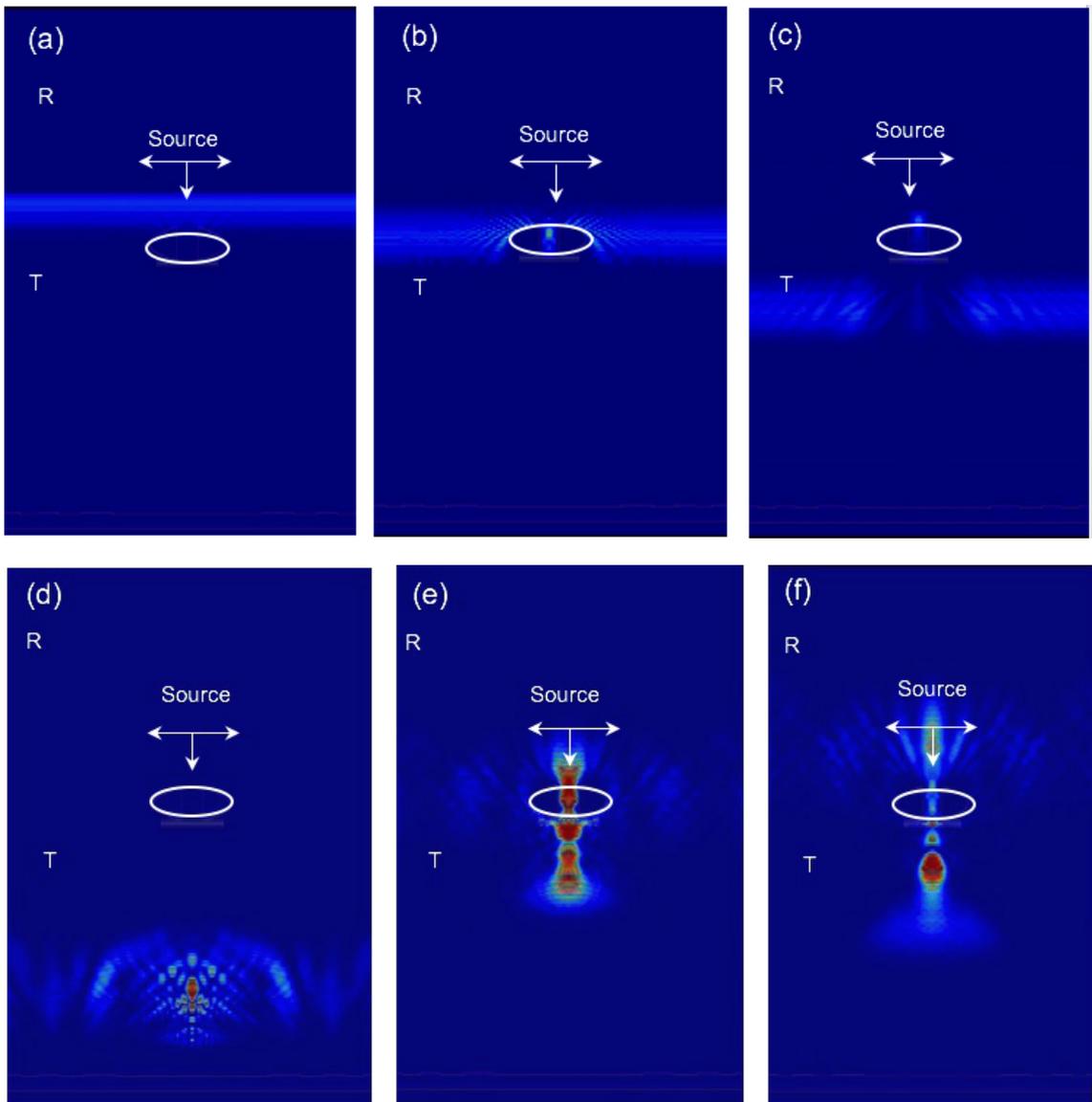
Figure 6.10: The simulated transmission(a-c) of beam through the acetate microfluidic channel using toroidal back reflector and reflection (d-f)of the beam from FZPR.

6.4   Experiment

The first microfluidic design was fabricated by bonding two silicon wafers each with a 300 μm thickness, where one of the wafers consists of the microfabricated channel. Silicon was chosen for building the microfluidic channel because of its optical transparency at terahertz frequencies despite its high refractive index ($\sim$3.42). The channel was etched to have a depth of 40 μm and width of 200 μm, leading to an inner volume of 20 μL. The device function was initially investigated to see how the empty device or a channel with liquid inside (water and IPA) behaved in the terahertz beam. Figures 6.11 and 6.12 schematically illustrate the experimental platform for this work which consists of the silicon microfluidic channel mounted at the focal point (f= 10 cm) of 90°off-axis parabolic mirrors, M2 and M3. The focused beam which is coming from the horn antenna is collimated by M1 and is focused on microfluidic channel by M2 and after going through M3 will be focused by M4 to the receiver horn antenna. In this measurement, the VNA provides transmission information of the terahertz beam through the microfluidic channel.
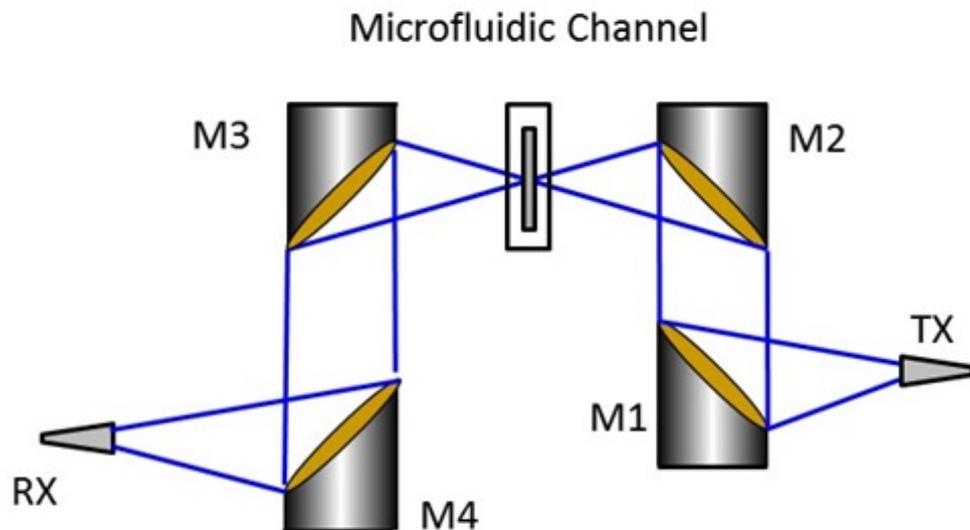
Figure 6.11: Schematic diagram of the experimental setup with Microfluidic channel in the THz-VNA.
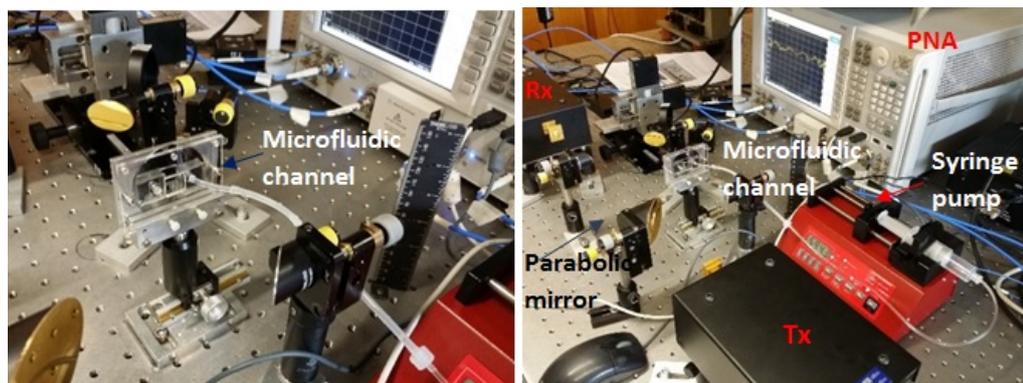
Figure 6.12: The experimental setup image with a microfluidic channel in the THz-VNA system.

Figure 6.13 shows the noise floor and transmission between the four parabolic mirrors without any sample in the system. By calculating the RMS power of a signal, the dynamic range of the system can be calculated. The dashed line shows the RMS value of the noise which is equal to -70 dB.
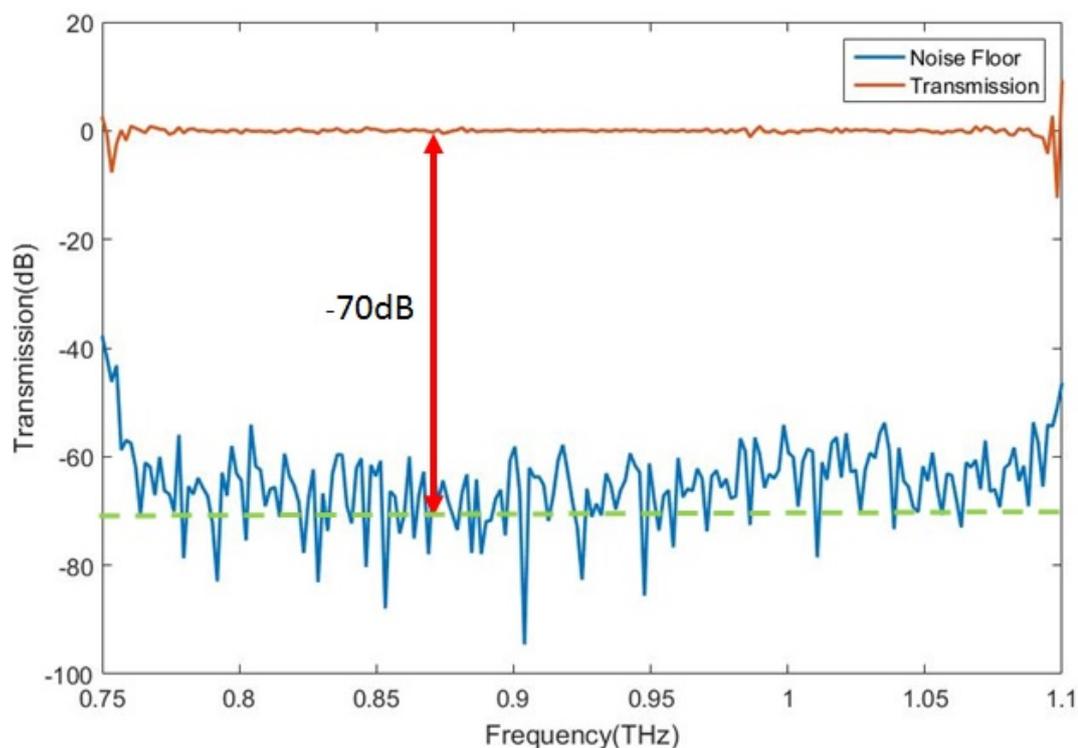
Figure 6.13: Dynamic range for the VNA frequency of 0.75-1.1 THz at 100 Hz IF bandwidth.

The transmission signal has been normalised to the empty microfluidic channel. By pumping water or IPA through the channel, the transmission signal will be changed. This change arises due to the different refractive indices and their mismatch with the material that forms the channel at terahertz frequencies. Various mixtures of deionised water and IPA were prepared. The transmission spectra of the IPA/H_2O mixtures are obtained by normalising to empty channel over the range of 0.75-1.1 THz. Normalization of the transmission signal to the water transmission signal is a method which helps to visualise the signal over the spectral range.

The transmission spectrum results for IPA can be seen in fig. 6.14. Examination of the transmission signal shows that there is an absolute reduction in the signal

amplitude as the water concentration is increased due to higher absorption of water compared with IPA [151]. Furthermore, the étalon oscillations occur with the high concentration of IPA (from 50% to 90% IPA) inside the channel as depicted in fig. 6.14. The spectra associated with a high concentration of water results in no standing waves occurring at 10% and 30% IPA. The data shows a change in the overall attenuation with a broad transmission peak at around 870 GHz for the 50% IPA/water concentration.

However, by increasing the IPA concentration, the amplitude of the oscillation peak (attributable to étalon effects) did not increase as expected. With no significant change observed in peak amplitude for 90% IPA, it is likely that there is still water present in the channel.
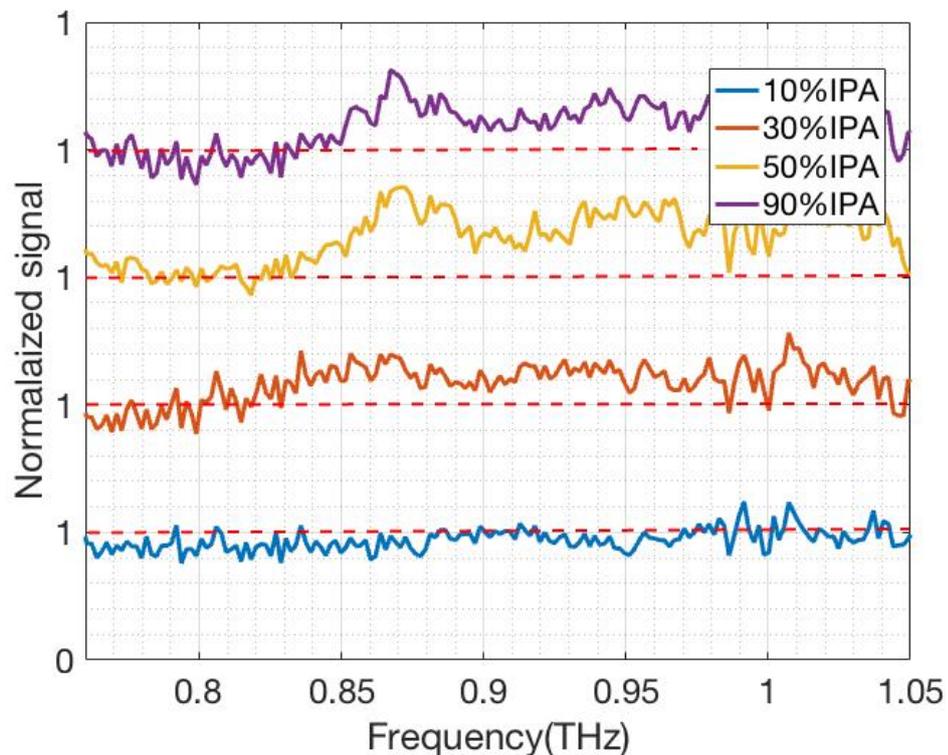
Figure 6.14: THz transmission spectra of the IPA-H_2O mixtures normalized to an empty channel with IPA concentration ranging 10%, 30%, 50% and 90%.

This measurement has been repeated by measuring 100% IPA followed by adding 50% water to the IPA which helps to have an accurate and reliable measurement. Figure 6.15 shows the measured THz transmission spectra of the 100% IPA and 50% IPA/H_2O mixtures normalized to empty channel. The measured transmission through the air-filled (empty) channel (cavity) results in no oscillation but maximum oscillations can be observed when 100% IPA is added to the channel due to the refractive index matching between the IPA and silicon. Adding water to the IPA reduces the signal oscillation due to the water absorption. The reflections at each material boundary, along with the étalon oscillation in the cavity (channel) have been considered.

For the THz wave passing through the channel, four different boundaries are presented in the previous section. The multiple reflections occur inside the channel when the beam is passing through the channel. When there is only IPA inside the channel due to the comparatively low absorption of IPA compared to water, the reflection reduces while the transmission increases.

However, it will still be affected by losses inside the channel. This could be improved by refractive index matching between the IPA and silicon. As the water is added to the IPA, the absorption at the sample increases rather than improving the index matching and a further reduction in signal amplitude will be achieved in the transmission signal compared to the empty channel. The level of the signal for the empty device is slightly lower than that of the 100% IPA, indicating good THz transmission (or low insertion-loss) of the silicon device. The THz signal amplitude increases when the IPA concentration is increased because of the decrease

in hydrogen bond density leading to lower THz absorption based on what was observed.
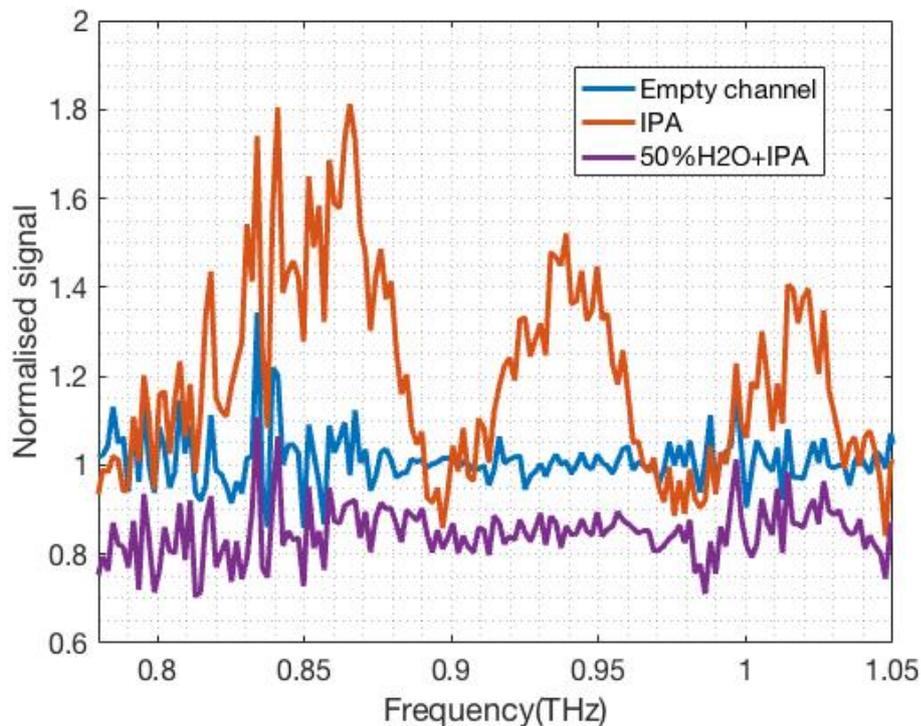
Figure 6.15: THz transmission spectra of the IPA-H_2O mixtures normalized to an empty channel with 100% IPA and 50% IPA/50% H2O mixtures.

6.4.1 Microfluidic channel integrated with FZPR

The microfluidic channel has been integrated with a micro-milled reflector and characterized by the THz-VNA. Figures 6.16 and 6.17 show the schematic diagram of the experimental setup with the FZPR and microfluidic channel placed at the distance of 20 mm (focal point of FZR) with respect to the FZR reflector. The 90°off-axis parabolic mirror collimates the focused beam from the horn antenna. This collimated beam, after going through the microfluidic channel, illuminates the FZPR and is reflected and focused at the focal point of FZPR, 20 mm on to the microfluidic channel.

The FZPR is as described in the previous chapter and has been designed and fabricated on an aluminium plate with 5 mm thickness leading to a focal length of 20 mm. In order to enable two-dimensional mapping, the FZPR is mounted on a computer-controlled XYZ positioning stage is shown fig. 6.17(b). As mentioned in the simulation section, to have multiple passes through the channel and bring back the beam to the FZPR, a back reflector in the setup is used. A toroidal shaped back reflector has been attached at the centre of the microfluidic channel as shown in fig. 6.17. Due to the ease of fabrication, a gold-coated washer with the 2 mm centre diameter is used as the toroidal back reflector.
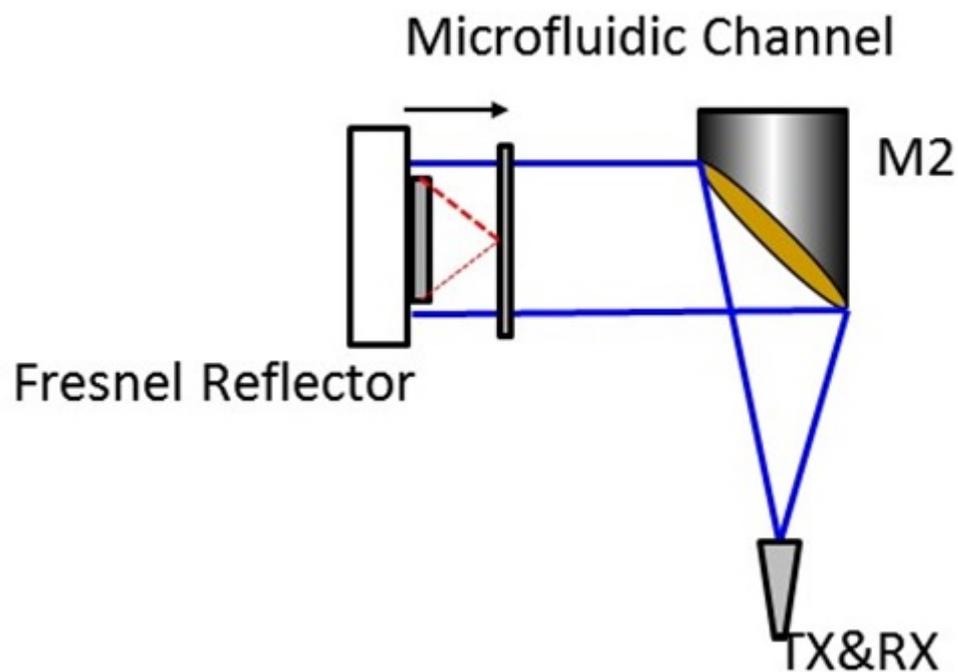
Figure 6.16: Schematic diagram of the experimental setup with microfluidic channel integrated with FZPR.
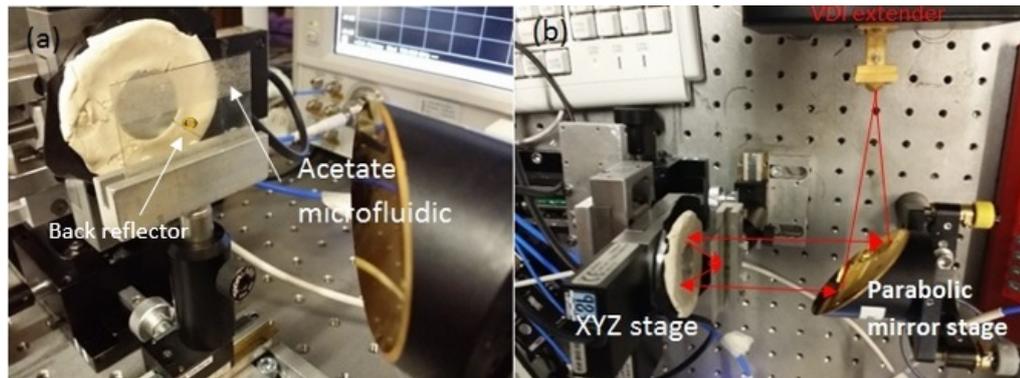
Figure 6.17: The photo showing experimental setup (a) side-view (b) top-view. Liquid samples are delivered to the microfluidic device through a syringe.

In order to obtain a reference measurement, an unstructured aluminium flat plate with a thickness of 5 mm is mounted on the XYZ stages. Figure 6.18 shows the S11 measurement of an aluminium flat plate, a FZPR, and the FZPR reflector with the microfluidic device placed at its focal point.

It is expected that the use of a metal plate in the setup with high reflectivity, results in high dynamic range and low loss in the transmission signal. With the FZPR in place of the flat plate, more pronounced étalon oscillations have been observed due to the change in optical path length and the structured surface of the FZPR. A cavity exits between the VNA emitter, parabolic mirror M2 and FZPR (as shown in fig. 6.16).

By placing the microfluidic channel at the focal point of the FZPR, the beam after it is reflected will be reflected a lot inside the channel which is evident from the S11 results in fig. 6.18 where the scan with the microfluidic channel shows a smaller period in the étalon oscillations, compared to the case without the channel.
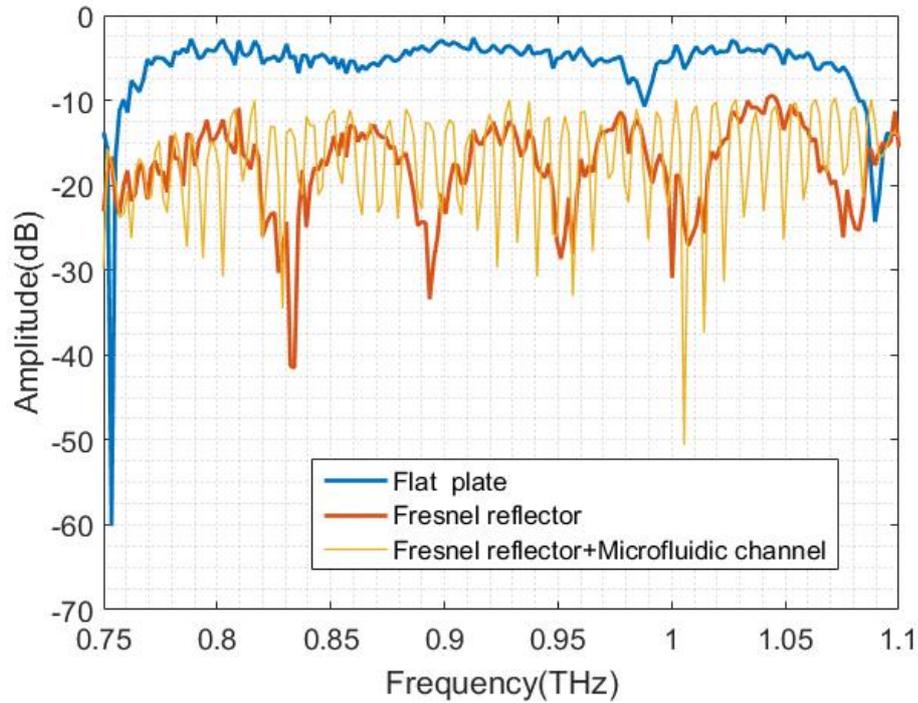
Figure 6.18: The S11 measurement from the flat plate, FZPR and empty microfluidic silicon channel.

The S11 parameter measurement for different materials such as a coffee-water mixture has been investigated. Two grams of dry instant coffee (contains approximately 0.0228 g caffeine [152]) was mixed with 20 ml of DI water and pumped through the channel. As we can see in fig. 6.19, the THz spectra of the coffee, water and empty channel are experimentally compared in the range of 0.75-1.1 THz. Due to the frequency dependence of the refractive index of the coffee (average refractive index of 1.56) at terahertz frequencies [153], adding water to the coffee results in a change in index-matching of material inside the channel. The coffee was a Nescafe instant coffee with the focus on observing a change in the attenuation of the coffee/water mixture, in this experiment just one concentration of coffee/ water is utilized for measurement.

In fact, by adding the water to coffee, water molecules fill the specific positions in

the crystalline lattice of the caffeine molecules (coffee) by forming hydrogen bonds.
Therefore, the hydrated coffee has different crystalline forms than the coffee without
water [154]. Consequently, its physiochemical properties will be changed. The
change in the spectrum of coffee/water mixture is the result of incorporation of
water molecules to the coffee which changes the energy vibrational modes of caffeine
inside the molecules and results in changing the dielectric constant of the medium.

Figure 6.19 shows the S11 measurement of a mixture of coffee and water through
the microfluidic channel. Signal drops in the S11 measurement of the coffee/water
mixture. As the absorption loss of water is much higher than the coffee/water, it is
expected that there is a massive reduction in signal amplitude of water.
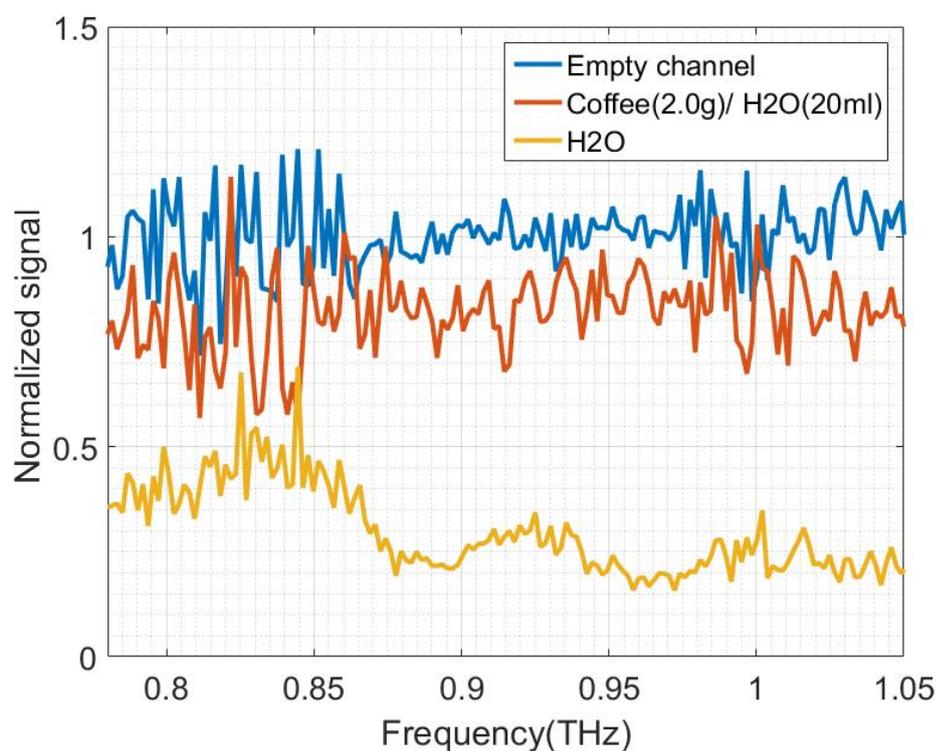
Figure 6.19: The S11 measurement from the flat plate, FZPR and empty microfluidic channel,
coffee and water mixture.

We also attempted the monitoring of chemicals through microfluidic channels

with a range of channel widths and depths. The initial design depth is 130 μm, which is small enough for reducing absorption loss and large enough for the liquid to pass. Channel depth is a key parameter to reduce the losses in aqueous media. The thickness of acetate film should be as thin as possible while maintaining its mechanical strength. We reduced the acetate channel depth to 80 μm. The width of the channel varies from 2 mm to 12 mm.

Figure 6.20 shows the measured S11 spectra of an empty acetate microfluidic channel placed at the focal point of a FZPR with a toroidal back reflector(a gold coated washer) at the focal point. The effect of a standing wave causes a significant oscillation, and it is observed with increasing frequency a clear increase of the signal amplitude is shown.
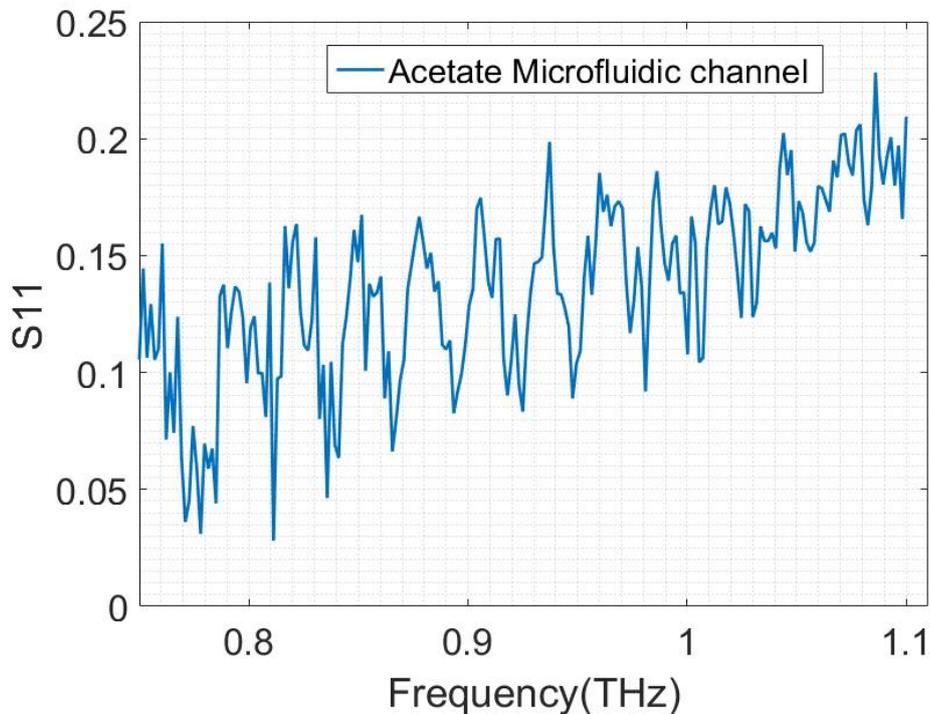
Figure 6.20: The S11 measurement from the flat plate, FZPR with an empty microfluidic channel.

The behaviour of the transmitted and reflected THz beam through the channel

are shown in fig. 6.21 along with a schematic showing reflections inside the channel. As it can be seen, a part of the transmitted beam is reflected back from the microfluidic channel fig. 6.21 (region A), and a part is passed through the channel. Based on the refractive index of IPA and IPA/water mixture passing through the channel, the transmission has been affected by the index-matching of material inside the channel. The THz beam has reflected back from the FZPR in fig. 6.21(region B) and at the interface with the channel a part of THz beam has reflected back, and the rest has passed through the channel.
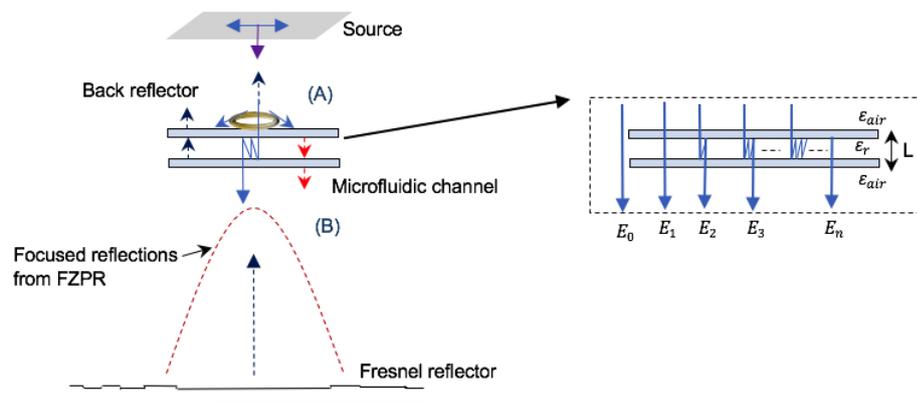
Figure 6.21: The sketch of measured transmission and refection of THz beam through the channel for before the channel(region A) and after channel(region B)(left), schematic showing reflections inside the channel(right).

Figure 6.22 shows the measured S11 spectra of the IPA/water mixtures obtained for the IPA concentrations at 50% and 90% through the acetate film microfluidic channel. It is clear when the concentration of IPA is increased, the amplitude of signal has increased due to the lower absorption in IPA compared with water, and an oscillation is observed at the higher concentration of (90%) IPA/Water, resulting from improved refractive index matching between the acetate film channel and the sample inside the channel.
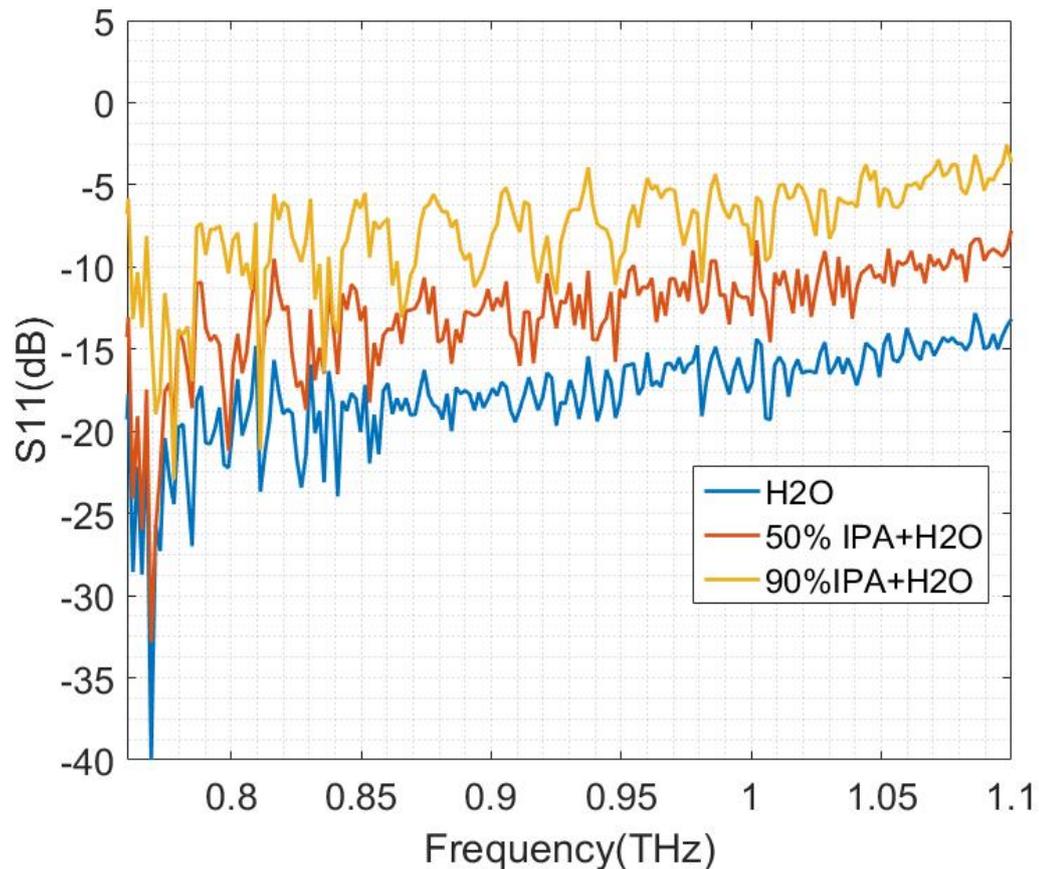
Figure 6.22: The S11 measurement through the acetate microfluidic channel for IPA for 50% and 90% IPA/water mixture with offset of 5 dB.

Different channel widths and depths have been investigated, shows fig. 6.23 the S11 measurement of water through the acetate channel with width of 12 mm. With the air-filled channel, étalon oscillations appear inside the cavity. Adding water inside the channel reduces the oscillations due to the water absoption. As can be seen the signal to noise ratio increases as the width of the channel is fig. 6.23 with 12 mm. In this plot the data has been smoothed and errorbars in the plot depicts the deviation in the measurement of both dry and wet channel.

A higher signal to noise ratio has been achieved with the channel width of 12 mm when compared to the smaller widths. One reason for the low SNR in the smaller channel widths could be due to collapse of acetate film layers when channel is filled

with water especially when their depth is also small. This causes to less amount of liquid to pass through the channel or it could be stuck in the channel.
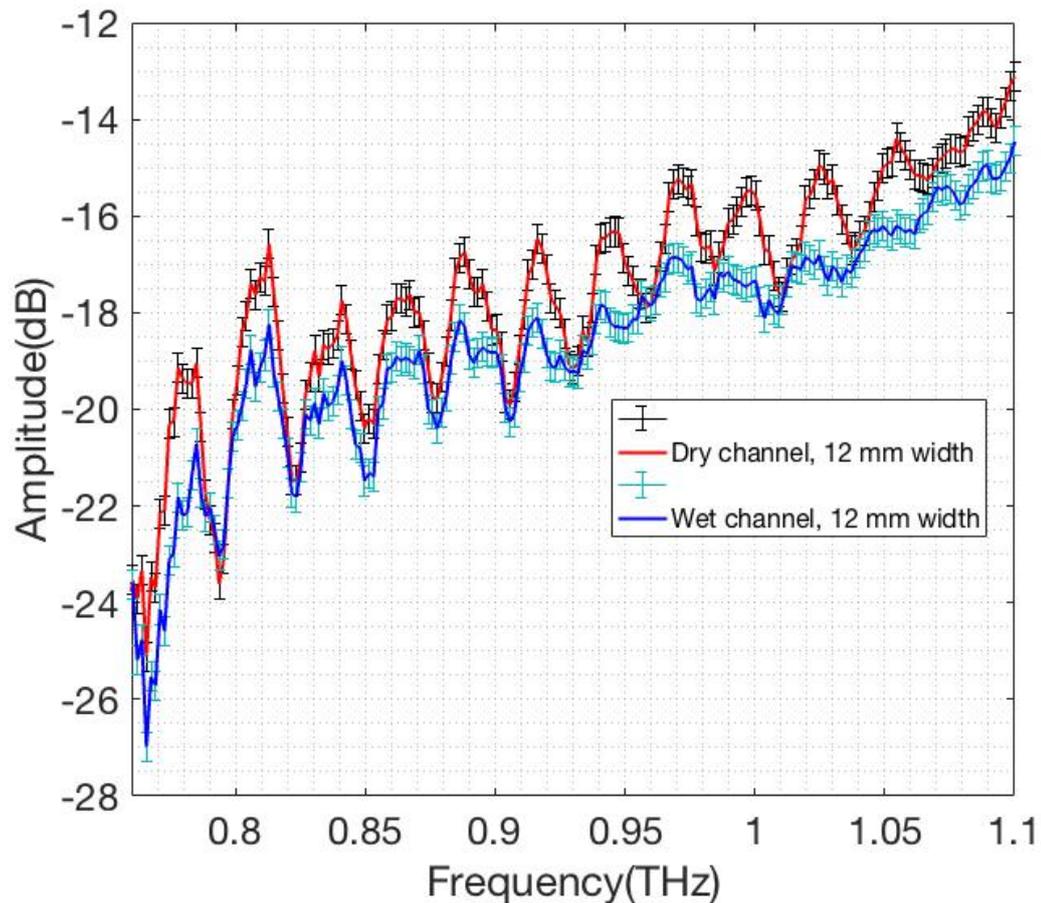
Figure 6.23: The S11 measurement through the acetate microfluidic channel with width of 12 mm, étalon effect appears inside the empty channel and oscillation drops due to the water inside the channel, the signals have been smoothed with error bars which shows the deviation at each point of measurement for this type of channel.

A rotational stage has been added to the XYZ stage to evaluate the alignment of the system. The direction of rotation of flat plat which is mounted on a rotational stage has been shown in fig. 6.24. The clockwise (CW) and counterclockwise (CCW) rotation of the flat plate has been investigated to find out the sensitivity of the system to such rotational misalignment.
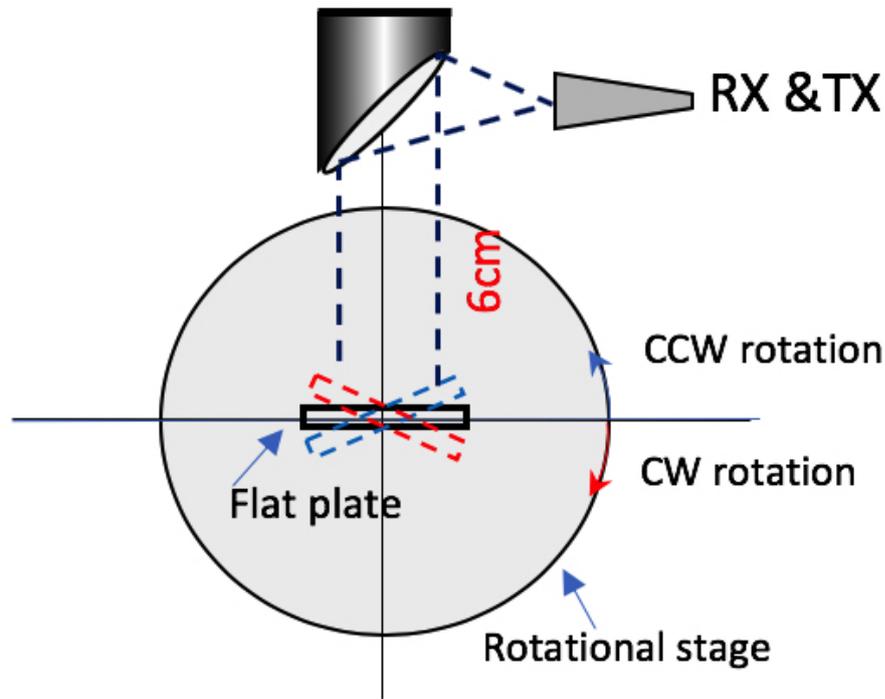
Figure 6.24: The top-view of direction of CW and CCW rotation of a flat plate which is mounted on a rotational stage.

The S11 measurement started by using the flat plate which is placed at about 6 cm from the parabolic mirror (focal point of 50 mm). As it can be seen in fig. 6.25 (a) a flat signal with no oscillation and high SNR is obtained when no rotation is applied to the flat plate. There is also a large dip in S11 at around 980 GHz due to the calibration error of the system. By rotating the flat plate clockwise, fig. 6.25(b-f) the measured large signal oscillation and reduction in signal amplitude would imply that a cavity has been created during alignment. This shows the sensitivity of system alignment to any small changes in alignment. The counter clockwise rotation of the flat plate is also shown in fig. 6.26(a-e) which represents the same signal oscillation with clockwise rotation. This means that in order to make sure the system is aligned properly we should try to reduce the étalon effect in the system during the alignment of system. Since the proposed configuration is compact and sensitive to any changes

148

in both the position and the angle of the optical components, a precise alignment of all components at the same time is necessary. The use of a kinematic micropositioner such as Hexapod with 6 degrees of freedom for optical alignments is the aim of next chapter to maximize the signal intensity. In both figs. 6.25 and 6.26 for very larger angle of rotation such that the signal is completely lost and large number of oscillation and be observed;and the data is completely meaningful.
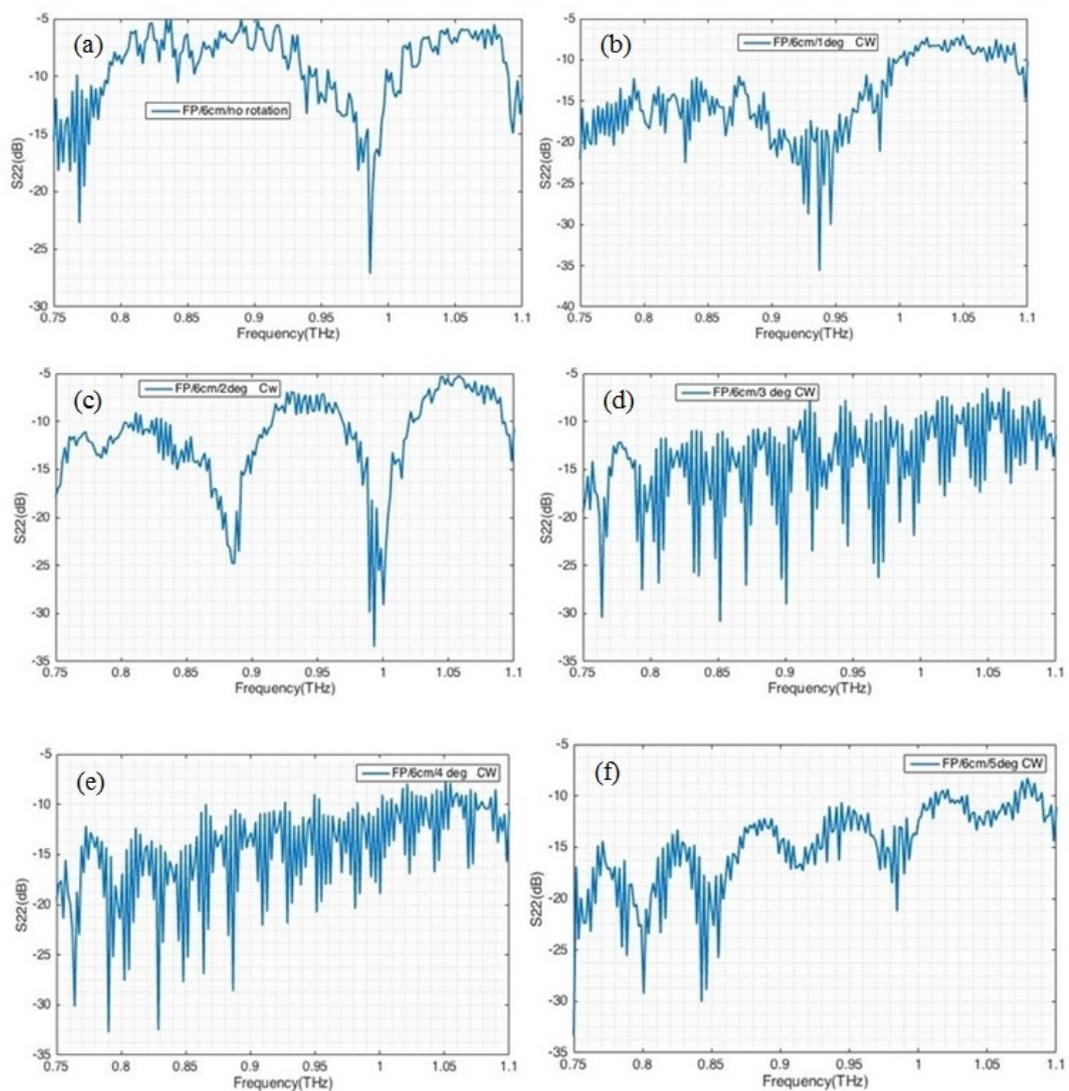
Figure 6.25: The S11 measurement of clockwise rotation of the flat plate at 6 *cm* from the parabolic mirror.
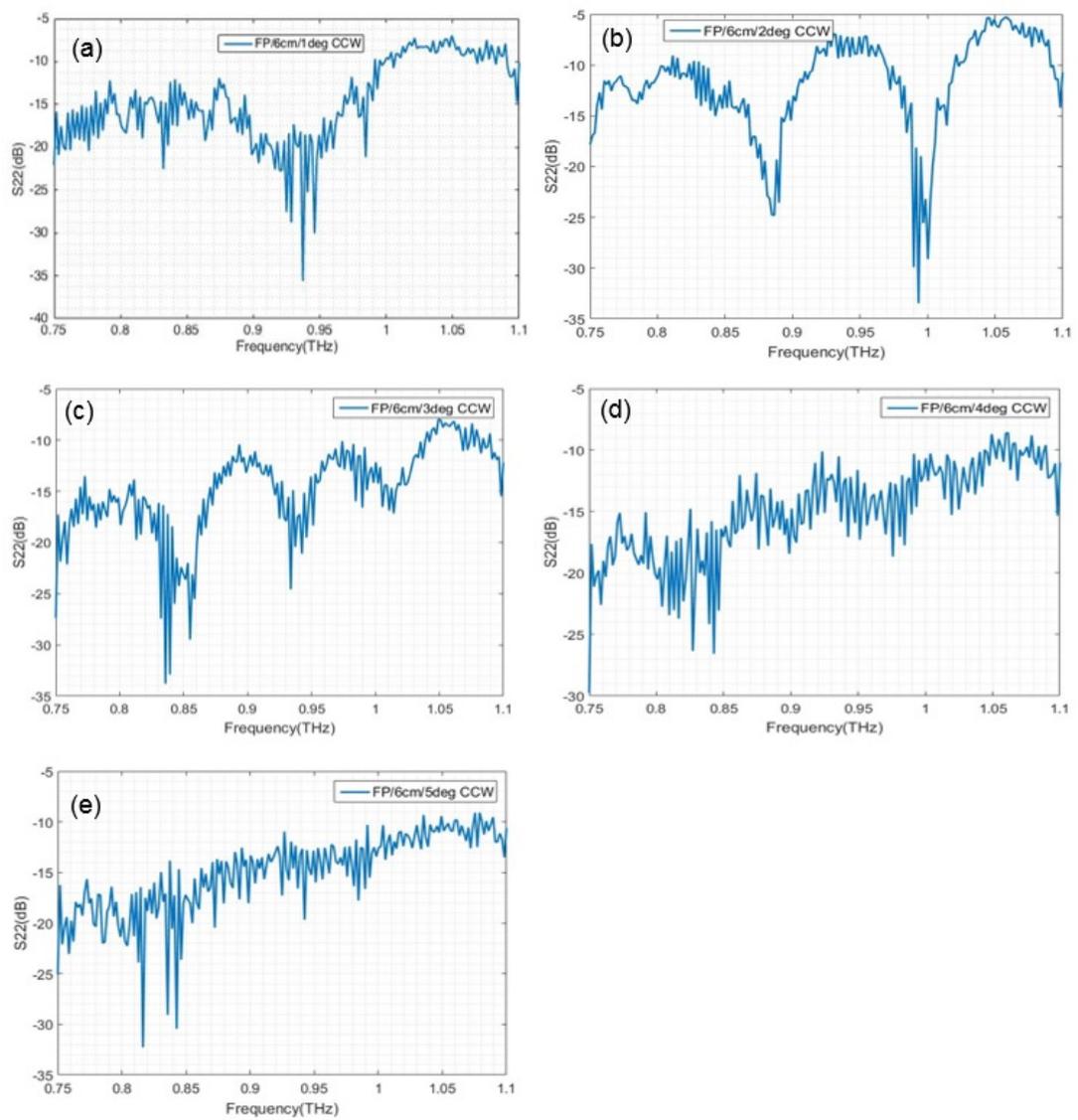
Figure 6.26: the S11 measurement of counterclockwise rotation of the flat plate at 6 *cm* from the parabolic mirror

6.5 Conclusion

In conclusion, we experimentally and numerically demonstrated a microfluidic channel based on the acetate film and silicon wafers which is integrated with a FZPR. In the fabrication of the microfluidic channel, standard lithography for silicon microfluidic channel as well as a simple process of attaching the two layers of acetate film for the acetate microfluidic channel has been used.

The benefits of the presented VNA measurement system configuration include the use of fewer parabolics, a smaller optical path length, higher spatial resolution, and focusing of the THz beam by the Fresnel reflector as well as signal detection after interacting with liquid inside the channel. Various ranges of IPA/water mixtures, coffee/water have been investigated. The analysis of IPA showed that the IPA has lower absorption than water but with the mixture of water due to the high absorption of water the signal amplitude will be reduced. Increasing the water concentration in the IPA/water mixture improves the index matching due to higher refractive index of samples inside the channel but provide more losses.

The system alignment sensitivity showed that small translational and rotational motion of Fresnel reflector influences in signal amplitude and étalon effect inside the channel. Both THz amplitude level and transmission and reflection spectra feature variations are observed, demonstrating system's capability for discriminating different chemicals.

Chapter 7

Systematic alignment of Terahertz optical system

In terahertz optical systems, precise positioning of optical components such as lenses and mirrors is required in order to maintain the intensity and alignment of the THz beam. This chapter covers the principles of terahertz (THz) optics alignment. In the previous chapter, S11 measurements were reported using a single VNA extender head, parabolic and reflector combination. It was found that this compact configuration is very sensitive to the position and angle of the reflector in the system. With the aim of progressing towards a self-aligning system, in this chapter, a Hexapod micropositioner has been used to sweep the position the samples in order to maximize the signal intensity. The Hexapod has 6 degrees of freedom (translational and rotational) and two different setup configurations are presented in this chapter.

7.1 Introduction

In terahertz systems, parabolic mirrors are the principal optical components used to guide the THz beam for imaging and focusing [155]. The OAPs are usually a part of a parent parabola, and it is essential that a point source is placed at the focal point of the OAP to produce a collimated beam, otherwise a misaligned, uncollimated beam will be produced which is unwanted [156].

One of the optical problems in parabolic mirrors are the strong aberrations that occur if the incoming beam is not perfectly aligned in the optical axis [157] and the other one is the changing of focal point. These aberrations come from the misalignment of the mirror. The combination of coma and astigmatism induced by mirror misalignment are known as alignment aberrations. Furthermore, because of different degrees of freedom which are associated with an OAP, its alignment is very challenging, and it has to be done with respect to a reference coordinate system. When a parabolic mirror is misaligned relative to the optical axis, two specific directions could be the source of misalignment. These are the tangential and radial directions, which are shown in fig. 7.1 can cause astigmatism and coma in the system [158].
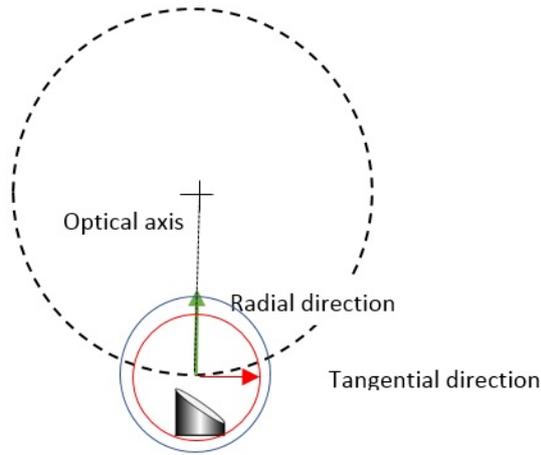
Figure 7.1: Tangential and radial direction of misalignment in parabolic mirror.

The OAPs with high reflectivity have gold coated surfaces and are the most commonly used optical components at THz frequencies. They can produce a collimated beam from a point source and focused beam from a collimated one [22].

In order to increase the amplitude of the terahertz signal and improve the dynamic range, it is essential to align the parabolics precisely [157]. Various techniques have been used for the alignment of the optical system and some of them are based on Zernike polynomials for correcting any off-axis aberration in the system [159]. As an example, this is used in optical interferometer null testing configurations where a parabolic mirror is used to collimate the beam and a flat mirror reflects the collimated beam back again [160]. This is also known as a FR(flat reference) method. In other set-ups, two parabolic mirrors can be used to correct astigmatism in the system but may induce distortion [129].

Another example, for OAP alignment, is based on the cyclic shearing interferometer and CCD camera for accurate alignment of the OAP using a five parallel laser beam alignment device [161]. In this method, straight fringes are visible, and any non-straightness is indicative of aberrations in the system.

Understanding the formation of the diffraction pattern helps to evaluate the performance of the optical component and is an important factor for aligning off-axis optical elements in the system [162, 163]. The effect of aberration on the diffraction pattern has been studied and characterized using special functions such as Zernike polynomials [164–167]. OAPs only produce diffraction patterns when focusing a collimated beam. A collimated beam incident upon the OAP from an off-axis focal angle will not produce a diffraction pattern.

In THz systems, due to the beam tracing difficulties (i.e. the beam is not visible) and optical components with various degrees of freedom, system alignment is much more difficult. In fact, we are interested in developing new alignment techniques for the terahertz region and the use of a Hexapod to provide 6 degrees of freedom positioning is one such option. There are some advantages with this method:(a) It is a rapid and simple alignment technique, (2) because of the kinematic positioning mechanism of the Hexapod, it can be readily aligned both translationally and rotationally. We need to know all the parameters that have an effect on alignment of a terahertz system and identify its inherent aberration due to the misalignment which can be attributed to the off-axis parabolic mirror or horn antenna receiver.

7.2   PI Hexapod

The conventional motion solution for optical system alignment consists of a stack of linear stages and may include a rotational stage. This kind of stage allows for linear motion in three directions and limited rotational movement, moreover the stack is typically bulky to use in many optical set-ups. A typical Thorlab XYZ

stage is shown in fig. 7.2.

Figure 7.2: A typical Thorlab stacked XYZ stage.

Alternatively, a Hexapod can be used which consists of one fixed and one movable platform. The movable platform is supported by six actuator legs (struts) which are placed on the base plate as shown in the fig. 7.3. The struts can expand independently which enables any objects attached to the movable platform to move in any direction. The movable platform has a low weight and low inertia relative to the stacked stage system which decreases settling time and improves the accuracy when positioning objects. In comparison to the stacked stages, which are affected by run-out or tilt errors, the Hexapod avoids these sources of error.

The Hexapod (model H-824) utilizes a Cartesian coordinate system for linear and rotational movements which define the position of the portable platform as shown in the fig. 7.3(b). In this coordinate system, a position (XYZ UVW) shows the X, Y, Z location of the centre point of the moving platform by using right-handed Cartesian coordinate system which incorporates with angular coordinates U, V, W

for the rotational axes.

(a)   (b)
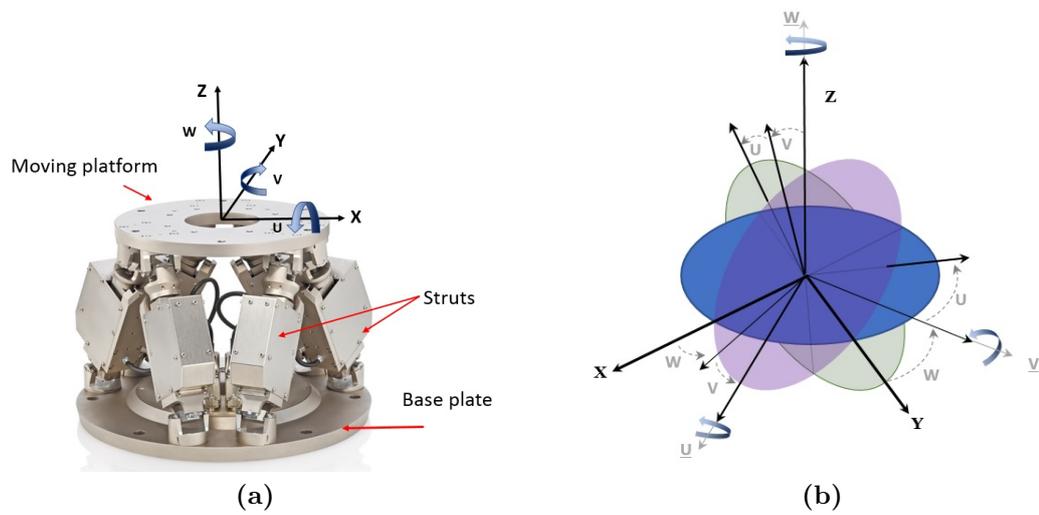
Figure 7.3: (a) the schematic digram of the H-824 Hexapod,consists of 6 adjustable struts to show the position of the motion platform [168](b) the Cartesian coordinate system used in H-824 Hexapod.

The Hexapod (H-824), used here, can hold attachments with weight up to 5 kg in any orientation. It has a stiffness of 1.7 $N/\mu m$ in the X and Y directions and 7 $N/\mu m$ in the Z direction. It has linear motion ranges of $\pm$ 22.5 mm in X and Y, and $\pm$ 12.5 mm in Z and angular ranges of $\pm$ 7.5(θ_x, θ_y), $\pm$ 12.5(θ_z) [168]. The motion system consists of a controller which can control the Hexapod through the PC and connects to the controller via RS-232 or TCP/IP.

The $PIMicroMove^{TM}$ is the controller's operating software which accepts motion commands via the serial communication link from a host PC. The controller can command motion of each axes, a combination of axes or all axes at the same time. Figure 7.4 shows the controller and the $PIMicroMove^{TM}$ software used for initializing the Hexapod. Using the Hexapod in system alignment provides high accuracy and resolution on all axes which reduces the accumulation of errors in the system. To gain a better understanding of how the desired position is reached in the Hexapod coordinate system, consider a move which starts by initializing the stage to the position (000 000) (XYZ UVW).

First, the position is set for (XYZ), then it rotates about the Z-axis of the Hexapod coordinate system (W), the new Y-axis of the Hexapod coordinate system (V) and the new X-axis of the Hexapod coordinate system (U). The clockwise rotation is for positive rotation in the system. After receiving the positioning commands in the Cartesian system, they are transferred to the Hexapod controller to the specific position for each of the six Hexapod struts. All the transferred positions to the six struts are defined as a unique position in location and orientation of Hexapod coordinate system.

(a)
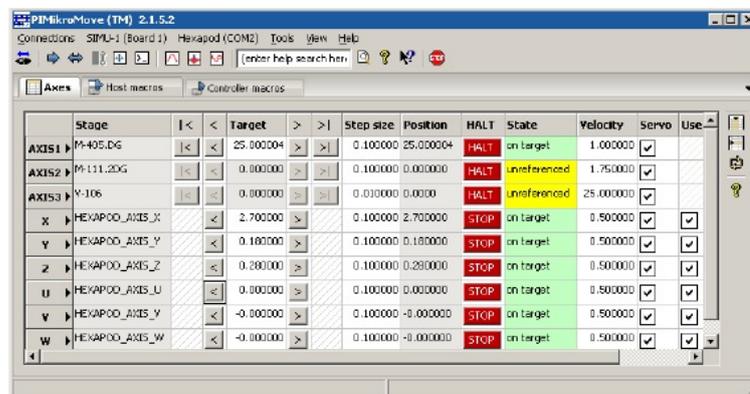
(b)

Figure 7.4: The image of C-887.52 Hexapod controller (a), the PIMicroMove software for manual motion control through the controller(b) [168].

7.3   Preliminary alignment

We developed a technique to align the terahertz optical system. This alignment technique has been applied to the THz region (near to 1 THz). The schematic diagram of the whole alignment setup which consists of the Vector Network Analyser, H-824 Hexapod, a 90°off-axis parabolic mirror and a flat reflector plate is shown in fig. 7.5.

159
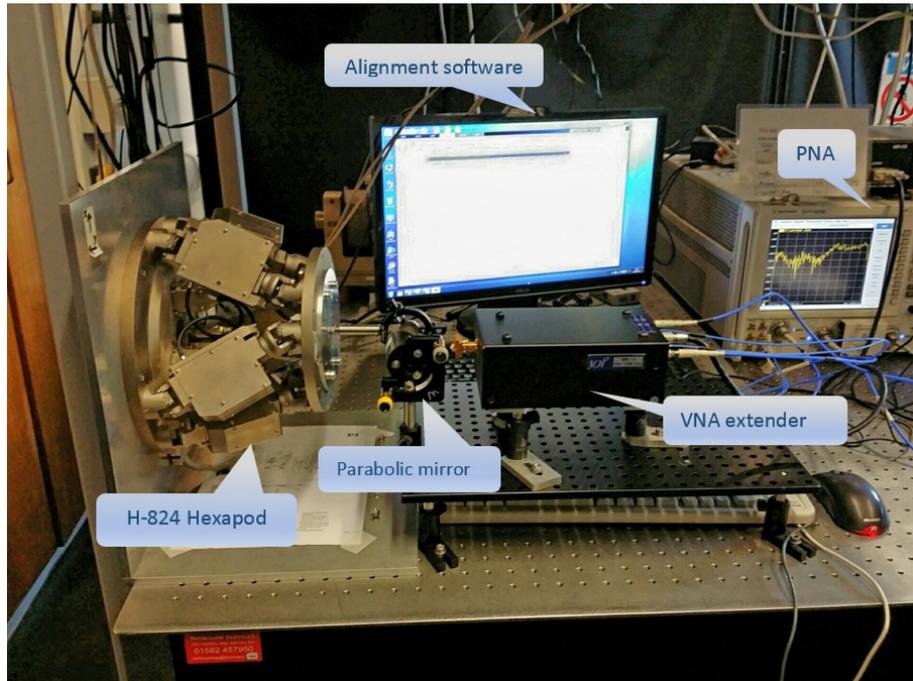
Figure 7.5: The H-824 Hexapod total setup for alignment process.

As a first step, the position of a two-inch off-axis parabolic mirror with focal length of 50 mm is set with respect to the VNA extender head and optical post.

Prior to the OAP, the incoming beam has to be at the desired system height (in our case 12.5 cm) and is propagating parallel to the optical bench. The Hexapod which is rotated 90 degrees is placed perpendicular to the optical axis. A flat gold-coated silicon wafer, as a sample is mounted on the Hexapod as shown in fig. 7.6 in the path of the reflected beam.

The parabolic mirror which collimates the beam from the extender head transmitter, is directed towards the flat plate and reflects back to the parabolic mirror M1 which focuses the beam back towards the receiver.

The measurement starts by placing the flat plate 60 mm from the parabolic mirror. All the 6-axes have been analysed and changed manually through the software mentioned in section 7.2 to achieve the estimated position of the aligned
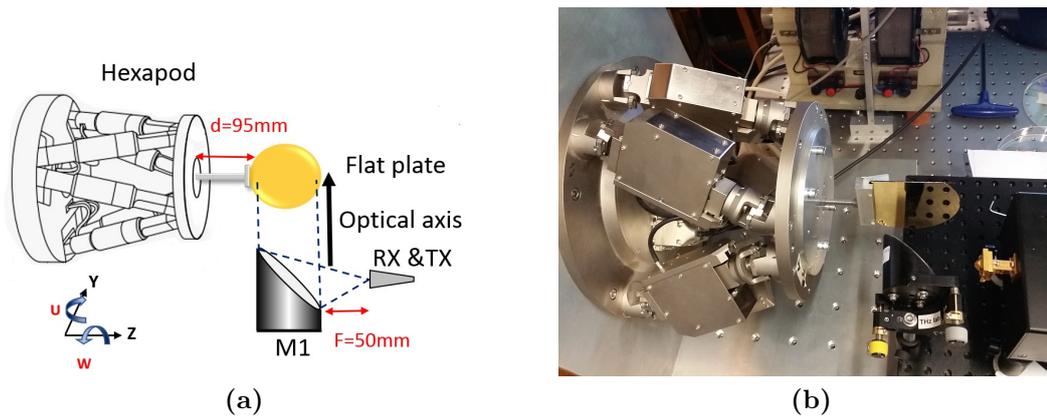
Figure 7.6: The schematic diagram of the THz system with Hexapod and VNA and parabolic mirror of 50 mm focal length.

system with the highest signal to noise ratio as shown on VNA. Based on our setup and the placement of the sample with respect to the parabolic mirror, three movement axes have been found to have the most influence on the alignment of the system. These are Y, W and U. Due to the large size of the flat plate in the setup, movement along the X, Z and V directions have minimum impact on the alignment of the system, and these three axes remain fixed during the experimental measurements. The movement along the optical axis is determined by the Y coordinate. The results from a sweep along the optical axis between 0 to -6 mm while U and W are fixed at the U=-0.3° and W=0.2° is shown in fig. 7.7.

The VNA measures S11 to obtain the reflection loss from the sample; the extracted data are complex numbers which contain the phase information and will be square rooted to obtain the magnitude of S11. The collected data have been post-processed by transferring to a Matlab programe which calculates the mean value of the magnitude in dB for each frequency. It has been observed that the S11 measurement, for the points between -2 mm to -3 mm have the highest signal.
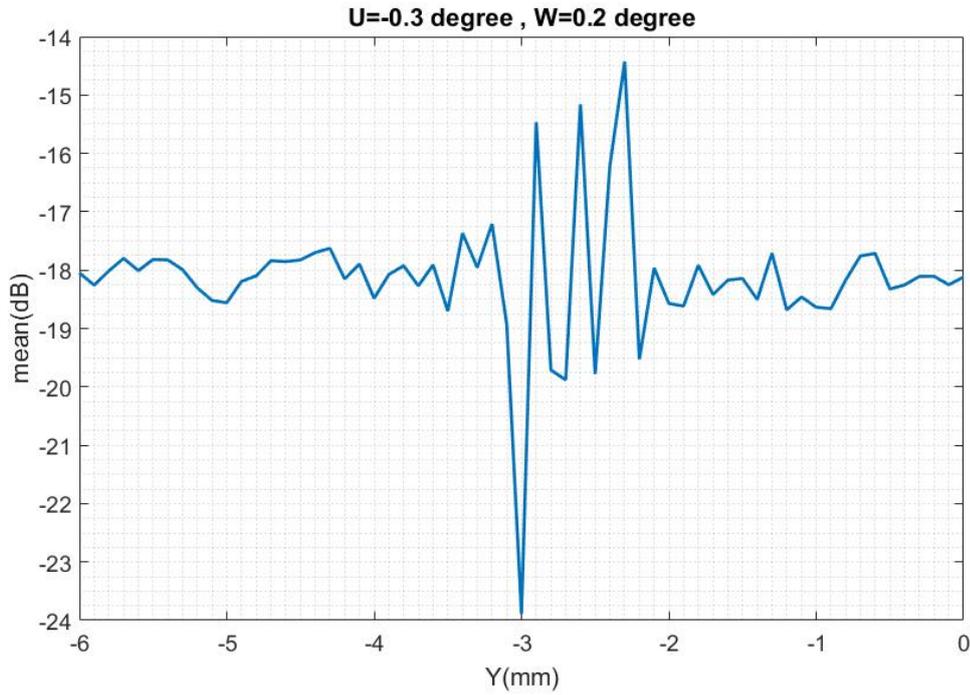
Figure 7.7: S11 measurement along the optical axis when U=-0.3°and W=0.2°,the highest peak observed between -2 *mm* to -3 *mm* along the optical axis.

When we apply rotation along the U axis, the reflector swings around as is shown in fig. 7.8. The rotation in the W axis does not affect the Y and Z positions, but U rotation does. During a U rotation, it is necessary to reposition the reflector in Y and Z. This compensation can be achieved by adding $L(sin\theta)$ to the Y-axis and $L(1 - \cos\theta)$ to the Z axis, where L is the length of the arm to the Hexapod from the flat plate. Without this compensation, a U rotation of the reflector also introduces a shift along the optical axis, Y, which is undesirable. The benefit of this configuration is that it allows the Hexapod to have the greatest displacement range along the optical axis (Y-axis); due to the limitation of Hexapod movement in Z which is only $\pm$ 12.5 *mm* and whereas the Y-axis has a travel range of $\pm$ 22.5 *mm*.

162
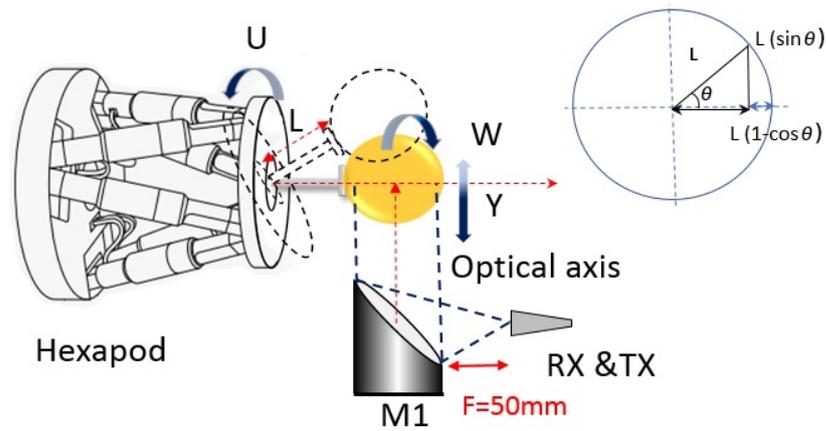
Figure 7.8: The schematic diagram of Hexapod alignment setup with rotation in the U and W axis.

The maximum peak signal along the optical axis is obtained at Y equal to -2.3 mm as is shown in fig. 7.7. By fixing Y at -2.3 mm and sweeping along the W and U axes, the S11 measurement as a function of W for compensated set-ups is shown in fig. 7.9. As it can be seen, the maximum peak signal is achieved at the angle between $0°$ to $+2°$ in the W axis in fig. 7.9.

The measured S11 as a function of U rotation between $-2.5°$ to $+2.5°$ has been shown in fig. 7.10. As it can be seen at $U = -0.5°$ a peak signal value is obtained compensated setup. At U between $-2.5°$ to $-1.5°$ signal oscillation can be observed due to the axis combination limitation of the Hexapod. The area to the left dashed line in the fig. 7.10 shows the axes limitation area of Hexapod.
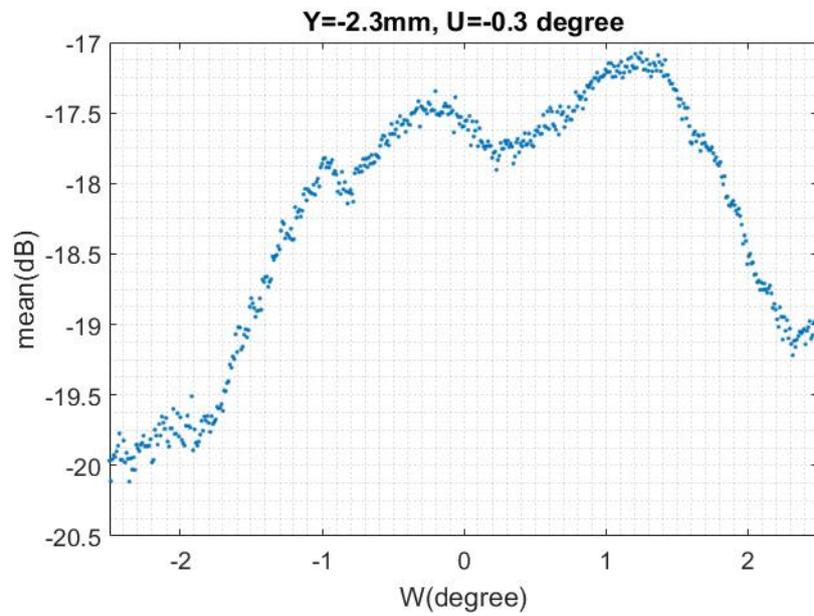
(a) Compensated

Figure 7.9: The measured S11 as a function of W(degree)for (a) compensated setup.
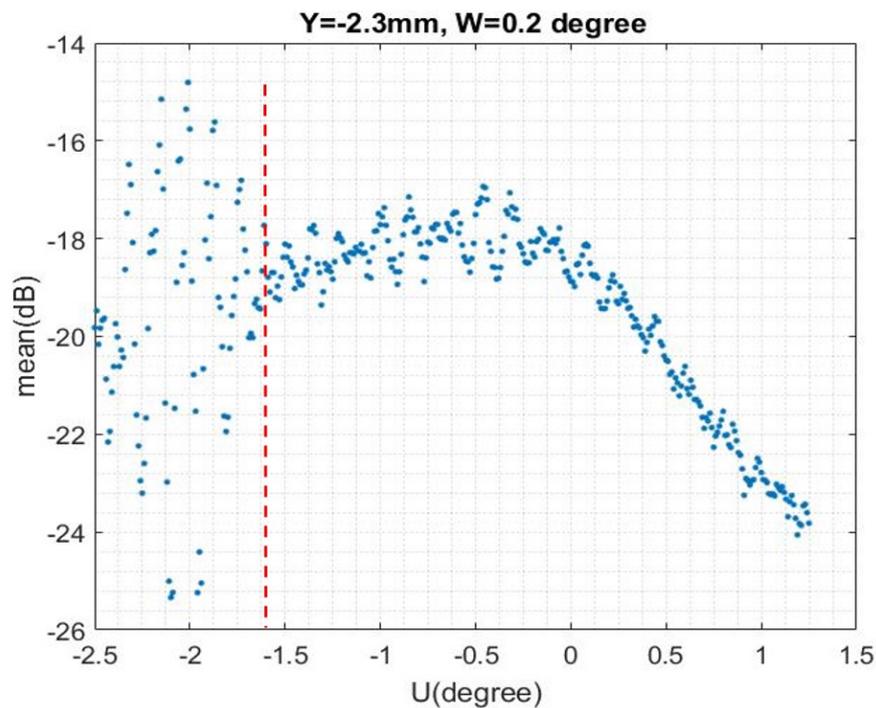
(a) Compensated

Figure 7.10: The measured S11 as a function of U(degree)for (a) compensated setup,the area to the left of the red line shows an axis limitation of the Hexapod, which has introduced significant oscillation in the measured S11 values.

164

Based on W and U rotation in figs. 7.9 and 7.10, the best position for Y is at -1 mm along the optical axis.

The next approach is to place the flat plate at Y=-1 mm where we are expecting to have the highest SNR and measure S11 for both W and U. The 2D surface plot of U and W rotation for frequencies(0.75-0.92 THz) and (0.93-1.1 THz) and also the frequency difference are shown in fig. 7.11. As can be seen, a high signal is obtained when the Hexapod rotates in both the U and W axes between $-3°$ to $1°$ whilst remaining at a fixed position in Y. The apparent rectangular shape around the $W = 1.5°$ could be attributed to an image of the horn antenna which is reflected back from the flat plate.

(a) (0.75-0.92 THz)

(b) (0.92-1.1 THz)
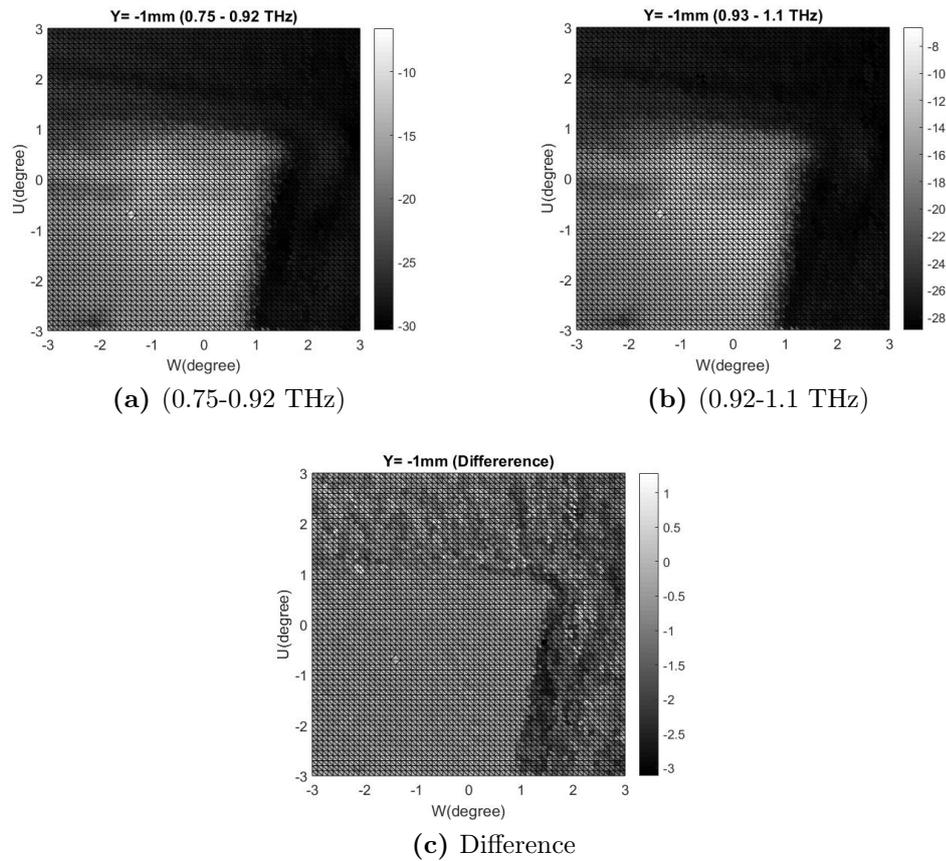
(c) Difference

Figure 7.11: The compensated S11 plots of flat plate along the optical axis 60 mm and frequencies (a) 0.75-0.92 THz and (b) 0.92-1.1 THz (c) Difference.

Now that the optimum position along the optical axis is known, the need for such large Y axis sweeps is no longer required. Therefore, in the next section, an alternative Hexapod configuration is used in which the reflector is mounted directly onto and parallel with the platform. This eliminates the need to apply geometric compensation during rotation.

7.4 Final alignment

7.4.1 Direct flat plate measurement configuration

In order to assess the effect of the OAP mirror on the alignment, in this section, we consider an even simpler configuration which includes only the VNA extender head and a flat plate reflector. The reflector is mounted directly onto the Hexapod platform as shown in shown in fig. 7.12. The gap between the THz antenna and the reflector is set at 65 mm. In this configuration, the Z direction defines the optical axis.

(a)   (b)
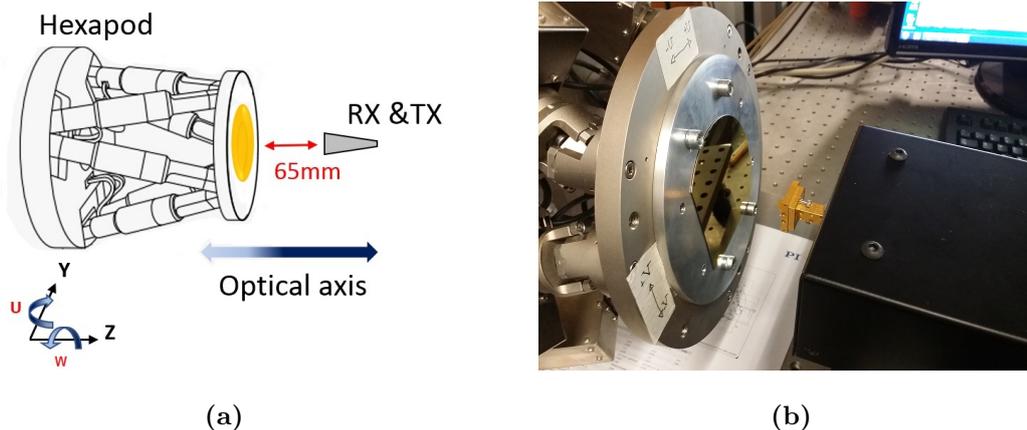
Figure 7.12: The schematic diagram of the THz system with Hexapod and VNA extender at 65 mm from the Hexapod.

The alignment between the flat plate and VNA extender head has been investigated for U and W rotation between the $-7°$ to $+7°$. A key benefit of this configuration is that the sweep angle range is much greater than that achievable compared to the previous setup. Figures 7.14 and 7.15 show the measured S11 at a range of frequencies between 0.75 and 1.1 THz for a sweep in the U and W axes. The results show a bright or dark circle in the centre flanked by series of concentric rings which are formed by the interference of the transmitted and

reflected beams from the gold-coated flat plate, placed at the distance 65 mm. The centre brightness intensity (or, in effect, polarity) and the number of rings changes with increasing frequency.

The patterns based on the near-field or far-field will be different. R and R_0 in the equations below represent the boundary of the near field and far field regions respectively (as a distance from an antenna which is larger than the wavelength of the radiated beam) [169].

$$R = 0.62(\sqrt{\frac{D^3}{\lambda}}), \tag{7.1}$$

$$R_0 \geq 2(\frac{D^2}{\lambda}), \tag{7.2}$$

where D is the length of antenna aperture and λ is the wavelength of radiated beam. For a horn antenna with 3 mm aperture size, a 1 THz beam will radiate from a distance of 60 mm from the antenna (i.e. beyond this distance is the far field region). In the experimental setup described above, the horn antenna is located at a distance of 65 mm from the flat plate and therefore should be in the far field. However, in figs. 7.14 and 7.15, it is evident that the electric field intensity, at zero degrees tilt in both U and W, varies significantly with frequency. For example, at 0.89 THz, the centre spot is of high intensity compared to 0.90 THz which is low intensity. As the frequency is increased, more rings are visible on the images. This would imply that the reflector is actually in the near field, or Fresnel zone in [170].

The E-field distribution has shown at the near-field region a large oscillation is placed on the oscillation which correspond to the Fresnel diffraction region and after this region the distribution contains no oscillations and the spectrum became wider as it can be seen in fig. 7.13. Unlike the far-field the radiation pattern shape changes

with distance [169].
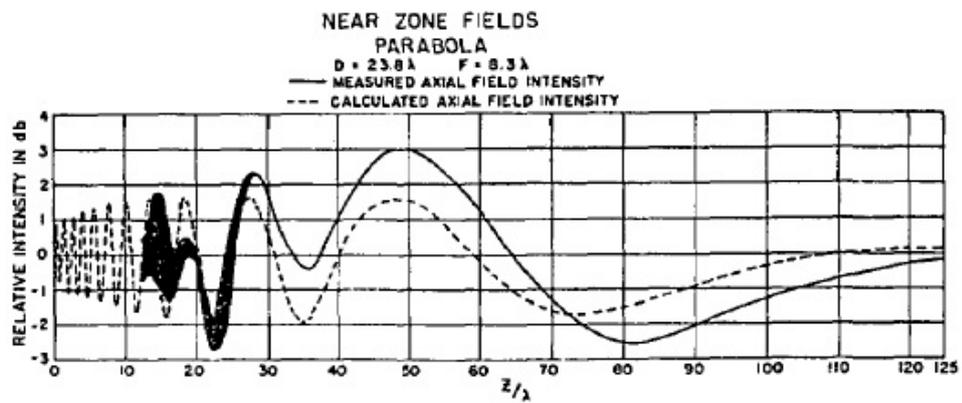
Figure 7.13: Distribution of the electric field intensity along the a paraboloidal reflector [170].

(a) 0.75THz

(b) 0.76THz

(c) 0.78THz

(d) 0.80THz

(e) 0.81THz

(f) 0.83THz

(g) 0.85THz

(h) 0.87THz

(i) 0.89THz

(j) 0.90THz

(k) 0.92THz
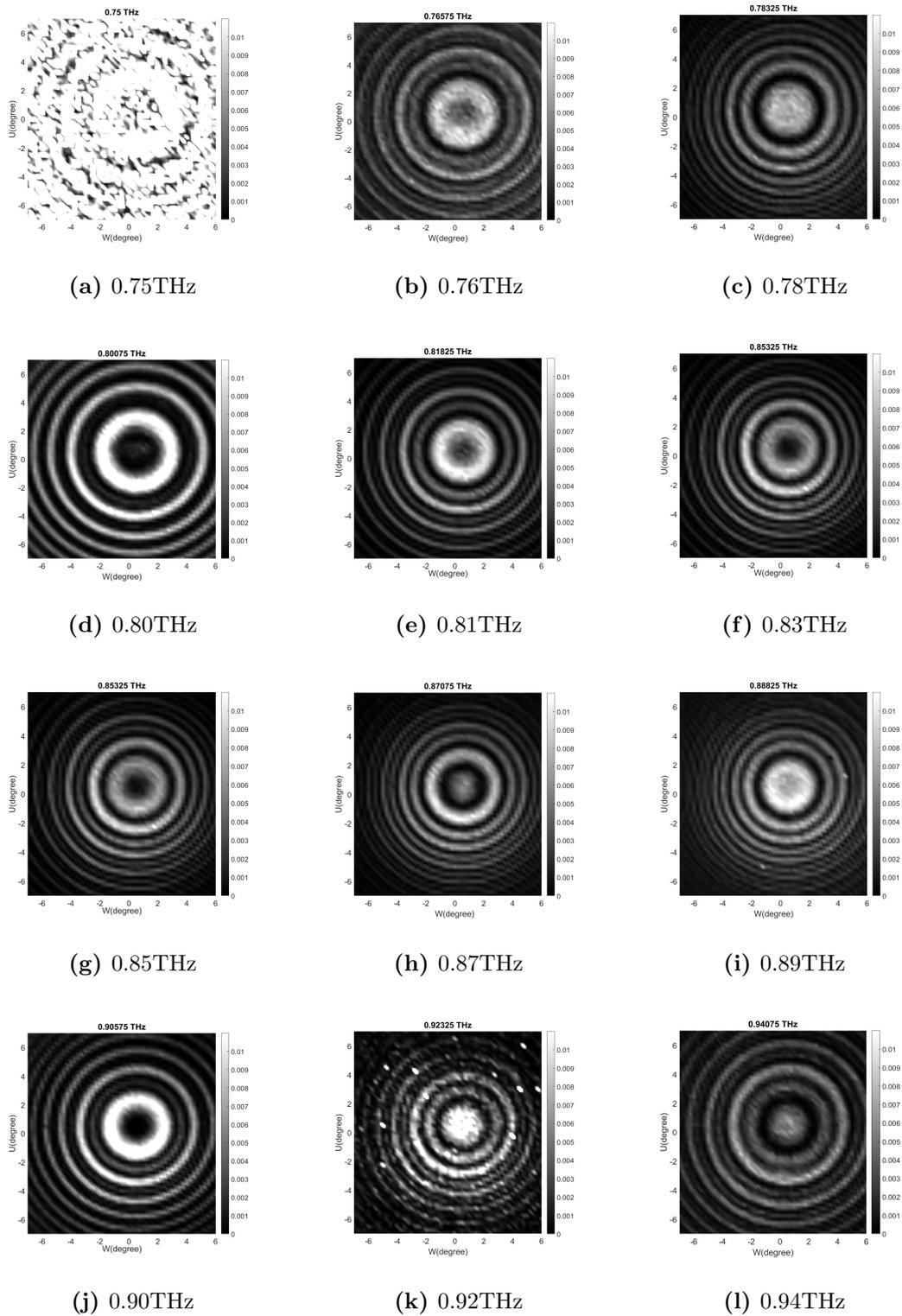
(l) 0.94THz

Figure 7.14: The electric field images of the U axis rotation as a function of W axis of flat plate placed at 65 mm for frequencies 0.75-0.94 THz(a-l).

(a) 0.95THz   **(b)** 0.97THz   **(c)** 0.99THz

(d) 1.01THz   **(e)** 1.02THz   **(f)** 1.04THz

(g) 1.06THz   **(h)** 1.08THz   **(i)** 1.1THz
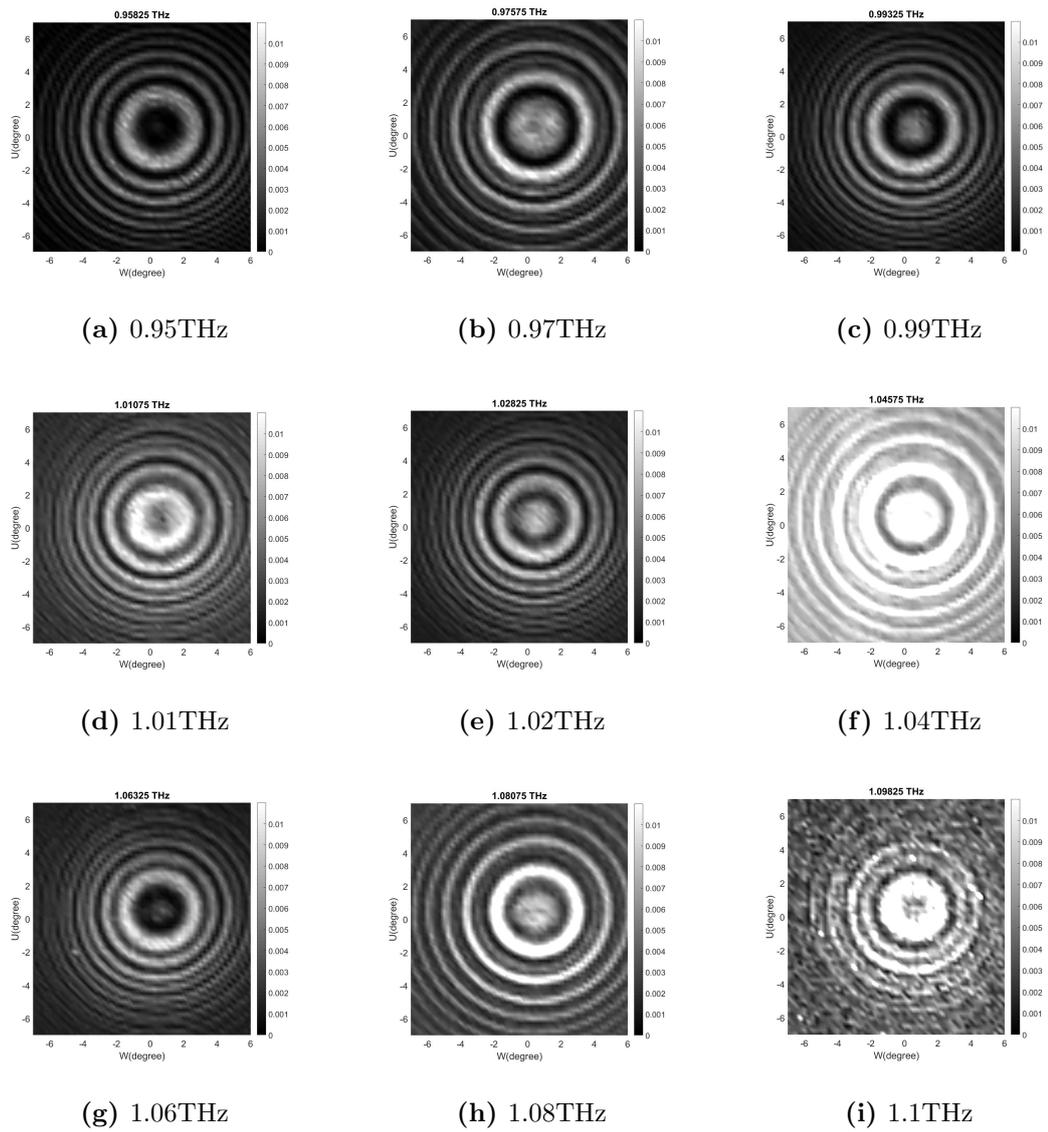
Figure 7.15: The electric field images of the U axis rotation as a function of W axis of flat plate placed at 65 *mm* for the frequencies 0.95-1.1 THz(a-i).

The diffraction patterns of in phase image have been shown in figs. 7.16 and 7.17, as it can be seen there is a $\sim \pi$ phase difference between frequencies.

(a) 0.75THz

(b) 0.76THz

(c) 0.78THz

(d) 0.80THz

(e) 0.81THz

(f) 0.83THz

(g) 0.85THz

(h) 0.87THz

(i) 0.895THz

(j) 0.90THz

(k) 0.92THz
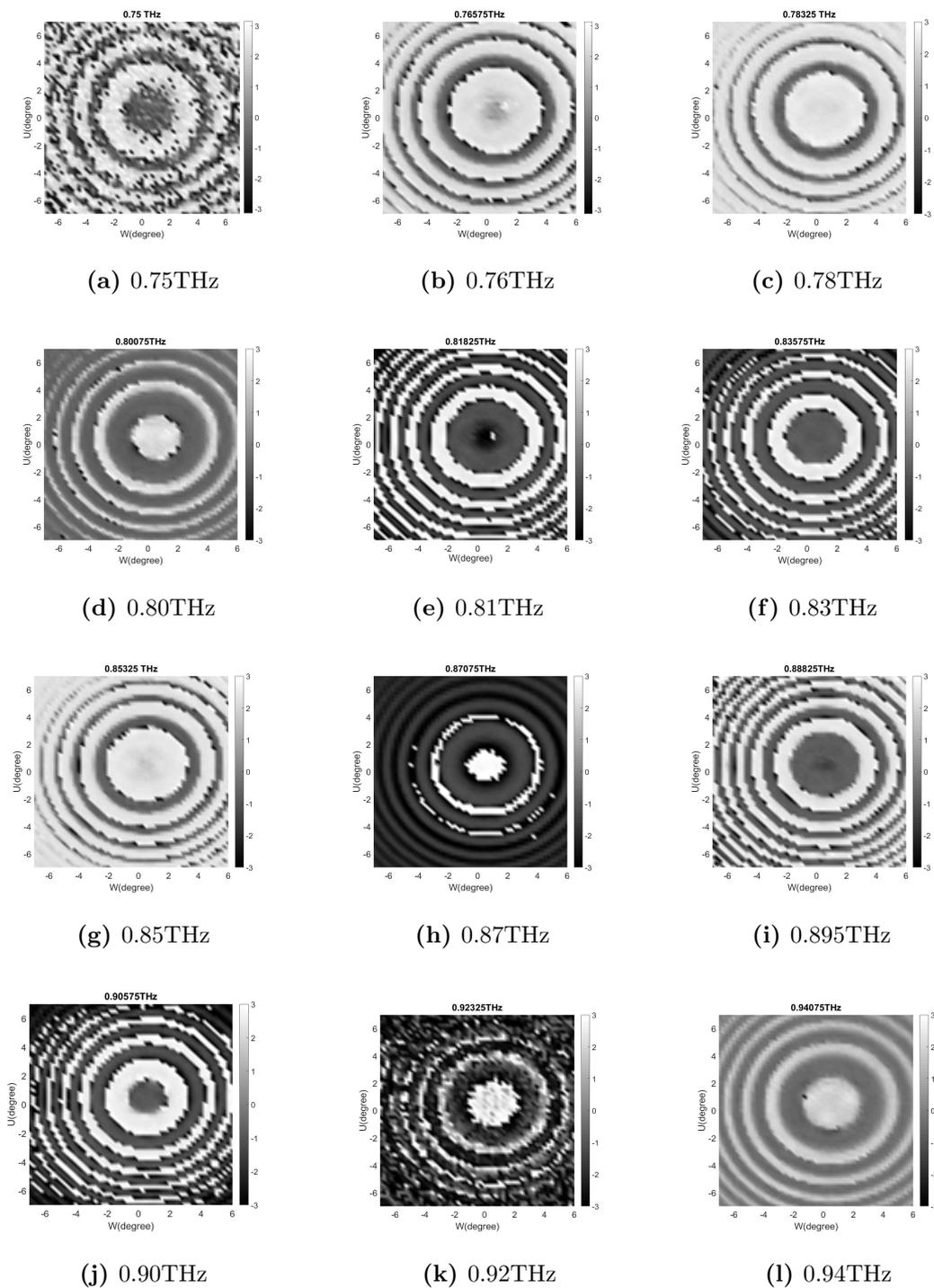
(l) 0.94THz

Figure 7.16: The phase images of the U axis rotation as a function of W axis of parabolic mirror placed at 65 *mm* from the flat plate with the frequencies 0.75-0.94 THz(a-l).

172

(a) 0.95THz **(b)** 0.97THz **(c)** 0.99THz

(d) 1.01THz **(e)** 1.02THz **(f)** 1.04THz

(g) 1.06THz **(h)** 1.08THz **(i)** 1.1THz
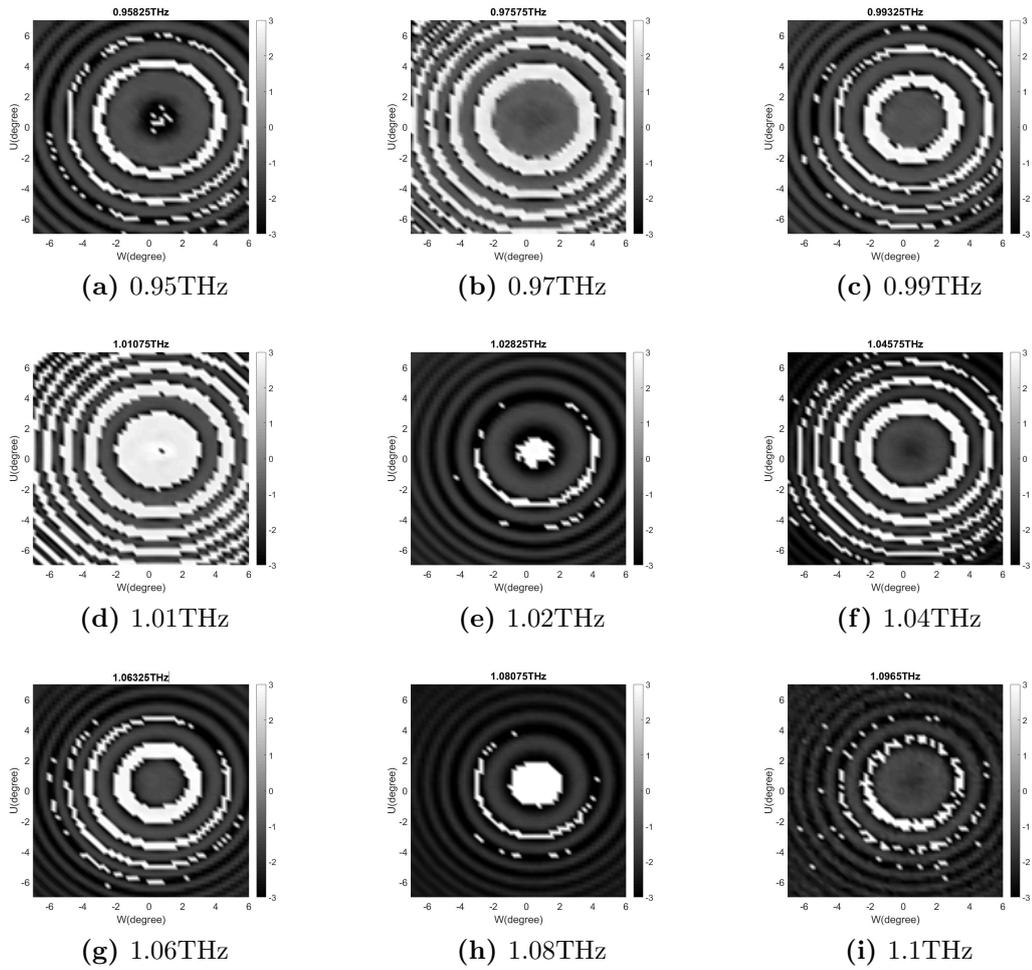
Figure 7.17: The phase images of the U axis rotation as a function of W axis of parabolic mirror placed at 65 *mm* from the flat plate with the frequencies 0.95-1.1 THz(a-i).

7.4.2   Parabolic mirror based configuration

The next configuration is based on an off-axis parabolic mirror(OAP) as is shown in fig. 7.18. A VNA extender has been placed at the focal point of the OAP with the 50 *mm* focal point to collimate the focused THz beam coming from the transmitter towards the gold-coated flat plate. The gold-coated flat plate is mounted directly on the movable platform of the Hexapod at 160 *mm* with respect to the OAP.

(a)   (b)
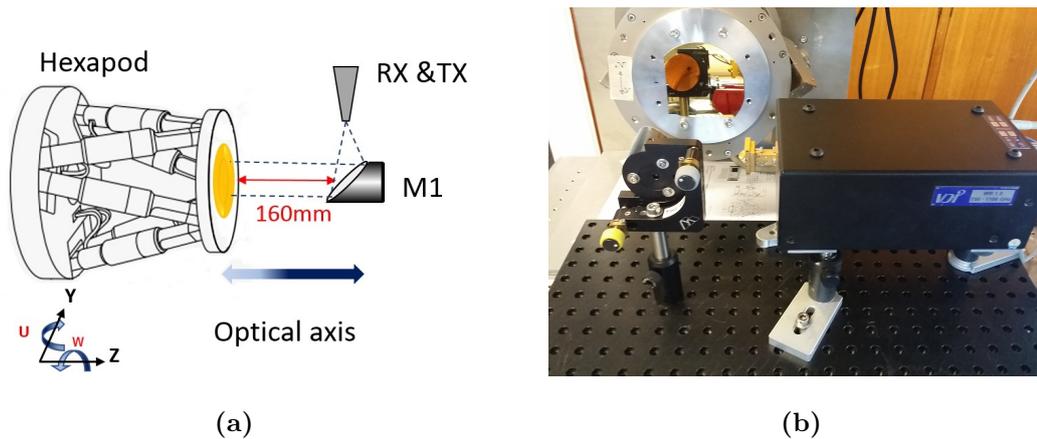
Figure 7.18: The schematic diagram of the THz system with a flat plate at 160 mm from OPA.

Using a flat plate as a reflective object in the system with an OAP will produce a diffraction pattern with straight fringes parallel to the optical axis of OAP when the beam is perfectly collimated and without aberrations [158]. Therefore, it is important to orient a reference line in parallel to the fringes and perpendicular to the the optical axis. The angle of the fringes relative to the reference line defines the state of collimation [157]. If the fringes are tilted, the beam is either converging or diverging, and the focal point of the OAP does not coincide with the origin of the beam. However, the spatial diffraction pattern is of less interest when considering the THz alignment because i) it is not practically visible and ii) the main objective is to maximize the signal. As in the previous section, here we consider the effect of tilting the flat reflector using the Hexapod, but now in the presence of an OAP.

In this setup, first the OAP alignment is fixed with the flat plate at the origin of the Hexapod axes, in order to achieve the highest signal. Tilt rotation is applied to the flat plate reflector in the U and W axes. As shown in fig. 7.19, this has the effect of changing the optical path length along the flat plate. Therefore, constructive or destructive interference can occur which is evident as fringes in the figs. 7.20

and 7.21.
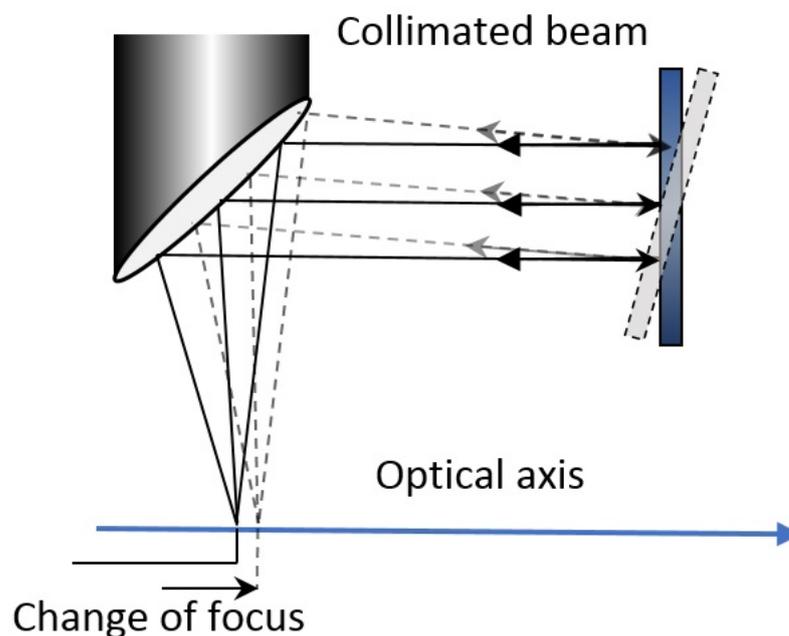
Figure 7.19: Focusing properties of an OAP. The solid lines are collimated beam from the flat plate and dashed lines are tilted from flat plate.

Unlike the measurements shown previously, that did not include the OAP, the centre intensity remains fairly constant throughout the frequency range, indicating that this is now in the far-field region. The shape is no longer circular which can be attributed to misalignment of the OAP, which cannot be corrected through adjustment of the flat plate reflector. Additional experiments, beyond the scope of this thesis, would be required to link the direction of the observed fringes to a particular axis of misalignment in the OAP, as has been done for conventional diffraction patterns. Since the setup is not perfect, even with minimum misalignment, there will always be a small aberration and astigmatism in the system which affects the fringes' size and shape.

By analyzing the fringe pattern, it is possible to determine the path length differences at any point in the setup.

The key finding is that with a seemingly simple single OAP, flat plate reflector combination the tilt alignment of the reflector is crucial in determining the measured S11 signal. Moreover, the OAP significantly influences the relationship between the tilt and S11.

(a) 0.75THz

(b) 0.76THz

(c) 0.78THz

(d) 0.80THz

(e) 0.81THz

(f) 0.83THz

(g) 0.85THz

(h) 0.87THz

(i) 0.89THz

(j) 0.90THz

(k) 0.92THz
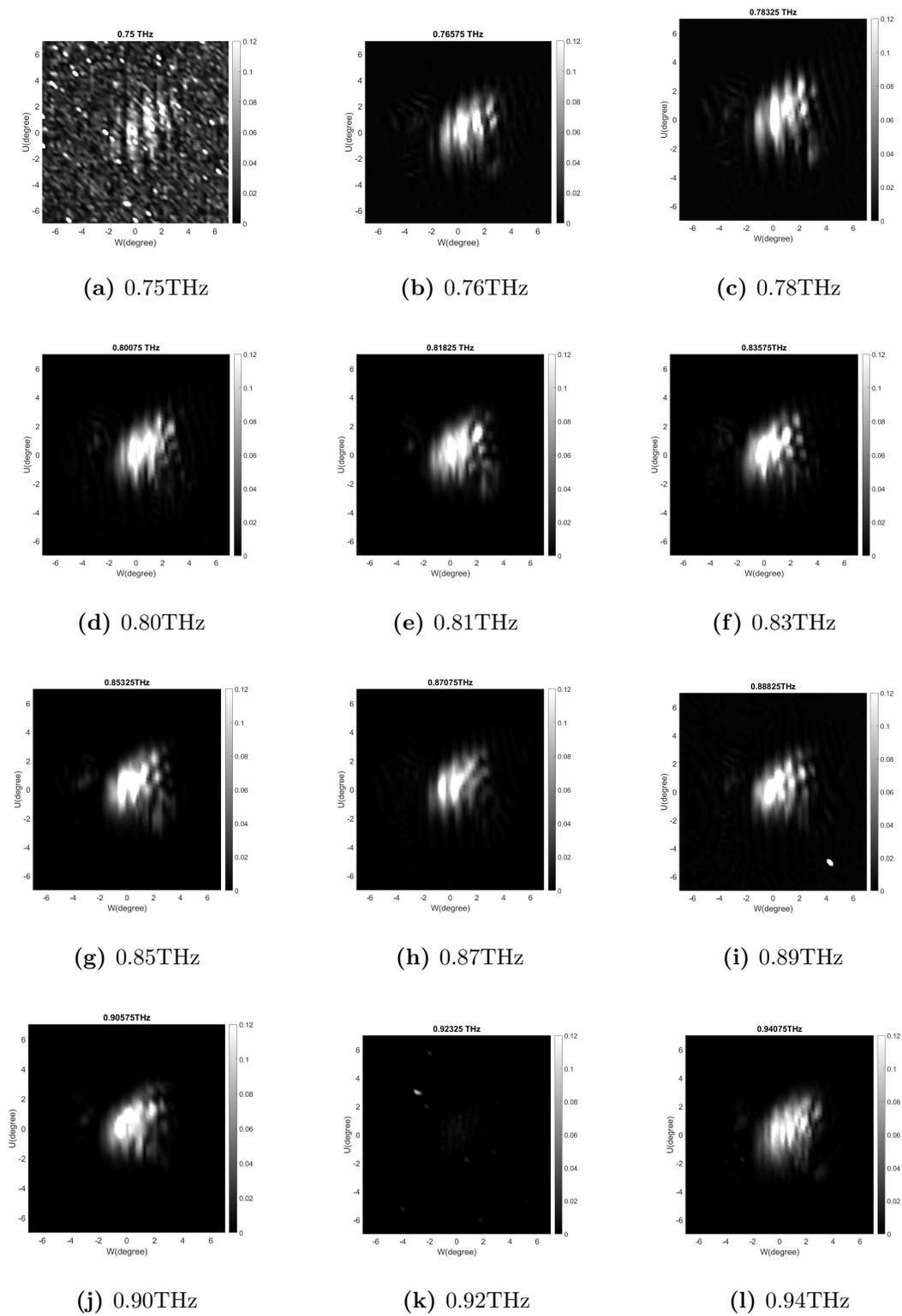
(l) 0.94THz

Figure 7.20: The U axis rotation as a function of W axis of parabolic mirror placed at 160 *mm* from the flat plate with the frequencies 0.75-0.94 THz(a-l).

177

(a) 0.95THz

(b) 0.97THz

(c) 0.99THz

(d) 1.01THz

(e) 1.02THz

(f) 1.04THz

(g) 1.06THz

(h) 1.08THz
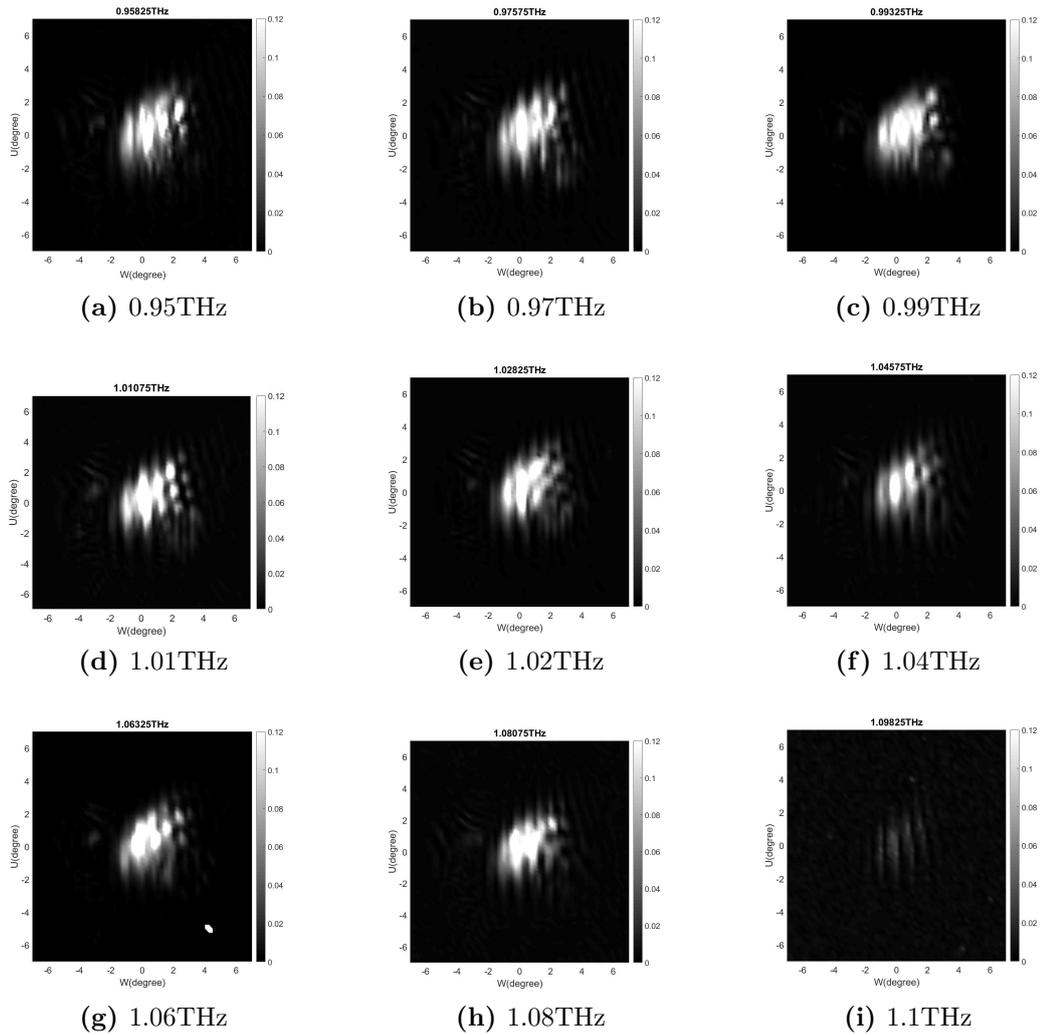
(i) 1.1THz

Figure 7.21: The U axis rotation as a function of W axis of parabolic mirror placed at 160 mm from the flat plate with the frequencies 0.95-1.1 THz(a-i).

7.5   Conclusion

In this chapter, we introduced a new alignment technique to simplify the process of aligning of a simple terahertz optical system. The alignment of the THz beam has sub-wavelength tolerances which need precision in the axial dimensions, and such alignment is complicated by the fact the THz beam is invisible to the naked eye. Due to the sensitivity of optical alignment in terahertz system, the new technique has minimized misalignment in the THz system using a Hexapod and vector network

178

analyzer. The Hexapod approach is well suited to automatic sweeping to identify the maximum signal. Misalignment in the terahertz optical system effects the dynamic range and system measurements operation of Hexapod with six degrees of freedom could provide minimum settling time and error for alignment of the system. Each component in the terahertz system has several degrees of freedom which makes the alignment procedure difficult. To reduce the number of alignment parameters associated with the system, the extender and off-axis parabolic mirror have been located in a fixed position.

In this study, two different configurations are introduced for effective alignment of the THz system. In the first approach, a sample has been aligned in the system with three degrees of freedom based on (UWY) axes with a larger distance along the optical axis which has the most impact on it. It has some drawbacks due to the combination of axis movement at the same time which produces misalignment in the configuration, and it needed to compensate these axes. The second approach is based on a direct measurement of the mounted sample on the Hexapod. The resulted diffraction patterns near to the far-field regarding the flat plate sample have shown that the system is perfectly aligned and other optical component such as FZPR can be placed on Hexapod and can be easily aligned in this simple configuration.

Chapter 8

Conclusions

In recent years, THz technology has developed rapidly. The properties of terahertz (THz) radiation have demonstrated potential in subsurface imaging and spectroscopy. THz imaging attracted attention for biomedical research [171] as well as in the food and pharmaceutical industry [172]. To improve the spatial resolution of terahertz imaging systems, refractive lenses and reflective metal mirrors should be replaced with components that are thinner, lighter, and more efficient in focusing performance [135, 173].

Although, recently various diffractive lenses have been fabricated in plastic by 3D printing [117, 174]; in paper by utilizing laser-cutting technology [126]; and from silicon by laser ablation [175]. This thesis has exploited the existing microfabrication techniques to fabricate diffractive optical elements such as the SU-8 Fresnel lens and aluminium Fresnel reflector to provide a direct solution to the problems associated with beam focusing and imaging in integrated systems. This innovation was achieved by developing and optimising a Fresnel structure which has been combined with microfluidic channels for chemical analysis and spectroscopy.

The microstructuring of a silicon surface has been shown to act as an antireflective layer which offers the possibility of being a spatially tunable dielectric layer, or Artifical Dielectric Layer (ADL). The improvement in transmission through the ADL has been demonstrated experimentally using a THz-VNA. The fabricated ADLs were also tested in THz-TDS setup and successfully reduced the reflected and suppressed internal reflection leading to reduction of the étalon effect. These types of structures could form the basis of future beam shaping and reflection reducing components in integrated systems.

Chapter 2 explored the state-of-the-art measurement techniques for both the generation and detection of THz radiation with a specific emphasis on THz-TDS, and the THz-VNA methods. The THz-VNA measurement technique operates directly in the frequency domain which provides many single-frequency measurements to increase SNR, and also eliminates the needs for the complicated system alignment. However, compared to THz-TDS it has frequency range limitations.

Chapter 3 presented the finite-difference time-domain (FDTD) simulation techniques. FDTD has been used as a computational method to design and simulate all of the THz components in this thesis. A sub-wavelength grating structure which is used for THz reflection loss reduction at air/material boundaries has been shown as an example. These sub-wavelength grating structures behaved as a homogeneous medium with an effective refractive index based on effective medium theory (EMT) because of the shorter grating period than the wavelength of the incident beam. The sub-wavelength grating has been simulated for various structural shapes such as rectangular, trapezoidal and triangular structures with

181

different pitches, widths and depths. Based on the simulation, the reflection loss of the rectangular-shaped was higher compared with the other two structures due to the change in the effective refractive index of grating along the beam propagation direction; triangular-shaped structures were shown to have the best transmission.

Chapter 4 documented the design, microfabrication and characterization of the simulated sub-wavelength grating of chapter 3. The grating structure was fabricated from KOH etching of silicon with 40 μm grooves depth and was characterized using both the THz-VNA and THz-TDS. Ultimately, this device came with the idea of minimising the unwanted signal losses caused by surface reflection in sub-wavelength features at the material-air interface in THz-TDS. The design which relies on an effective medium type approach offers the potential to have the precise control over the dielectric properties, which have the scope to be varied spatially.

Chapter 5 looked into the fundamental principles of diffractive and reflective optics such as micro multilevel Fresnel lens up to 1 mm in diameter, and with a 5 mm in focal point; and a Fresnel reflector with 13 mm diameter and focal point of 20 mm for operation in the terahertz region. The FDTD solver has been used for design and simulation of these structures. The microfabrication of multilevel Fresnel lens was created using negative photoresist SU-8, with overlapping of three level of concentric structures. Measurements obtained by THz-VNA are compared to simulation data which are shown good agreement between simulation and experiment.

In the second part of this chapter, a micromilled Fresnel reflector has been fabricated based on a Fresnel zone plate structure. To obtain the E-field intensity and phase, the FZPR was scanned in 3D space by mounting on an XYZ stage with a

fixed VNA head extender in the optical configuration. The measurements have been compared with FDTD simulations where the focal spot of FZPR for both simulation and experiment has been obtained at 20 mm away from the reflector surface. Ultimately, the use of these configurations with smaller, lighter diffractive optics allowes a wide range of beam shaping devices for incorporation into next-generation THz systems.

The work presented in chapter 6, investigated the fabrication of microfluidic channels based on the acetate film and silicon wafers which are combined with the developed FZPR in chapter 5 in a very compact THz optical setup. Various samples such as IPA/water mixtures and coffee/water were pumped through the microfluidic channel while the THz beam was interacting with the aqueous samples. The VNA measurements have shown the transmission increases with better refractive index matching inside the channel. The advantages of using the compact THz configuration with a lower number of optical components includes minimising the optical path length through a fluidic sample, higher spatial resolution, and focusing of the THz beam by the Fresnel reflector which provides better signal interaction with fluidic samples. Ultimately, this configuration provides the necessary means to analyse fluidic samples in the THz system.

Chapter 7 presented a new alignment technique to make the process of alignment in the THz system much simpler by exploiting a Hexapod micropositioner with 6 degrees of freedom.The same compact configuration introduced in chapter 6 has been used as a part of the new alignment system. Two different configurations have been investigated for the alignment of the THz system. In the first configuration,

the Hexapod could have the longest displacement along the optical axis due to the limitation in the Z axis. In the second configuration, the near-field and far-field of a paraboloidal reflector has been investigated for a flat plate mounted on the Hexapod and directly illuminated by the horn antenna. The induced circular diffraction patterns of the flat sample show that the reflector is actually in the far field due to the observed unchanged diffraction pattern shape by changing in different angles. But the change in phase diffraction pattern from one frequency to another frequency is observed. It is also shown that this setup is completely aligned which allow other optical components such as FZPR to be aligned in this system. The system alignment is an essential factor to achieve precise control on the spatial resolution in any THz system which can attain by a high level of adjustment using micropositioner.

8.1   Future Work

The work presented in this thesis has concentrated on diffractive optical components and their applications in THz systems. Up to now, most attention has been focused on terahertz imaging system compactness and providing lighter and thinner lenses or reflectors. Various materials have been studied during the last few years for the fabrication of diffractive lenses based on Fresnel structures. The fabricated lens in this thesis is based on a SU-8 negative photoresist [176] with refractive index of 1.5 at THz frequencies. SU-8 is commonly used for the creation of high aspect ratio structures and is compatible with microfabrication techniques which are highly production scalable. Other materials could be used to form these

3D Fresnel structures. In general, the usage of plastic materials at high frequencies and in integrated systems with high numerical aperture(NA) is limited due to their low refractive index and dielectric absorption loss. If a stamped embossing approach is used (n.b. where the master stamp is formed via micromachining), then cyclo-olefin copolymers such as Topas could be investigated. Topas has been reported to have a stable index of refraction and very low absorption in terahertz region compared to other polymers [177].

The acetate based microfluidic devices presented in chapter 6 suffered from channel collapse (which, as to be expected, was not observed in the silicon devices). This collapse occurred for the large area, smallest depth structures. Future work could explore methods to overcome this problem, for example, by placing a piece of paper which is transparent to the THz frequencies inside the channel to absorb the aqueous solutions and prevent to any collapse inside the channel and easily can be removed from the channel. Another solution to increase the performance of the microfluidic channel is to provide a multi-channel (with multiple inlets/outlets) inside the chamber to inject liquid samples into the channel with one or more samples at the same time to form a multi-stream flow and have better control on the concentration of mixed-samples.

The presented ADL with the sub-wavelength structure in chapters 3 and 4 has shown the highest transmission with the triangular-shaped grooves structure in FDTD simulation. The fabrication of the triangular structure on a silicon wafer with KOH etching was challenging. Therefore a trapezoidal structure was produced. An alternative approach could be the laser ablation of silicon wafers to obtain the

triangular-shaped structure [178] or using the 3D printer to fabricate a double-sided sub-wavelength structure from plastic [106] but the surface roughness is likely to be significantly higher with both of these techniques.

The use of Hexapod has been shown to be well suited for automatic sweeping in order to maximize the THz signal. In the direct measurement of the flat plate, the angle was swept over a large range but its position along the optical axis was fixed. In order to investigate the diffraction pattern at near and far field, one approach would be sweeping along the optical axis at difference distances from flat plate. The resulted diffraction pattern from the flat plate showed that the configuration is aligned correctly and can be used for other optical components in this thesis such as the Fresnel reflector. The Fresnel reflector can be mounted on the moveable platform of Hexapod and, by analysing the diffraction pattern of the FZPR, it is possible to obtain the exact position focal point.

One final experiment could be providing a fully automated algorithm for alignment which could have better control on adjustment. When a setup has a massive number of optical elements, it is difficult to divide this system into parts that can be aligned separately. This level of complexity makes automatic alignment a necessity. This kind of system requires an autonomous or remotely controlled adjustment and also needs to optimize the system performance in the presence of errors. The alignment system needs to be able to recover from a wide range of unknown initial states of misalignment. In the near and far-field measurements, the intensity distribution can be captured and evaluated by the alignment algorithm. The algorithm computes a set of commands to the Hexapod and sends them,

through appropriate interfaces, to move the struts which adjust the positions of the optical elements. The alignment process is iterative: the algorithm tries combinations of commands until a desired far-field spot quality is achieved.

Bibliography

[1] H. Rubens and B. W. Snow, "II. on the refraction of rays of great wave-length in rock-salt, sylvite, and fluorite," *The London, Edinburgh, and Dublin Philosophical Magazine and Journal of Science*, vol. 35, no. 212, pp. 35–45, 1893.

[2] H. Rubens and O. Von Baeyer, "Lxxx. on extremely long waves, emitted by the quartz mercury lamp," *The London, Edinburgh, and Dublin Philosophical Magazine and Journal of Science*, vol. 21, no. 125, pp. 689–695, 1911.

[3] A. G. Arkadiewa, "Short electromagnetic waves of wave-length up to 92 μ," *Nature*, vol. 113, p. 640, 1924.

[4] R. B. Barnes, W. Benedict, and C. Lewis, "The far infrared spectrum of H_2O," *Physical Review*, vol. 47, no. 12, p. 918, 1935.

[5] M. J. Golay, "A pneumatic infra-red detector," *Review of Scientific Instruments*, vol. 18, no. 5, pp. 357–362, 1947.

[6] W. Boyle and K. Rodgers, "Performance characteristics of a new low-temperature bolometer," *JOSA*, vol. 49, no. 1, pp. 66–69, 1959.

[7] S. Fray and J. Oliver, "Photoconductive detector of radiation of wavelength greater than 50 μ," *Journal of Scientific Instruments*, vol. 36, no. 4, p. 195, 1959.

[8] E. Putley, "Impurity photoconductivity in n-type InSb," *Proceedings of the Physical Society*, vol. 76, no. 5, p. 802, 1960.

[9] F. J. Low, "Low-temperature germanium bolometer," *JOSA*, vol. 51, no. 11, pp. 1300–1304, 1961.

[10] A. Crocker, H. Gebbie, M. Kimmitt, and L. Mathias, "Stimulated emission in the far infra-red," *Nature*, vol. 201, no. 4916, p. 250, 1964.

[11] T. Chang, T. Bridges, and E. Burkhardt, "CW submillimeter laser action in optically pumped methyl fluoride, methyl alcohol, and vinyl chloride gases," *Applied Physics Letters*, vol. 17, no. 6, pp. 249–251, 1970.

[12] R. Köhler, A. Tredicucci, F. Beltram, H. E. Beere, E. H. Linfield, A. G. Davies, D. A. Ritchie, R. C. Iotti, and F. Rossi, "Terahertz semiconductor-heterostructure laser," *Nature*, vol. 417, no. 6885, p. 156, 2002.

[13] B. Hu and M. Nuss, "Imaging with terahertz waves," *Optics Letters*, vol. 20, no. 16, pp. 1716–1718, 1995.

[14] D. F. Plusquellic, K. Siegrist, E. J. Heilweil, and O. Esenturk, "Applications of terahertz spectroscopy in biosystems," *ChemPhysChem*, vol. 8, no. 17, pp. 2412–2431, 2007.

[15] P. U. Jepsen, D. G. Cooke, and M. Koch, "Terahertz spectroscopy and imaging–modern techniques and applications," *Laser & Photonics Reviews*, vol. 5, no. 1, pp. 124–166, 2011.

[16] J. Jackson, M. Mourou, J. Whitaker, I. Duling III, S. Williamson, M. Menu, and G. Mourou, "Terahertz imaging for non-destructive evaluation of mural paintings," *Optics Communications*, vol. 281, no. 4, pp. 527–532, 2008.

[17] "Terahertz medical imaging, dental imaging." `http://www.teraview.com/.htm`. Accessed: 2017-12-01.

[18] V. Wallace, A. Fitzgerald, S. Shankar, N. Flanagan, R. Pye, J. Cluff, and D. Arnone, "Terahertz pulsed imaging of basal cell carcinoma ex vivo and in vivo," *British Journal of Dermatology*, vol. 151, no. 2, pp. 424–432, 2004.

[19] D. Crawley, C. Longbottom, V. P. Wallace, B. Cole, D. Arnone, and M. Pepper, "Three-dimensional terahertz pulse imaging of dental tissue," *Journal of Biomedical Optics*, vol. 8, no. 2, pp. 303–307, 2003.

[20] A. J. Adam, P. C. Planken, S. Meloni, and J. Dik, "Terahertz imaging of hidden paint layers on canvas," *Optics Express*, vol. 17, no. 5, pp. 3407–3416, 2009.

[21] K. H. Jin, Y.-G. Kim, S. H. Cho, J. C. Ye, and D.-S. Yee, "High-speed terahertz reflection three-dimensional imaging for nondestructive evaluation," *Optics Express*, vol. 20, no. 23, pp. 25432–25440, 2012.

[22] W. Withayachumnankul and M. Naftaly, "Fundamentals of measurement in terahertz time-domain spectroscopy," *Journal of Infrared, Millimeter, and Terahertz Waves*, vol. 35, no. 8, pp. 610–637, 2014.

[23] J. L. Hesler, Y. Duan, B. Foley, and T. W. Crowe, "THz vector network analyzer measurements and calibration," in *21st International Symposium on Space Terahertz Technology, Oxford, UK*, 2010.

[24] J. Hammler, A. J. Gallant, and C. Balocco, "Free-space permittivity measurement at terahertz frequencies with a vector network analyzer," *IEEE Transactions on Terahertz Science and Technology*, vol. 6, no. 6, pp. 817–823, 2016.

[25] M. Naftaly, R. G. Clarke, D. A. Humphreys, and N. M. Ridler, "Metrology state-of-the-art and challenges in broadband phase-sensitive terahertz measurements," *Proceedings of the IEEE*, vol. 105, no. 6, pp. 1151–1165, 2017.

[26] S. Dhillon, M. Vitiello, E. Linfield, A. Davies, M. C. Hoffmann, J. Booske, C. Paoloni, M. Gensch, P. Weightman, G. Williams, *et al.*, "The 2017 terahertz science and technology roadmap," *Journal of Physics D: Applied Physics*, vol. 50, no. 4, p. 043001, 2017.

[27] P. Dean, A. Valavanis, J. Keeley, K. Bertling, Y. Lim, R. Alhathlool, A. Burnett L. Li, S. Khanna, D. Indjin, *et al.*, "Terahertz imaging using quantum cascade lasers a review of systems and applications," *Journal of Physics D: Applied Physics*, vol. 47, no. 37, p. 374008, 2014.

[28] Y.-S. Lee, *Principles of terahertz science and technology*, vol. 170. Springer Science & Business Media, 2009.

[29] X.-C. Zhang and J. Xu, *Introduction to THz wave photonics*, vol. 29. Springer, 2010.

[30] D. Auston, K. Cheung, and P. Smith, "Picosecond photoconducting hertzian dipoles," *Applied Physics Letters*, vol. 45, no. 3, pp. 284–286, 1984.

[31] P. R. Smith, D. H. Auston, and M. C. Nuss, "Subpicosecond photoconducting dipole antennas," *IEEE Journal of Quantum Electronics*, vol. 24, no. 2, pp. 255–260, 1988.

[32] G. Gallot and D. Grischkowsky, "Electro-optic detection of terahertz radiation," *JOSA B*, vol. 16, no. 8, pp. 1204–1212, 1999.

[33] M. Venkatesh, S. R. Konda, and A. K. Chaudhary, "Generation of THz radiation from bow tie photoconductive antennas based on semi insulating gallium arsenide," in *International Conference on Fibre Optics and Photonics*, pp. TPo–11, Optical Society of America, 2012.

[34] M. R. Stone, M. Naftaly, R. E. Miles, J. R. Fletcher, and D. P. Steenson, "Electrical and radiation characteristics of semilarge photoconductive terahertz emitters," *IEEE Transactions on Microwave Theory and Techniques*, vol. 52, no. 10, pp. 2420–2429, 2004.

[35] L. Hou and W. Shi, "An LT-GaAs terahertz photoconductive antenna with high emission power, low noise, and good stability," *IEEE Transactions on Electron Devices*, vol. 60, no. 5, pp. 1619–1624, 2013.

[36] Y. Huang, N. Khiabani, Y. Shen, and D. Li, "Terahertz photoconductive antenna efficiency," in *Antenna Technology (iWAT), China ,2011 International Workshop on*, pp. 152–156, IEEE, 2011.

[37] M. Tani, S. Matsuura, K. Sakai, and S.-i. Nakashima, "Emission characteristics of photoconductive antennas based on low-temperature-grown GaAs and semi-insulating GaAs," *Applied Optics*, vol. 36, no. 30, pp. 7853–7859, 1997.

[38] G. Zhao, R. Schouten, N. Van der Valk, W. T. Wenckebach, and P. Planken, "Design and performance of a THz emission and detection setup based on

a semi-insulating GaAs emitter," *Review of Scientific Instruments*, vol. 73, no. 4, pp. 1715–1719, 2002.

[39] C. Winnewisser, P. U. Jepsen, M. Schall, V. Schyja, and H. Helm, "Electro-optic detection of THz radiation in LiTaO 3, LiNbO 3 and ZnTe," *Applied Physics Letters*, vol. 70, no. 23, pp. 3069–3071, 1997.

[40] Z. Piao, M. Tani, and K. Sakai, "Carrier dynamics and terahertz radiation in photoconductive antennas," *Japanese Journal of Applied Physics*, vol. 39, no. 1R, p. 96, 2000.

[41] I. Wilke and S. Sengupta, "Nonlinear optical techniques for terahertz pulse generation and detection optical rectification and electrooptic sampling," *Terahertz Spectroscopy: Principles and Applications, Optical Science and Engineering*, vol. 131, p. 41, 2007.

[42] K.-E. Peiponen, A. Zeitler, and M. Kuwata-Gonokami, *Terahertz spectroscopy and imaging*, vol. 171. Springer, 2012.

[43] G. Gallerano, S. Biedron, *et al.*, "Overview of terahertz radiation sources," in *Proceedings of the 2004 FEL Conference, Italy*, no. 1, pp. 216–221, 2004.

[44] C.-R. Haas, R. Dinger, and D. Hoffmann, "Optically pumped solid-state laser," Mar. 27 2003. US Patent App. 10/223,512.

[45] A. Davies, E. H. Linfield, and M. B. Johnston, "The development of terahertz sources and their applications," *Physics in Medicine and Biology*, vol. 47, no. 21, p. 3679, 2002.

[46] L.-A. Yang, Y. Hao, Q. Yao, and J. Zhang, "Improved negative differential mobility model of GaN and AlGaN for a terahertz gunn diode," *IEEE Transactions on Electron Devices*, vol. 58, no. 4, pp. 1076–1083, 2011.

[47] D. M. Pozar, "Power dividers and directional couplers," *Microwave Engineering*, pp. 308–369, 2012.

[48] R. J. Trew, "High-frequency solid-state electronic devices," *IEEE transactions on electron devices*, vol. 52, no. 5, pp. 638–649, 2005.

[49] J. Tucek, D. Gallagher, K. Kreischer, and R. Mihailovich, "A compact, high power, 0.65 THz source," in *Vacuum Electronics Conference, 2008. IVEC 2008. IEEE International*, pp. 16–17, IEEE, 2008.

[50] J. Faist, F. Capasso, D. L. Sivco, C. Sirtori, A. L. Hutchinson, and A. Y. Cho, "Quantum cascade laser," *Science*, vol. 264, no. 5158, pp. 553–556, 1994.

[51] B. S. Williams, S. Kumar, Q. Hu, and J. L. Reno, "High-power terahertz quantum-cascade lasers," *Electronics Letters*, vol. 42, no. 2, pp. 89–91, 2006.

[52] S. Kumar, B. S. Williams, S. Kohen, Q. Hu, and J. L. Reno, "Continuous-wave operation of terahertz quantum-cascade lasers above liquid-nitrogen temperature," *Applied Physics Letters*, vol. 84, no. 14, pp. 2494–2496, 2004.

[53] B. S. Williams, "Terahertz quantum-cascade lasers," *Nature Photonics*, vol. 1, no. 9, pp. 517–525, 2007.

[54] S. Verghese, K. Mclntosh, S. Duffy, and E. Duerr, "Continuous-wave terahertz generation using photomixers," in *Terahertz Sources and Systems*, pp. 145–165, Springer, 2001.

[55] S. Verghese, K. McIntosh, S. Calawa, W. Dinatale, E. Duerr, and K. Molvar, "Generation and detection of coherent terahertz waves using two photomixers," *Applied Physics Letters*, vol. 73, no. 26, pp. 3824–3826, 1998.

[56] P. U. Jepsen, R. H. Jacobsen, and S. Keiding, "Generation and detection of terahertz pulses from biased semiconductor antennas," *JOSA B*, vol. 13, no. 11, pp. 2424–2436, 1996.

[57] P. H. Siegel, "Terahertz technology," *IEEE Transactions on Microwave Theory and Techniques*, vol. 50, no. 3, pp. 910–928, 2002.

[58] E. Brigham, "Fourier series and sampled waveforms," *The Fast Fourier Transform*, pp. 75–90, 1974.

[59] "Network analyzer measurements." `http://literature.cdn.keysight.com/litweb/pdf/5965-7710E.pdf`. Accessed: 2018-02-30.

[60] N.-N. Feng, G.-R. Zhou, and W.-P. Huang, "Space mapping technique for design optimization of antireflection coatings in photonic devices," *Journal of Lightwave Technology*, vol. 21, no. 1, pp. 281–285, 2003.

[61] M. Nevière and E. Popov, *Light propagation in periodic media: differential theory and design*. CRC Press, 2002.

[62] M. Born *et al.*, "Principles of Optics," *Pergamon Press*, vol. 6, pp. 188–189, 1980.

[63] S. Berthier and J. Lafait, "Effective medium theory: mathematical determination of the physical solution for the dielectric constant," *Optics Communications*, vol. 33, no. 3, pp. 303–306, 1980.

[64] V. D. Bruggeman, "Berechnung verschiedener physikalischer konstanten von heterogenen substanzen. i. dielektrizitätskonstanten und leitfähigkeiten der mischkörper aus isotropen substanzen," *Annalen Der Physik*, vol. 416, no. 7, pp. 636–664, 1935.

[65] J. E. Oswald and P. H. Siegel, "The application of the FDTD method to millimeter-wave filter circuits including the design and analysis of a compact coplanar strip filter for THz frequencies," in *Microwave Symposium Digest, 1994., IEEE MTT-S International*, pp. 309–312, IEEE, 1994.

[66] K. Yee, "Numerical solution of initial boundary value problems involving maxwell's equations in isotropic media," *IEEE Transactions on Antennas and Propagation*, vol. 14, no. 3, pp. 302–307, 1966.

[67] A. Taflove and M. E. Brodwin, "Numerical solution of steady-state electromagnetic scattering problems using the time-dependent maxwell's equations," *IEEE Transactions on Microwave Theory and Techniques*, vol. 23, no. 8, pp. 623–630, 1975.

[68] A. Taflove and S. C. Hagness, *Computational electrodynamics: the finite-difference time-domain method.* Artech house, 2005.

[69] K. Han and C.-H. Chang, "Numerical modeling of sub-wavelength anti-reflective structures for solar module applications," *Nanomaterials*, vol. 4, no. 1, pp. 87–128, 2014.

[70] K. S. Deshpande, *Simulation and implementation of moth-eye structures as a broadband anti-reflective layer.* Rochester Institute of Technology, 2013.

[71] F. Yan, E. P. Parrott, X. D. Liu, and E. Pickwell-MacPherson, "Low-cost and broadband terahertz antireflection coatings based on DMSO-doped PEDOT/PSS," *Optics Letters*, vol. 40, no. 12, pp. 2886–2889, 2015.

[72] J. B. Schneider, "Understanding the finite-difference time-domain method," *School of electrical engineering and computer science Washington State University.–URL: http://www.Eecs.Wsu.Edu/~ schneidj/ufdtd/(request data: 29.11. 2012)*, 2010.

[73] Z. Fu, Q. Gan, Y. J. Ding, and F. J. Bartoli, "From waveguiding to spatial localization of THz waves within a plasmonic metallic grating," *IEEE Journal of selected topics in quantum electronics*, vol. 14, no. 2, pp. 486–490, 2008.

[74] J. Shibayama, Y. Uchizono, S. Ozaki, J. Yamauchi, and H. Nakano, "Treatment of metal for the FDTD analysis of terahertz devices," *Optical and Quantum Electronics*, vol. 46, no. 2, pp. 345–356, 2014.

[75] W. Yu, *Electromagnetic simulation techniques based on the FDTD method*, vol. 221. John Wiley & Sons, 2009.

[76] G. Mur, "Absorbing boundary conditions for the finite-difference approximation of the time-domain electromagnetic-field equations," *IEEE transactions on Electromagnetic Compatibility*, no. 4, pp. 377–382, 1981.

[77] J.-P. Berenger, "A perfectly matched layer for the absorption of electromagnetic waves," *Journal of Computational Physics*, vol. 114, no. 2, pp. 185–200, 1994.

[78] S. D. Gedney, "An anisotropic perfectly matched layer-absorbing medium for the truncation of FDTD lattices," *IEEE transactions on Antennas and Propagation*, vol. 44, no. 12, pp. 1630–1639, 1996.

[79] W.-J. Tsay and D. M. Pozar, "Application of the FDTD technique to periodic problems in scattering and radiation," *IEEE Microwave and Guided Wave Letters*, vol. 3, no. 8, pp. 250–252, 1993.

[80] G. Turner and C. Christodoulou, "Broadband periodic boundary condition for FDTD analysis of phased array antennas," in *Antennas and Propagation Society International Symposium, 1998. IEEE*, vol. 2, pp. 1020–1023, IEEE, 1998.

[81] N. Ashcroft and N. Mermin, "Solid state physics, holt-saunders international editions: Science: Physics," 1976.

[82] "Symmetric/anti-symmetric BCs , fields at symmetry boundary." `https://kb.lumerical.com/en/ref_sim_obj_symmetric_anti-symmetric.html`. Accessed: 2018-06-01.

[83] J. Olkkonen, *Finite difference time domain studies on sub-wavelength aperture structures*. VTT, 2010.

[84] C. D. Sarris, "Adaptive mesh refinement for time-domain numerical electromagnetics," *Synthesis Lectures on Computational Electromagnetics*, vol. 1, no. 1, pp. 1–154, 2007.

[85] M. D. Brzeska, *RF modelling and characterization of tyre pressure sensors and vehicle access systems*, vol. 78. KIT Scientific Publishing, 2015.

[86] Z. Popovic and B. D. Popovic, *Introductory electromagnetics*. Prentice hall Upper Saddle River, NJ, USA:, 2000.

[87] P. Harms, R. Mittra, and W. Ko, "Implementation of the periodic boundary condition in the finite-difference time-domain algorithm for FSS structures," *IEEE Transactions on Antennas and Propagation*, vol. 42, no. 9, pp. 1317–1324, 1994.

[88] K. ElMahgoub, F. Yang, A. Z. Elsherbeni, V. Demir, and J. Chen, "FDTD analysis of periodic structures with arbitrary skewed grid," *IEEE Transactions on Antennas and Propagation*, vol. 58, no. 8, pp. 2649–2657, 2010.

[89] M. Naftaly and R. Miles, "A method for removing etalon oscillations from THz time-domain spectra," *Optics Communications*, vol. 280, no. 2, pp. 291–295, 2007.

[90] M. Pancaldi, R. Freeman, M. Hudl, M. C. Hoffmann, S. Urazhdin, P. Vavassori, and S. Bonetti, "Anti-reflection coating design for metallic terahertz meta-materials," *Optics Express*, vol. 26, no. 3, pp. 2917–2927, 2018.

[91] D. Stroud, "The effective medium approximations: Some recent developments," *Superlattices and Microstructures*, vol. 23, no. 3-4, pp. 567–573, 1998.

[92] Y. W. Chen and X.-C. Zhang, "Anti-reflection implementations for terahertz waves," *Frontiers of Optoelectronics*, vol. 7, no. 2, pp. 243–262, 2014.

[93] H. Kikuta, H. Yoshida, and K. Iwata, "Ability and limitation of effective medium theory for subwavelength gratings," *Optical Review*, vol. 2, no. 2, pp. 92–99, 1995.

[94] E. B. Grann, M. Moharam, and D. A. Pommet, "Artificial uniaxial and biaxial dielectrics with use of two-dimensional subwavelength binary gratings," *JOSA A*, vol. 11, no. 10, pp. 2695–2703, 1994.

[95] A. Drauschke, "Analysis of nearly depth-independent transmission of lamellar gratings in zeroth diffraction order in TM polarization," *Journal of Optics A: Pure and Applied Optics*, vol. 8, no. 6, p. 511, 2006.

[96] C. Brückner, T. Käsebier, B. Pradarutti, S. Riehemann, G. Notni, E.-B. Kley, and A. Tünnermann, "Broadband antireflective structures applied to high resistive float zone silicon in the THz spectral range," *Optics Express*, vol. 17, no. 5, pp. 3063–3077, 2009.

[97] W. L. Bragg and A. B. Pippard, "The form birefringence of macromolecules," *Acta Crystallographica*, vol. 6, no. 11-12, pp. 865–867, 1953.

[98] S.-i. Kuroo, S. Oyama, K. Shiraishi, H. Sasho, and K. Fukushima, "Reduction of light reflection at silicon-plate surfaces by means of subwavelength gratings in terahertz region," *Applied Optics*, vol. 49, no. 15, pp. 2806–2812, 2010.

[99] J. M. Dos Santos and L. M. Bernardo, "Antireflection structures with use of multilevel subwavelength zero-order gratings," *Applied Optics*, vol. 36, no. 34, pp. 8935–8938, 1997.

[100] G. Hernández, *Fabry-Perot interferometers*. No. 3, Cambridge University Press, 1988.

[101] D. Nazarova, B. Mednikarov, and P. Sharlandjiev, "Resonant optical transmission from a one-dimensional relief metalized subwavelength grating," *Applied Optics*, vol. 46, no. 34, pp. 8250–8255, 2007.

[102] R. Fastampa, L. Pilozzi, and M. Missori, "Cancellation of Fabry-Perot interference effects in terahertz time-domain spectroscopy of optically thin samples," *Physical Review A*, vol. 95, no. 6, p. 063831, 2017.

[103] A. Yariv, "Optical electronics, 3rd," *Edition (Holt, Rinehart and Winston, New York, 1985)*, 1985.

[104] L. Duvillaret, F. Garet, and J.-L. Coutaz, "A reliable method for extraction of material parameters in terahertz time-domain spectroscopy," *IEEE Journal of selected topics in quantum electronics*, vol. 2, no. 3, pp. 739–746, 1996.

[105] C. Brückner, B. Pradarutti, O. Stenzel, R. Steinkopf, S. Riehemann, G. Notni, and A. Tünnermann, "Broadband antireflective surface-relief structure for THz optics," *Optics Express*, vol. 15, no. 3, pp. 779–789, 2007.

[106] J. Bomba, J. Suszek, M. Makowski, A. Sobczyk, and M. Sypek, "3-D printed anti-reflection structures for the terahertz region," *Journal of Infrared, Millimeter, and Terahertz Waves*, vol. 39, no. 1, pp. 24–35, 2018.

[107] T. D. Dorney, R. G. Baraniuk, and D. M. Mittleman, "Material parameter estimation with terahertz time-domain spectroscopy," *JOSA A*, vol. 18, no. 7, pp. 1562–1571, 2001.

[108] P. U. Jepsen and B. M. Fischer, "Dynamic range in terahertz time-domain transmission and reflection spectroscopy," *Optics Letters*, vol. 30, no. 1, pp. 29–31, 2005.

[109] Y. Song and Y. Lee, "Simulation of antireflective subwavelength grating structures for optical device applications," in *Numerical Simulation of Optoelectronic Devices, 2009. NUSOD 2009. 9th International Conference on*, pp. 103–104, IEEE, 2009.

[110] M. J. Madou, *Fundamentals of microfabrication: the science of miniaturization.* CRC press, 2002.

[111] K. Sato, M. Shikida, Y. Matsushima, T. Yamashiro, K. Asaumi, Y. Iriye, and M. Yamamoto, "Characterization of orientation-dependent etching properties of single-crystal silicon: effects of KOH concentration," *Sensors and Actuators A: Physical*, vol. 64, no. 1, pp. 87–93, 1998.

[112] E. D. Walsby, R. Cheung, R. J. Blaikie, and D. R. Cumming, "Fabrication of multilevel silicon diffractive lenses for terahertz frequencies," in *Proc. SPIE*, vol. 3879, pp. 79–87, 1999.

[113] S. Wang, T. Yuan, E. Walsby, R. Blaikie, S. Durbin, D. Cumming, J. Xu, and X.-C. Zhang, "Characterization of T-ray binary lenses," *Optics Letters*, vol. 27, no. 13, pp. 1183–1185, 2002.

[114] D. Feng, Y. Yan, G. Jin, and S. Fan, "Beam focusing characteristics of diffractive lenses with binary subwavelength structures," *Optics Communications*, vol. 239, no. 4, pp. 345–352, 2004.

[115] M. Rachon, K. Liebert, A. Siemion, J. Bomba, A. Sobczyk, W. Knap, D. Coquillat, J. Suszek, and M. Sypek, "Geometrical aberration suppression for large aperture sub-THz lenses," *Journal of Infrared, Millimeter, and Terahertz Waves*, vol. 38, no. 3, pp. 347–355, 2017.

[116] A. Siemion, A. Siemion, J. Suszek, A. Kowalczyk, J. Bomba, A. Sobczyk, N. Palka, P. Zagrajek, A. Kolodziejczyk, and M. Sypek, "THz beam shaping based on paper diffractive optics," *IEEE Transactions on Terahertz Science and Technology*, vol. 6, no. 4, pp. 568–575, 2016.

[117] W. D. Furlan, V. Ferrando, J. A. Monsoriu, P. Zagrajek, E. Czerwińska, and M. Szustakowski, "3D printed diffractive terahertz lenses," *Optics Letters*, vol. 41, no. 8, pp. 1748–1751, 2016.

[118] J. Soret, "Ueber die durch kreisgitter erzeugten diffractionsphänomene," *Annalen der Physik*, vol. 232, no. 9, pp. 99–113, 1875.

[119] S. Karimkashi and A. A. Kishk, "Focusing properties of Fresnel zone plate lens antennas in the near-field region," *IEEE Transactions on Antennas and Propagation*, vol. 59, no. 5, pp. 1481–1487, 2011.

[120] W. Pan and W. Zeng, "Far-field characteristics of the square grooved-dielectric lens antenna for the terahertz band," *Applied Optics*, vol. 55, no. 26, pp. 7330–7336, 2016.

[121] S. F. Busch, S. Schumann, B. Scherger, C. Jansen, M. Scheller, B. Fischer, and M. Koch, "Optically controlled terahertz filtering, beam steering, and imaging," in *Infrared, Millimeter, and Terahertz Waves (IRMMW-THz), 2012 37th International Conference on*, pp. 1–2, IEEE, 2012.

[122] C. Rizza, A. Ciattoni, L. Columbo, M. Brambilla, and F. Prati, "Terahertz optically tunable dielectric metamaterials without microfabrication," *Optics Letters*, vol. 38, no. 8, pp. 1307–1309, 2013.

[123] X. Wang, Z. Xie, W. Sun, S. Feng, Y. Cui, J. Ye, and Y. Zhang, "Focusing and imaging of a virtual all-optical tunable terahertz Fresnel zone plate," *Optics Letters*, vol. 38, no. 22, pp. 4731–4734, 2013.

[124] L. Cohen and M. Schneider, "Microlenses for coupling junction lasers to optical fibers," *Applied Optics*, vol. 13, no. 1, pp. 89–94, 1974.

[125] K. Iga, M. Oikawa, S. Misawa, J. Banno, and Y. Kokubun, "Stacked planar optics: an application of the planar microlens," *Applied Optics*, vol. 21, no. 19, pp. 3456–3460, 1982.

[126] A. Siemion, A. Siemion, M. Makowski, J. Suszek, J. Bomba, A. Czerwiński, F. Garet, J.-L. Coutaz, and M. Sypek, "Diffractive paper lens for terahertz optics," *Optics Letters*, vol. 37, no. 20, pp. 4320–4322, 2012.

[127] L. d'Auria, J. Huignard, A. Roy, and E. Spitz, "Photolithographic fabrication of thin film lenses," *Optics Communications*, vol. 5, no. 4, pp. 232–235, 1972.

[128] A. Firester, D. Hoffman, E. James, and M. Heller, "Fabrication of planar optical phase elements," *Optics Communications*, vol. 8, no. 2, pp. 160–162, 1973.

[129] C. Brückner, G. Notni, and A. Tünnermann, "Optimal arrangement of 90°off-axis parabolic mirrors in THz setups," *Optik-International Journal for Light and Electron Optics*, vol. 121, no. 1, pp. 113–119, 2010.

[130] J. Jahns and S. J. Walker, "Two-dimensional array of diffractive microlenses fabricated by thin film deposition," *Applied Optics*, vol. 29, no. 7, pp. 931–936, 1990.

Bibliography

[131] N. Kitaura, S. Ogata, and Y. Mori, "Spectrometer employing a micro-Fresnel lens," *Optical Engineering*, vol. 34, no. 2, pp. 584–589, 1995.

[132] S. Yu-Lei, Z. Qing-Li, and Z. Cun-Lin, "Diffraction of terahertz waves after passing through a Fresnel lens," *Chinese Physics B*, vol. 18, no. 12, p. 5511, 2009.

[133] C.-C. Tsui, H.-C. Wei, W.-F. Chang, and G.-D. J. Su, "Design and fabrication of a mid-wavelength infrared Fresnel lens via liquid poly (methyl methacrylate)," *Journal of Micromechanics and Microengineering*, vol. 22, no. 4, p. 045010, 2012.

[134] Y. Gao, J. Lin, P. Jin, J. Tan, G. Davies, and P. D. Prewett, "Stop grating for perfect replication of micro Fresnel lens by thermal imprinting," *Journal of Micromechanics and Microengineering*, vol. 22, no. 6, p. 065018, 2012.

[135] M. Sypek, M. Makowski, E. Hérault, A. Siemion, A. Siemion, J. Suszek, F. Garet, and J.-L. Coutaz, "Highly efficient broadband double-sided Fresnel lens for THz range," *Optics Letters*, vol. 37, no. 12, pp. 2214–2216, 2012.

[136] E. Hecht and A. Zajac, "Optics, vol. 4," 2002.

[137] A. Gallant, M. Kaliteevski, S. Brand, D. Wood, M. Petty, R. Abram, and J. Chamberlain, "Terahertz frequency bandpass filters," *Journal of Applied Physics*, vol. 102, no. 2, p. 023102, 2007.

[138] D. Headland, W. Withayachumnankul, M. Webb, H. Ebendorff-Heidepriem, A. Luiten, and D. Abbott, "Analysis of 3D-printed metal for rapid-prototyped reflective terahertz optics," *Optics Express*, vol. 24, no. 15, pp. 17384–17396, 2016.

[139] D. Atwood, "Soft X-rays and extreme ultraviolet radiation," *Principles and Applications*, 1999.

[140] J.-P. Bérenger, "Perfectly matched layer (PML) for computational electromagnetics," *Synthesis Lectures on Computational Electromagnetics*, vol. 2, no. 1, pp. 1–117, 2007.

[141] K. Ajito and Y. Ueno, "THz chemical imaging for biological applications," *IEEE Transactions on Terahertz Science and Technology*, vol. 1, no. 1, pp. 293–300, 2011.

[142] T. Globus, A. Bykhovski, T. Khromova, B. Gelmont, L. Tamm, and L. Salay, "Low-terahertz spectroscopy of liquid water," in *Proc. SPIE*, vol. 6772, p. 67720S, 2007.

[143] J. Xu, K. W. Plaxco, and S. J. Allen, "Absorption spectra of liquid water and aqueous buffers between 0.3 and 3.72 THz," *The Journal of Chemical hysics, volume=124, number=3, pages=036101, year=2006, publisher=AIP*.

[144] A. J. Baragwanath, P. Swift, D. Dai, A. Gallant, and M. Chamberlain, "Silicon based microfluidic device for THz frequencies," in *35th International Conference on Infrared Millimeter and Terahertz Waves (IRMMW-THz), Rome, Italy*, pp. 1–2, IEEE, 2010.

[145] Q. Tang, M. Liang, Y. Lu, P. K. Wong, G. J. Wilmink, D. D. Zhang, and H. Xin, "Microfluidic devices for terahertz spectroscopy of live cells toward lab-on-a-chip applications," *Sensors*, vol. 16, no. 4, p. 476, 2016.

[146] L. Liu, Z. Jiang, S. Rahman, M. I. B. Shams, B. Jing, A. Kannegulla, and L.-J. Cheng, "Quasi-optical terahertz microfluidic devices for chemical sensing and imaging," *Micromachines*, vol. 7, no. 5, p. 75, 2016.

[147] P. A. George, W. Hui, F. Rana, B. G. Hawkins, A. E. Smith, and B. J. Kirby, "Microfluidic devices for terahertz spectroscopy of biomolecules," *Optics Express*, vol. 16, no. 3, pp. 1577–1582, 2008.

[148] H. Kitahara, T. Yagi, K. Mano, M. W. Takeda, S. Kojima, and S. Nishizawa, "Dielectric characteristics of water solutions of ethanol in the terahertz region," *Journal of the Korean Physical Society*, vol. 46, no. 1, pp. 82–85, 2005.

[149] G. G. Raju, *Dielectrics in electric fields*. CRC press, 2016.

[150] R. H. Giles, A. Gatesman, J. Fitzgerald, S. Fisk, and J. Waldman, "Tailoring artificial dielectric materials at terahertz frequencies," in *Proc. of Fourth Int. Symp. of Space THz Technology*, 1993.

[151] L. Liu, R. Pathak, L.-J. Cheng, and T. Wang, "Real-time frequency-domain terahertz sensing and imaging of isopropyl alcohol–water mixtures on a microfluidic chip," *Sensors and Actuators B: Chemical*, vol. 184, pp. 228–234, 2013.

[152] J. Forsyth, R. Grünewald, A. Rostami-Hodjegan, M. Lennard, H. Sagar, and G. Tucker, "Parkinson's disease and cyp1a2 activity," *British Journal of Clinical Pharmacology*, vol. 50, no. 4, pp. 303–309, 2000.

[153] J. Shen, G. Wang, D. Jiang, L. Liang, and X. Xu, "Terahertz spectroscopic investigations of caffeine and 3-acetylmorphine," *Optik-International Journal for Light and Electron Optics*, vol. 121, no. 18, pp. 1712–1716, 2010.

[154] H.-B. Liu, Y. Chen, and X.-C. Zhang, "Characterization of anhydrous and hydrated pharmaceutical materials with THz time-domain spectroscopy," *Journal of Pharmaceutical Sciences*, vol. 96, no. 4, pp. 927–934, 2007.

[155] D. M. Mittleman, R. H. Jacobsen, and M. C. Nuss, "T-ray imaging," *IEEE Journal of selected topics in quantum electronics*, vol. 2, no. 3, pp. 679–692, 1996.

[156] P. Arguijo and M. S. Scholl, "Exact ray-trace beam for an off-axis paraboloid surface," *Applied Optics*, vol. 42, no. 16, pp. 3284–3289, 2003.

[157] C. Bond and C. A. Pipan, "How to align an off-axis parabolic mirror," in *Reflective Optics II*, vol. 1113, pp. 236–249, International Society for Optics and Photonics, 1989.

[158] P. Su, *Absolute measurements of large mirrors.* The University Of Arizona, 2008.

[159] G. Lemaitre and M. Wang, "Active mirrors warped using zernike polynomials for correcting off-axis aberrations of fixed primary mirrors. I. theory and elasticity design.," *Astronomy and Astrophysics Supplement Series*, vol. 114, p. 373, 1995.

[160] J. Burke, "Null test of an off-axis parabolic mirror. II. configuration with planar reference wave and spherical return surface," *Optics Express*, vol. 17, no. 5, pp. 3242–3254, 2009.

[161] F.-M. Yeh, D.-C. Chen, C.-L. Tien, and S.-C. Lee, "The off-axis parabolic mirror optical axis adjustment based on cyclic shearing interferometer," in *Optoelectronics Global Conference (OGC), 2015*, pp. 1–4, IEEE, 2015.

[162] V. P. Koronkevich, G. A. Lenkova, and A. E. Matochkin, "Special features of newton-type fringe formation in a diffraction interferometer," *Applied Optics*, vol. 45, no. 1, pp. 44–52, 2006.

[163] P. Arguijo, M. S. Scholl, and G. Paez, "Diffraction patterns formed by an off-axis paraboloid surface," *Applied Optics*, vol. 40, no. 17, pp. 2909–2916, 2001.

[164] J. E. Harvey, C. L. Vernold, A. Krywonos, and P. L. Thompson, "Diffracted radiance: a fundamental quantity in nonparaxial scalar diffraction theory," *Applied Optics*, vol. 38, no. 31, pp. 6469–6481, 1999.

[165] V. N. Mahajan, "Aberrated point-spread functions for rotationally symmetric aberrations," *Applied Optics*, vol. 22, no. 19, pp. 3035–3041, 1983.

[166] R. Barakat and A. Houston, "Diffraction effects of coma," *JOSA*, vol. 54, no. 9, pp. 1084–1088, 1964.

[167] R. Barakat and A. Houston, "The aberrations of non-rotationally symmetric systems and their diffraction effects," *Optica Acta: International Journal of Optics*, vol. 13, no. 1, pp. 1–30, 1966.

[168] "Motion control software,Hexapod." `https://www.physikinstrumente.co.uk/en/technology/controllers-software/motion-control-software/`. Accessed: 2018-04-01.

[169] "antenna-theory, field region." `http://www.antenna-theory.com/basics/fieldRegions.php/`. Accessed: 2018-04-20.

[170] S. Silver, "Microwave aperture antennas and diffraction theory," *JOSA*, vol. 52, no. 2, pp. 131–139, 1962.

[171] K. W. Kim, K.-S. Kim, H. Kim, S. H. Lee, J.-H. Park, J.-H. Han, S.-H. Seok, J. Park, Y. Choi, Y. I. Kim, *et al.*, "Terahertz dynamic imaging of skin drug absorption," *Optics Express*, vol. 20, no. 9, pp. 9476–9484, 2012.

[172] J. A. Zeitler, P. F. Taday, D. A. Newnham, M. Pepper, K. C. Gordon, and T. Rades, "Terahertz pulsed spectroscopy and imaging in the pharmaceutical setting-a review," *Journal of Pharmacy and Pharmacology*, vol. 59, no. 2, pp. 209–223, 2007.

[173] H. Hristov, J. Rodriguez, and W. Grote, "The grooved-dielectric Fresnel zone plate: An effective terahertz lens and antenna," *Microwave and Optical Technology Letters*, vol. 54, no. 6, pp. 1343–1348, 2012.

[174] E. Walsby, S. Wang, J. Xu, T. Yuan, R. Blaikie, S. Durbin, X.-C. Zhang, and D. Cumming, "Multilevel silicon diffractive optics for terahertz waves," *Journal of Vacuum Science & Technology B: Microelectronics and Nanometer Structures Processing, Measurement, and Phenomena*, vol. 20, no. 6, pp. 2780–2783, 2002.

[175] M. S. Komlenok, B. O. Volodkin, B. A. Knyazev, T. Kononenko, V. Kononenko, V. I. Konov, V. Soifer, V. Pavel'ev, K. N. Tukmakov, and Y. Y. Choporova, "Fabrication of a multilevel THz Fresnel lens by femtosecond laser ablation," *Quantum Electronics*, vol. 45, no. 10, p. 933, 2015.

[176] N. Ghalichechian and K. Sertel, "Permittivity and loss characterization of SU-8 films for mmW and terahertz applications," *IEEE Antennas and Wireless Propagation Letters*, vol. 14, pp. 723–726, 2015.

[177] G. Khanarian, "Optical properties of cyclic olefin copolymers," *Optical Engineering*, vol. 40, no. 6, pp. 1024–1030, 2001.

[178] L. Minkevičius, S. Indrišiūnas, R. Šniaukas, B. Voisiat, V. Janonis, V. Tamošiūnas, I. Kašalynas, G. Račiukaitis, and G. Valušis, "Terahertz multilevel phase Fresnel lenses fabricated by laser patterning of silicon," *Optics Letters*, vol. 42, no. 10, pp. 1875–1878, 2017.